



HAL
open science

Mathematical models for understanding lithium sulfur batteries phenomena

Vigneshwaran Thangavel

► **To cite this version:**

Vigneshwaran Thangavel. Mathematical models for understanding lithium sulfur batteries phenomena. Other. Université de Picardie Jules Verne, 2019. English. NNT : 2019AMIE0017 . tel-03638140

HAL Id: tel-03638140

<https://theses.hal.science/tel-03638140>

Submitted on 12 Apr 2022

HAL is a multi-disciplinary open access archive for the deposit and dissemination of scientific research documents, whether they are published or not. The documents may come from teaching and research institutions in France or abroad, or from public or private research centers.

L'archive ouverte pluridisciplinaire **HAL**, est destinée au dépôt et à la diffusion de documents scientifiques de niveau recherche, publiés ou non, émanant des établissements d'enseignement et de recherche français ou étrangers, des laboratoires publics ou privés.



Thèse de Doctorat

Mention : Chimie

Spécialité : Chimie Informatique Théorique

présentée à *l'Ecole Doctorale en Sciences Technologie et Santé (ED 585)*

de l'Université de Picardie Jules Verne

par

Vigneshwaran THANGAVEL

pour obtenir le grade de Docteur de l'Université de Picardie Jules Verne

*Mathematical models for understanding lithium sulfur
batteries phenomena*

Soutenue le 05/11/2019, après avis des rapporteurs, devant le jury d'examen :

M^{me} C. Guéry, Professeur

M. T. Vegge, Professeur

M. R. Dominko, Professeur de recherche

M^{me} M. Marinescu, Maître de Conférences

M. C. Jordy, Ingénieur

M. M. Morcrette, Chargé de Recherches

M. A. A. Franco, Professeur

Président

Rapporteur

Rapporteur

Examineur

Examineur

Co-encadrant

Directeur de thèse



“Ever tried. Ever failed. No matter. Try again. Fail again. Fail better.”

– Samuel Beckett (*Worstward Ho*).

Dedicated to my parents
Chitra and Thangavel

Acknowledgements

First, I would like to sincerely thank my supervisors, Alejandro Franco and Mathieu Morcrette for providing me the opportunity to work on this PhD topic. I am grateful for their guidance and motivation, which helped me immensely throughout the four years my PhD.

I wish to convey my sincere thanks to the members of the jury, Tejs Vegge of DTU, Robert Dominko of NIC, Monica Marinescu of Imperial college, Claude Guéry of LRCS and Christian Jordy of SAFT batteries, for accepting our invitation to evaluate this PhD work.

My PhD work is a part of the European Union (EU)'s Horizon 2020 project called High Energy Lithium Sulphur cells and batteries (HELiS). Therefore, I would like thank the EU and CNRS for funding this work. I deeply appreciate the useful discussions with all the HELiS project partners, especially Robert Dominko and Patrik Johansson. I also specially thank Sara Drvarič Talian for her collaboration and for providing the potentiostatic experimental result, which is presented in the chapter 6.

During the entire time of my PhD, I worked at Laboratoire de Réactivité et Chimie des Solides (LRCS), where I had the opportunity to work and become friends with some of the wonderful people. I like to thank Claude Guéry, Afef Mastouri, Mattia Giannini, Carine Davoisne, Jacob Lee and Mariem Belhadj for helpful discussions and collaborative work on Li-S batteries. I am deeply thankful to Kan-Hao Xue, Matias Quiroga, Yinghui Yin, Alexis Rucci and Oscar Xavier Geurrerro, for their discussions and multiple collaborations on modelling work. I also like thank Matthieu Courty and Christine Surcin for helping me with some experiments. I like to thank Christian Masquelier for the accepting me to the class #10 of the MESC Master program, without which I may have not had the opportunity to work at LRCS. I also thank my Master thesis supervisor, Dominique Larcher, whose lessons on experiments helped me a lot during my PhD. I am also grateful to Nathalie Saulnier and Anne Charbonnier for their help with the administrative work. I sincerely thank Youcef Mammeri and Jean-Paul Chehab at LAMFA (UPJV), for their lessons on numerical methods. I like thank my friends at LRCS, Amangeldi Torayev, Jose Vivo Vilches, Garima Shukla, Rakes Elango, Vijay Challuri, Ronan Le Ruyet, Laura Cristina Loaiza Rodriguez, Omer Ulas Kudu, Carlos Eduardo Alarcón Suesca, Emiliano Primo, Abbas Shodiev, Zeliang Su, Iryna Sagaidak, Fan Chen, Damien Cléménçon and many others for making my time at the lab, enjoyable.

I also like to thank my friends from the MESC Master program, Alagaraj Paulraj, Yasemin Duygu Yücel, Violetta Arszewska and Daria Iermakova for their continuous support. I am grateful to my friends back in India, Bineesh, Gautam, Shriram, Vignesh Kumar and Srinivasan Viswanathan, for their perpetual support. Lastly, I would like thank my parents, Chitra and Thangavel and my brother, Srinivasan, whose love and moral support helped me survive during this PhD work.

Table of Contents

| | |
|--|----|
| Chapter 1. General Introduction | 12 |
| 1.1. Energy demand, consumption and production | 12 |
| 1.2. Renewable energy technologies | 16 |
| 1.3. Need for energy storage systems | 18 |
| 1.4. Rechargeable batteries | 21 |
| 1.5. Objective of my thesis | 24 |
| 1.6. Manuscript structure | 25 |
| Chapter 2. State of the art of lithium sulfur batteries | 27 |
| 2.1. Introduction to Li-S batteries | 27 |
| 2.2. Working principle of Li-S batteries | 27 |
| 2.3. Challenges in Li-S batteries | 29 |
| 2.4. Developments in the components of Li-S batteries | 31 |
| 2.4.1. Positive electrode | 31 |
| 2.4.2. Negative electrode..... | 34 |
| 2.4.3. Electrolyte | 35 |
| 2.5. Modelling of Li-S batteries | 36 |
| 2.5.1. Atomistic and Molecular level modelling | 36 |
| 2.5.2. Mesoscopic modelling | 39 |
| 2.5.3. Continuum level modelling..... | 39 |
| 2.6. Conclusions | 42 |
| Chapter 3. A 3D kinetic Monte-Carlo model for Li-S batteries | 44 |
| 3.1 Background and Motivation | 44 |
| 3.2 Theoretical methodology | 45 |
| 3.2.1 Creation of initial C/S mesostructure..... | 45 |
| 3.2.2. Development of the 3D kMC-VSSM model and its assumptions..... | 47 |
| 3.2.3. Equations for rate constants of different types of events..... | 49 |
| 3.2.4. Working principle of the 3D kMC-VSSM code | 52 |
| 3.3. Impact of discharge rate | 55 |
| 3.3.1. General effective evolutions of C/S mesostructure..... | 56 |
| 3.3.2. Mesoscale evolutions of Li ₂ S deposits over carbon | 64 |
| 3.4. Impact of sulfur loading | 73 |
| 3.5. Conclusions | 77 |
| Chapter 4. Microstructurally resolved continuum discharge model | 81 |

| | |
|---|------------|
| 4.1. Introduction | 81 |
| 4.2. Methodology: overall assumptions | 82 |
| 4.3. Methodology: Overall construction and governing equations | 87 |
| 4.3.1. Structural properties of cathode | 87 |
| 4.3.2. Electrochemical reaction kinetics | 88 |
| 4.3.3 Chemical reaction rates | 89 |
| 4.3.4. Transport in the electrolyte | 90 |
| 4.3.5. Intra-flux..... | 91 |
| 4.3.6. Dynamic viscosity evolution..... | 92 |
| 4.3.7. Active surface area and porosity | 94 |
| 4.3.8. Film thickness..... | 95 |
| 4.3.9 Current balance..... | 97 |
| 4.3.10. Cell voltage..... | 97 |
| 4.4. Computational implementation | 98 |
| 4.4.1. Physical model | 99 |
| 4.5. Results and discussion | 100 |
| 4.5.1. Rate capability..... | 101 |
| 4.5.2. Impact of porosity..... | 105 |
| 4.5.3. Impact of particle and pore sizes | 108 |
| 4.5.4. Impact of C/S ratio | 111 |
| 4.6. Conclusions and perspectives | 113 |
| A.4. Appendix: Numerical Schemes | 114 |
| Chapter 5. Cyclic voltammetry model | 118 |
| 5.1. Background and motivation | 118 |
| 5.2. Experimental Section | 122 |
| 5.3.1. Cell setup..... | 122 |
| 5.2.2. Preparation of polysulfides containing electrolyte solutions | 123 |
| 5.2.3. Cyclic voltammetry measurements | 123 |
| 5.3. Theoretical Methodology | 124 |
| 5.3.1. Simulated domain and governing equations | 124 |
| 5.3.2. Computational implementation | 128 |
| 5.4. CVs of dissolved S₈ | 132 |
| 5.4.1. Determining reaction mechanism for the model | 132 |
| 5.4.2. Impact of scan rate on the characteristics of the CV of S ₈ | 139 |
| 5.5. CV of dissolved Li₂S₈ | 141 |
| 5.6. CV of dissolved Li₂S₆ | 144 |

| | |
|--|------------|
| 5.7. Conclusions | 146 |
| A.5 Appendix: Numerical Schemes | 147 |
| A.5.1. Finite volume method | 147 |
| Chapter 6. Nucleation and growth of Li₂S | 153 |
| 6.1 Introduction | 153 |
| 6.2. Experimental Setup | 155 |
| 6.3. Theoretical methodology..... | 156 |
| 6.3.1. Thermodynamics and kinetics of Li ₂ S nucleation | 156 |
| 6.3.2. Other reaction steps and their kinetic equations | 161 |
| 6.3.3. Population balance of Li ₂ S particles | 163 |
| 6.4. The electrochemical measurement | 169 |
| 6.5. Results and discussion | 170 |
| 6.5.1 The experimental vs the simulated electrochemical signals | 170 |
| 6.5.2. The simulated dissolved species concentrations and the individual reaction currents ... | 170 |
| 6.5.3 Simulated evolutions of the Li ₂ S deposits..... | 173 |
| 6.6. Conclusion and perspectives..... | 175 |
| A.6 Appendix: Numerical Schemes | 175 |
| A.6.1. Discretization of the population balance equation | 175 |
| Chapter 7. Experimental work and discharge model validation | 181 |
| 7.1. Introduction | 181 |
| 7.2. Materials used..... | 181 |
| 7.3. Surface area and porosimetry analyses of carbon nano powder | 181 |
| 7.4. Sulfur impregnation..... | 184 |
| 7.5. C/S electrode film fabrication | 188 |
| 7.5.1. Slurry preparation | 188 |
| 7.5.2. Coating of electrode film | 189 |
| 7.6. Coin cell assembly | 190 |
| 7.7. Galvanostatic measurement..... | 190 |
| 7.8. Theoretical methodology..... | 191 |
| 7.9. Results and discussion | 195 |
| 7.9.1 Galvanostatic cycling..... | 195 |
| 7.9.2. The experimental vs the simulated discharge curves..... | 196 |
| 7.9.3. The simulated evolutions of cathode porosities, solid and dissolved species..... | 197 |
| 7.10. Conclusions | 200 |
| Chapter 8. General conclusions and perspectives | 203 |
| Résumé développé de la thèse en Français (Summary in French) | 210 |

| | |
|---|-----|
| Bibliography | 221 |
| Appendix I: List of acronyms and abbreviations | 234 |
| Appendix II: List of nomenclatures | 237 |
| Abstract (Résumé) | 241 |

Chapter 1. General Introduction

Contents

| | |
|---|----|
| 1.1. Energy demand, consumption and production..... | 12 |
| 1.2. Renewable energy technologies | 16 |
| 1.3. Need for energy storage systems..... | 18 |
| 1.4. Rechargeable batteries..... | 21 |
| 1.5. Objective of my thesis | 24 |
| 1.6. Manuscript structure..... | 25 |

Chapter 1. General Introduction

1.1. Energy demand, consumption and production

We now live in a technological world, and energy is more crucial than ever in our day to day lives. Additionally, we like the current technologies such as smart phones, computers, self-driving cars, etc., to become smarter and faster in the future, which could mean that they may consume more energy. These technological innovations and developments, have aided the economic growth of countries around the world, which in turn increased the demand for energy (Fig. 1.1) [1].

Growth in GDP and energy

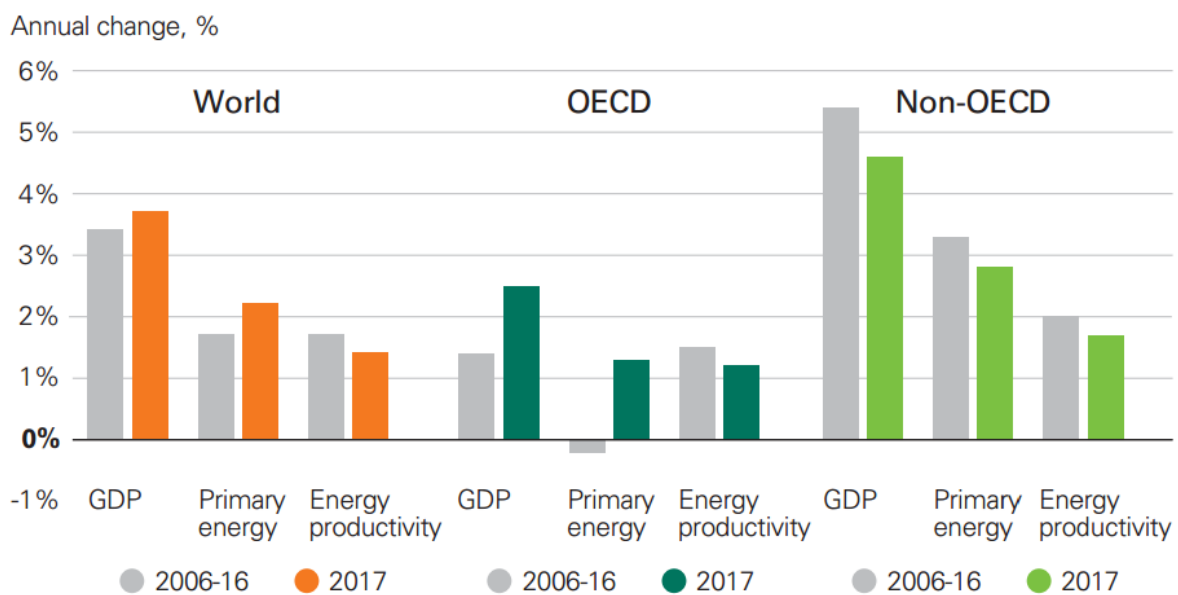


Figure 1.1. Rates of change in Gross Domestic Products (GDP), primary energy demand and energy productivity, in the world and in the countries within and outside the Organisation for Economic Co-operation and Development (OECD) [1].

These economic and technological developments have also improved the living conditions, increased life expectancy [2], reduced child mortality [3], etc. in developing countries like India and China. Therefore these improvements have also led to the growth in human

population until the year 2100 [4]. Since the people around the world will continue to strive for the betterment of their lives and living conditions, the global energy consumption is projected to increase in the future due to the population growth (Fig. 1.2) [5].

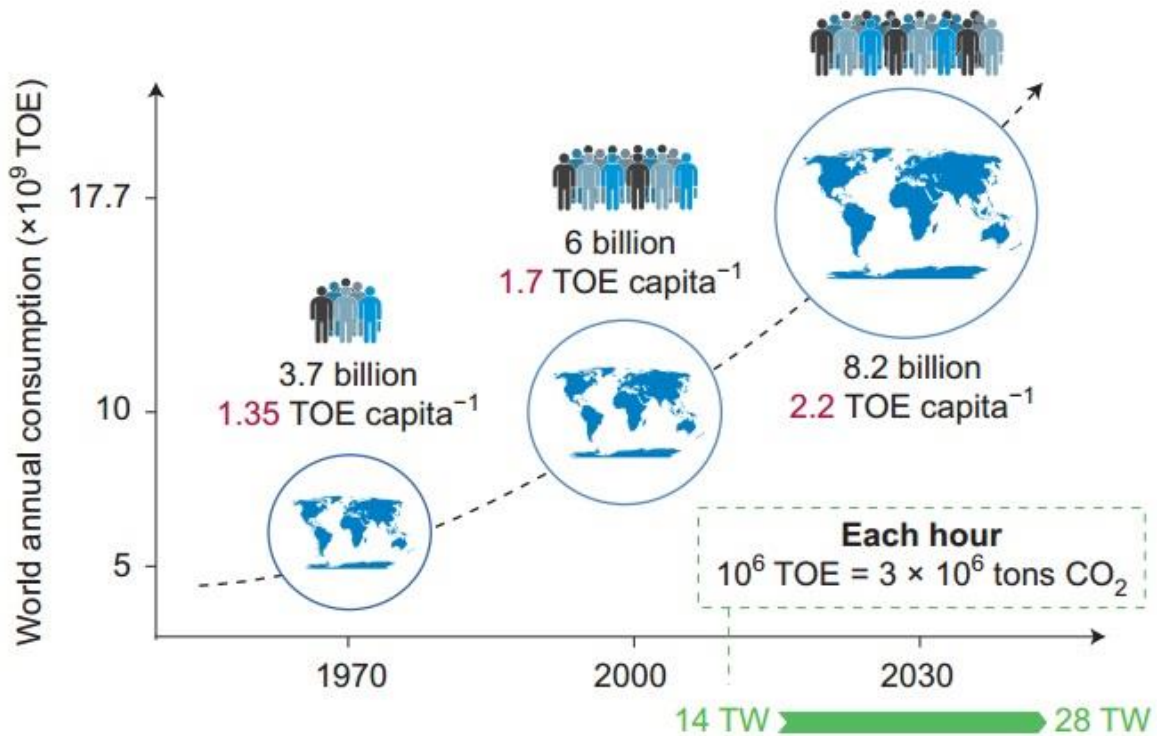


Figure 1.2. Relationship between annual global energy consumption given in ton of oil equivalent and human population [5].

For the good of the many, the current trends in the technological and socio-economic progress cannot be stopped. Therefore, it is highly necessary to increase the production of energy to meet the demand. However, the majority of the energy currently being consumed is produced from fossil fuel sources (Fig. 1.3) [1]. This energy consumption trend is not sustainable, since the reserves for fossil fuels such as oil and natural gas will be exhausted within the next fifty years, while coal will be exhausted within the next 115 years [6]. Further issues with the fossil fuels are the emissions of greenhouse gases (GHG) and particulates matter which cause serious damage to environment, health, global climate, etc. In the year

2018, the emission of GHG like carbon dioxide emission (CO₂) is projected to increase by 2.7% which could be correlated to the increase in the consumption of fossil fuels in countries such as India, China and the United States of America (USA) [7]. This growth in the global CO₂ emission is the largest in the recent years, since it was 1.6% in the year 2017 which was preceded by a period of three years with very low or no growth [7].

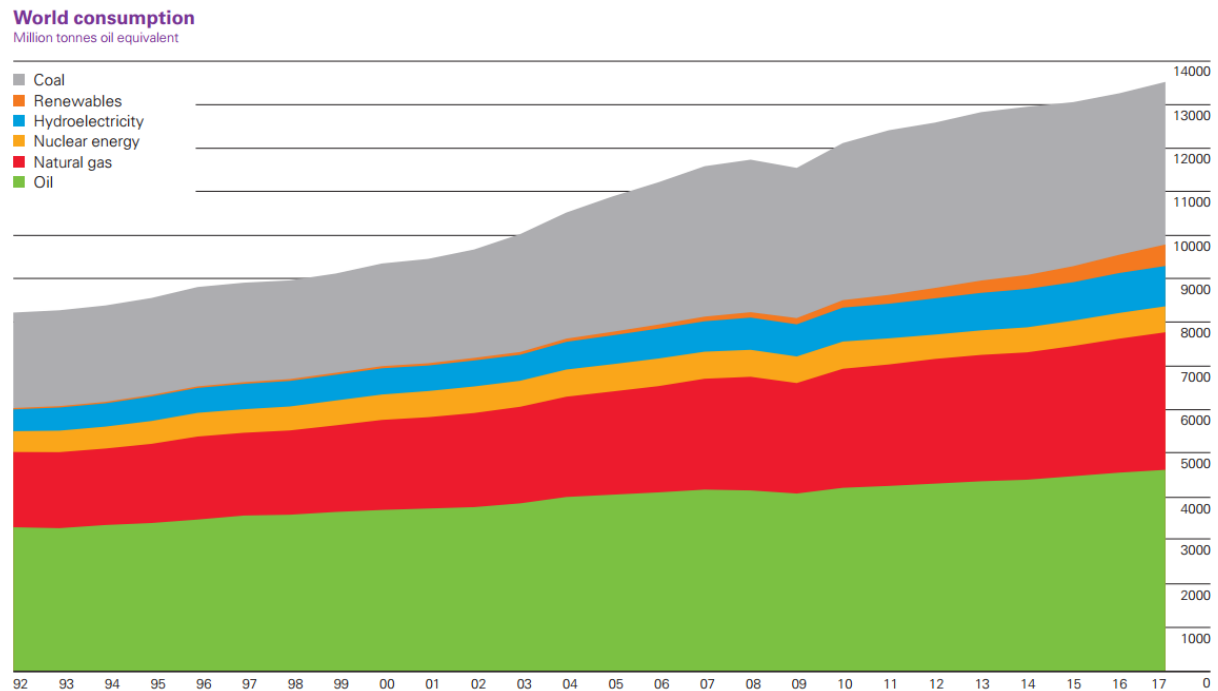


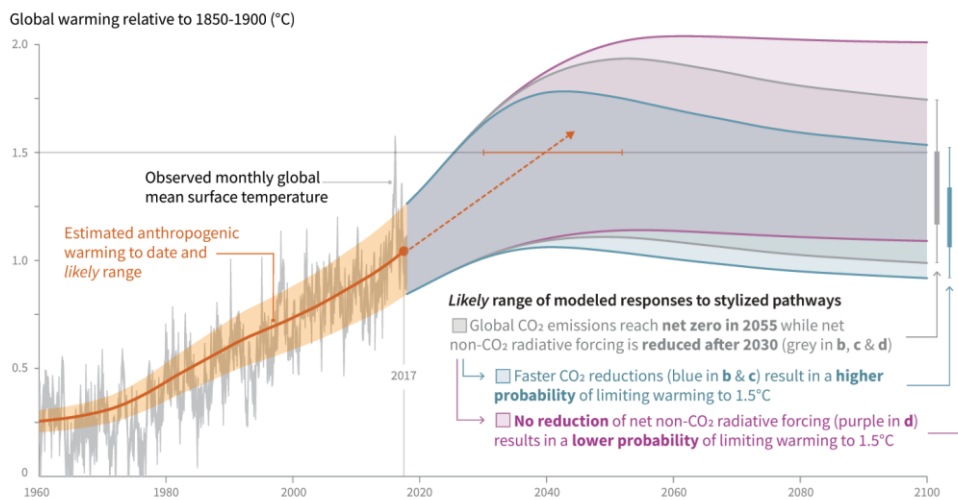
Figure 1.3. World consumption of energy in million tonnes oil equivalent produced using different energy sources [1].

The most important crisis related to the emission of GHG like CO₂, is the phenomenon called global warming, which refers to the increase in the global average sea and surface air temperatures during a period of thirty years. In October of 2018, the Intergovernmental Panel for Climate Change (IPCC), published a report stating that the human activities have currently caused global warming of approximately 1.0 °C (Fig. 1.4) above the temperature level of the pre-industrial era (1850-1900 AD) [8]. The report recommends to reduce the net global CO₂ emission (i.e. the difference between the anthropogenic emission and removal of CO₂) to zero by the year 2040 (Fig. 1.4), in order to limit the global warming to 1.5 °C [8]. Since the risks to natural and human systems are higher for the global warming above 1.5 °C (e.g. 2.0 °C) –

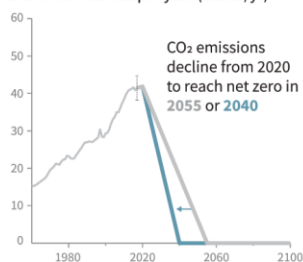
it is crucial to drastically reduce the CO₂ emission by the year 2040. The reduction of CO₂ emission could be achieved only by transitioning from a fossil fuels-based energy economy to a renewable one [9] and failing to do so could lead to catastrophic events around the world. The non-CO₂ radiative forcing refers to the rise in global temperature due to the GHGs other than CO₂ in the atmosphere, which block of power radiated from the Earth's crust back to space.

Cumulative emissions of CO₂ and future non-CO₂ radiative forcing determine the probability of limiting warming to 1.5°C

a) Observed global temperature change and modeled responses to stylized anthropogenic emission and forcing pathways

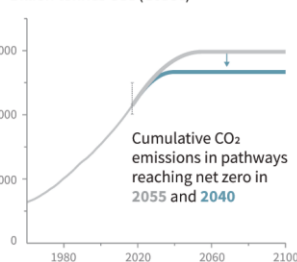


b) Stylized net global CO₂ emission pathways
Billion tonnes CO₂ per year (GtCO₂/yr)



Faster immediate CO₂ emission reductions limit cumulative CO₂ emissions shown in panel (c).

c) Cumulative net CO₂ emissions
Billion tonnes CO₂ (GtCO₂)



Maximum temperature rise is determined by cumulative net CO₂ emissions and net non-CO₂ radiative forcing due to methane, nitrous oxide, aerosols and other anthropogenic forcing agents.

d) Non-CO₂ radiative forcing pathways
Watts per square metre (W/m²)

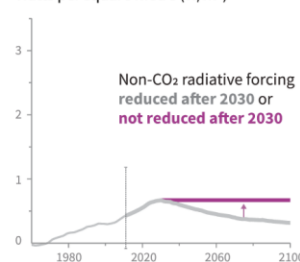


Figure 1.4. Global warming relative to pre-industrial era (1850-1900 AD) temperature level and projections for the future with three different scenarios, where the blue, grey and pink curves respectively correspond to global CO₂ emissions reaching net zero in the years 2040, 2055 with and without reduction of non-CO₂ radiative forcing [8].

1.2. Renewable energy technologies

Renewable energy refers to the energy produced from the sources which could be naturally replenished therefore sustainable and produce limited or zero GHG emission. Some of the types of renewable energies include hydropower, wind, solar, bioenergy and geothermal energy. The International Renewable Energy Agency (IRENA) reported that the global renewable power generation capacity accounted to 2179 GW in the year 2017 (Fig. 1.5) [10]. Hydropower constitutes about 53% of the renewable power generation capacity, whereas wind and solar constitute 23% and 18% respectively [10]. The costs of all the renewable energy technologies have been in steady decline in the recent year and are projected to become more competitive to those of the fossil fuels based technologies in the near future [11].

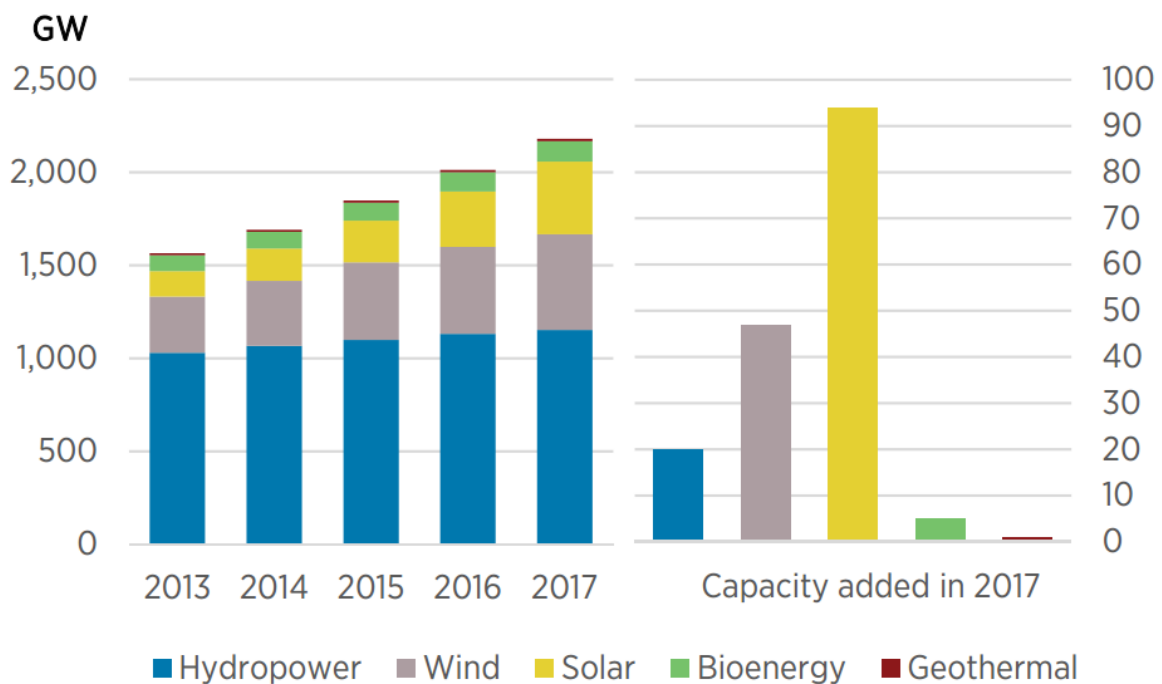


Figure 1.5. Global renewable power generation capacity in gigawatt (GW) and increase in capacity of different renewable power sources [10].

Some fundamentals of the different types of renewable energies are as follows,

- Hydropower – is generated from the energy of flowing water in dams. Recently, there has been a boom in the construction of hydropower dams to increase its global capacity to 1700 GW, which will not sufficient to meet energy demands. Furthermore, the mitigation CO₂ emissions due to them will also be low [12]. Moreover, hydropower dams negatively impact the social and ecological conditions of the surrounding areas due to relocation of the local population, fragmentation of free-flowing rivers, higher risk to freshwater biodiversity, etc. [12].
- Wind power is generated by the wind turbines, which convert the free and renewable kinetic energy of the wind into electricity [13]. The wind power generation involves zero CO₂ and other pollutant emissions. However, the ideal locations for the wind power plants have wind speeds above 20 km.h⁻¹ [13], which are unevenly distributed in the world and often in remote areas away from cities [14].
- The solar power – is generated by the photovoltaic devices which convert the Sun's radiation energy into electricity. The solar power generation also does not involve any GHG and particulate emissions.
- Bioenergy – is generated by the combustion of carbon based fuels which are available in the biosphere such as parts of plants, trees, etc. and the products extracted from them (e.g. ethanol) [15]. The bioenergy generation involves the emission of CO₂ gas, which was initially absorbed from the atmosphere by the biosphere [16]. Furthermore, the CO₂ emitted during the bioenergy generation could be reabsorbed by the biosphere provided that the land use change (LUC) is managed properly.
- Geothermal energy – refers to the naturally replenishable heat energy which is stored in rocks and trapped steam or liquid water in the Earth's interior [15]. This trapped steam or liquid water is extracted through wells and fed into turbines to generate electricity in the geothermal power plants. The geothermal energy generation depends on the properties such as the temperature of the hydrothermal resource in the Earth's interior, etc. [17]. Therefore, the power plants are mostly located in hot spots with volcanic activities, which are unevenly distributed in the world [18].

1.3. Need for energy storage systems

The demand for electricity varies significantly with the time of the day (Fig. 1.6) and season. Therefore, the conventional electricity generation technologies use a complex energy production and transmission system to level the load on the electric power grid [19]. This is done with the help of the energy supply and demand predictions. A very small percentage of the electricity produced is stored before it is transmitted. The global electricity storage capacity as of September 2017 was 176 GW, which amounted to less than 2% of the global power generation capacity [20].

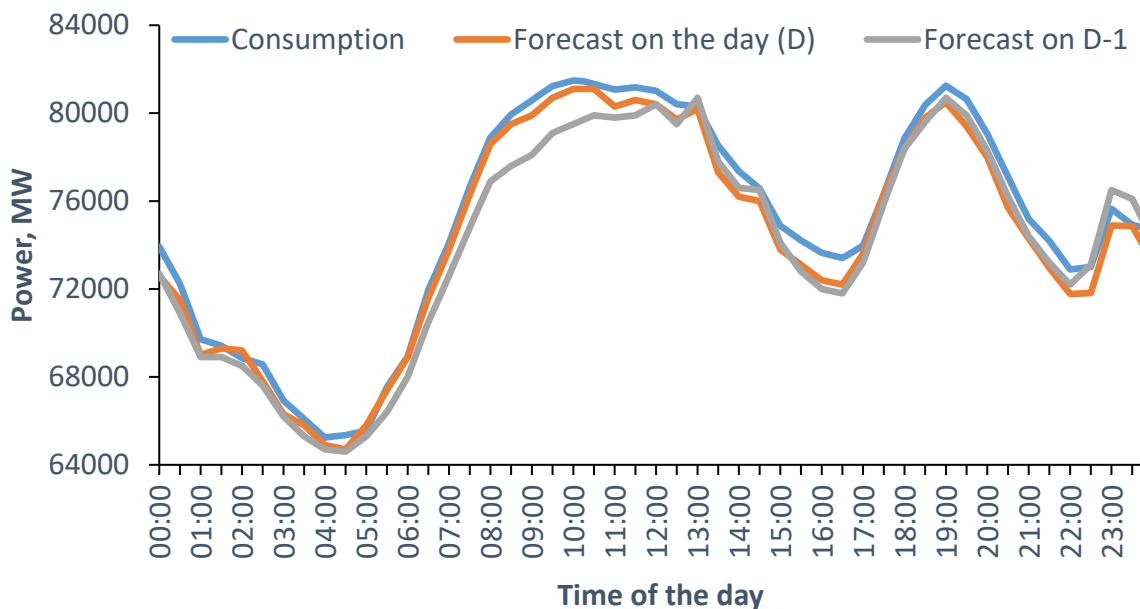


Figure 1.6. Actual and forecasted (D: made on the day and D-1: made on the day ahead) electricity demand in France on January 4th, 2019. Data acquired from the website of Réseau de Transport d'Électricité France (RTE France) [21].

Furthermore, the power generated by the fastest growing renewable energy technologies such as solar and wind (Fig. 1.5), fluctuates independently from the electricity demand (Fig. 1.7) [22]. This is due to the intermittent nature of their energy sources such as the sunlight and wind speed [23]. Due to this imbalance between the renewable energy supply and the demand for electricity, it is difficult to stabilize the power grid [19]. Therefore, storing the

electricity produced by the renewable energy technologies has become an absolute necessity for transitioning from the fossil fuels-based technologies. In order to reduce losses, increase efficiency and security of electricity supply from renewable power sources, a new type of power grid infrastructure called smart grid has emerged [24]. It uses enhanced sensors, automated controls, advanced communication and computing devices, to optimize the way in which electricity is transmitted, consumed and generate [24]. Energy storage systems are the core components that stabilize the smart grid, since they store the excess energy generated by the renewable sources and balance the electricity demand and supply [25].

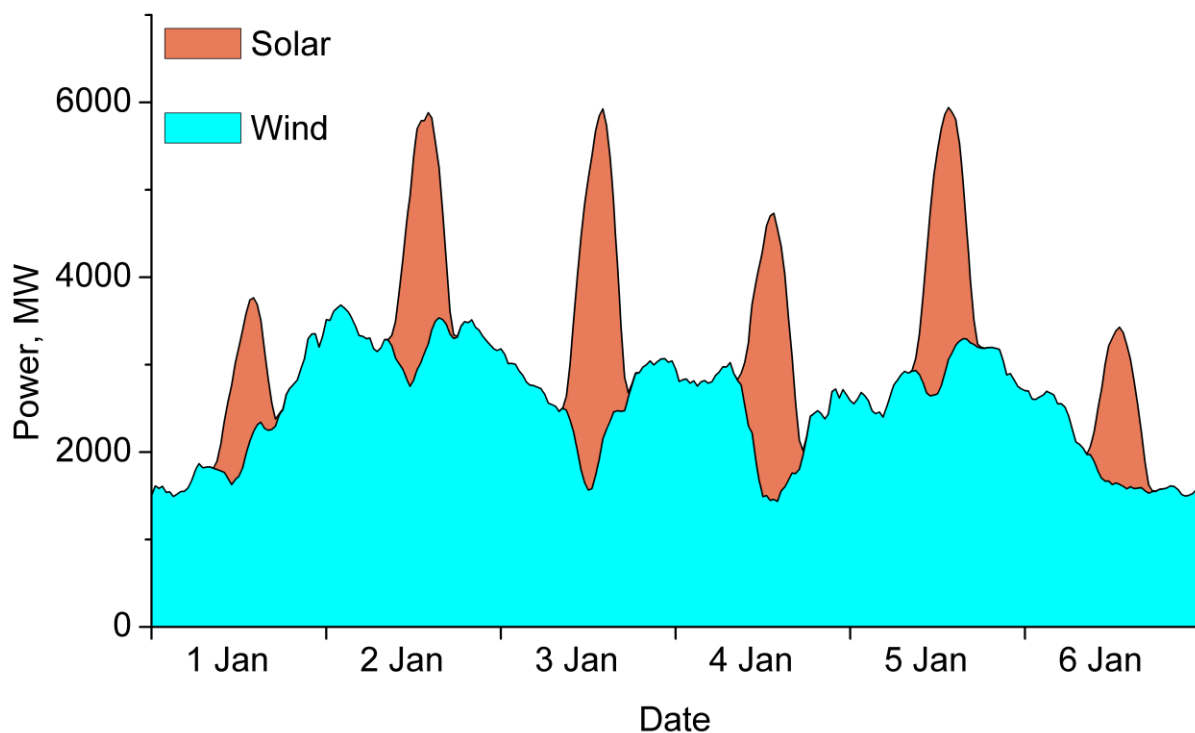


Figure 1.7. Electricity generated using wind and solar energy technologies in France from 1st to 6th January, 2019. Data acquired from the website of RTE France [22].

Electricity can be converted and stored in different forms of energies such as mechanical (e.g. pumped hydro storage, flywheels and compressed air storage), electrical (e.g. capacitors and super conducting coil) and electrochemical (e.g. hydrogen and batteries) [19,20,25]. Pumped

storage hydropower (PSH) accounts for about 98% (172 GW) of the electricity storage capacity of the world [26]. PSH involves the conversion of electricity into mechanical potential energy. Where water is pumped using an electric pump from a lower to higher elevation, when the electricity demand is low [19]. During high electricity demand, the stored water is allowed to flow from the higher to lower elevation via a turbine, which generates electricity [19]. Large scale pumped storage facilities are geographically centralized and they are not suitable for smart grids which require decentralized energy storage [25]. Therefore, other energy storage technologies are being developed. Among them rechargeable batteries such as the lithium-ion (Li-ion), redox flow, sodium-based batteries (e.g. sodium sulfur), etc. accounts for about 46% of the available non-PSH storage volume (Fig. 1.8) [26].

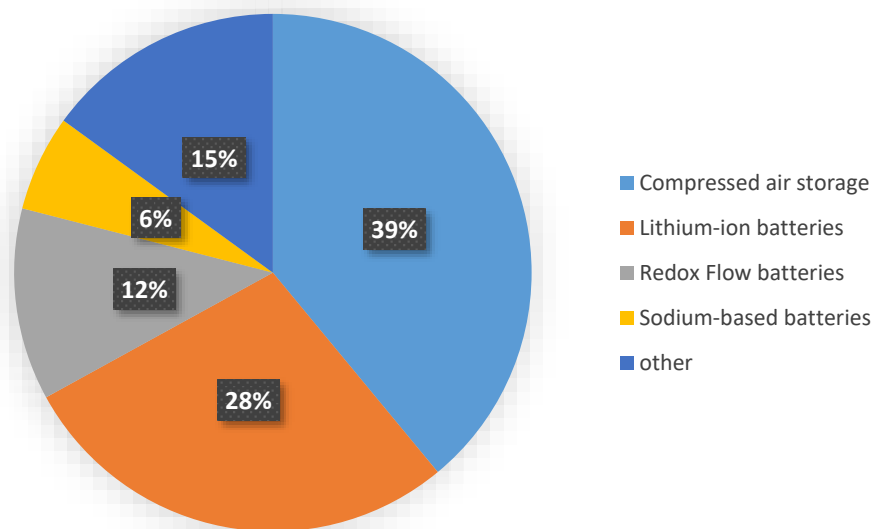


Figure 1.8. Shares of different non-PSH storage volumes (15300 MWh) which are available in the world as of 2017 [26].

In addition to electricity, transportation is another sector which is dominated by the fossil fuels. Even in the developed countries such as the 28 member states of the European Union (EU), GHG emissions from transportation sector are on the rise [27], which increased by 3% in the year 2016 [28]. The transportation sector contributed to 27% of the total GHG emissions by the EU, in which 72% of the emissions came from road transport (Fig. 1.9) [28]. This is because most of the vehicles on the road have internal combustion engines (ICEs)

which are powered by fossil fuels such as diesel and gasoline. Therefore, to reduce the GHG emissions, the ICE vehicles on the road must be switched with electric vehicles (EVs), which are powered by electrochemical energy storage and conversion devices such as rechargeable batteries and fuel cells.

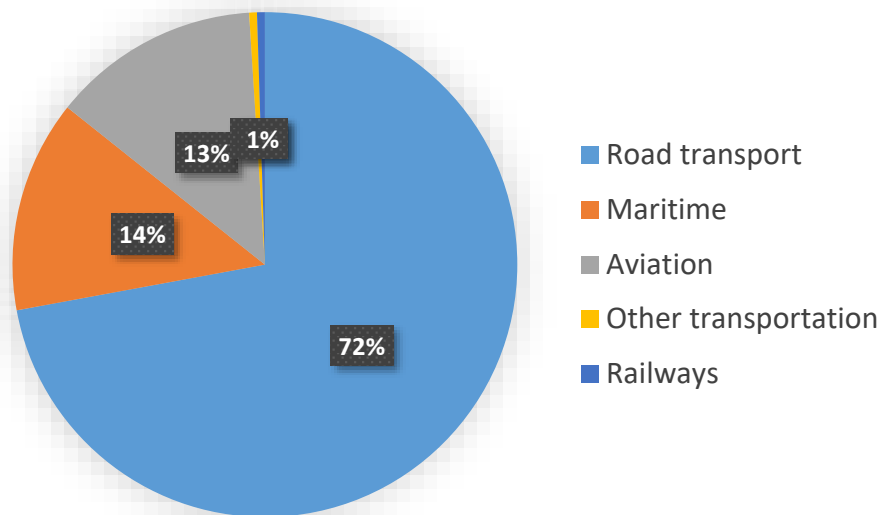


Figure 1.9. Share of GHG emissions from different transportation sectors in the EU in the year 2016 [28].

1.4. Rechargeable batteries

Batteries are electrochemical devices which convert chemical energy to electrical energy. Rechargeable batteries are also called secondary batteries in which redox reactions of the anodes and cathodes are reversible. Therefore, these batteries store electricity as chemical energy during charge, and they convert it back to electricity during discharge. Rechargeable batteries have been in existence for the last 160 years. The first rechargeable battery called lead-acid battery was invented in the year 1859 by a French physicist named Gaston Planté [29]. Lead-acid batteries are still used in conventional automobiles with ICEs for purposes such as starting, lighting and ignition (SLI) [30]. Furthermore, they are also used in invertors and uninterruptible power supply (UPS) [31]. However, the gravimetric energy density which refers to the amount of energy stored per unit mass of the battery is very low for lead-acid

batteries, since lead (Pb) is a heavy metal. This has made the lead-acid batteries heavier and unsuitable for energy storage requirements of today and in the past. Therefore, rechargeable batteries with different chemistries and materials such as nickel-cadmium, nickel-metal hydride, Li-ion, lithium-sulfur (Li-S) etc. have been developed [32]. Due to these developments, gravimetric energy density has increase at an annual rate of 5% since 1970 (Fig. 1.10) [33].

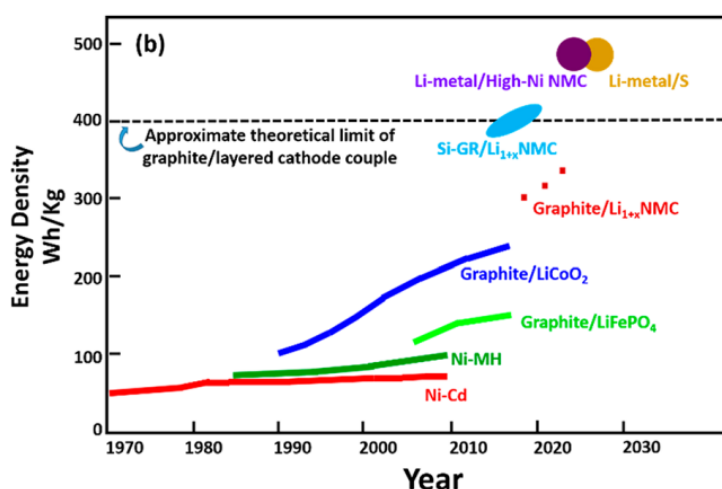


Figure 1.10. Energy density evolutions of different battery chemistries [33].

The energy stored in a battery (Wh) is the product of its cell potential (V) and capacity (Ah), both of which depend on the chemistries of its anode and cathode [32]. Therefore, the energy density which refers to the energy stored per unit mass (Wh.kg^{-1}) or volume (Wh.L^{-1}) of the battery, also depends on its chemistries. Lithium (Li) is the lightest metal and it has an extremely low reduction potential (-3.045 V vs standard hydrogen electrode) [34], which makes it a very attractive anode material with very high gravimetric capacity (3860 mAh.g^{-1}). Therefore, in the early 1970s, Li metal batteries were developed, which had metallic Li as the anode and Lithium-ion (Li^+) intercalation materials such as the layered TiS_2 as the cathode [35]. However, these batteries suffered a serious drawback due to the formation of dendrites during Li plating which lead to short circuiting and fires [32,35]. In order to circumvent the issues related to Li metal anode, it was replaced with Li^+ intercalation anodes. This led to emergence of Li-ion batteries involving rocking chair mechanism between two intercalation

electrodes [36,37]. Further developments such as the high potential Li^+ intercalation cathode like LiCoO_2 and stable low potential carbon-based anodes (Fig. 1.11) have led to the commercialization of Li-ion batteries by Sony in June 1991 [38].

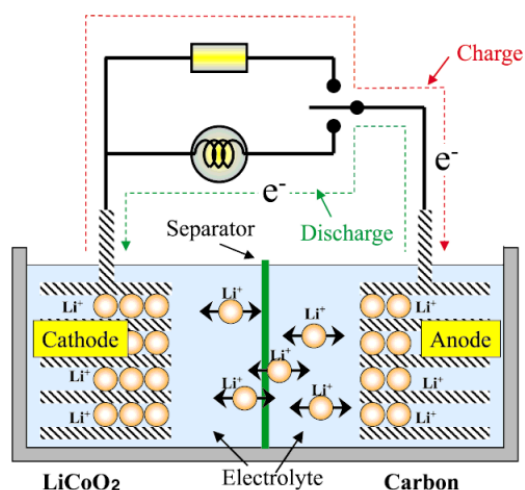


Figure 1.11. Schematic of the working principle of Li-ion batteries [39].

Today, Li-ion batteries (LIBs) dominate the market share of portable electronics and EVs. The energy densities of LIBs have been improved in the recent year through the development of new cathode [40] and anode materials. However, the energy densities of LIBs are primarily limited by the specific capacities (charge stored per unit mass of the active material) of their cathode materials [40]. Therefore, further improvements to the energy density of LIBs ($150\text{--}250 \text{ Wh.kg}^{-1}$) (Fig. 1.12(a)) and the driving of the EVs powered by them are highly limited. In order to increase the driving ranges of EVs, next generation batteries such Li-S, Li-air or Li-oxygen (Li-O_2) batteries, etc. are being developed [41]. Although Li-O_2 battery can potentially offer very high energy density ($\approx 900 \text{ Wh.kg}^{-1}$), it suffers from issues such as poor rechargeability [42], irreproducibility [43,44], etc. – which make it unviable for commercialization in the near future. In contrast, Li-S batteries are already available for commercial purchase [45] and it is used in some niche applications like the Unmanned Aerial Vehicle (UAV) [46,47].

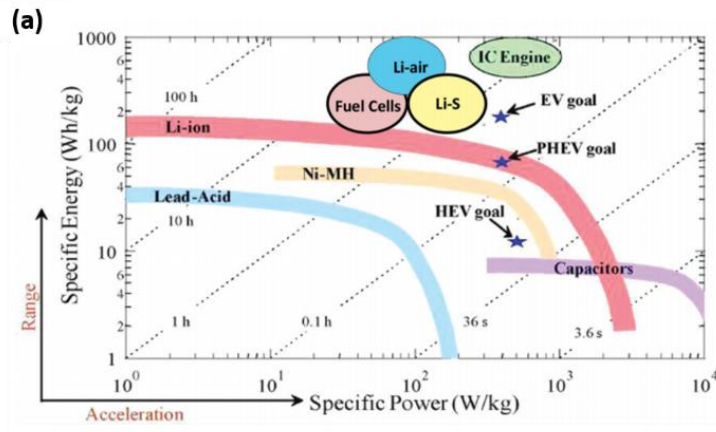


Figure 1.12. Ragone plot of different energy storage and conversion systems [40].

Sulfur (S_8) is initial active material of the fully charged Li-S batteries cathode, which is one of the most abundant elements in the world and a by-product of the petroleum and natural gas refining [48]. It is also extremely cheap (≈ 40 \$/ton) [49]. Furthermore, the overall reaction of a Li-S batteries (eq. 1.1) involves transfer of two electrons and Lithium ions (Li^+) per sulfur atom. Therefore, the complete conversion of S_8 to Li_2S , theoretically delivers a very high specific capacity of $1675 \text{ mAh}\cdot\text{g}^{-1}$ and energy density of $2567 \text{ Wh}\cdot\text{kg}^{-1}$ based on the mass of the solid sulfur in the cathode [50]. Therefore, Li-S batteries could be cheaper and they can offer 2 to 3 times the energy density of the Li-ion batteries [51].



Despite the progresses made in the past years, there are still several challenges facing the Li-S batteries which impede the further improvements of their performance.

1.5. Objective of my thesis

Li-S batteries has a complex working principle (explained in Chapter 2), which involves multiple of phenomena such as chemical and electrochemical reactions of different species

that occur simultaneously. This makes it difficult to assess certain underlying mechanisms and limitations behind the electrochemical operation of Li-S batteries. Therefore, the objective of this thesis work is to develop mathematical models which assist in understanding the phenomena behind electrochemical experimental results of Li-S batteries and the impacts of cathode design parameters on the discharge capacities. This thesis work also aims to provide suggestions to optimize the discharge performance of Li-S batteries through the assessments achieved using our models.

This work is a part of the European Union's Horizon 2020 project called High Energy Lithium Sulfur batteries and cells (HELiS). The entirety of the work presented in this manuscript except the potentiostatic experimental result in Chapter 6, was carried out at Laboratoire de Réactivité et Chimie des Solides (LRCS), CNRS UMR 7314, Université de Picardie Jules Verne, Hub de l'Énergie, Amiens, France.

1.6. Manuscript structure

The rest of the manuscript is organized as follows,

- Chapter 2 – discusses the operating principles, challenges and developments of Li-S batteries, along with the detailed review of the state of the art of Li-S battery models;
- Chapter 3 – reports the development of a novel kinetic Monte-Carlo (kMC) which is used to study the impact of discharge rate and sulfur loading on the mesostructural evolution of a carbon/sulfur cathode composite;
- Chapter 4 – reports the theoretical development of a microstructural resolved continuum discharge model, which is used to investigate the impact of cathode design on the performance;
- Chapter 5 – presents a cyclic voltammetry model which is used to investigate the cyclic voltammograms of different polysulfides dissolved in the electrolyte;
- Chapter 6 – presents a nucleation and growth model which is used to investigate the electrodeposition of Li_2S over carbon surface;
- Chapter 7 – summarizes the experimental work carried out in this thesis work along with few comparative discharge modelling results.

Chapter 2. State of the art of lithium sulfur batteries

Contents

| | |
|--|-----------|
| 2.1. Introduction to Li-S batteries | 27 |
| 2.2. Working principle of Li-S batteries | 27 |
| 2.3. Challenges in Li-S batteries | 29 |
| 2.4. Developments in the components of Li-S batteries | 31 |
| 2.4.1. Positive electrode | 31 |
| 2.4.2. Negative electrode | 34 |
| 2.4.3. Electrolyte | 35 |
| 2.5. Modelling of Li-S batteries | 36 |
| 2.5.1. Atomistic and Molecular level modelling | 36 |
| 2.5.2. Mesoscopic modelling | 39 |
| 2.5.3. Continuum level modelling | 39 |
| 2.6. Conclusions | 42 |

Chapter 2. State of the art of lithium sulfur batteries

2.1. Introduction to Li-S batteries

The concept of using sulfur and lithium metal or its alloy respectively as the electro-positive and the electro-negative electrodes in storage batteries, was first introduced in the mid-1960s by Herbert *et al.* [52]. Electrolyte containing Li-salt dissolved in propyl, butyl or amyl amine was also proposed by the same authors. Therefore, the concept of Li-S batteries has existed for more than 5 decades. However, the inherent issues related to the cathode such as insulating nature of solid sulfur [32,50], formation of highly soluble polysulfides intermediates which migrate and react with lithium metal anode, etc. have limited the specific capacity and the cyclability of the Li-S batteries [53]. Due to these reasons, the development of Li-S batteries was held back for several years. The sulfur loaded porous carbon cathode, which had improved electronic conductivity was first introduced by Peled *et al.* [54]. Their Li-S cell delivered better specific capacity at low discharge rate, however the capacity faded upon cycling due to the loss of active materials from the cathode [54]. In the year 2009, Nazar *et al.* used a mesoporous carbon as the cathode host material, which was impregnated with sulfur at 155°C [55]. Their cells containing the aforementioned sulfur impregnated mesoporous carbon delivered better capacity and had good cyclability. This work by Nazar *et al.*, rejuvenated the interest in Li-S batteries which led to the explosive growth in the amount of Li-S research works carried out in the past decade.

2.2. Working principle of Li-S batteries

A conventional Li-S battery consists of a carbon/sulfur (C/S) composite cathode and a lithium metal anode which are electronically separated by a porous polymer membrane (Fig. 2.1). A non-aqueous organic electrolyte exists in the pores of the cathode and the separator which provide ionic conductivity between anode and cathode. The carbon particles in the cathode are bound by a polymer binder to form a porous matrix, which provides electronic wiring and acts as a host for solid sulfur based precipitates such as $S_{8(s)}$ and $Li_2S_{(s)}$ [56].

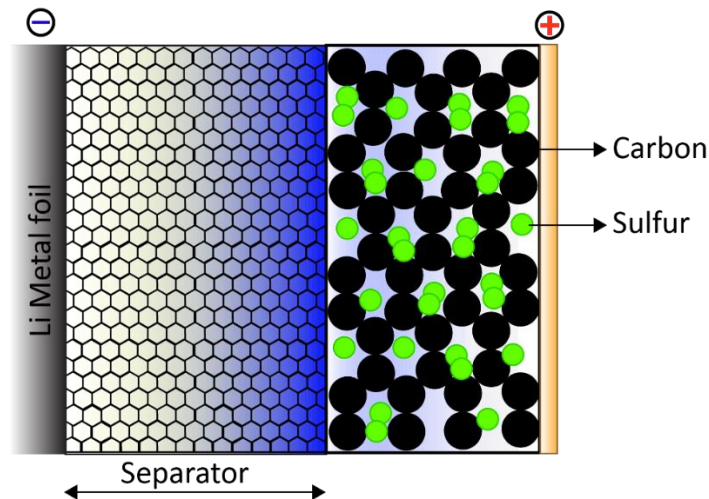


Figure 2.1. Schematic representation of a conventional Li-S cell.

The typical charge and discharge curves of a Li-S batteries consist of low and high potential plateaus (Fig. 2.2) [57]. During the high plateau stage of the discharge the solid sulfur ($S_{8(s)}$) initially undergoes dissolution and reduction to produce dissolved sulfur and higher order polysulfides, which subsequently get reduced to medium order polysulfides [58,59]. Further reductions of the medium to low order polysulfides and the precipitation of Li_2S take place during the low potential plateau stage of the discharge. During charge, the reversal of the aforementioned reactions occurs.

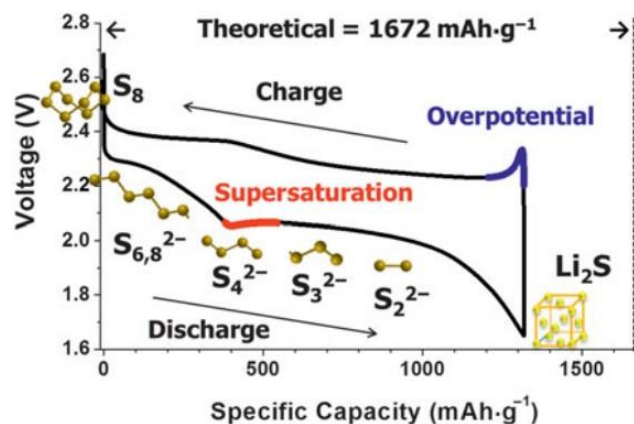


Figure 2.2. The typical charge and discharge curves of a Li-S batteries [57].

The aforementioned reaction mechanism is the simplest one, since the dissolved polysulfides in the electrolyte are known to undergo reaction such as dissociation, disproportionation, etc. [60,61]. Furthermore, the reaction mechanism of Li-S batteries can change based on the aforementioned properties polysulfides in the electrolyte [62]. Moreover, Dibden *et al.* showed that the characteristics of theoretical discharge based on the proportions of solid and dissolved sulfur based species at different stages of using a ternary S_8 - Li_2S -electrolyte phase diagram (Fig. 2.3) [63]. The potential profiles which had two plateaus correspond to the discharge trajectories (A and B) consisting of three equilibrium stages namely S_8 -liquid electrolyte, completely liquid electrolyte and Li_2S -liquid electrolyte (Fig. 2.3).

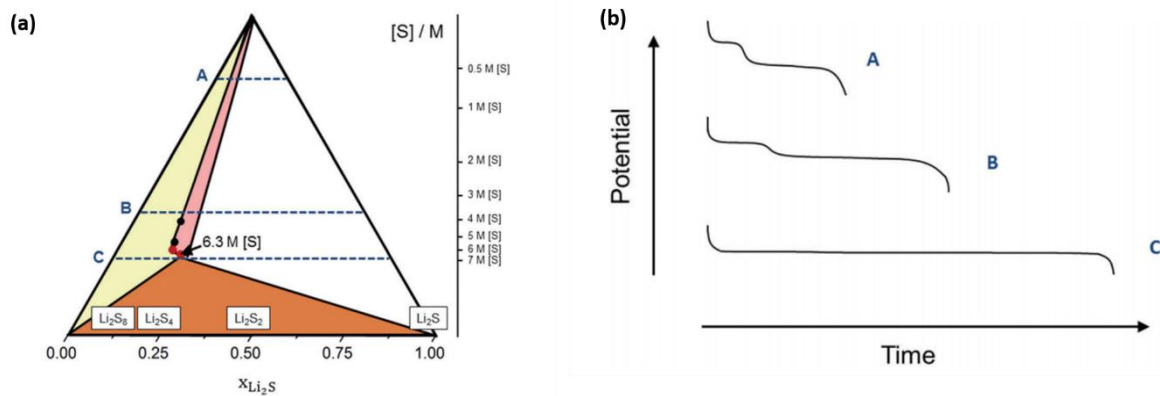


Figure 2.3. (a) The experimental phase diagram of the $S_{8(s)}$, $Li_2S_{(s)}$ and 1 M LiTFSI in 1,3 dioxolane system [63]. The lines A, B and C in the phase diagram are discharge trajectories in which have different proportions of solid and dissolved precipitate at different depths of discharge (x_{Li_2S}). (b) Theoretical discharge profiles of three different discharge trajectories [63].

2.3. Challenges in Li-S batteries

The components of Li-S batteries such as the cathode active materials (solid sulfur and Li_2S), polysulfides dissolvable electrolytes and the lithium metal anode pose several challenges to the improvement of Li-S batteries performance. Some of the challenges are listed below,

- The solid sulfur which is the initial active material of a fully charged cathode is electronically insulating in nature [50]. Therefore, a proper contact between the solid sulfur and the electron conducting host material should be maintained to ensure full utilization of the active material during the operation of Li-S batteries [56].
- The sulfur is also soluble up to a certain extent in the conventionally used Li-S batteries electrolytes. The dissolved sulfur will migrate to the lithium metal anode, where it gets reduced to polysulfides [64]. This phenomenon results in the self-discharge of the Li-S batteries.
- Furthermore, the reaction of the dissolved sulfur with the lithium metal anode could produce insulating film over its surface, which results in the irreversible loss of active material from the cathode [50].
- During charge, the higher order polysulfides produced in the cathode will migrate to the lithium metal anode, where they get reduced to medium or low order polysulfides, which will then transport back to cathode and get oxidized once again (Fig. 2.4a) [65,66]. The aforementioned reduction and oxidation processes will make the polysulfides to shuttle between the electrodes depending on the charge current, total polysulfides concentration in the electrolyte and temperature [65,67]. Furthermore, this shuttling mechanism will reduce the Coulombic efficiency, since the oxidation of polysulfides during charging will take longer time (Fig. 2.4b).

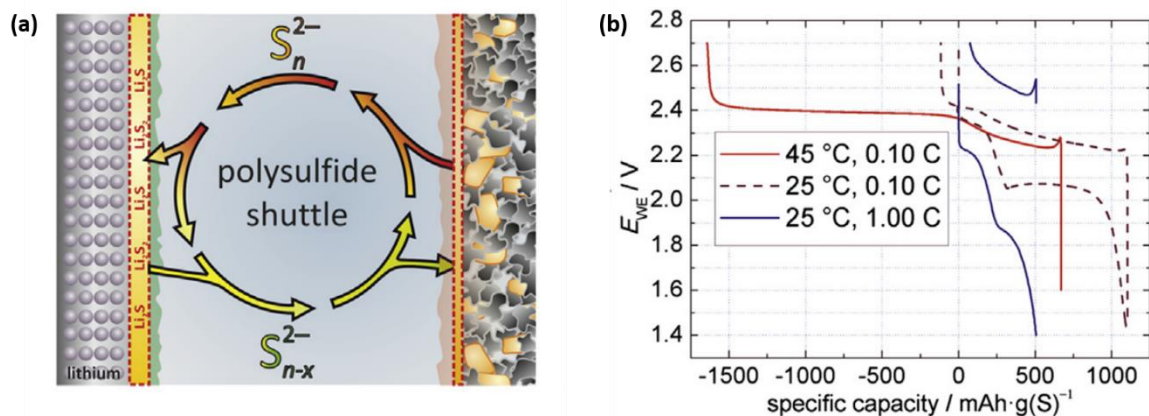


Figure 2.4. (a) Schematic representation of polysulfides shuttle mechanism and (b) the influence of polysulfides shuttle on charge and discharge curves measured at different discharge rates and temperatures [65].

- The Li_2S precipitates produced during the discharge are also insulating in nature, which could passivate electroactive surface of the cathode [68]. Furthermore, the Li_2S is more voluminous than solid sulfur, therefore it could result in the blocking of cathode pores [53]. Additionally, the volume expansion of the cathode due to the precipitation of Li_2S could also result in the disintegration of porous conductive matrix [69].
- Lithium metal anode is highly reactive to the electrolyte used in the Li-S batteries. Therefore, any damage in the protective Solid Electrolyte Interphase (SEI), will result in the degradation of electrolyte and adverse reactions of the lithium with polysulfides [70].

2.4. Developments in the components of Li-S batteries

2.4.1. Positive electrode

In order to mitigate the issues involving the cathode, the majority of the Li-S batteries research was dedicated to the tailoring the architecture of the carbon/sulfur composites. As mentioned before, Nazar *et al.* used a sulfur impregnated highly order mesoporous composite called CMK-3/S-155 as the cathode material which delivered better capacity and cyclability [55]. The better performance was achieved through improved conductivity, since the sulfur was impregnated inside the ordered mesopores (Fig. 2.5a). The performance of the CMK-3/S composite was further improved by coating a thin layer of polyethylene glycol (PEG) over it, which inhibited the transport of polysulfides out of the cathode (Fig. 2.5b).

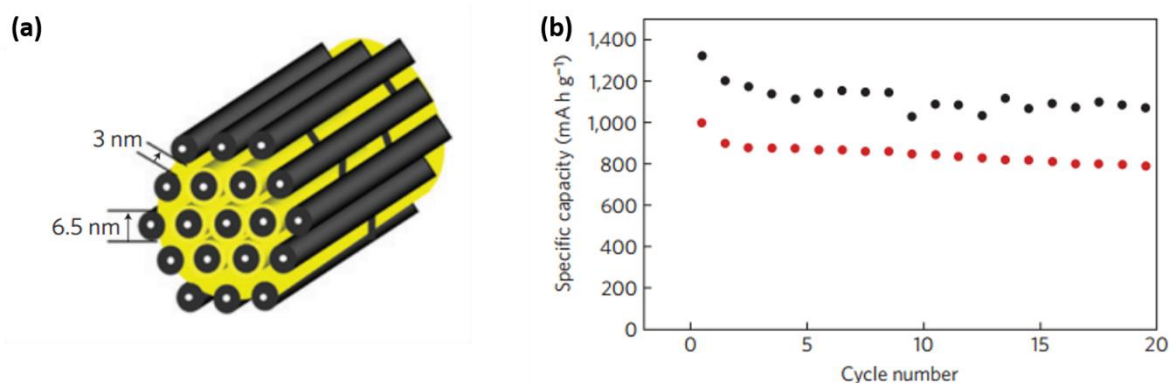


Figure 2.5. Schematic representation of CMK-3/S-155 composite and (b) discharge capacities during cycling of pure (in red) and PEG coated CMK-3/S composites (in black) [55].

Following the work of Nazar *et al.*, several porous carbon/sulfur composites containing microporous carbon sphere, spherical ordered mesoporous carbon nanoparticles, porous hollow carbon were developed [71–73]. Furthermore, reduced graphene oxide coated over carbon/sulfur nanocomposites had improved rate capability and Coulombic efficiency due to the increase of electronic conductivity and the inhibition of polysulfides shuttle, respectively [74]. The sulfur coated graphene oxide sheets also had good cyclability due to the immobilisation of dissolved sulfur and polysulfides [75].

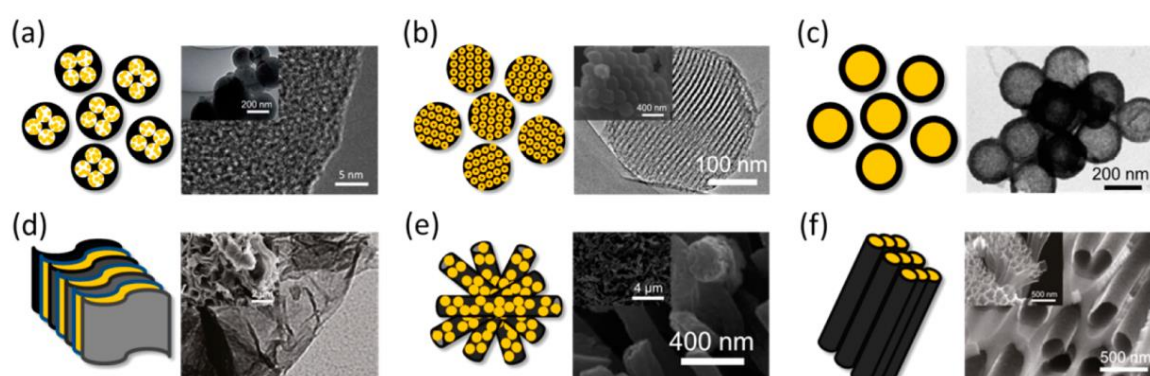


Figure 2.6. Schematics and SEM images of porous carbon/sulfur composites containing (a) microporous carbon, (b) spherically ordered mesoporous carbon, (c) mesoporous hollow carbon, (d) graphene oxide sheets (e) porous carbon nanofiber and (c) hollow carbon nanofiber [56].

The utilization of the sulfur was improved (1400 mAh.g^{-1} at 0.1C) by its confinement inside the pores of the porous carbon nanofiber [76]. It was achieved through high surface area and electronic conductivity of carbon nanofiber. Furthermore, the composite containing sulfur confined inside the hollow carbon nanofiber limited the diffusion of polysulfides, thereby it improved the retention of capacity over 150 cycles [77].

Wang *et al.*, confined the sulfur inside the micropores of a microporous-mesoporous carbon and the galvanostatic discharge curves of their cell containing mixed carbonate-based electrolyte consisted of only one plateau similar to those of the solid-state Li-S batteries [78]. The micropores restricted the intrusion of electrolyte and the dissolution of polysulfides [79], but allowed reversible lithiation and de-lithiation of sulfur. This type of reaction mechanism is called Quasi-Solid-State Reaction (QSSR). Markevich *et al.*, later showed that the stability of the SEI layer over the microporous carbon containing sulfur within their micropores, was crucial for achieving QSSR mechanism in Li-S batteries (Fig. 2.7) [80]. The QSSR type Li-S batteries delivered better cyclability due to the restriction to the dissolution of polysulfides [81].

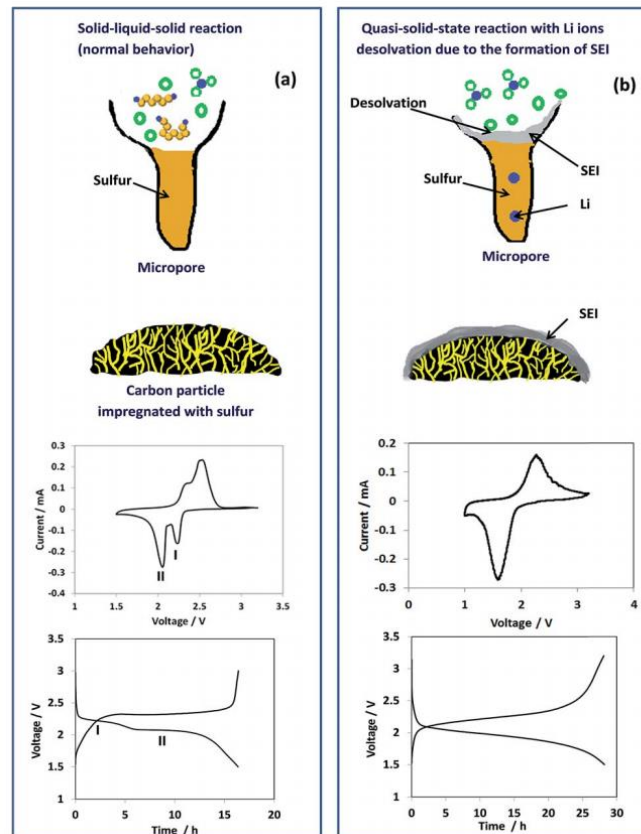


Figure 2.7. The schematics, cyclic voltammograms and galvanostatic discharge/charge curves sulfur impregnated microporous carbon (a) ether-based and (b) FSI-based ionic liquid electrolytes [80].

2.4.2. Negative electrode

Few strategies have been adopted to mitigate the aforementioned issues related to the lithium (Li) metal anode [82]. The widely used strategy is the SEI formation over the Li metal anode using electrolyte additive such as LiNO_3 , which improved the cyclability and Coulombic efficiency due to the elimination of polysulfides shuttle [83]. Demir-Cakan *et al.*, showed that SEI produced by coating sulfur over the Li metal anode assisted in capacity retention of Li-S batteries [84].

Another strategy is the use of a passivation layer which physically separates the Li metal and the electrolyte. Several polymer and solid-state electrolytes were explored as the passivation layer which assisted in reducing polysulfide shuttle but had very low Li^+ conductivities. The solid electrolyte layers also suppressed the dendrite formation over the Li metal anode. The passivation layer containing Nafion membrane which selectively blocks the diffusion of polysulfides, largely enhanced the capacity

retention and Coulombic efficiency (Fig. 2.8) [85]. Furthermore, the Li-Al coating over the Li-anode assisted in the suppression of dendrite formation in Li-S batteries [86].

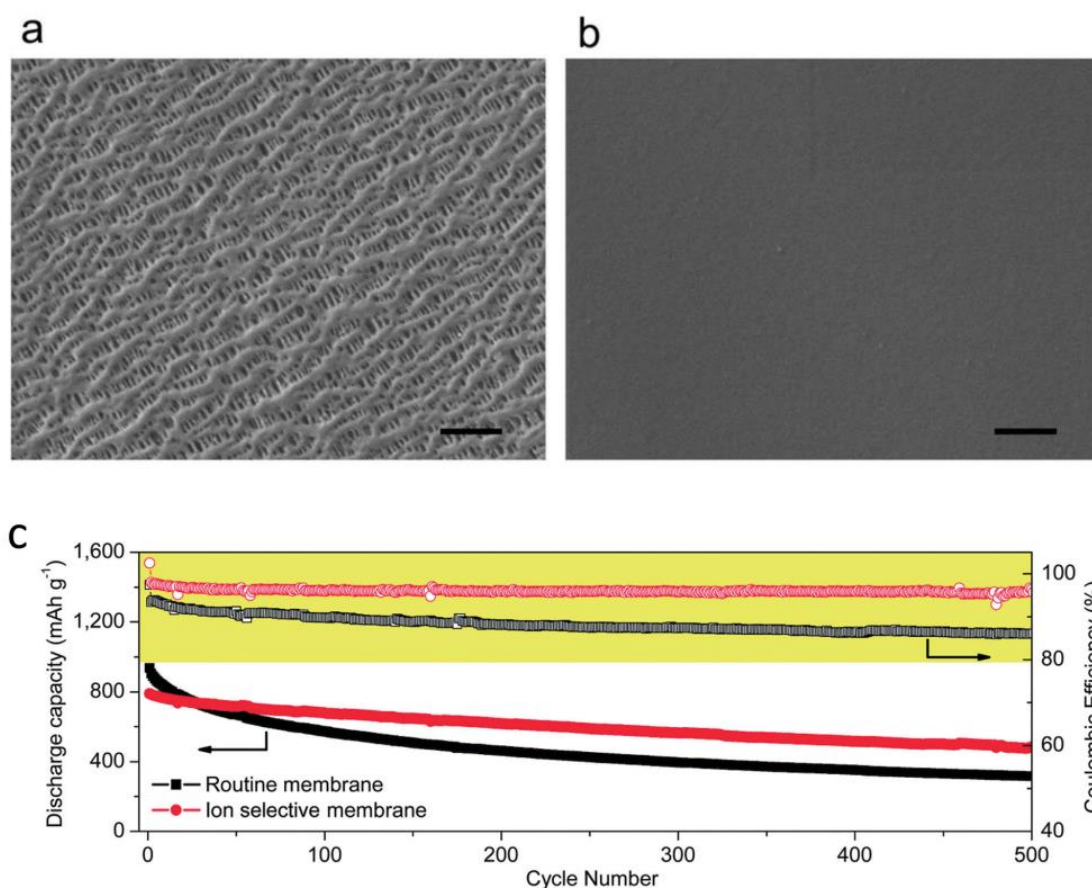


Figure 2.8. The SEM images of routine (a) PP/PE/PP, and (b) ion selective Nafion-PP/PE/PP layers of Li metal and (c) their corresponding discharge capacities and Coulombic efficiencies for different cycles [85].

2.4.3. Electrolyte

Ether-based electrolytes account for about 70 to 80% of the electrolyte used in the Li-S battery research [87]. The linear ethers called glymes are mainly used in Li-S batteries. These are different oligomers of polyethylene glycol dimethyl ether (PEGDME) such as 1,2 dimethoxyethane (DME) or monoglyme (G1), diglyme (G2), triglyme (G3) and tetraglyme (G4) or Tetraethylene glycol dimethyl ether (TEGDME). Cyclic ethers such as the tetrahydrofuran (THF) and 1,3 dioxolane (DOL) are also used. Lithium bis(trifluoromethanesulfonyl)imide (LiTFSI) is the most commonly used salt and 1 M LiTFSI in DME:DOL (1:1 v/v) is the widely used

electrolyte. Moreover, a class of electrolyte called the solvent-in-salt which contains ultrahigh concentration of LiTFSI (7 mol.l^{-1}) in DME:DOL were investigated by Suo *et al.* [88]. This class of electrolyte had very high transference number and inhibited the dissolution of polysulfides. Furthermore, they also assisted in suppressing the formation of dendrites over the Li metal anode.

In the recent years, sparingly soluble electrolytes containing hydrofluorinated ether (HFE):TEGDME (4:1) and ACN₂-LiTFSI:HFE (1:1) have been investigated [89]. Since, these electrolytes inhibit the dissolution of polysulfides in Li-S batteries and they lower the electrolyte/sulfur (E/S) ratio, thereby they assist in increasing the energy density. Finally, the advent of QSSR type Li-S batteries have led to the comeback of carbonate-based electrolytes such as 1M LiPF₆ in ethylene carbonate (EC) and dimethyl carbonate (DMC) (1:1) and in EC and diethyl carbonate (DEC) (1:1) [90].

2.5. Modelling of Li-S batteries

Due to the complex operating principle of Li-S batteries, the mathematical models are used to assess the phenomena taking place in them [91]. Numerous modelling techniques have been used to study the phenomena occurring at different spatial and temporal scales. However, modelling works on Li-S batteries are quite recent. The very first Li-S battery model was developed by Mikhaylik *et al.* in 2004 and it was used to study the polysulfides shuttle [67]. In 2008, Kumaresan *et al.* developed the first comprehensive 1D continuum model to simulate the discharge of Li-S batteries [92].

2.5.1. Atomistic and Molecular level modelling

Density functional theory (DFT) is an atomistic modelling technique and it has been used to determine the properties of the materials used in the Li-S batteries. It was used to explore reaction mechanism of Li-S by predicting the structures and reduction potentials of polysulfides (Fig. 2.9) [93] and nanoconfined Li₂S [94]. It was also used to investigate the oxidation potentials of electrolytes [94]. DFT was widely used to study the interaction of polysulfides with different electrode surfaces such as sulfur terminated Ti₂C MXene [95], 2D layered materials [96], nitrogen-doped graphene [97], functionalized graphene [98], silicene

[99], heteroatom-doped nanocarbon [100], etc. The results of the aforementioned studies will assist in development of new cathode materials for Li-S batteries.

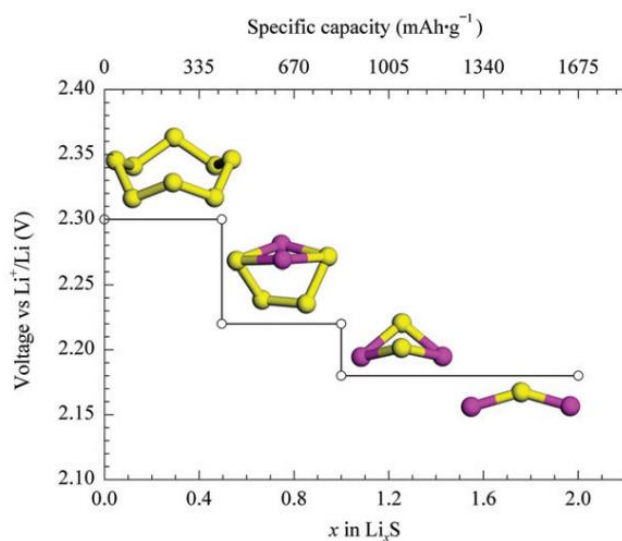


Figure 2.9. Structure and discharge plateau potentials of different polysulfides.

DFT is also used to study the energetics, electronic structure [101] and charge transport mechanisms in Li₂S₂ [102]. Furthermore, different charge transport mechanisms in α -S and Li₂S were also studied using the combination of DFT and Marcus theory (Fig. 2.10) [103]. This study revealed that the sluggish charge transports in α -S and Li₂S are due to their low equilibrium carrier concentrations.

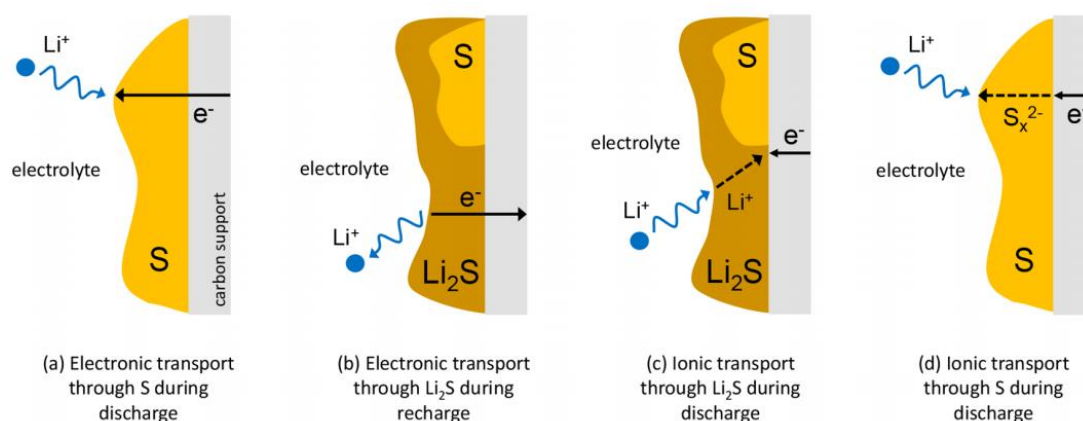


Figure 2.10. Schematic representations of possible charge and ionic transport mechanisms in α -S and Li₂S [103].

Jeschke *et al.*, used a computational fluid phase thermodynamics approach, called conductor-like screening model for real solvent (COSMO-RS), to predict the solubility of cyclo-S₈ in different LiTFSI containing binary and ternary electrolytes [104]. COSMO-RS combines DFT and statistical thermodynamics to predict the solubility cyclo-S₈ by calculating its chemical potential in different electrolytes.

DFT and first principles molecular dynamics techniques are also used to investigate and predict the results of different analytical techniques such as Raman, IR, X-ray absorption spectroscopy (XAS), etc. [105]. These techniques are widely used to analyse the dissolved polysulfides in the electrolyte. The Raman spectra of different polysulfides predicted using the DFT method has confirmed the production of S₃⁻ radicals during the operation of Li-S batteries containing 1 M LiTFSI in TEGDME:DOL [106]. Wujcik *et al.* estimated the composition of polysulfides at different stages discharge by predicting XAS spectra using first-principles molecular dynamics method (Fig. 2.11) [107].

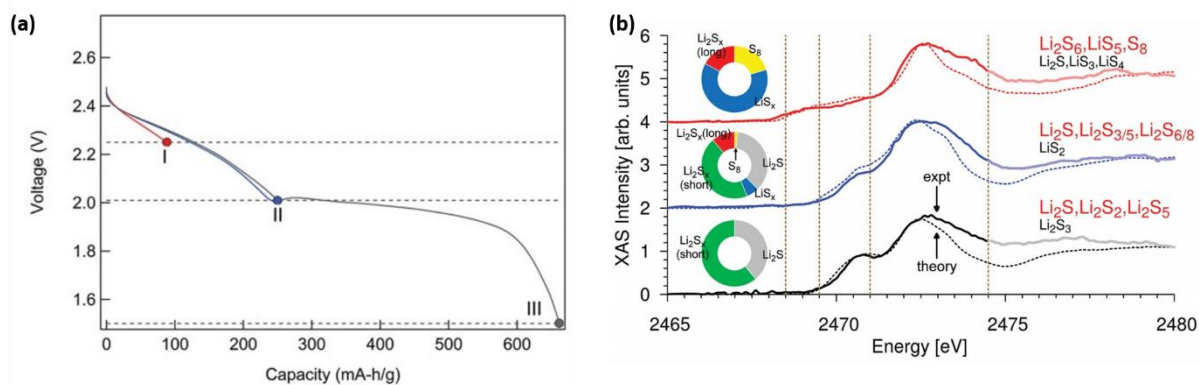


Figure 2.11. Discharge curves measured using a modified pouch cell with X-ray transparent window and (b) theoretical and experimental XAS spectra at different stage of discharge [107].

Park *et al.* used a classical molecular dynamics method to predict the structure and transport properties of 1 M LiTFSI in DME:DOL [108]. Li *et al.* predicted the radius of gyration of different dissolved Li⁺ and polysulfides in different electrolyte using molecular dynamics simulations

[109]. These results were used to design polysulfides blocking microporous polymer membrane.

2.5.2. Mesoscopic modelling

Mesoscopic modelling of Li-S batteries is carried out mostly using molecular dynamics. Mesoscopic models are widely used to investigate the interfacial phenomena such as the polysulfides interaction [110] and Li_2S over carbon surface [111], volume expansion of carbon/sulfur composite and impregnation of liquid sulfur into the micropores [112].

Li *et al.* performed reactive molecular dynamics calculations on different large-scale Li-S nanoparticles (10 nm) such as bulk- α - S_8 , Li_2S_8 , amorphous and crystalline Li_2S to predict the particle structures at different stages of discharge (Fig. 2.12). The core-shell Li_2S_8 particle with Li_2S core and S shell had the lowest energy, which suggest that this type of structure is likely formed when Li_2S are de-lithiated during charging.

Few more mesoscopic modelling works have been discussed in the introduction of chapter 3.

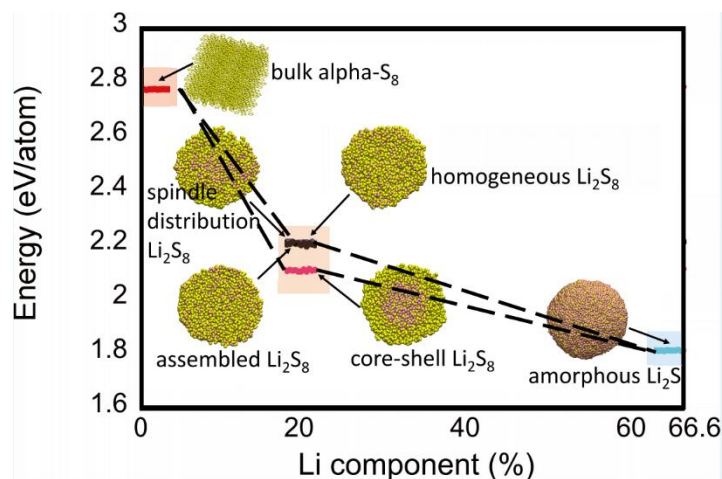


Figure 2.12. Structures and energies of different Li-S nanoparticles.

2.5.3. Continuum level modelling

The continuum models are conventionally used to identify the phenomena behind the characteristics of charge/discharge curves and the performance limitations of Li-S batteries. The first comprehensive one-dimensional (1D) continuum model for Li-S batteries was developed by Kumaresan *et al.* [92]. This model is based on the porous electrode theory, where the cathode and the separator are considered to be homogenous porous media (Fig. 2.13a). The transport of dissolved species through these porous media are described using the dilute solution theory. Furthermore, this model considers multiple reduction and precipitation/dissolution reactions of different polysulfides and it is capable of simulating the typical discharge curve of a Li-S battery (Fig. 2.13b).

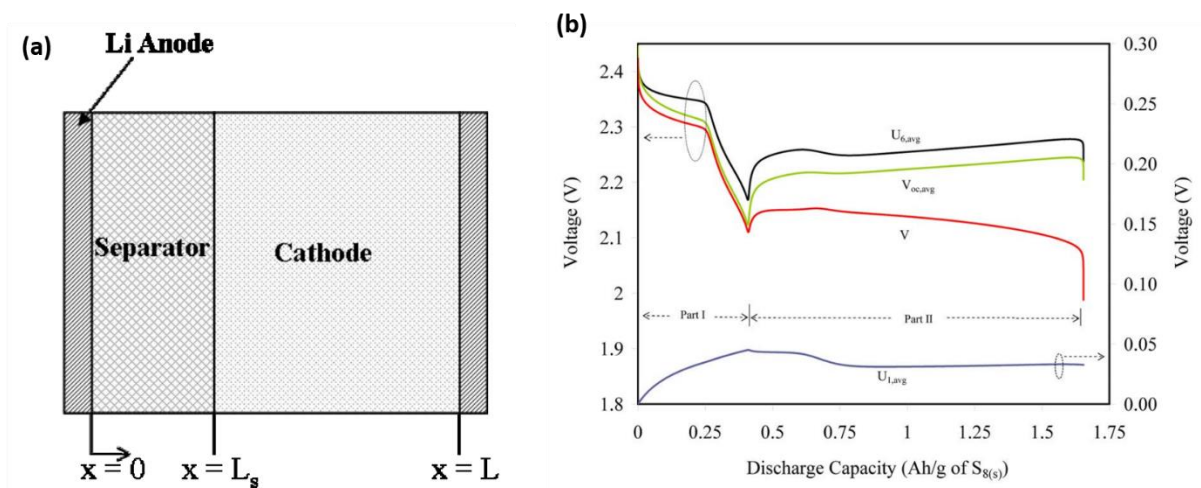


Figure 2.13. (a) Schematic representation of the Li-S cell design considered in the Kumaresan *et al.*'s model and (b) the simulated average open circuit potential curves of different reactions and the full discharge curves [92].

Hofmann *et al.*, developed a similar 1D continuum model which had fewer reaction steps but considered the polysulfides shuttle mechanism [113]. This model was capable of simulating the galvanostatic discharge and charge curves of Li-S batteries and it was used to investigate the impact current densities on the overcharging due to polysulfides shuttle phenomena (Fig. 2.14a). This model also predicted the capacity loss upon cycling due to irreversible precipitation of Li_2S over the Li metal anode (Fig. 2.14b).

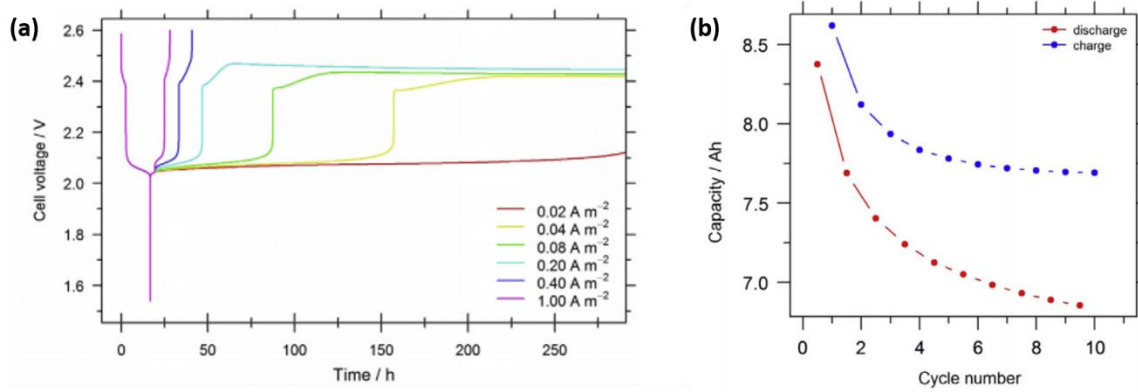


Figure 2.14. (a) Simulated galvanostatic charge and discharge curves for different current density and (b) simulated charge and discharge capacities for 10 cycles calculated using Hofmann *et al.*'s model [113].

Zhang *et al.* utilized a modified Kumaresan *et al.*'s model with low ionic diffusion coefficients to investigate the reduction of discharge capacity at high discharge rate (1C) [114]. They showed that due to the slow transport of Li^+ , polysulfides were forced to migrate to the separator to maintain charge neutrality which lead to the reduction of discharge capacity at high discharge rate (Fig. 2.15a). They also showed that this capacity loss could be recovered by relaxing the cell for 1 hour (Fig. 2.15b). Therefore, they concluded that the discharge capacity of Li-S is mainly limited by the slow transport of Li^+ during fast discharge.

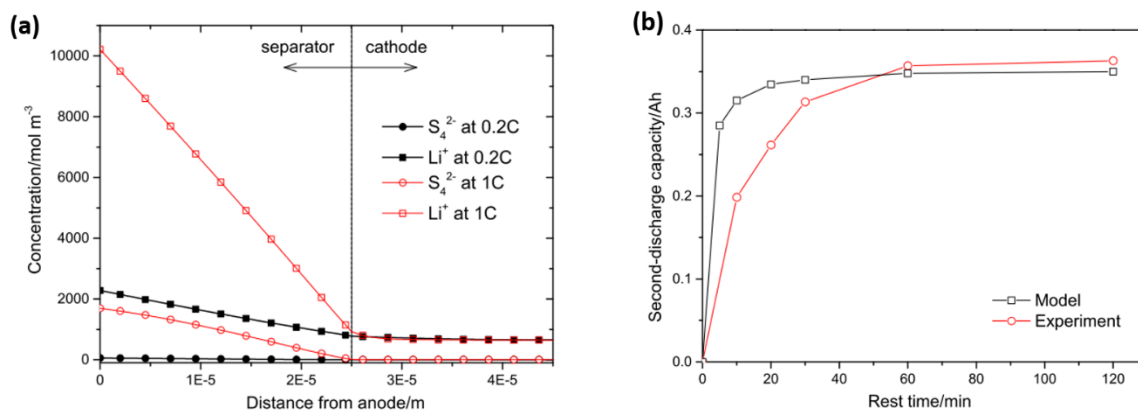


Figure 2.15. Simulated Li^+ and S_4^{2-} concentrations along the Li-S cell at the end of 0.2C and 1C discharge and (b) experimental and simulated capacities after relaxation following the 1C discharge [114].

The discussions about the few other continuum models are presented in the introductions of chapters 3, 4, 5 and 6.

2.6. Conclusions

Although the concept of Li-S batteries exists for several decades, the improvements to its performance such as the increase of its discharge capacity, coulombic efficiency and cyclability were achieved only in the last decade. Most of the improvements were achieved through the tailoring of the architecture of the carbon/sulfur composites. However, they were also improved by inhibiting the adverse reactions of the polysulfides with the Li metal anode either through SEI formation using electrolyte additives or by using protective coatings or layers. Even after all these developments, the assessment of Li-S batteries phenomena and optimization of its performance is not trivial, due to its complex operating principle. Therefore, numerous models were also developed to investigate the phenomena behind the experimental results and observations of the Li-S batteries. The models applied to Li-S batteries are based on different approaches and the phenomena that they are used to assess span different spatial and temporal scales. Majority of the Li-S batteries models are atomistic/molecular level models which are used to estimate the properties of the materials used such as solid sulfur, Li_2S and polysulfides, etc. Atomistic/molecular level models also assist in simulating and analysing the experimental spectroscopic results. Continuum models are used to simulate and analyse the electrochemical experiments of Li-S batteries. They also help in the identification of certain phenomena and limitations during the operation of Li-S batteries. However, most of the continuum models do not consider the detailed architecture of the carbon/sulfur composites used in the cathode. Therefore, they do not provide insights into the impacts of the carbon/sulfur composite design on the performance of Li-S batteries. Furthermore, there are very limited mesoscopic models were developed to investigate the phenomena occurring at the mesoscopic level in Li-S batteries. In this PhD, we have attempted to address the issues such as evolution of carbon/sulfur cathode mesostructures during discharge, impacts of cathode design parameters on discharge and understanding the reaction steps involving dissolved polysulfides and electrodeposition of Li_2S .

Chapter 3. A 3D kinetic Monte-Carlo model for Li-S batteries

Contents

| | |
|---|-----------|
| 3.1 Background and Motivation | 44 |
| 3.2 Theoretical methodology..... | 45 |
| 3.2.1 Creation of initial C/S mesostructure..... | 45 |
| 3.2.2. Development of the 3D kMC-VSSM model and its assumptions..... | 47 |
| 3.2.3. Equations for rate constants of different types of events | 49 |
| 3.2.4. Working principle of the 3D kMC-VSSM code | 52 |
| 3.3. Impact of discharge rate | 55 |
| 3.3.1. General effective evolutions of C/S mesostructure..... | 56 |
| 3.3.2. Mesoscale evolutions of Li ₂ S deposits over carbon..... | 64 |
| 3.3.2.1. Distribution of Li ₂ S particles from the carbon surface..... | 65 |
| 3.3.2.2. Size distribution of Li ₂ S _(s) clusters..... | 69 |
| 3.4. Impact of sulfur loading..... | 73 |
| 3.5. Conclusions | 77 |

Chapter 3. A 3D kinetic Monte-Carlo model for Li-S batteries

3.1 Background and Motivation

The carbon/sulfur (C/S) composite cathodes of lithium sulfur batteries undergo mesostructural evolutions during discharge due to the dissolution/precipitation reactions of solid sulfur ($S_{8(s)}$) and Li_2S [56,115]. Where, the morphology of the Li_2S precipitates depends on the operation and cathode designs such as discharge rate, sulfur loading, etc. [116,117]. Since these Li_2S precipitates are insulating, they impact the discharge performance due to phenomena such as surface passivation [118] and pore-clogging [119]. Therefore, the interest to investigate the impact of discharge performance on the mesostructural properties of the Li_2S precipitate and vice-versa using mathematical models have increased recently [118,120]. However, most of the continuum models used for the investigation of charge and discharge performances of Li-S batteries, only consider the effective cathode structural properties [92,113,114,121,122]. Thereby, they overlook the three-dimensional (3D) nature of the C/S mesostructure and the Li_2S deposits.

Recently, Mistry *et al.* developed a modelling framework, where the precipitates are grown randomly (i.e. without explicitly describing the reaction mechanisms) in 3D porous carbon microstructures based on deposition energy and a morphology parameter [123]. They also calculated the effective cathode structural evolutions of those microstructures and incorporated them in their 1D continuum discharge model to predict the impacts of Li_2S morphologies, sulfur loading, etc. on the performance. Contrary to the aforementioned models, Beltran *et al.* developed a classical reactive molecular dynamics model which explicitly simulates the discharge of a 3D graphene/sulfur microstructure [124]. This model is capable of predicting the reduction of sulfur, interactions between different atoms, discharge potential and volume expansion of graphene/sulfur microstructures upon lithiation. However, this model is too local and it does not provide details about the mesostructural evolutions such as porosity, coverage of Li_2S precipitates on carbon, etc. [124].

Kinetic Monte Carlo (kMC) models have the inherent advantage of being able to simulate longer time scales than classical molecular dynamics by keeping the atomistic/molecular resolution. In the context of Li-S batteries, Liu *et al.* developed a kinetic Monte-Carlo (kMC)

model which includes phenomena such as adsorption, desorption and surface diffusion of Li_2S over a flat carbon substrate [125]. This model is capable of predicting the impact of temperature, S^{2-} concentration, etc. on the mesoscale properties such as thickness and coverage $\text{Li}_2\text{S}_{(s)}$ deposits [125]. However, this model cannot be used to study the direct impact of the discharge on the deposition, since it does not consider any electrochemical reduction process [125].

Therefore, we have developed a novel 3D kMC model which explicitly simulates structural evolutions of C/S mesostructure and Li_2S precipitation during discharge. Our model includes phenomena such as dissolution reaction of $\text{S}_{8(s)}$, diffusions and reduction reactions of dissolved sulfur and polysulfides and electrodeposition of Li_2S . The main objective of this chapter is to present the development our kMC model as a methodology to understand the mesoscale evolutions of C/S composite cathodes and Li_2S deposits during discharge. Note that the impacts of discharge C-rate on the performance such as the capacity limitation and polarization of the discharge curves are due to certain macroscopic phenomena. Some of these phenomena are the overpotential due to electrolyte resistance [126], anode and cathode activation overpotentials [127], transport overpotential [114,128], etc. Since, our kMC model simulates the discharge of C/S composite cathodes at mesoscopic level, the aforementioned macroscopic phenomena cannot be described by it. The impact of the cathode design and the C-rate on the discharge performance is discussed in the Chapter 4.

The contents of this chapter were reported in a research paper titled, 'A three dimensional kinetic Monte Carlo model for simulating the carbon/sulfur mesostructural evolutions of discharging lithium sulfur batteries', which was published in the journal called Energy Storage Material [129]. This research paper was co-authored by V. Thangavel, O. X. Guerrero, M. Quiroga, A. M. Mikala, A. Rucci and A. A. Franco.

3.2 Theoretical methodology

3.2.1 Creation of initial C/S mesostructure

An *in silico* method was used to create a 3D simulation box based on the structural and geometrical properties of the desired initial C/S mesostructure used in our kMC model (Fig. 3.1). Initially, a cubic box containing randomly distributed spherical carbon particles

representing the porous carbon mesostructure was created using a commercial software called Geodict. The side length of this cubic box and the diameter of the carbon particles were set to 50 and 25 nm respectively. The porosity of the entire mesostructure was set to 67%. The cubic box was then meshed along each side into 100 cubic volumetric elements called voxels. Although the carbon mesostructure presented here is not tied to a direct experimental measurement, its continuum-level descriptors are relevant with the previously reported carbon host materials. Ma *et al.*, utilized cauliflower like carbon/sulfur composite cathode material, in which the size of the carbon particles is 25 nm [130]. The volume percentage of the pores in their cathode material with sizes above 20 nm is 63% which is closer to the porosity of the mesostructure (67%) presented in our manuscript. Zheng *et al.*, used Acetylene Black (AB) carbon nanoparticles in the cathode whose surface area is $123.6 \text{ m}^2 \cdot \text{g}^{-1}$ [131], which is closer to that of our mesostructure ($133.3 \text{ m}^2 \cdot \text{g}^{-1}$).

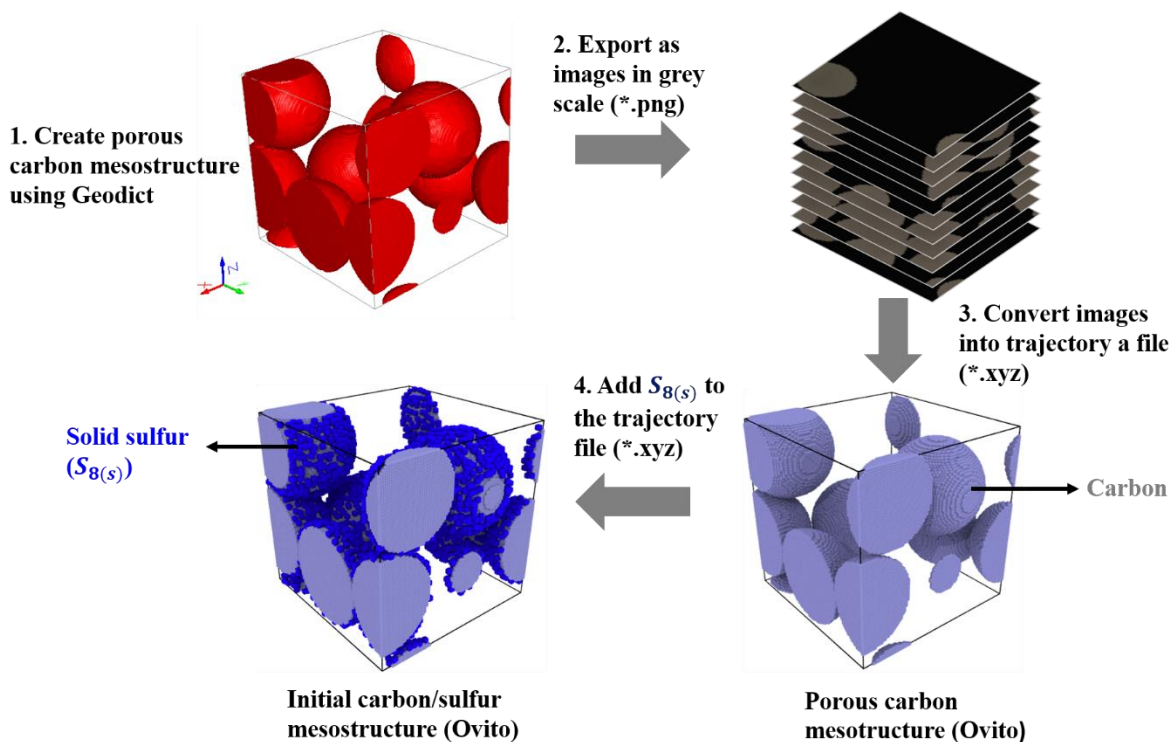


Figure 3.1. Schematics of the *in silico* method to create the initial C/S mesostructure.

The side length of each voxel was set to 5 \AA which is close to the S-S bond length (3.1 \AA) in an isothermally stabilized graphene/S microstructure [124] which was simulated using a

classical reactive molecular dynamics model. Therefore, this distance was set as the resolution between the coarse-grained atoms which are in contact with each other. The resulting structure was exported as a stack of images (*.png). An *in house* developed python code uses the grey scale values of these images to create the simulation box with voxels containing carbon atoms. Locations of the carbon atoms in the simulation box were exported to location file (*.xyz) along with those of the solid sulfur ($S_{8(s)}$) particles (Fig. 3.1). The visualizations of the simulation box were done using the open source software Ovito [132]. The locations of each coarse-grained carbon (C) and sulfur (S) atoms in $S_{8(s)}$ were identified using the integer numbers 1 and 2. Each $S_{8(s)}$ particle consists of eight coarse-grained S atoms that are in contact with each other (Fig. 3.2). The $S_{8(s)}$ particles were randomly distributed next to the coarse-grained C atoms at the carbon particle surface since the impregnated $S_{8(s)}$ sticks to the surface of the carbon particles [55]. Furthermore, the mass ratio between C and S atoms was set to 1:0.27. We have used this low sulfur loading in our simulations to reduce the computational cost.

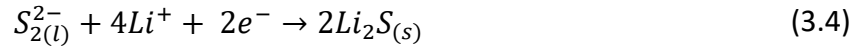
Finally, the resulting location file is read by our *in house* developed kMC python code, which reconstructs the simulation box and utilizes it as the initial C/S mesostructure. It should be noted that our *in silico* C/S mesostructure creation method and kMC code are not specific to the aforementioned dimensions, structural and geometric parameters. In fact, we can customize the initial C/S mesostructure by changing the parameters such as of the shape and size of the carbon particles, mesostructure porosity, sulfur loading, etc. In the future, this *in silico* method will also be used to transform the tomographic images of a real C/S composite electrode into a simulation box which will then be used as the initial C/S mesostructure of our kMC code.

3.2.2. Development of the 3D kMC-VSSM model and its assumptions

In the past, an on-lattice kMC algorithm called Variable Step Size Method (VSSM) was developed and used by us to describe the reaction and diffusion events in Fuel cells [133] and Li-O₂ batteries [134,135] and Brownian motion of suspended particles in slurry redox flow batteries [136,137]. Here, we have adopted a similar method to select and execute the reaction and diffusion events (Fig. 3.2) during the discharge simulation of an *in silico* created C/S mesostructure (Fig. 3.1).

Although there could be several reactions involving multiple dissolved polysulfide species that occur during the operation of Li-S batteries, a reduced set of reaction steps (Eqs. 3.1-3.4) was considered in our kMC model. The aforementioned simplification was done in order to limit the computational costs of our simulations and complexities arising through multiple unknown parameters. This approximation is common in many previously reported Li-S batteries models [113,138–141].

The reaction events considered in the 3D kMC model are as follows,



where, Eq. 3.1 is the chemical dissolution of $S_{8(s)}$ to dissolved $S_{8(l)}$ and Eqs. 3.2 and 3.3 are the electrochemical reduction reactions of dissolved $S_{4(l)}^{2-}$ and $S_{2(l)}^{2-}$ respectively. Finally, Eq. 3.4 is the electrodeposition of solid $Li_2S_{(s)}$.

Just as the S atoms in $S_{8(s)}$ particles, the coarse-grained atoms in $S_{8(l)}$, $S_{4(l)}^{2-}$, $S_{2(l)}^{2-}$ and $Li_2S_{(s)}$ particles are also identified using unique set of integer numbers namely 3, 4, 5 and 6 respectively. The coarse-grained structures of the different sulfur based particles along with the schematic representation of the reaction events between them and the directions in which the dissolved particles can diffuse are shown in Fig. 3.2. Each of the $S_{8(l)}$, $S_{4(l)}^{2-}$ and $S_{2(l)}^{2-}$ particles have 8, 4 and 2 coarse-grained S atoms, respectively (Fig. 3.2). The distance between centers of the atoms which are within a sulfur-based particle is equal to the mesh size (5 Å). Our kMC model does not include Li atoms explicitly, thus each $Li_2S_{(s)}$ particle is simulated using a single coarse-grained atom. Among the reactions considered in our model (Eq. 3.1-3.4), only the Li_2S electrodeposition involves dissolved $Li_{(l)}^+$ in the electrolyte. Moreover, the $Li_{(l)}^+$ concentration in Li-S batteries electrolyte is much larger (≈ 1000 – 5000 mM) than that of

$S_{2(l)}^{2-}$ (≈ 10 mM) [92], therefore the kinetics of Li_2S electrodeposition will primarily depend on the latter. Since the dissolved $Li_{(l)}^+$ and anion of Li salt are highly concentrated in the electrolyte, the probabilities of our kMC model selecting their diffusion events are much higher. This will ultimately increase the simulation cost. Therefore, the Li salt containing supporting electrolyte is not explicitly considered in our model, and we assume that they are uniformly distributed in the void volume of the simulation box.

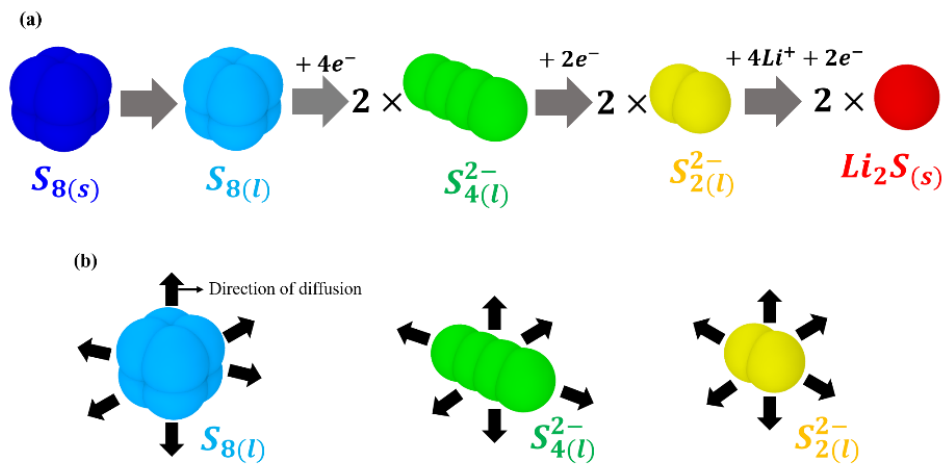


Figure 3.2. Schematic representations, of (a) the reaction events considered in our model along with the coarse-grained structures of the different types sulfur based particles and (b) the six directions in which the dissolved particles ($S_{8(l)}$, $S_{4(l)}^{2-}$ and $S_{2(l)}^{2-}$) can diffuse.

3.2.3. Equations for rate constants of different types of events

According to the VSSM algorithm used in our 3D KMC model presented here, an event is selected and executed in a given time step or an iteration based on the weighted probabilities of all the possible events which depend on their corresponding rate constants. Therefore, it is important to determine the rate constants for different types of events.

The rate constants of the electrochemical reactions in our model (Eqs. 3.2-3.4) could be calculated using Butler Volmer type equations [134,135]. However, the overpotentials in the Butler Volmer equations vary a lot during the discharge of Li-S batteries [126]. Since we intend

to simulate the discharge of our in-silico created C/S mesostructures under a galvanostatic condition, we have derived the rate constants of the electrochemical reactions based on the discharge current (I) which remains constant at any given time. Therefore, the kinetic rate constant (K_j^{ele}) of an electrochemical reaction (j) is given by a Faraday's law type equation,

$$K_j^{ele} = \frac{I}{n_j q_e} \Theta(\delta_e) \quad (3.5)$$

The discharge current I is determined from the discharge C-rate and initial mass of $S_{8(s)}$ present inside simulation box. n_j and q_e in eq. 3.5 are the number of electrons transferred in an electrochemical reaction (j) and the charge of the electron respectively. According to eq. 5, the applied current is equal to the Faradaic current at each iteration. We have neglected the double layer phenomenon [142] in our kMC model, since its impact on the simulated results and mechanisms in the Li-S batteries are still unclear. Furthermore, implementation of double layer dynamics would increase the computational cost of our model, since it would require us to simulate the supporting electrolyte explicitly or coupling the KMC model with a physical double layer model.

In order for the electrochemical reactions to occur, the dissolved polysulfides should be present within the electron tunnelling distance (δ_e) from the carbon surface and the electron tunnelling probability ($\Theta(\delta_e)$) is given by a simple function [134],

$$\Theta(\delta_e) = \begin{cases} 1, & 0 \leq \delta_e \leq 10 \text{ nm} \\ 0, & \delta_e > 10 \text{ nm} \end{cases} \quad (3.6)$$

Furthermore, the kinetic rate constant of the $Li_2S_{(s)}$ deposition reaction is considered only when the $S_{2(l)}^{2-}$ particles are present next to either a carbon atom or a $Li_2S_{(s)}$ particle. This condition mimics the nucleation and growth processes of $Li_2S_{(s)}$ observed in Li-S batteries. In few chronoamperometric investigations of $Li_2S_{(s)}$ electrodeposition [49,143], Bewick,, Fleischman, and Thirsk (BFT) model [144,145] and Scharifker-Hills (SH) Model were used fit

the dimensionless current signals. These models assume that the charge transfer step of the electrodeposition is fast and the growth of the existing Li_2S nuclei is controlled by mass transport of dissolved species to the electrode surface. However the model developed by Ren *et al.*, uses a modified Tafel equation to calculate current for the growth of Li_2S nuclei, [141] which is the rate of charge transfer step. Therefore, we have considered the charge transfer steps along with the diffusion $S_{2(l)}^{2-}$ for the $\text{Li}_2\text{S}_{(s)}$ nucleation and growth reactions.

The transport rates of electrons through solid $S_{8(s)}$ and $\text{Li}_2\text{S}_{(s)}$ are quite low [103]. Therefore, we have currently neglected the electronic conductivities of solid $S_{8(s)}$ and $\text{Li}_2\text{S}_{(s)}$ in our kMC model. However, the inclusion of these conductivities could be a further improvement of our model and it could be carried out in the future.

As mentioned before, our model also considers the diffusion of dissolved particles such as $S_{8(l)}$, $S_{4(l)}^{2-}$ and $S_{2(l)}^{2-}$ along six directions (Fig. 3.2). The diffusion rate constant of a dissolved particle (i) is given by the Stokes-Einstein's equation,

$$K_i^{dif} = \frac{\kappa_B T}{6\pi\mu r_i z^2} \quad (3.7)$$

where μ and r_i are the viscosity of the electrolyte and radius of gyration of a dissolved particle (i) respectively. z is the distance displaced by the dissolved particle along a given direction. The parameters used in the kMC model is listed in Table 3.1.

Since our model simulates the redox reaction of the dissolved particles in the electrolyte phase near the electrode surface instead of solid-state-like reactions [81], the ionic transport events through $S_{8(s)}$ and $\text{Li}_2\text{S}_{(s)}$ deposits [103] are neglected.

Table 3.1. Parameters used in our Li-S kMC model

| Parameter | Name | Value | unit |
|---|---|-----------------------|--------------------|
| $r_{S_{8(l)}}$ | Radius of gyration of $S_{8(l)}$ | 2.0×10^{-9b} | m |
| $r_{S_{4(l)}^{2-}}$ | Radius of gyration of $S_{4(l)}^{2-}$ | 3.0×10^{-9b} | m |
| $r_{S_{2(l)}^{2-}}$ | Radius of gyration of $S_{2(l)}^{2-}$ | 2.0×10^{-9b} | m |
| η | Viscosity of the electrolyte | 2.5^a | $kg.m^{-1}.s^{-1}$ |
| z | Distance for diffusion | 24×10^{-9a} | m |
| $K_{S_{8(s)} \rightarrow S_{8(l)}}^{che}$ | Rate constant for chemical dissolution of $S_{8(s)}$ | 10^a | s^{-1} |
| U^0 | Standard potential for $S_{4(l)}^{2-}/S_{2(l)}^{2-}$ electrochemical reaction | 2.1^c | V |

^aAssumed parameters which are chosen to speed up the discharge simulation.

^bRadius of gyration values adopted from Ref. [109].

^cStandard potential adopted from Ref. [121].

3.2.4. Working principle of the 3D kMC-VSSM code

Reconstruction of the simulation box containing our *in silico* C/S mesostructure, is the initial step of our model, after which the kMC code enters into an iterative loop to execute the reaction and diffusion events during discharge simulation (Fig. 3.3).

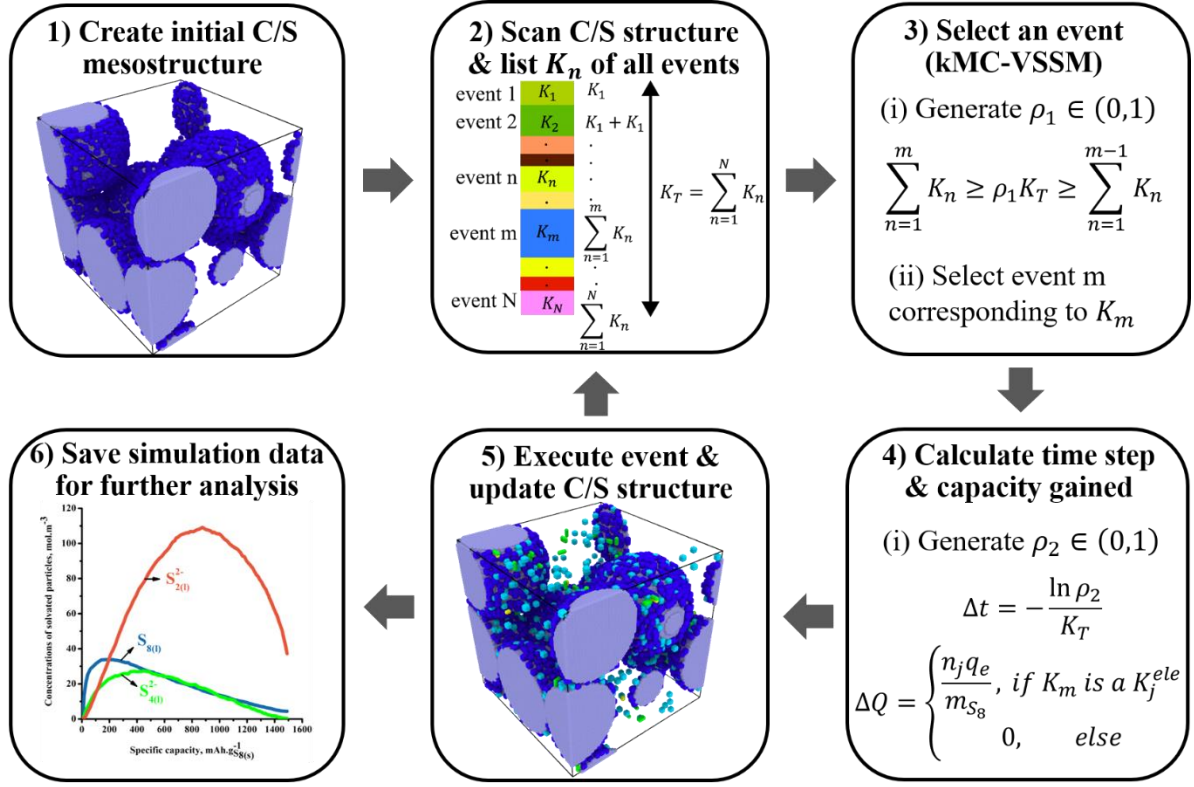


Figure 3.3. Workflow of the 3D kMC-VSSM code.

In any given iterative cycle, the entire simulation box is initially scanned in order to find all the different types of particles and the possible events which could be performed by them. A list containing all the possible events is then stored in the computer memory, along with their corresponding particle types, individual and cumulative sums of rate constants, current and final locations inside the simulation box. After this step, the sum of all the possible events (K_T) is calculated as follows,

$$K_T = \sum_{n=1}^N K_n \quad (3.8)$$

where N is the total number of all the possible events in a given iterative cycle and K_n is the rate constant of n th event in the aforementioned list. K_n could be either a rate constant of a diffusion (k_i^{dif}) or a chemical (k_k^{che}) or an electrochemical reaction event (k_j^{ele}).

After calculating K_T , a random number (ρ_1) $\in (0,1)$ is generated. According to the conditional algorithm of our kMC-VSSM model – an event is selected based on the cumulative sums of the rate constants of all the possible events and the product of ρ_1 and K_T as follows,

$$\sum_{n=1}^m K_n \geq \rho_1 K_T \geq \sum_{n=1}^{m-1} K_n \quad (3.9)$$

where m is the number of the selected event in the list.

According to Eq. 3.9, the product of the first random number and the sum of the rate constants of all the events ($\rho_1 K_T$) – is within the range between the partial cumulative sums of the rate constants of $(m - 1)^{\text{th}}$ and m^{th} event in the list. Therefore, according to the condition Eq. 3.9, in any given iterative cycle, the events with large rate constants have larger probabilities to be selected. Furthermore, an event type has a large probability of being selected, when there is a large number of events of that type present in the list of possible events.

Since diffusion rate constants are normally larger than electrochemical rate constants, our kMC code has to go through a large number of iterative cycles which select diffusion events before an electrochemical reaction event is selected. Therefore, in each iterative cycle, we only consider the diffusion rates of dissolved particles which could be displaced to a particular distance along anyone of the six directions within the simulation box. This criterion will increase the frequency in which electrochemical events are selected, and thereby it aids the discharge simulation to progress faster.

Following the event selection process of an iterative cycle, its corresponding time step (Δt) is calculated as follows,

$$\Delta t = -\frac{\ln \rho_2}{K_T} \quad (3.10)$$

where ρ_2 is the second random number $\in (0,1)$. Since Δt is inversely proportional to K_T , it varies from one iterative cycle to another and it also makes the calculated time (t) after each iteration to be low. However, since we are interested in comparing the simulated results of two different discharge rates, it is much more relevant to represent them as functions of specific capacity (Q). Therefore, we also calculate the specific capacity gained (ΔQ) during each iteration using the following equation,

$$\Delta Q = \begin{cases} \frac{n_j q_e}{m_{S_{8(S)}}}, & \text{if } K_m \text{ is a } K_j^{\text{ele}} \\ 0, & \text{else} \end{cases} \quad (3.11)$$

where the product of n_j and q_e in Eq. 3.11 is the charge transferred during the selected electrochemical event (j) and $m_{S_{8(S)}}$ is the initial mass of $S_{8(S)}$ present in the simulation box.

The final step in the iterative loop our kMC code is the execution of the selected event and the evolution of the C/S mesostructure inside the simulation box. This evolved C/S mesostructure, once again goes through another subsequent cycle consisting of steps such as scanning to find all possible events, selection and execution of an event and evolution C/S mesostructure. After a selected amount of cycles of this iterative process, the details of the simulation box such as number and locations of different types of particles, specific capacity, time and porosity are saved for further analysis. Discharge simulations were carried out on a server, which consists of thirty-two 3.30 GHz Intel(R) Xenon(R) CPU cores and 2.46 TB of total memory. Discharge simulations can go on for several days and they are stopped either when all the $S_{8(S)}$ and dissolved sulfur based particles are converted to $Li_2S_{(S)}$ or if they have been running for too long with very few changes in the type of sulfur particles inside the simulation box.

3.3. Impact of discharge rate

In this section, we have presented the discharge simulation results for two different C-rates namely C/2 and 2C. The same initial C/S mesostructure created using our *in silico* method

(presented in subsection 3.2.1) was used for both the simulations. The C/2 and 2C discharge simulations were concluded at 1230 and 1400 mAh.g_{S₈(s)}⁻¹, respectively. Around these capacities diffusion events dominated over reaction events, resulting in very few changes in the types of sulfur-based particles inside the simulation box. However, the results produced using these simulations were still used to compare the impact of C-rates on the evolutions inside the C/S mesostructure. Due to the stochastic nature of our kMC model, each of these simulations were carried out three times to determine the confidence region which are presented as shaded regions or error bars.

3.3.1. General effective evolutions of C/S mesostructure

As mentioned in the subsection 3.2.4, the locations of the different types of sulfur-based particles are saved to a location file after a selected number of cycles during the discharge simulation. This file can be used to track and visualize the evolution of the simulation. The visualization of the simulation box could be done even when the simulation is performing. Fig. 3.4, shows the visual evolution of the mesostructure inside the simulation box at different depths of discharge (DoDs) or specific capacities, during the 2C discharge simulation.

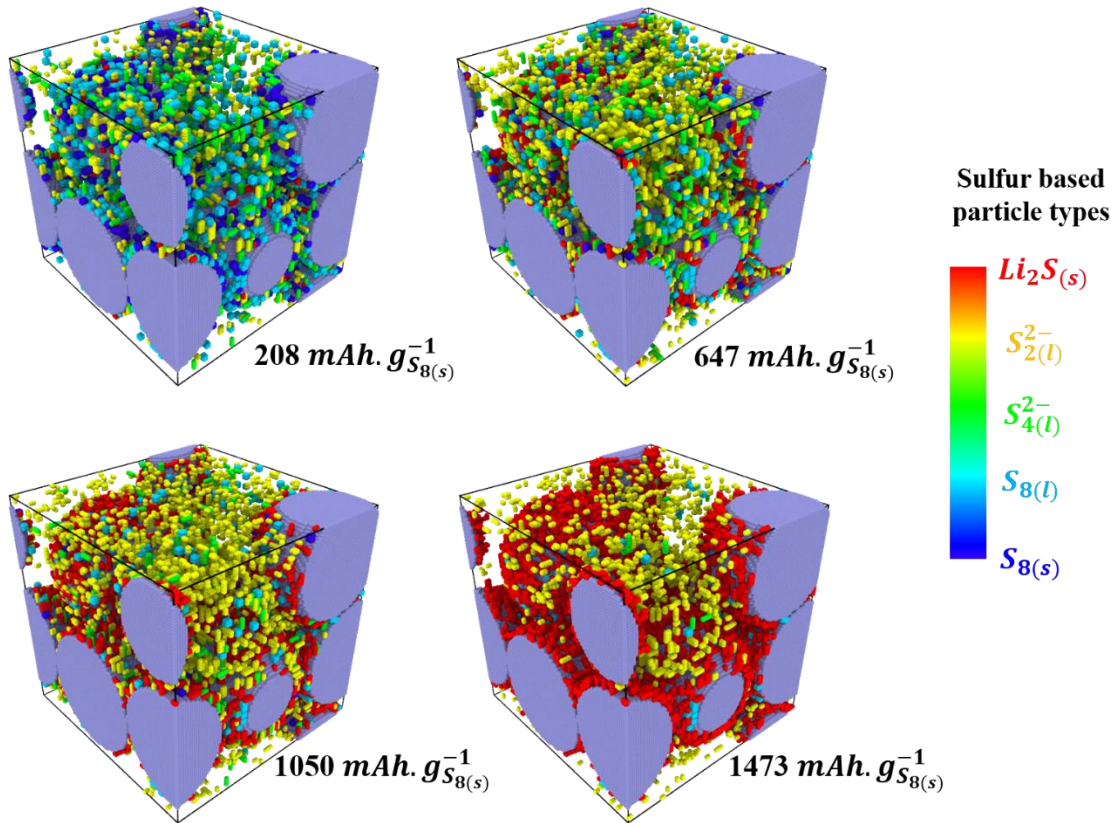


Figure 3.4. Visualization of the simulation box at 208, 647, 1050 and 1473 mAh. $g_{S_{8(s)}}^{-1}$ during the 2C discharge simulation. The colour map in the image shows the colour coding assigned to different types of sulfur based particle types, where $S_{8(s)}$, $S_{8(l)}$, $S_{4(l)}^{2-}$, $S_{2(l)}^{2-}$ and $Li_2S_{(s)}$ particles are shown in navy blue, sky blue, green, yellow and red respectively.

When the simulation box is visualized, each type of sulfur-based particle is assigned a unique colour (Fig. 3.4). Therefore, it is possible to visually get an idea about the DoD of the simulation just from the colours of the particles inside the simulation box (Fig. 3.4). Furthermore, this colour coding visually aids us to see the different types of events taking place inside the simulation box at different DoDs. In addition to visualization, the quantification of the different types of particles in the simulation box can be used to predict the effective properties such as concentrations of dissolved particles, porosity of the mesostructure, etc.

The concentration of a dissolved particle (c_i) inside the porous volume of C/S mesostructure is determined using the equation,

$$c_i = \frac{n_i}{N_A \varepsilon V} \quad (3.12)$$

where N_A and n_i respectively are the Avogadro's number and the total number of dissolved particles of type i (i.e. $S_{8(l)}$ or $S_{4(l)}^{2-}$ or $S_{2(l)}^{2-}$). V is the total volume of the simulation box and ε is the porosity of the C/S mesostructure, which is determined from the fraction between the number of voxels which are unoccupied by the atoms of solid particles (such as carbon, S_8 and Li_2S particles) and the total number of voxels in the simulation box.

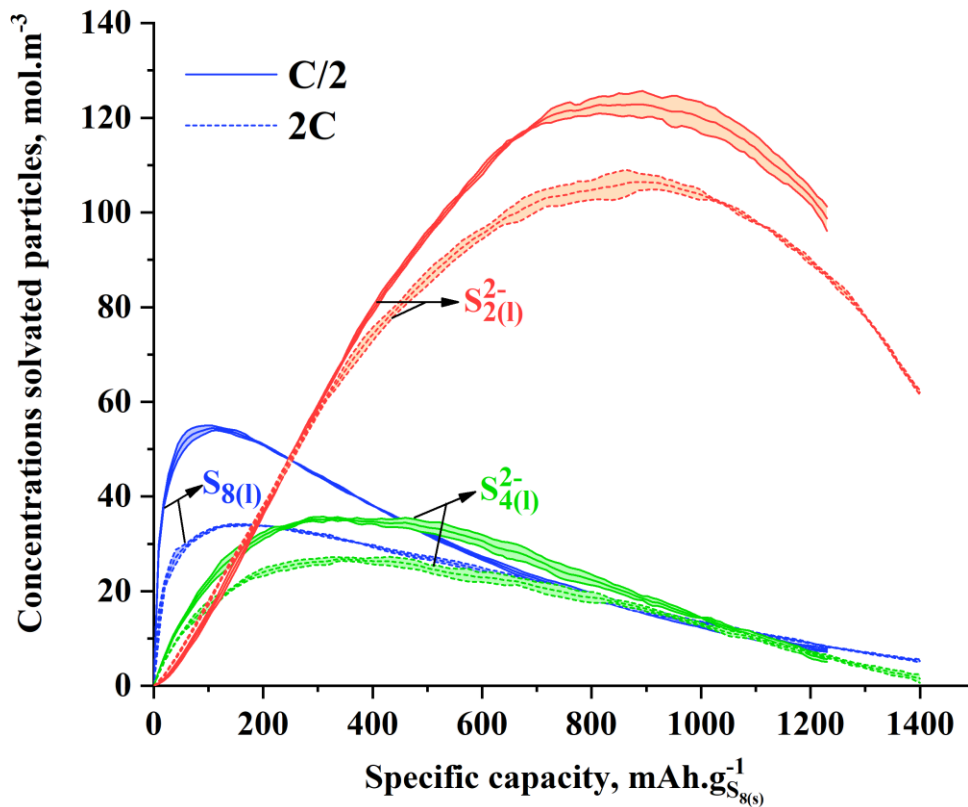


Figure 3.5. Evolutions of the concentrations of $S_{8(l)}$ (royal blue lines), $S_{4(l)}^{2-}$ (green lines) and $S_{2(l)}^{2-}$ (orange lines) during C/2 (solid lines) and 2C (dashed lines) discharge simulations.

Since the rate constants of the electrochemical reactions increase with the C-rates, the dissolved particles during the fast discharge are consumed faster. Therefore, the

concentrations of all the dissolved particles during 2C discharge simulation are always lower than those of the C/2 (Fig. 3.5). The evolutions of concentrations of different dissolved particles (Fig. 3.5) and numbers of $S_{8(S)}$ and $Li_2S_{(S)}$ particles in the simulation box (Fig. 3.8), assist in providing insights into the reactions taking place at different stages of discharge simulations. A typical discharge curve of a conventional Li-S battery, consists of a high and a low potential plateaus, with an intermediate slopy stage, during which the cell potential decreases [57,92]. The cell potentials in the continuum models are derived from the current balance equation [92,113,114]. However, our kMC model does not have equations that directly relate current and potential. Therefore, here we have predicted the approximate discharge curves (Fig. 3.6) from the concentrations of dissolved particles such as $S_{4(L)}^{2-}$ and $S_{2(L)}^{2-}$ using Nernst's equation [92],

$$U = U^o + \frac{RT}{2F} \left(\ln \frac{c_{S_{4(L)}^{2-}}}{1000} - \ln \left(\frac{c_{S_{2(L)}^{2-}}}{1000} \right)^2 \right) \quad (3.13)$$

where U is the approximate discharge potential and U^o is the standard potential for the $S_{4(L)}^{2-}/S_{2(L)}^{2-}$ electrochemical reaction. A similar Nernst's equation was used to predict equilibrium potentials during the discharge in a published Li-S batteries model [119].

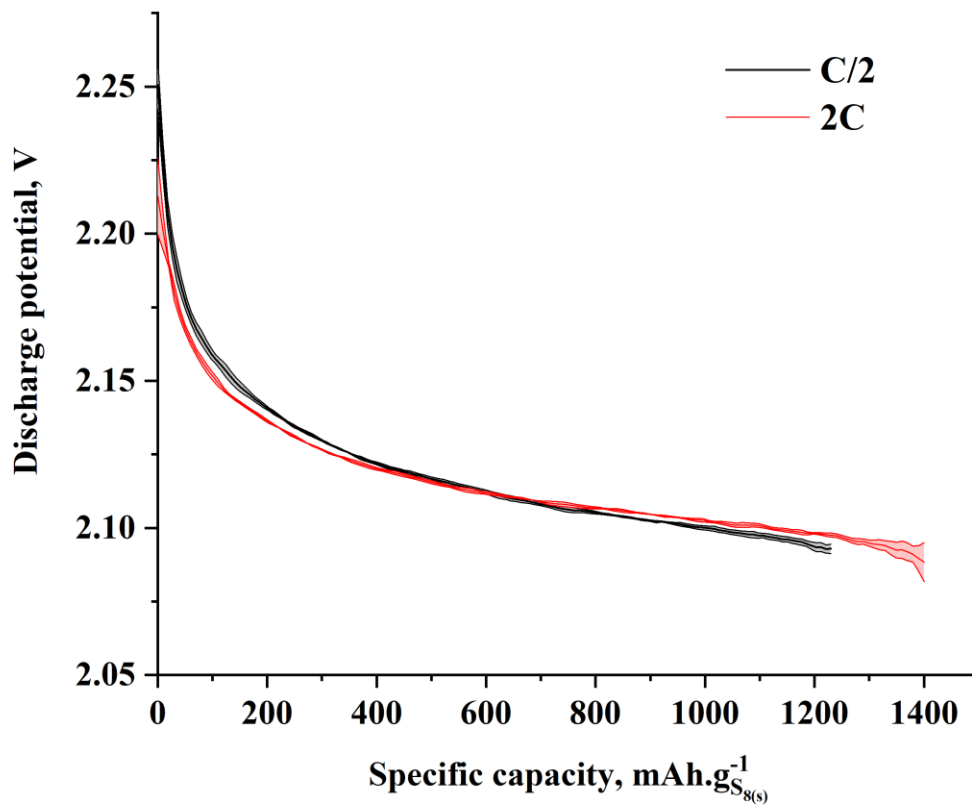


Figure 3.6. Approximate C/2 and 2C discharge curves. Calculated using Nernst's equation for $S_{4(l)}^{2-}/S_{2(l)}^{2-}$ electrochemical reaction.

The calculated approximate discharge curves shown in Fig. 3.6 qualitatively resemble certain experimental results with highly slopy first stage and a relatively flat second stage (Fig. 3.7). The details about this galvanostatic discharge experiment, such as electrode preparation, electrolyte loading, etc. are given in Chapter 7.

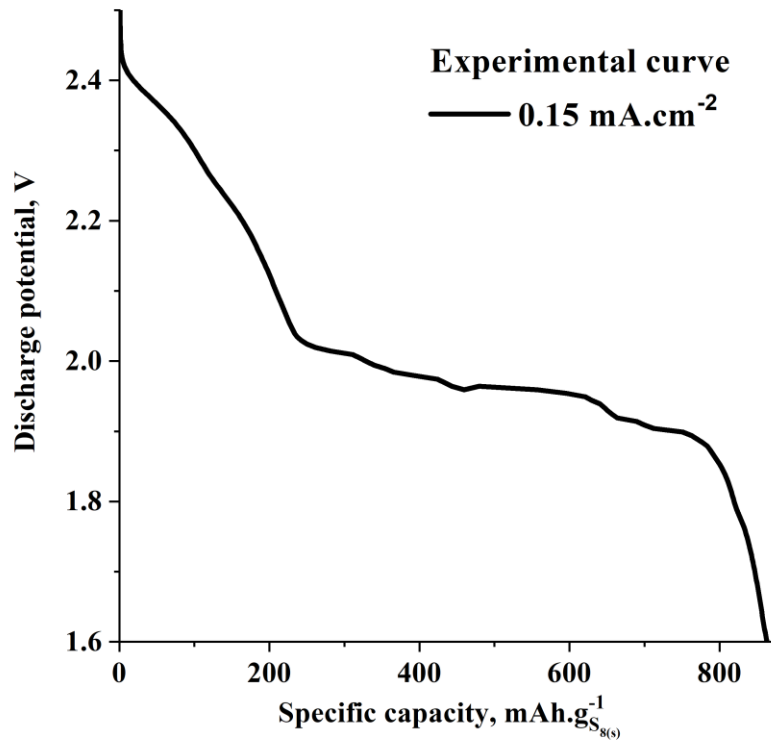


Figure 3.7. Experimental discharge curve of a Li-S coin cell with 1.85 mg.cm^{-2} of sulfur in the cathode.

As mentioned before, the calculated discharge curves are only used to correlate the stages of our simulations with the experiments and we did not make any attempt to predict discharge curves that quantitatively match the experimental results. Since we have used the Nernst's equation, discharge curves correspond to theoretical equilibrium potentials, which is why the variation between them are smaller in comparison with the experiments.

Initially, during the first slopy discharge stage, the concentrations of the dissolved $S_{8(l)}$ and $S_{4(l)}^{2-}$ particles (Fig. 3.5) increase due to the chemical dissolution of $S_{8(s)}$ particles and subsequent reduction of some $S_{8(l)}$ particles to $S_{4(l)}^{2-}$, respectively. This could be understood from the decrease in the number of $S_{8(s)}$ during this initial stage in both C/2 and 2C discharge simulations (Fig. 3.8). However, in the middle of the first slopy discharge stage ($\approx 100 \text{ mAh.g}_{S_{8(s)}}^{-1}$), the $S_{8(l)}$ concentrations for both C/2 and 2C simulations start to decrease (Fig.

3.5), while the concentrations of $S_{4(L)}^{2-}$ continue to increase and those of the $S_{2(L)}^{2-}$ start to increase. This indicates that the $S_{4(L)}^{2-}/S_{2(L)}^{2-}$ reduction reaction starts at this stage in both the discharge simulations. Furthermore, the electrodeposition of $Li_2S_{(s)}$ also starts at this stage ($\approx 100 \text{ mAh} \cdot \text{g}_{S_{8(s)}}^{-1}$), since the numbers of $Li_2S_{(s)}$ particles for both C/2 and 2C simulations start to increase (Fig. 3.8).

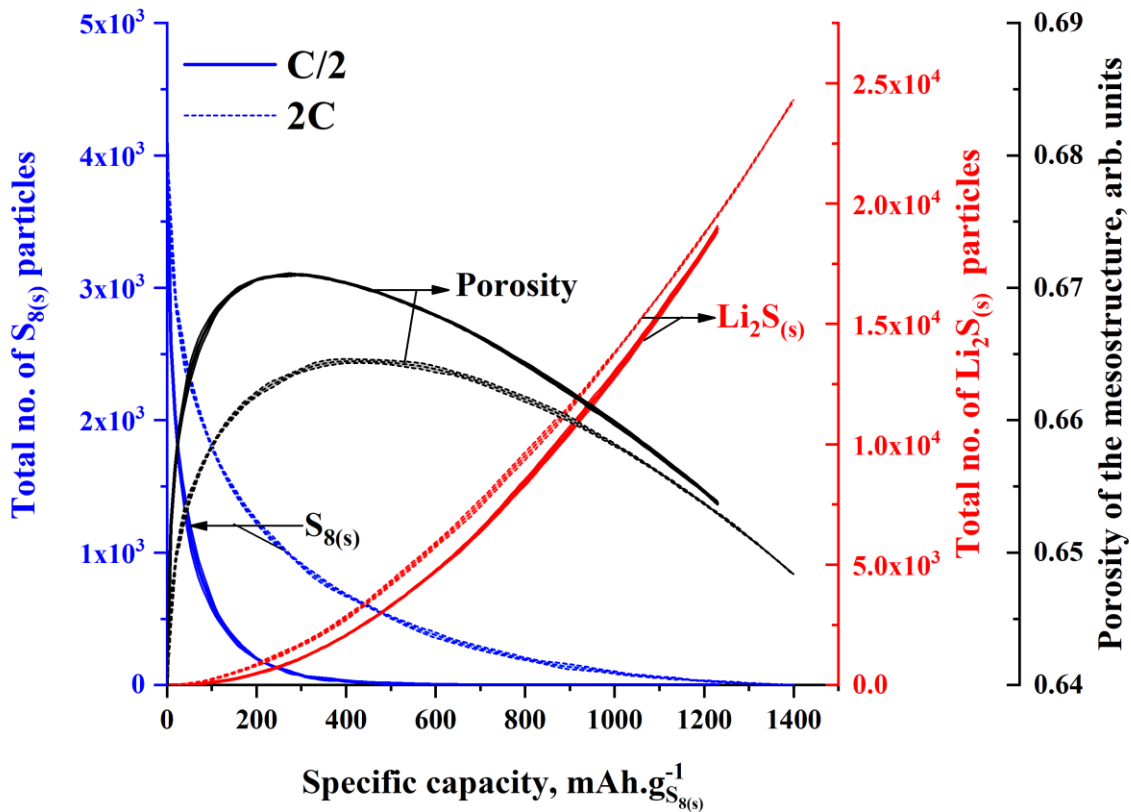


Figure 3.8. Evolutions of number of $S_{8(s)}$ (navy blue lines) and Li_2S (red lines) particles and the porosity of the C/S mesostructure during the C/2 (solid lines) and 2C (dashed lines) discharge simulations.

At around $250 \text{ mAh} \cdot \text{g}_{S_{8(s)}}^{-1}$ when the approximate discharge curves start to become relatively flat – the $S_{4(L)}^{2-}$ concentrations for both simulations start to decrease, whereas the numbers of $Li_2S_{(s)}$ particles start to increase at a faster rate. This suggest that the $S_{4(L)}^{2-}/S_{2(L)}^{2-}$ and

$S_{2(l)}^{2-}/Li_2S_{(s)}$ reduction reactions start to become dominant at around 250 mAh. $g_{S_{8(s)}}^{-1}$ in both the simulations. The simulated discharge curves remain relatively flat from 250 to 1200 mAh. $g_{S_{8(s)}}^{-1}$: this stage in the discharge simulations correspond to the second low discharge plateau seen in experiments (Fig. 3.7). The number of $Li_2S_{(s)}$ particles continue to increase during this relatively flat discharge stage and until the end of the simulations (Fig. 3.8), whereas the concentrations $S_{2(l)}^{2-}$ particles start to decrease at around 800 mAh. $g_{S_{8(s)}}^{-1}$ (Fig. 3.5), which suggest that the electrodeposition of $Li_2S_{(s)}$ particles is the most dominant reaction from this specific capacity. Since, the $S_{8(s)}$ dissolves during the slopy first stage of the predict discharge curve, it corresponds to the high potential plateau and slopy intermediate stage of a typical Li-S battery discharge curve [146]. Whereas, the relatively flat second stage corresponds to the low potential plateau of a typical discharge curve [146]. These trends are consistent with the numerous continuum scale simulation results.

Since the rate constant of the $Li_2S_{(s)}$ electrodeposition reaction increases with the C-rate, the number of $Li_2S_{(s)}$ particles increase slightly faster during 2C than C/2. This impact of the discharge rate on the precipitation rate is consistent with the continuum simulation results [119]. However, an opposite trend is observed for the decrease in the number of $S_{8(s)}$ particles (Fig. 3.8). The rate constant for the chemical dissolution of $S_{8(s)}$ particles does not depend on the C-rate of the discharge simulation. Since the $S_{8(s)}$ particles have more time to dissolve during the C/2 discharge simulation, the number of $S_{8(s)}$ particles decreases faster with the specific capacity. Whereas, the number of $S_{8(s)}$ particles decreases very slowly with the specific capacity during 2C discharge simulation, since $S_{8(s)}$ particles have less time to dissolve. Due to the combined effect of slow $S_{8(s)}$ dissolution and fast $Li_2S_{(s)}$ electrodeposition, the mesostructure porosity of 2C is always lower than that of the C/2 (Fig. 3.8). However, the mesostructure porosities of both the simulations, increase during the first slopy discharge stage and decrease during the second relatively flat one, which is consistent with many of the previously reported modelling results [92,119,140]. Finally, the decrease of discharge potential from around 1200 mAh. $g_{S_{8(s)}}^{-1}$ (Fig. 3.6) is due to the significant depletion in the concentrations of all the dissolved sulfur based particles (Fig. 3.5).

3.3.2. Mesoscale evolutions of $Li_2S_{(s)}$ deposits over carbon

Since the deposition of $Li_2S_{(s)}$ over the carbon surface impacts the discharge performance due to the surface passivation, it is important to understand the impact of the C-rates on the evolutions of mesoscale properties.

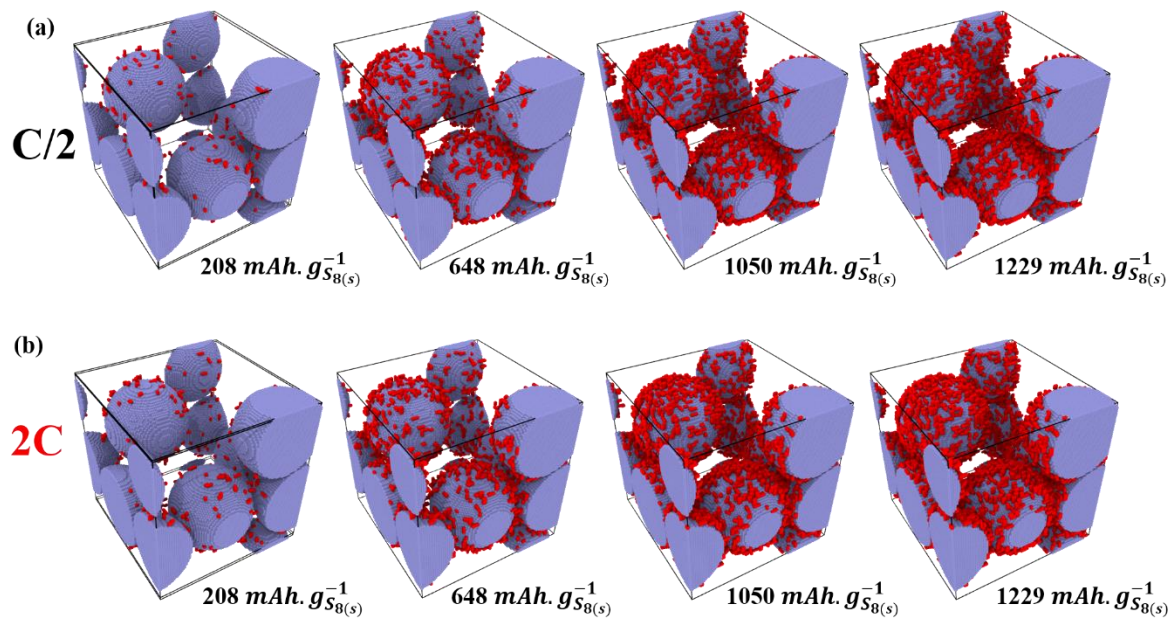


Figure 3.9. Visualizations of $Li_2S_{(s)}$ deposits (in red) over the surface of the carbon particles at 208, 648, 1050 and 1229 $mAh \cdot g_{S_{8(s)}}^{-1}$ during (a) C/2 and (b) 2C discharge simulations.

The visualizations of $Li_2S_{(s)}$ deposits over the surface of carbon particles at different DoDs during C/2 and 2C discharge simulations are shown in Fig. 3.9. Visually the evolutions $Li_2S_{(s)}$ deposits over the carbon surface look similar for both simulations. At 208 $mAh \cdot g_{S_{8(s)}}^{-1}$ the $Li_2S_{(s)}$ deposits exist in the form isolated nuclei and then at 648 $mAh \cdot g_{S_{8(s)}}^{-1}$ clusters of $Li_2S_{(s)}$ particles are formed, which then grow bigger along with the formation of newer clusters occur during the subsequent stages of the discharge simulations. A similar type of $Li_2S_{(s)}$ deposition process over the carbon surface was experimentally observed by Fan *et al.* [116]. However, it

is difficult to make conclusions about the impact of C-rates on the mesoscale properties of $Li_2S_{(s)}$ deposits over the carbon surface just from the visualizations. Therefore, in the following, we have presented the analysis of the post-processed results of the $Li_2S_{(s)}$ deposits produced using computational tools such as radial distribution function and cluster recognition algorithm.

3.3.2.1. Distribution of Li_2S particles from the carbon surface

Due to the discrete nature of our model, we decided to approximate the radial distribution function (RDF) as a histogram of the distances between the particles and the carbon surface. Therefore, RDF assist in determining the distribution of the number of $Li_2S_{(s)}$ particles at different distances from the the carbon particles (Fig. 3.11). At first, we used the results of the RDF to predict the coverage of $Li_2S_{(s)}$ particles over carbon surface ($\theta_{Li_2S_{(s)}}$), which quantifies the fraction of carbon surface that is directly blocked by $Li_2S_{(s)}$ and it is calculated using the following equation,

$$\theta_{Li_2S_{(s)}} = \frac{N_c^{Li_2S_{(s)}}}{N_c^T} \quad (3.14)$$

where, $N_c^{Li_2S_{(s)}}$ and N_c^T respectively are the number of surface C atoms covered by $Li_2S_{(s)}$ particles and the total number of surface C atoms in simulation box. It should be noted that $N_c^{Li_2S_{(s)}}$ is also the number of $Li_2S_{(s)}$ particles present at 5 \AA from the surface of the carbon particles, since this distance refers to the voxels that are present right next to the C atoms.

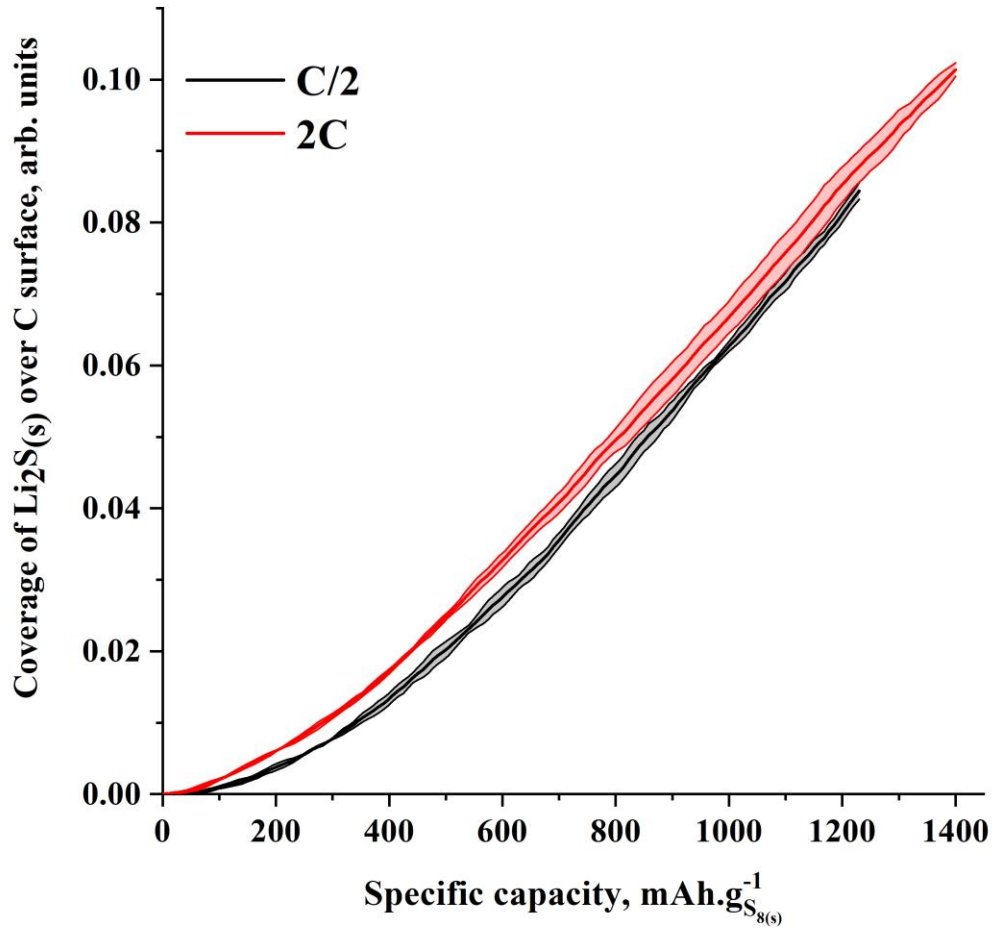


Figure 3.10. The evolutions of coverages of $\text{Li}_2\text{S}_{(s)}$ over carbon surface for both C/2 (black line) and 2C (red line) discharge simulations.

The increase of $\text{Li}_2\text{S}_{(s)}$ coverage over carbon surface during 2C discharge simulation is faster than during C/2 (Fig. 3.10). This trend is consistent with the previously observed modelling results of Andrei *et al.* [118]. Furthermore, the number of $\text{Li}_2\text{S}_{(s)}$ particles at different distances from the carbon surface (Fig. 3.11), show that the some of the $\text{Li}_2\text{S}_{(s)}$ deposits, produced during both simulations are away from the carbon surface (3D growth). This is the reason behind the low coverages of $\text{Li}_2\text{S}_{(s)}$ over carbon surface. Although there is only a slight difference between the average numbers of $\text{Li}_2\text{S}_{(s)}$ particles produced at around 1229 $\text{mAh.g}_{\text{S}_{8(s)}}^{-1}$ during 2C and C/2 discharge simulations (Fig. 3.8), the difference between the

average coverages of $Li_2S_{(s)}$ over the carbon surface is relatively larger at this specific capacity (Fig. 3.11). This suggests that the $Li_2S_{(s)}$ deposits, produced at $1229 \text{ mAh.g}_{S_{8(s)}}^{-1}$ during C/2 discharge simulation, have slightly more $Li_2S_{(s)}$ particles that are away from the surface than those produced during 2C. This can also be understood from the distributions of $Li_2S_{(s)}$ particles on the carbon surface at $1229 \text{ mAh.g}_{S_{8(s)}}^{-1}$ during C/2 and 2C discharge simulations (Fig. 3.11). At this capacity, the average number of Li_2S particles present at distances beyond 2.5 nm from the carbon surface during C/2, are slightly larger than those of during 2C.

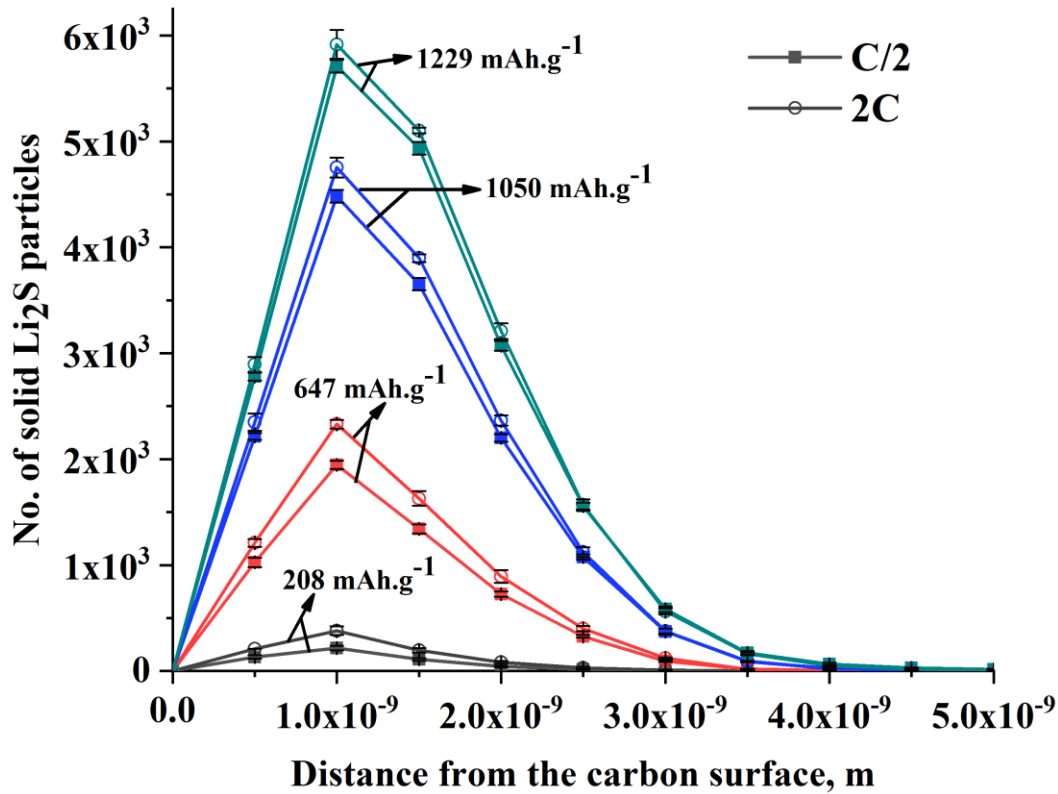


Figure 3.11. The Number of $Li_2S_{(s)}$ particles at different distances from the carbon surface at 208 (grey lines), 648 (red lines), 1050 (blue lines) and 1229 (green lines) $\text{mAh.g}_{S_{8(s)}}^{-1}$ during C/2 (lines with squares) and 2C (lines with open circles) discharge simulations. The error bars in the plot are shown in black.

The impact of C-rates on the nucleation and growth dynamics of $Li_2S_{(s)}$ deposition during discharge simulations, could be understood from the comparisons of the evolutions of the $Li_2S_{(s)}$ distributions on the carbon surface (Fig. 3.11). The peaks of all the $Li_2S_{(s)}$ distributions for the both discharge simulations – are situated at 1 nm from the carbon surface. This indicates that the $Li_2S_{(s)}$ electrodepositions during C/2 and 2C discharge simulations are dominated by the nucleation of $Li_2S_{(s)}$ deposits since they are very close to the carbon surface (Fig. 3.11). Initially, at 208 and 648 $mAh.g_{S_{8(s)}}^{-1}$, the $Li_2S_{(s)}$ distributions of C/2 discharge simulation are all lower than those of 2C. Furthermore, at 1050 $mAh.g_{S_{8(s)}}^{-1}$ $Li_2S_{(s)}$ distributions for both C/2 and 2C discharge simulations are relatively close to each other. Moreover, the numbers of $Li_2S_{(s)}$ particles beyond 2 nm for both C/2 and 2C discharge simulations start to overlap each other at 1050 $mAh.g_{S_{8(s)}}^{-1}$ (Fig. 3.11). Finally, at 1229 $mAh.g_{S_{8(s)}}^{-1}$, the average numbers of $Li_2S_{(s)}$ particles beyond 2.5 nm for C/2 discharge simulation are slightly larger than those of the 2C (Fig. 3.11). These evolutions show that 3D growth of $Li_2S_{(s)}$ particles over carbon during C/2 discharge is slightly faster than during 2C, which is also consistent with the modelling predictions of Ren *et al.*[120].

Since the rate constant of the $Li_2S_{(s)}$ electrodeposition reaction increases with the C-rate, S_2^{2-} particles tend to react more when they come closer to the carbon surface during 2C than C/2 (Fig. 3.12). Whereas, they tend to diffuse more during C/2 than during 2C. Therefore, this competition between reaction and diffusion events of S_2^{2-} particles, could be the reason why the 3D growth of $Li_2S_{(s)}$ deposits of C/2 discharge simulation is slightly faster than those of the 2C.

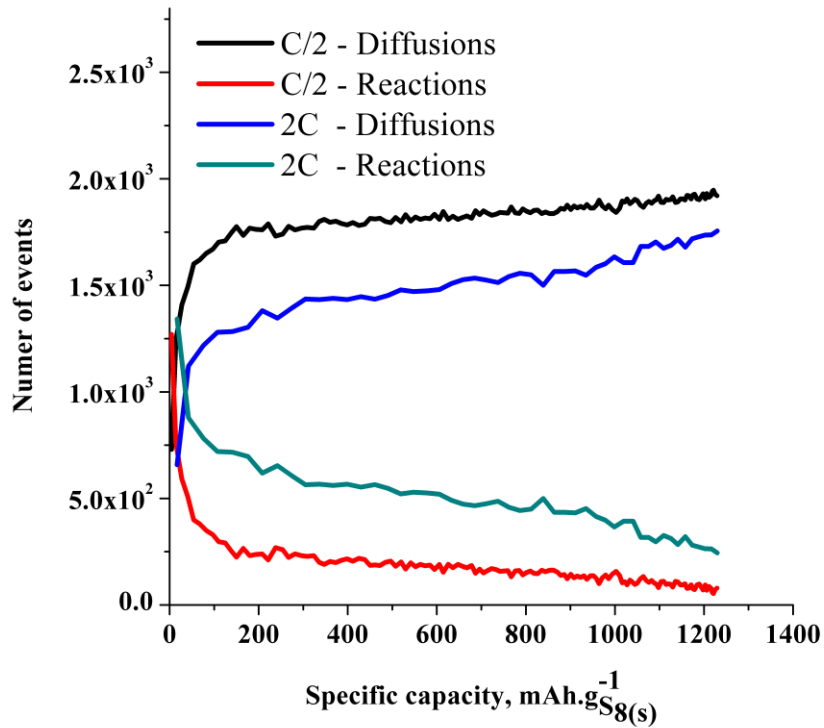


Figure 3.12. Number of diffusion and reactions events selected during C/2 and 2C discharge simulations.

3.3.2.2. Size distribution of $\text{Li}_2\text{S}_{(\text{s})}$ clusters

As mentioned in subsection 3.3.2, clusters of $\text{Li}_2\text{S}_{(\text{s})}$ particles are formed during discharge simulations (Fig. 3.9). The sizes of these clusters provide us details about the proximity of the $\text{Li}_2\text{S}_{(\text{s})}$ deposits with each other. Here, the size of a cluster refers to the number of $\text{Li}_2\text{S}_{(\text{s})}$ particles in that cluster and it assists in providing insights about the local passivation of carbon surface. Since a large $\text{Li}_2\text{S}_{(\text{s})}$ cluster could cover a large area of the carbon surface, locally the surface passivation by that cluster will be higher than if a small cluster is formed at that same area. This local passivation of carbon surfaces could have an impact on the electrochemical performance towards the end of discharge when the concentrations of dissolved polysulfides are low and unevenly distributed. Therefore, we have estimated the size distributions of $\text{Li}_2\text{S}_{(\text{s})}$ clusters formed at $1229 \text{mAh} \cdot \text{g}_{\text{S}_8(\text{s})}^{-1}$ (Fig. 3.13 and 3.14), using a cluster recognition algorithm called Density-based Spatial clustering of Applications with Noise (DBSCAN) [147].

DBSCAN does not require prior knowledge about the shapes and amounts of clusters, which is its main advantage over other cluster recognition algorithms. Here, we have implemented the DBSCAN algorithm in a python code and we specially adjusted it to analyse the $Li_2S_{(s)}$ particles data which were produced using our kMC code. The input parameters that DBSCAN requires are – minimum number of particles required for a region to be considered as a cluster (MinPts) and minimum distance between the particles to be considered belonging to the same cluster (ϵ). In this chapter, MinPts and ϵ were set to 5 particles and 1.5 voxel sides (7.5 Å) respectively, in order to reduce the background noise.

The visualizations and size distributions of $Li_2S_{(s)}$ clusters formed at 1229 mAh. $g_{S_{(s)}}^{-1}$ during the both discharge simulations are shown in Fig. 3.13 and 3.14. The cluster sizes vary from 4 to 367, which is too wide a range to visualize using a single image and to represent its size distribution in a single histogram. Therefore, we have classified clusters based on their cluster size classes such as 4-8, 9-13, 14-18 and so on until 39-43 $Li_2S_{(s)}$ particles per cluster (Fig. 3.13). There are a large number of small clusters (<19) formed during both C/2 and 2C simulations. Therefore, to clearly highlight the differences between the cluster sizes formed during C/2 and 2C discharge simulations, the visualizations and size distributions of the clusters with sizes above 43, are shown in Fig. 3.14. Here, we classified the clusters based on the cluster size such as 44-79, 80-115, 116-151 and so on until 332-367 $Li_2S_{(s)}$ particles per cluster.

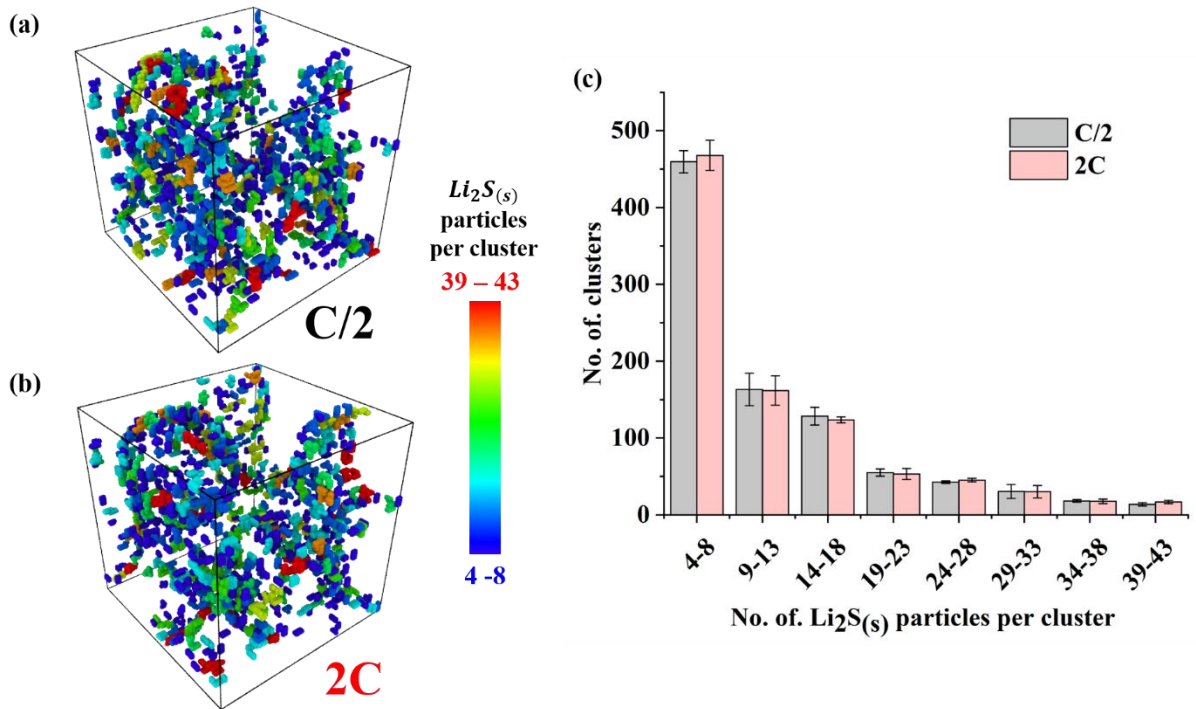


Figure 3.13. Visualizations of $Li_2S_{(s)}$ clusters of belonging to size classes of 4-8, 9-13, 14-18 and so on until 39-43 formed at $1229 \text{ mAh} \cdot g_{S_{(s)}}^{-1}$ during (a) C/2 and (b) 2C discharge simulations and (c) their corresponding cluster size distributions, where the cluster size distributions of C/2 and 2C are given in grey and pink bars respectively. The error bars over the histograms are shown in black. The colour map in the image shows the colour coding assigned to different cluster size classes (e.g. 4-8 and 39-43 are shown in navy blue and red, respectively) during visualization.

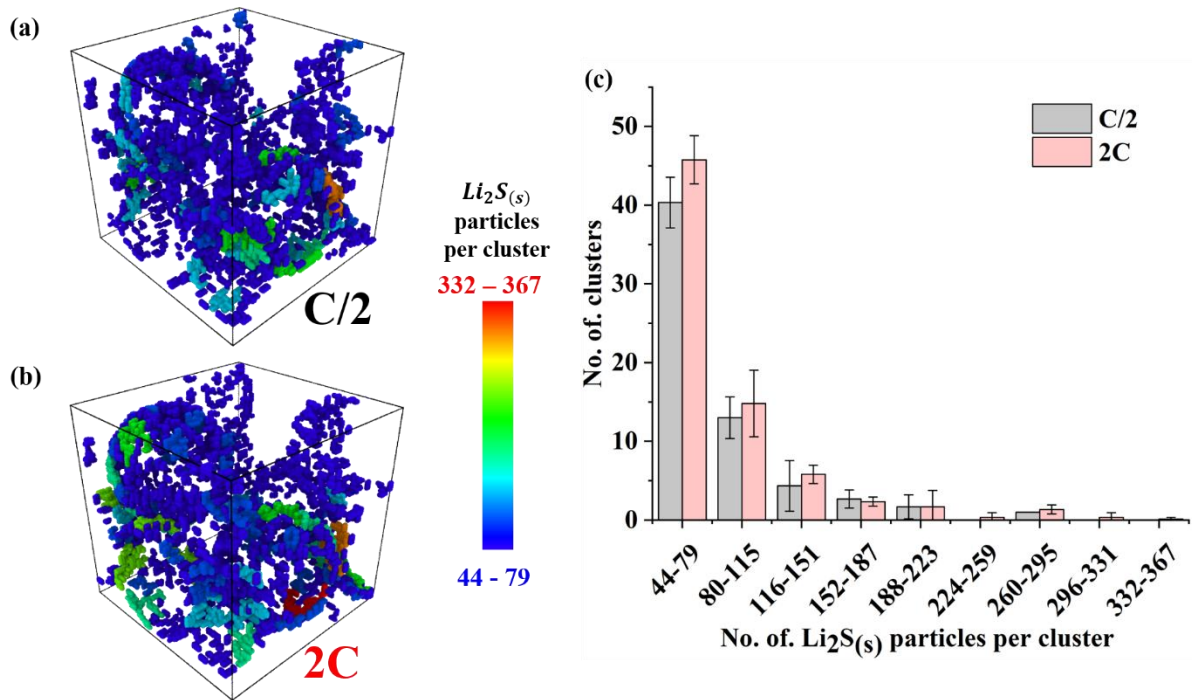


Figure 3.14. Visualizations of $Li_2S_{(s)}$ clusters of belonging to size classes of 44-79, 80-115, 116-151 and so on until 332-367 formed at $1229 \text{ mAh} \cdot g_{S_{8(s)}}^{-1}$ during (a) C/2 and (b) 2C discharge simulations and (c) their corresponding cluster size distributions, where the cluster size distributions of C/2 and 2C are given in grey and pink bars respectively. The error bars over the histograms are shown in black. The colour map in the image shows the colour coding assigned to different cluster size classes (e.g. 64-94 and 95-125 are shown in navy blue and red, respectively) during visualization.

On average, the number of very small clusters (4-8) formed during 2C discharge simulation is larger than that of C/2. However, the number of $Li_2S_{(s)}$ clusters with sizes between 9 to 38 during 2C and C/2 discharge simulations are similar (Fig. 3.13). Whereas, the average number of $Li_2S_{(s)}$ clusters produced during 2C discharge simulation are larger in most of cluster size classes beyond 34-38. These differences between C/2 and 2C discharge simulations are more evident in cluster size classes such as 39-43 (Fig. 3.13), 44-79, 80-115 and 116-151 (Fig. 3.14). Therefore, we can conclude that on average relatively larger number of $Li_2S_{(s)}$ clusters with moderate (39-43) and big sizes (44-367) are formed during 2C (Figs. 3.13 and 3.14).

$Li_2S_{(s)}$ clusters with big sizes represent the $Li_2S_{(s)}$ deposits which are closer to each other. Therefore, the $Li_2S_{(s)}$ deposits produced during 2C are relatively closer than those produced during C/2. This means the local passivation of carbon surfaces are relatively high for 2C. This effect could also be due to the competition between reaction and diffusion events of $S_{2(l)}^{2-}$ particles during 2C and C/2 discharge simulations. Since $S_{2(l)}^{2-}$ particles diffuse more during C/2 discharge (Fig. 3.11), they get separated more from each other, which could result in isolated deposits of $Li_2S_{(s)}$.

3.4. Impact of sulfur loading

This subsection presents the 2C discharge simulation results of a C/S mesostructure with 1:0.54 C/S mass ratio. The structural parameters such as the shape and size of the carbon particles, and the carbon porosity of this mesostructure are same as the one with 1:0.27 C/S mass ratio (Fig. 3.1). Therefore, the discharge simulation results of the aforementioned C/S mesostructures (i.e. 1:0.27 and 1:0.54 C/S mass ratios) are compared to assess the impact of the sulfur loading on the overall and $Li_2S_{(s)}$ mesostructural evolutions.

The number of S particles in the mesostructure with 1:0.54 C/S mass ratio (high- S loaded mesostructure) is twice that in the low- S loaded one (i.e. 1:0.27 C/S mass ratio). Therefore, to compare the evolution rates of $S_{8(s)}$ and $Li_2S_{(s)}$ particles in high and low- S loaded mesostructures, we have normalized their amounts with the corresponding maximum possible number of particles (Fig. 3.15). During discharge, the porosity of the high- S loaded mesostructure is significantly lower than that of the low- S loaded one (Fig. 3.15). This is because the absolute total number of $S_{8(s)}$ and $Li_2S_{(s)}$ particles in the high- S loaded mesostructure is always larger than that of the low- S loaded one.

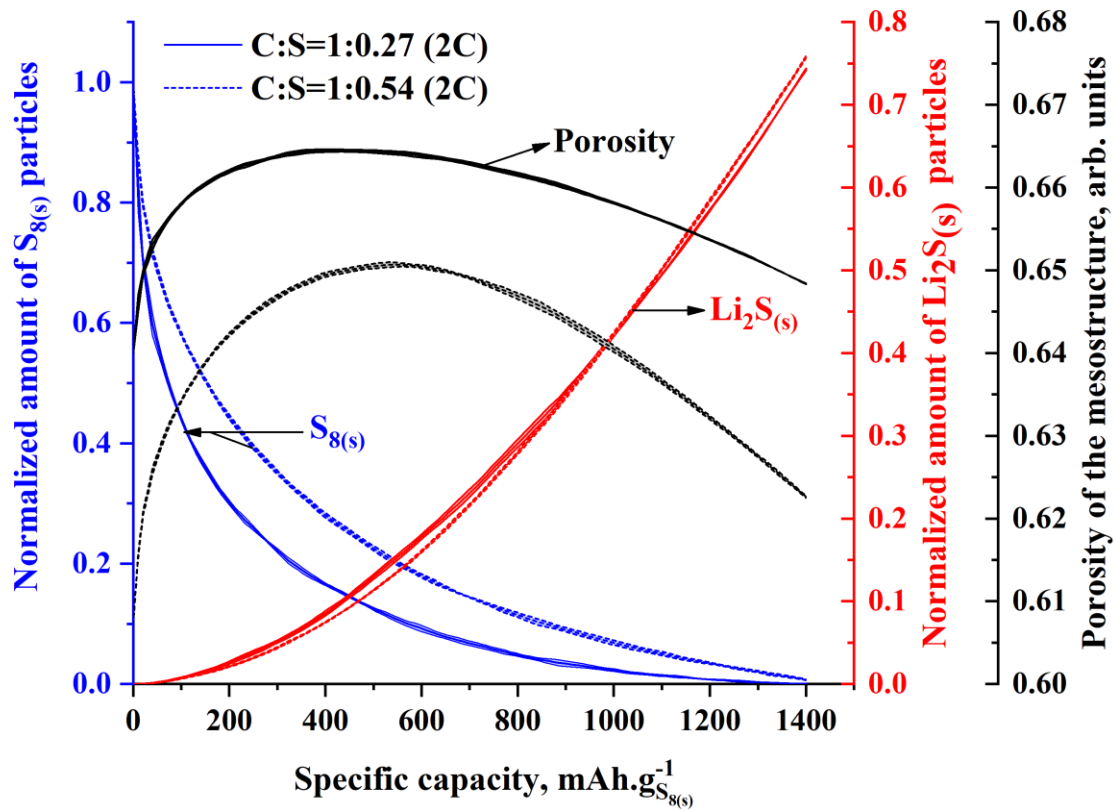


Figure 3.15. Evolutions of the normalized amounts of $S_{8(s)}$ (navy blue lines) and Li_2S (red lines) particles and the porosities of the C/S mesostructures with 1:0.27 (solid lines) and 1:0.54 (dashed lines) C/S mass ratios during 2C discharge simulation.

The rate of dissolution of $S_{8(s)}$ in high- S loaded mesostructure is slower than that in the low- S one (Fig. 3.15). Since the discharge current increases with the S loading, the absolute rates of all the electrochemical reactions will also increase with it. Therefore, around 200 $\text{mAh} \cdot \text{g}_{S_{8(s)}}^{-1}$, the normalized amount of $Li_2S_{(s)}$ particles in the high- S loaded mesostructure starts to increase significantly, even when there is a large amount undissolved $S_{8(s)}$ in it. Initially, the increase in the normalized amount of $Li_2S_{(s)}$ particles in high- S loaded mesostructure is relative slower than that in the low- S loaded one, which is due to the slow dissolution $S_{8(s)}$ particles. However, beyond 1000 $\text{mAh} \cdot \text{g}_{S_{8(s)}}^{-1}$ much of the $S_{8(s)}$ particles are dissolved, therefore the rate of increase in the normalized $Li_2S_{(s)}$ particles in high- S loaded mesostructure becomes relatively faster. The visual comparison of the $Li_2S_{(s)}$ deposits over

the carbon surface during discharge in the mesostructures with different S -loading show that the absolute number $Li_2S_{(s)}$ particles are always higher in the high- S mesostructure (Fig. 3.16).

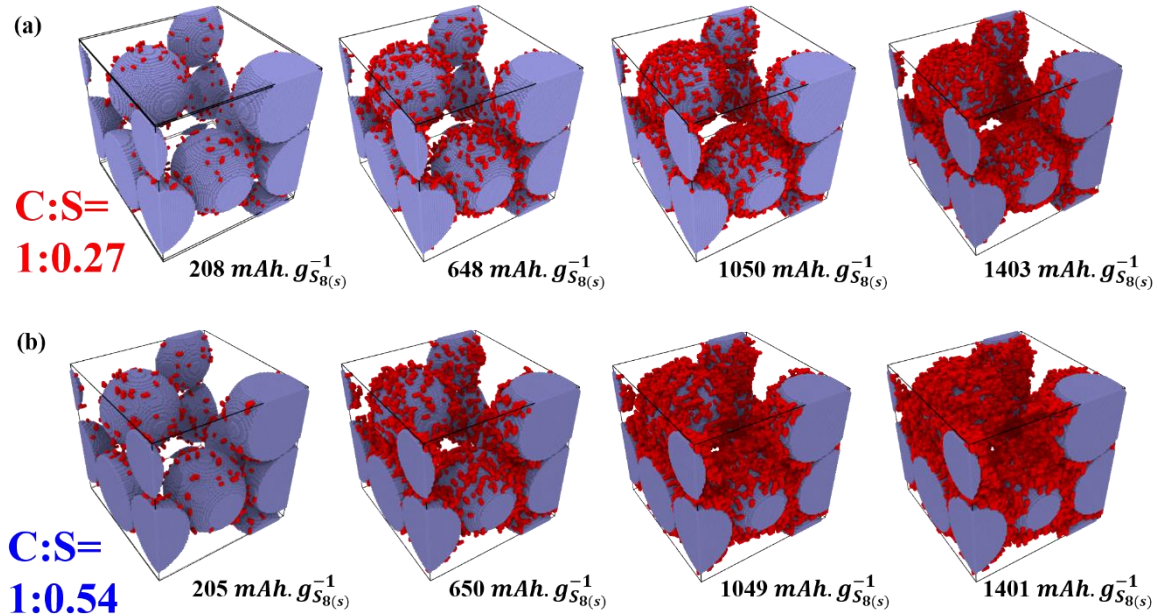


Figure 3.16. Visualizations of $Li_2S_{(s)}$ deposits (in red) over the surface of the carbon particles in the mesostructures with (a) 1:0.27 and (b) 1:0.54 C/S mass ratios and at different DoDs during 2C discharge simulations.

At the initial stage of discharge, the coverage of $Li_2S_{(s)}$ over the carbon surface in the high- S loaded mesostructure increases at faster rate than that in the low- S loaded mesostructure (Fig. 3.17). This effect is due to the increase in the discharge current with the S loading. However, at the mid stage ($\approx 800 \text{ mAh} \cdot g_{S_{8(s)}}^{-1}$), the increase in the $Li_2S_{(s)}$ coverage in the high- S loaded mesostructure starts to slow down (Fig. 3.17). This is due to the low availability of free carbon surface, since a significant amount of it is covered by the previously deposited $Li_2S_{(s)}$ and undissolved $S_{8(s)}$ particles (Fig. 3.15). Since, beyond $1000 \text{ mAh} \cdot g_{S_{8(s)}}^{-1}$ the $Li_2S_{(s)}$ distributions at different distances from carbon surface in the high- S loaded mesostructure are significantly broader than those in the low- S loaded one (Fig. 3.18), they limit the transport of S_2^{2-} to the carbon surface. Therefore, the $Li_2S_{(s)}$ coverage in the high- S loaded

mesostructure remain relative lower even when the majority of $S_{8(s)}$ particles have dissolved beyond this specific capacity. Ultimately, the $Li_2S_{(s)}$ coverage in the high- S mesostructure at the end discharge is relatively lower than the that of the low- S loaded one (Fig. 3.17).

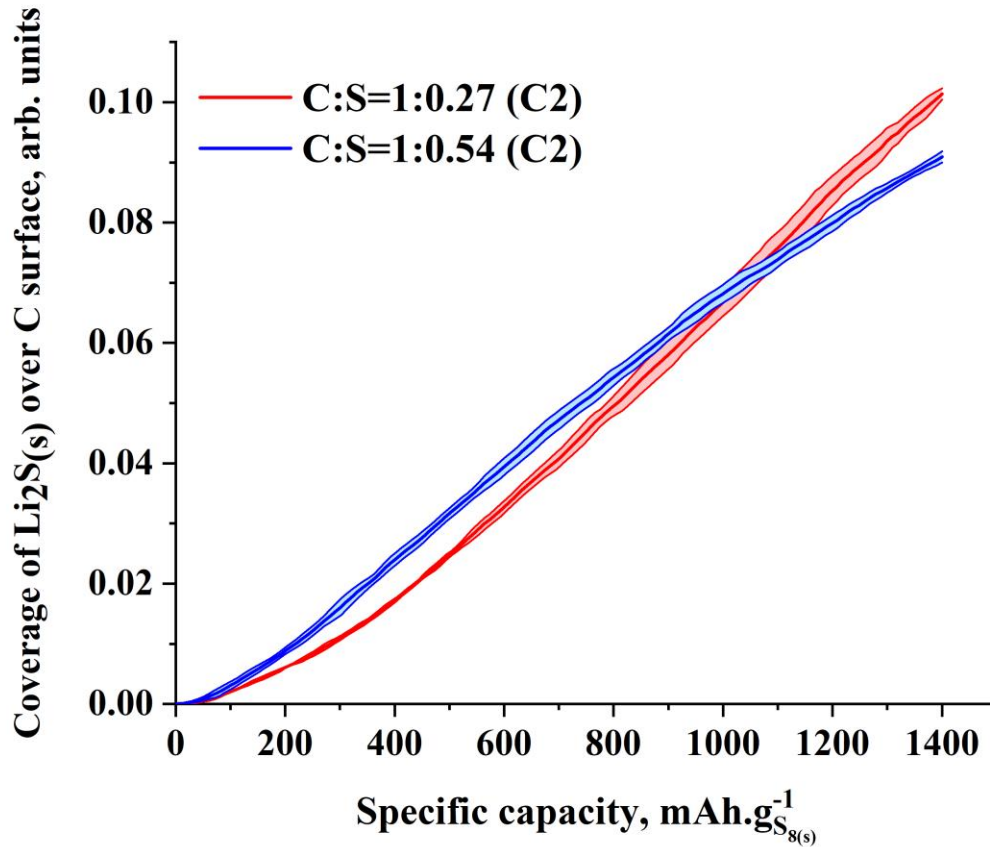


Figure 3.17. The evolutions of coverages of $Li_2S_{(s)}$ over carbon surface in mesostructures with 1:0.27 (red lines) and 1:0.54 (blue lines) C/S mass ratios, during 2C discharge simulations.

During discharge, the peaks of the $Li_2S_{(s)}$ distributions over carbon surface in the high- S loaded mesostructure shift from 1.0 to 1.5 nm (Fig. 3.18). This indicates that the growth dynamics of $Li_2S_{(s)}$ electrodeposition is more dominant than the nucleation dynamics in the high- S loaded mesostructure. This is also due to the low availability of free carbon surface in the high- S loaded mesostructure during discharge, since most of it is covered by previously deposited $Li_2S_{(s)}$ and undissolved $S_{8(s)}$ particles. Furthermore, the slow nucleation dynamics in the high- S loaded mesostructure is also due to the thick $Li_2S_{(s)}$ deposits over its carbon surface which limit the diffusion of S_2^{2-} .

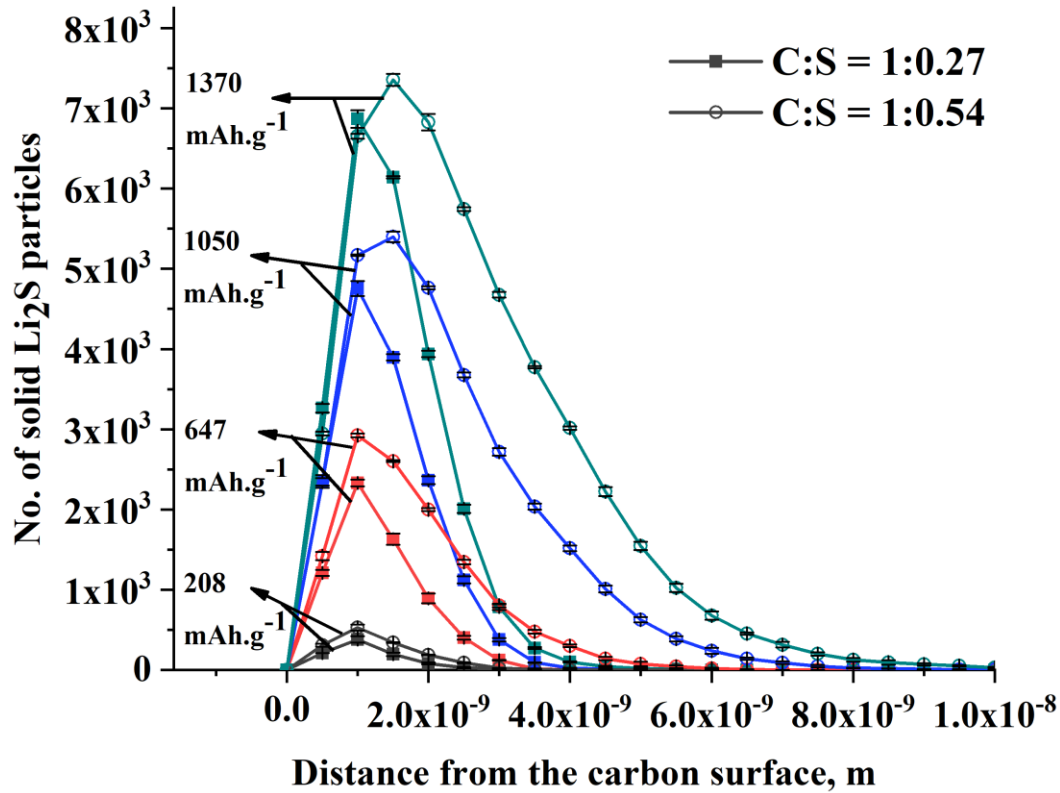


Figure 3.18. The distributions of $Li_2S_{(s)}$ particles at different distances from the carbon surface in the mesostructures with 1:0.27 (lines with squares) and 1:0.54 C/S (lines with open circles) mass ratio and at 208 (grey lines), 647 (red lines), 1050 (blue lines) and 1370 (green lines) $mAh.g^{-1}$ during 2C discharge simulations. The error bars are shown in black.

3.5. Conclusions

In this chapter, we presented a novel 3D kMC model which is capable of simulating the evolutions inside a C/S mesostructure during discharge. Our model can predict effective evolutions inside the mesostructure such as concentrations of dissolved particle, numbers of solid sulfur based particles and mesostructure porosity. Furthermore, the approximate discharge curves calculated from the results of our kMC model, assist in assessing the phenomena taking place at different stages of discharge. The evolutions of mesostructure porosities, such as their increase during the first slopy discharge stage and decrease during

the second relative flat discharge stage are consistent with the previously reported continuum modelling results [92,119,140]. Furthermore, the reduction of long chain (S_8) to medium chain polysulfides (S_4^{2-}) during the first slopy stage and subsequent reduction of S_4^{2-} to S_2^{2-} and precipitation of $Li_2S_{(s)}$ during the relatively flat stage are consistent with the continuum simulation [119,141] and experimental results [58,59].

The post-processed results of $Li_2S_{(s)}$ data produced by the simulations our kMC model, assist in assessing the impact of C-rates on the mesoscale properties of $Li_2S_{(s)}$. The results produced using the radial distribution function, show that $Li_2S_{(s)}$ coverage over carbon increases with the C-rate, while the $Li_2S_{(s)}$ deposits formed during slow C-rate (C/2) have relative large number of $Li_2S_{(s)}$ particles away from the carbon surface. These effects are due to nucleation and growth dynamics of $Li_2S_{(s)}$ electrodepositions, where the evolutions of the $Li_2S_{(s)}$ distributions over the carbon surface indicate that growth process of $Li_2S_{(s)}$ is slightly faster during slow C-rate (C/2). These aforementioned conclusions made from our kMC model are consistent with previously reported modelling and experimental results of Andrei et al. [118] and Ren *et al.* [120]. Furthermore, comparison of the size distributions of $Li_2S_{(s)}$ clusters of C/2 and 2C discharge simulations, show that relatively small number of big deposits are produced during slow discharge. This could be due to the competition between reaction and diffusion S_2^{2-} . Due to the insulating nature of $Li_2S_{(s)}$, the mesoscale properties of its deposits over carbon will impact the surface passivation [118,123]. Since the $Li_2S_{(s)}$ coverage over carbon increases faster during fast discharge (2C), we believe that the overall surface passivation is also faster during fast discharge. Furthermore, since a relatively large number of bigger clusters are formed during fast discharge, local passivation of carbon surface is also larger during the fast discharge. These passivation effects could explain, at least partially, why the discharge capacity decreases when the C-rate increases.

The results of the radial distribution function show that the $Li_2S_{(s)}$ deposits over the carbon surface in high- S loaded mesostructure (i.e. 1:0.54 C/S mass ratio) are relative thicker than those in low- S loaded mesostructure. This is also evident from the relatively low $Li_2S_{(s)}$ coverage over carbon surface in high- S loaded mesostructure at the end of the 2C discharge simulation. Therefore, the growth process of the $Li_2S_{(s)}$ electrodeposition in high- S loaded mesostructure is more dominant than the $Li_2S_{(s)}$ nucleation process. These phenomena are

primarily due to the lack of free carbon surface in high- S loaded mesostructure, since most of the surface is covered by previously deposited $Li_2S_{(s)}$ and undissolved $S_{8(s)}$. Due to the combined effect of thick $Li_2S_{(s)}$ deposits and coverage of undissolved $S_{8(s)}$ in high- S loaded mesostructure, surface passivation increases significantly with the S loading. This conclusion about the impact of S loading on the surface passivation is consistent with the experimental results reported by Fan *et. al.* [117]. Furthermore, thick $Li_2S_{(s)}$ deposits will also limit the transport of solvate species towards the electrode surface, which could impede the electrochemical reactions. Finally, our kMC results show that porosity of the high- S loaded mesostructure throughout 2C discharge simulation is lower than that of the low- S loaded mesostructure. This suggest that the possibility of pore blocking during discharge could increase with the S loading. Therefore, the increase in the surface passivation rate and possibility of pore blocking can explain, why the discharge capacity of Li-S batteries decreases when the S loading in the cathode is increased.

Chapter 4. Microstructurally resolved continuum discharge model

Contents

| | |
|---|------------|
| 4.1. Introduction | 81 |
| 4.2. Methodology: overall assumptions..... | 82 |
| 4.3. Methodology: Overall construction and governing equations | 87 |
| 4.3.1. Structural properties of cathode | 87 |
| 4.3.2. Electrochemical reaction kinetics | 88 |
| 4.3.3. Chemical reaction rates | 89 |
| 4.3.4. Transport in the electrolyte | 90 |
| 4.3.5. Intra-flux..... | 91 |
| 4.3.6. Dynamic viscosity evolution..... | 92 |
| 4.3.7. Active surface area and porosity | 94 |
| 4.3.8. Film thickness..... | 95 |
| 4.3.9. Current balance..... | 97 |
| 4.3.10. Cell voltage..... | 97 |
| 4.4. Computational implementation..... | 98 |
| 4.4.1. Physical model | 99 |
| 4.5. Results and discussion | 100 |
| 4.5.1. Rate capability..... | 101 |
| 4.5.2. Impact of porosity..... | 105 |
| 4.5.3. Impact of particle and pore sizes | 108 |
| 4.5.4. Impact of C/S ratio | 111 |
| 4.6. Conclusions and perspectives | 113 |
| A.4. Appendix: Numerical Schemes | 114 |

Chapter 4. Microstructurally resolved continuum discharge model

4.1. Introduction

As mentioned in Chapter 2, mesoporous carbon/sulfur composites for Li-S batteries were developed to improve the electronic conductivity of the cathode, to confine polysulfides and to accommodate excess volume of the Li_2S precipitates in the cathode [55,71,72]. A large variety of mesoporous carbon exists, therefore assessing the impact of their architecture on the discharge performance could be time consuming. Alternatively, mathematical models could be used to accelerate the assessment of the mesoporous carbon/sulfur composite design on the discharge performance. The continuum models applied to Li-S batteries have been successful in simulating various battery operation phenomena [148–154]. However, most of them, model the cathode as a homogenous porous medium, described by an effective porosity, not accounting for the microstructure, thus not enabling any study of the impact of different architectures. In contrast, Danner *et al.* developed a full cycle model using a mesoporous cathode containing microporous carbon particles [155]. However, this model assumes the sulfur-based species to be electrochemically active only as long as they remain confined in the micropores within the carbon particles, hence ignoring the transport of these species along the cell and their electrochemistry over the external surface of the carbon particles. Dysart *et al.* reported a multi-scale analysis of Li-S batteries using a stochastic model to reconstruct the cathode microstructure [156] and calculated the associated effective transport properties, but without evolving the microstructure upon discharge.

In this chapter, we report a multi-scale model devoted to the simulation of the discharging Li-S cells using a cathode made up of mesoporous carbon particles with inter-particle pores in-between. Our model brings novel features such as the consideration of the mass exchange of all the electrolyte solutes between mesopores within carbon particles and inter-particle pores, of the chemical and electrochemical reactions in both types of pores, and of the dynamical evolution of species diffusion coefficients. The novel features in our model permit the exploration of the impact on the discharge performance by the properties such as the inter-particle porosity between the carbon particles, the mesoporosity within the carbon particles, the particle and the mesopore sizes, and the sulfur loading at two different pore scales. These are features either impossible to study or simply not studied in previously

reported models. In the following, we present the physical and geometrical assumptions and demonstrate how it can be utilized to study the effects of the initial cathode microstructure and sulfur repartition within on the overall discharge cell performance. Although our model has limitations of experimentally non-validated assumptions and assumed parameters, it can still qualitatively predict some experimentally observed discharge trends and provide insights on the limiting reasons behind them.

The contents of this chapter were reported in a research paper titled, ‘A microstructurally resolved model for Li-S batteries assessing the impact of the cathode design on the discharge performance’, which was published in the Journal of the Electrochemical Society [157]. This research paper was co-authored by V. Thangavel, k.-H. Xue, Y. Mammeri, M. Quiroga, A. Mastouri, C. Guéry, P. Johansson, M. Morcrette and A. A. Franco.

4.2. Methodology: overall assumptions

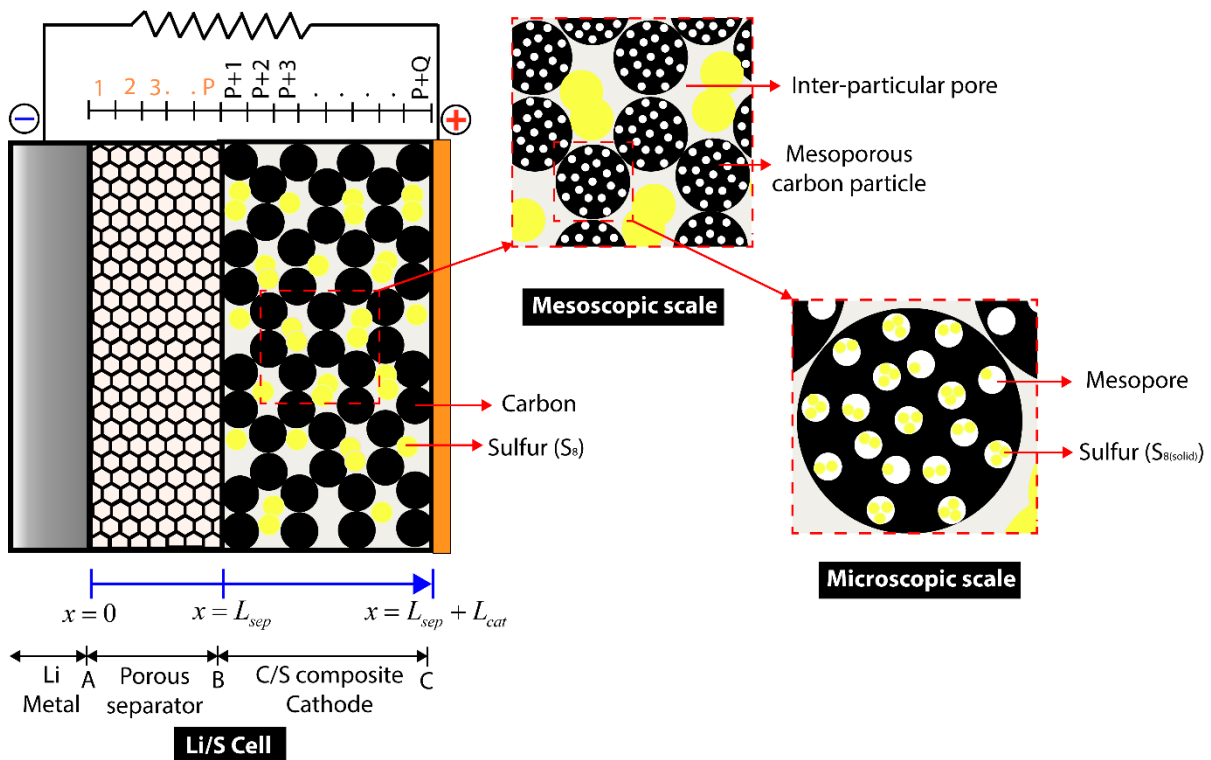


Figure 4.1. Schematic representation of our Li-S cell model at various resolutions.

The assumptions on which our model (Fig. 4.1) is based are the following:

Chapter 4. Microstructurally resolved continuum discharge model

- The separator and cathode components are represented in one-dimension;
- The cathode consists of mesoporous spherical carbon particles with a uniform size distribution;
- Each carbon particle contains spherical mesopores with a uniform pore size distribution;
- The impregnated sulfur initially exists both in mesopores within the carbon particles and in the inter-particle pores between them;
- The active surface area of the mesopores within each carbon particle is assumed to remain unchanged after loading $S_{B(\text{solid})}$ inside them;
- Transport of all the electrolyte solutes, such as sulfur, polysulfides, and lithium ions, is considered along the cell, as well as their mass exchange between the mesopores within the carbon particles and inter-particle pores;
- The transport of the electrolyte solutes is assumed to be diffusive and thus described by using Fick's laws;
- The diffusion coefficients of the solutes are assumed to depend on the electrolyte viscosity, calculated on-the-fly as dependent on the concentration of long chain polysulfides;
- Due to precipitation/dissolution reactions the porous volume of the cathode evolves along the discharge which is assumed to be completely filled with electrolyte;
- The concentration of the dissolved species in the electrolyte evolve due to transport, electrochemical and precipitation/dissolution reactions and their resulting evolution of porous/ electrolyte volume.
- The equilibrium potentials of all the electrochemical reactions follow Nernst's equations;
- The porous carbon matrix is perfectly percolated allowing proper electron wiring for all the particles;
- The carbon is assumed to be a perfect electronic conductor;
- The cathode surface area and porosity losses due to the presence of binder are neglected.
- The electrochemical reaction kinetics are assumed to follow the Butler-Volmer equations;

Chapter 4. Microstructurally resolved continuum discharge model

- The capacitive current due to the electrochemical double layer effect is neglected;
- The parasitic chemical and electrochemical reactions involving the polysulfide species reduction at the anode are neglected.

For the discharge reaction scheme at the anode we simply assume that lithium metal oxidation takes place, while at the cathode the reaction mechanism is assumed to be much more complex. Here, a part of the solid sulfur ($S_{8(\text{solid})}$) contained in the cathode dissolves into the electrolyte to produce uncharged dissolved sulfur ($S_{8(\text{soln})}$). The dissolved sulfur subsequently undergoes a series of reduction reactions to $S_{2(\text{soln})}^{2-}$. The reduction reactions take place in the electrolyte by accepting electrons from the surface of the carbon particles. The cathode reduction reactions and the anode side oxidation reactions are listed in Table 4.1. The cathode reactions can take place both in the mesopores of the carbon particles and in the inter-particle pores. For the sake of clarity all the electrochemical reactions were indexed with angular brackets "<>".

Table 4.1. Electrochemical reactions and physical parameters.

| Electrochemical reactions | E_B / E_F^a (J. mol ⁻¹) | Species Index (i) | Species formula | D (m ² .s ⁻¹) | $(C_{ref})_i$ mM ^c | $U_{<j>}^\theta$ V |
|---|--|-------------------------|---------------------------|---|----------------------------------|-----------------------|
| $Li_{(\text{solid})} \rightarrow Li_{(\text{soln})}^+ + e^-$ | 9680 | (1) | $Li_{(\text{soln})}^+$ | 7.5×10^{-11a} | 1007.64 ^b | 0 ^b |
| $\frac{1}{2} S_{8(\text{soln})} + e^- \rightarrow \frac{1}{2} S_{8(\text{soln})}^{2-}$ | 4000 | (2) | $S_{8(\text{soln})}$ | 2×10^{-10a} | 19 ^b | 2.46 ^a |
| $\frac{3}{2} S_{8(\text{soln})}^{2-} + e^- \rightarrow 2 S_{6(\text{soln})}^{2-}$ | 22807 | (3) | $S_{8(\text{soln})}^{2-}$ | 6×10^{-11a} | 3 ^a | 2.43 ^a |
| $S_{6(\text{soln})}^{2-} + e^- \rightarrow \frac{3}{2} S_{4(\text{soln})}^{2-}$ | 26242 | (4) | $S_{6(\text{soln})}^{2-}$ | 8×10^{-11a} | 0.8 ^a | 2.33 ^a |
| $\frac{1}{2} S_{4(\text{soln})}^{2-} + e^- \rightarrow \frac{3}{2} S_{2(\text{soln})}^{2-}$ | 28512 | (5) | $S_{4(\text{soln})}^{2-}$ | 10^{-10b} | 0.02 ^a | 2.23 ^a |
| $\frac{1}{2} S_{2(\text{soln})}^{2-} + e^- \rightarrow S_{(\text{soln})}^{2-}$ | 35935 | (6) | $S_{2(\text{soln})}^{2-}$ | 10^{-10b} | 1.01×10^{-5a} | 2.16 ^a |
| | | (7) | $S_{(\text{soln})}^{2-}$ | 10^{-10b} | 1.5×10^{-8a} | |

^a Assumed parameters.

^b Assumed parameters taken from reference [148].

^c Calculated based on the assumed densities.

Since, the equations of our model are solved using numerically the initial concentrations and the volume fraction of the species cannot be zero. Therefore, we assumed certain values for the concentrations and volume fractions of the dissolved and solid species, respectively. The dissolved lithium salt concentration in the electrolyte is assumed to be 1000 mM (1 M), however in order to ascertain electroneutrality, the initial lithium ion concentration (Table 4.1) is determined by the total negative charge due to anion of lithium salt and polysulfides ions.

Assumed parameters are calibrated by qualitatively matching the calculated discharge profile trends with those experimentally observed for different current densities or C-rate [158–160].

The dissolved polysulfides ($S_{y(\text{soln})}^{2-}$) may react with lithium ions ($Li_{(\text{soln})}^+$) and produce insoluble lithium polysulfide that precipitates ($Li_2S_{y(\text{solid})}$). These chemical reactions are reversible, hence termed as precipitation/dissolution reactions (Table 4.2), and indexed by curly brackets “{}”.

Table 4.2. Precipitation/dissolution reactions and physical parameters.

| React. Index | Precipitation/dissolution reactions | $k_k^{prec_a}$ ($\text{mol}^2 \cdot \text{m}^{-6} \cdot \text{s}^{-1}$) | Species formula | K_k^{sp} ($\text{mol}^3 \cdot \text{m}^{-9}$) | Molar volume ($\text{m}^{-3} \cdot \text{mol}$) |
|--------------|--|---|---------------------------|---|---|
| {1} | $S_{8(\text{solid})} \rightleftharpoons S_{8(\text{soln})}$ | 35 (s^{-1}) | $S_{8(\text{solid})}$ | 19 ($\text{mol} \cdot \text{m}^{-3}$) ^b | 1.239×10^{-4b} |
| {2} | $2 Li_{(\text{soln})}^{2+} + S_{8(\text{soln})}^{2-} \rightleftharpoons Li_2S_{8(\text{solid})}$ | 10^{-20} | $Li_2S_{8(\text{solid})}$ | 500 ^a | 1.5×10^{-4c} |
| {3} | $2 Li_{(\text{soln})}^{2+} + S_{6(\text{soln})}^{2-} \rightleftharpoons Li_2S_{6(\text{solid})}$ | 10^{-20} | $Li_2S_{6(\text{solid})}$ | 500 ^a | 1.1×10^{-4c} |
| {4} | $2 Li_{(\text{soln})}^{2+} + S_{4(\text{soln})}^{2-} \rightleftharpoons Li_2S_{4(\text{solid})}$ | 10^{-20} | $Li_2S_{4(\text{solid})}$ | 500 ^a | 7.5×10^{-5c} |
| {5} | $2 Li_{(\text{soln})}^{2+} + S_{2(\text{soln})}^{2-} \rightleftharpoons Li_2S_{2(\text{solid})}$ | 10^{-9} | $Li_2S_{2(\text{solid})}$ | 30 ^a | 4.317×10^{-5b} |
| {6} | $2 Li_{(\text{soln})}^{2+} + S_{(\text{soln})}^{2-} \rightleftharpoons Li_2S_{(\text{solid})}$ | 5×10^{-7} | $Li_2S_{(\text{solid})}$ | 10 ^a | 2.768×10^{-4b} |

^a Assumed parameters.

^b Assumed parameters taken from reference [148].

^c Calculated based on the assumed densities.

All parameters and expressions corresponding to inter-particle pores are henceforth assigned the subscript 1 and those of the mesopores within the carbon particles subscript 2.

The mathematical flow chart of our model is shown in Fig. 4.2, where the global input is the applied current density and the global output is the electrode potential.

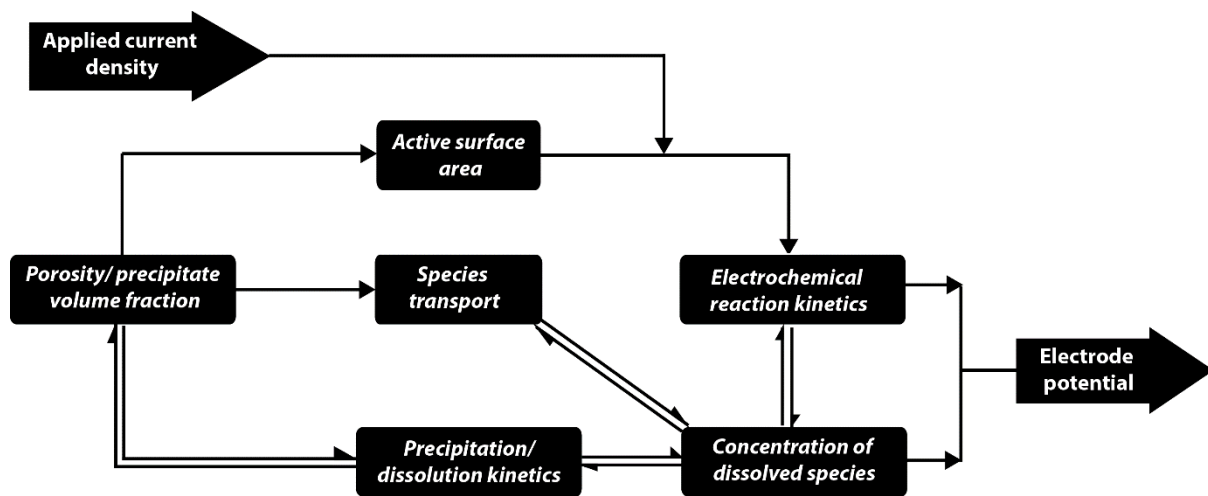


Figure 4.2. Flow chart of our model.

The electrochemical reaction rates depend on the current density, the concentration of electrolyte solutes and the active surface area of the cathode. The precipitation/dissolution reaction rates depend on the concentration of electrolyte solutes and the volume fraction of precipitates in the cathode. The concentration of electrolyte solutes evolve with the discharge and is coupled to the precipitation of $Li_2S_{y(solid)}$, whereby the porosities and the active surface area of the cathode also evolve with the discharge, which in turn affect the chemical/electrochemical reaction rates and the transport of electrolyte solutes. The cathode potential is the equilibrium potential and the kinetic overpotential combined, the former depends on the concentration of polysulfides in the electrolyte and the latter being determined from the current balance equation. The total cell potential finally results from the

anode potential being related to the concentration of lithium ions at the separator/anode interface.

4.3. Methodology: Overall construction and governing equations

4.3.1. Structural properties of cathode

The inter-particle porosity and the carbon mesoporosity before sulfur impregnation are given by Eqs. 4.1 and 4.2 respectively

$$\varepsilon_1^{max} = 1 - \rho_c \left(\frac{4\pi R_p^3}{3} \right) \quad (4.1)$$

$$\varepsilon_1^{max} = N_p \rho \left(\frac{4\pi r_p^3}{3} \right) \quad (4.2)$$

Where ρ_c and R_p are the number density and radius of the carbon particles. N_p and r_p are the number and radius of mesopores within each carbon particle.

After $S_{8(solid)}$ impregnation the initial porosities are given by Eqs. 4.3 and 4.4 respectively

$$\varepsilon_1^{init} = \varepsilon_1^{max} - (\varepsilon_1)_{S_8} \quad (4.3)$$

$$\varepsilon_2^{init} = \varepsilon_2^{max} - (\varepsilon_2)_{S_8} \quad (4.4)$$

where $(\varepsilon_1)_{S_8}$ and $(\varepsilon_2)_{S_8}$, are the volume fractions of the $S_{8(solid)}$ impregnated.

The maximum carbon surface areas of the inter-particle pores and the mesopores are given by Eqs. 4.5 and 4.6, respectively

$$a_1^{max} = \rho_c (4\pi R_p^2) \quad (4.5)$$

$$a_2^{max} = \rho_c (4\pi r_p^2) \quad (4.6)$$

Due to their smaller size, the mesopores have a very high specific surface area and the passivation effect by $S_{8(solid)}$ is considered to be negligible, therefore the initial surface area is given by

$$a_2^{init} = a_2^{max} \quad (4.7)$$

However, the carbon active surface area of the inter-particle pores is reduced, given by Bruggeman relation [161],

$$a_1^{init} = a_1^{max} \left(\frac{\epsilon_1^{init}}{\epsilon_1^{max}} \right)^\beta \quad (4.8)$$

where β Bruggeman coefficient.

4.3.2. Electrochemical reaction kinetics

The rate of each electrochemical reaction reported in Table 1 is given by the Butler-Volmer equation

$$(i_1)_j = n_j q_e \left((K_1^a)_j e^{\left(\frac{\eta F}{2RT}\right)} - (K_1^c)_j e^{\left(-\frac{\eta F}{2RT}\right)} \right) \quad (4.9)$$

where n_j is the absolute number of elementary charges transferred in reaction, $q_e = 1.602 \times 10^{-19}$ C is the elementary charge, and η is the kinetic overpotential. $(K_1^a)_j$ and $(K_1^c)_j$ are the anodic and cathodic rate constants from transition-state theory

$$(K_1^a)_j = \left(\frac{k_B T}{h}\right) \kappa A e^{\left(-\frac{E_j^B}{RT}\right)} \prod_i \left(\frac{(c_1)_i}{(c_{ref})_i}\right)^{P_{ij}} \quad (4.10)$$

and

$$(K_1^c)_j = \left(\frac{k_B T}{h}\right) \kappa A e^{\left(-\frac{E_j^F}{RT}\right)} \prod_i \left(\frac{(c_1)_i}{(c_{ref})_i}\right)^{Q_{ij}} \quad (4.11)$$

where k_B is the Boltzmann constant, T is the temperature, h is the Planck constant, κ is the frequency factor, A is an area factor, c_{ref} is the reference concentration, and E^F and E^B are the forward and backward activation energies, respectively. The subscript i in the Eqs. 4.10 and 4.11 corresponds to the species index (Table 4.1). P_{ij} and Q_{ij} are the absolute values of the stoichiometric coefficients of the oxidized and reduced species, respectively which are involved in the electrochemical reactions listed in Table 4.1.

The Eqs. 4.9-4.11, hold for both the electrochemical reactions in the inter-particle pores and in the mesopores, but all concentration variables must be substituted accordingly.

4.3.3 Chemical reaction rates

As in previously reported models [148,152–154], the chemical reaction rates of the dissolution/precipitation reactions (Table 4.2) depend on the concentration of dissolved species in the electrolyte c_i , and the volume fraction of the solid precipitates in the cathode

ϵ_k . Since the physics are the same for both inter-particle pores and mesopores, the rate equation is given without the subscripts. The rate of a dissolution/precipitation reaction R_k is given by

$$R_k = k_k^{perc} \epsilon_k \left(\prod_i (c_i)^{\gamma_{ik}} - K_k^{sp} \right) \quad (4.12)$$

where k_k^{perc} is the chemical rate constant, K_k^{sp} is the solubility product and γ_{ik} is the coefficient of the species involved in the chemical precipitation/dissolution reaction k .

4.3.4. Transport in the electrolyte

Generally, the electrolytes used in Li-S batteries are highly viscous and the dissolved species concentrations will reach very high values along discharge, thus for the sake of simplicity we assume transport of species in the electrolyte to be diffusive. Apart from the anion of the dissolved lithium salt, the evolution of the concentrations of all the other solutes in the inter-particle pores is given by the mass conservation expression

$$\frac{\partial(c_1 \epsilon_1)}{\partial t} = \frac{\partial}{\partial x} \left(D \epsilon_1^\beta \frac{\partial c_1}{\partial x} \right) + g_1 - G_1 + f \quad (4.13)$$

where ϵ_1 is the inter-particle porosity, c_1 is the dissolved species concentration, D is the diffusion coefficient, g_1 and G_1 are the rates of the electrochemical and chemical reactions. The final term f is called the "intra-flux"; accounting for the exchange of dissolved species between inter-particle pores and mesopores. The factor ϵ^β represents the classical Bruggeman correction to the diffusion coefficient in porous media [162],[163].

A similar equation is used to describe the concentration evolution inside the mesopores, but the global diffusion flux term is removed:

$$\frac{\partial(c_2\varepsilon_2)}{\partial t} = g_2 - G_2 - f \quad (4.14)$$

The electrochemical reaction source term (g_1/g_2) for a specific species i is given by

$$g_i = -a \sum_j \frac{S_{ij}i_j}{n_jF} \quad (4.15)$$

where a is the active surface area and S_{ij} the coefficients of the species and number of electrons involved, respectively (Table I).

The chemical reaction source term (G_1 or G_2) for a species i is given by

$$G_i = \sum_k \gamma_{ik} R_k \quad (4.16)$$

For the separator the evolution of the concentration is also given by the mass conservation Eq. 4.13. However, the chemical, electrochemical and intra-flux source terms are not applicable as the separator is assumed to be a homogenous porous medium without any chemical or electrochemical reactions occurring inside.

4.3.5. Intra-flux

The intra-flux term f used in Eqs. 4.13 and 4.14 is a key concept in our multi-scale model. It is featured as "intra" rather than "inter-" as it describes the exchange of species between the inter-particle pores and mesopores only within the same control volume of the discretized cathode (Fig. 4.3).

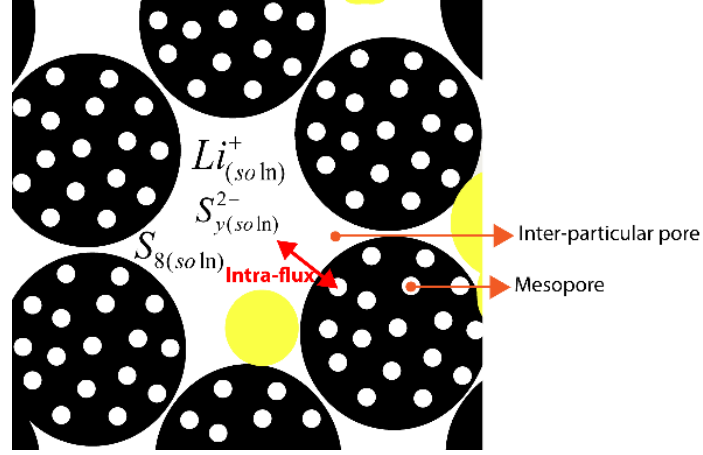


Figure 4.3. Schematic of the exchange of mass between mesopores and inter-particle pores.

The intra-flux of a given species within a control volume is given by

$$f = K_{flux} D (c_2 - c_1) \Xi(\delta_1) \quad (4.17)$$

Where K_{flux} is a rate constant and the “choking function”, $\Xi(\delta_1)$ describes the resistance to mass exchange between the inter-particle pores and the mesopores,

$$\Xi(\delta_1) = \frac{1 - \operatorname{erf}\left(\frac{\delta_1 - \delta_{chok}}{L_{chok}}\right)}{2} \quad (4.18)$$

In Eq. (4.18), erf is the error function, δ_1 is the thickness of the $Li_2S_{(solid)}$ thin film covering the external surface of the carbon particles, δ_{chok} is a characteristic $Li_2S_{(solid)}$ thin film thickness of halved probability of mass exchange, and L_{chok} is a scaling factor. When $\Xi = 0$ and the mesopores are fully choked, there will be no intra-flux within that finite volume element.

4.3.6. Dynamic viscosity evolution

The diffusion coefficient D in Eq. (4.13) is assumed to be affected by the long chain polysulfides generated during discharge, increasing the viscosity of the electrolyte. The

diffusion coefficient of a spherical species in a viscous solution is expressed through the Stokes-Einstein relation as

$$D = \frac{k_B T}{6\pi\mu r_i} \quad (4.19)$$

Where μ is the viscosity and r_i is the radius of gyration of the species i . For non-spherical species, a correction factor will appear in the denominator, but the relation between diffusion coefficient and viscosity remains as

$$D \propto \frac{1}{\mu} \quad (4.20)$$

Since $S_{8(\text{soln})}$ and $S_{8(\text{soln})}^{2-}$ are larger than the solvent molecules and other solutes in the electrolyte, we account for them as suspended particles. The relative viscosity is hence calculated using Einstein's formula for a monodispersed suspension [164],

$$\frac{\mu}{\mu_0} = \frac{1 + 0.5\varphi}{(1 - \varphi)^4} \quad (4.21)$$

where μ_0 is the viscosity of the pure electrolyte and μ is the viscosity with suspended particles, whose volume fraction is φ . We assume that,

$$\varphi = (c_1)_{S_8} \bar{V}_{S_8} + (c_1)_{S_8^{2-}} \bar{V}_{S_8^{2-}} \quad (4.22)$$

where \bar{V}_{S_8} and $\bar{V}_{S_8^{2-}}$ are the partial molar volumes of $S_{8(\text{soln})}$ and $S_{8(\text{soln})}^{2-}$, respectively. While indeed, Eq. 4.21 neglects the effects of other solutes, the long chain polysulfides can potentially affect the transport of all the solutes in the confined environment of the porous media, especially as the $S_{8(\text{soln})}^{2-}$ concentration can be very large and contribute significantly to the electrolyte viscosity. There is lack of experimental data on the evolution of electrolyte

viscosity during discharge and the contributions of different solutes, but this approach suggests a viable path towards a better understanding.

4.3.7. Active surface area and porosity

The loss of inter-particle active surface area due to solid sulfur loading is calculated based on a phenomenological expression also adopted by previous models [148,152–154]. Since we assume that the $Li_2S_{(solid)}$ film passivates the carbon particle surface, its active surface is calculated based on the film thickness using an electron tunnelling probability function modified from a model for Li-O₂ batteries [165] by some of us

$$a_1 = a_1^{max} \left(1 - \frac{(\epsilon_1)_{S_8}}{\epsilon_1^{max}} \right)^\beta \Theta(\delta_1) \quad (4.23)$$

where $\Theta(\delta_1)$ is the electron tunneling probability function,

$$\Theta(\delta_1) = \frac{1 - \operatorname{erf}\left(\frac{\delta_1 - \delta_{tun}}{L_{tun}}\right)}{2} \quad (4.24)$$

δ_1 comes from Eq. (4.18), δ_{tun} is a threshold thickness at halved electron tunnelling probability, and L_{tun} is a scaling factor.

The passivation effect due to the loaded $S_{8(solid)}$ is neglected, but the losses due to the passivation by the $Li_2S_{(solid)}$ film on the internal mesoporous surface and the choking of some mesopores entrances by the film formed over the external particle surface are both included. The fraction of mesopores that are not choked are computed using the choking function (Eq 4.18).

$$a_2 = a_2^{max} \left(\frac{R_p - \delta_2}{R_p} \right)^2 \Theta(\delta_2) \Xi(\delta_1) \quad (4.25)$$

where the term $\left(\frac{R_p - \delta_2}{R_p}\right)^2$ characterizes the decrease of the mesoporous surface area (Fig. 4.4).

Similar to previous models [148,152–154], the inter-particle porosity and the mesoporosity are evaluated based on the volume fraction of the solid precipitates within the pores. The precipitation rate of a solid precipitate k in the inter-particle pores is,

$$\frac{\partial(\epsilon_1)_k}{\partial t} = \left(\frac{M_k}{\rho_k}\right) \epsilon_1 (R_1)_k \quad (4.26)$$

Similarly, the precipitation rate of a solid precipitate k in the mesopores is,

$$\frac{\partial(\epsilon_2)_k}{\partial t} = \left(\frac{M_k}{\rho_k}\right) \epsilon_2 (R_2)_k \quad (4.27)$$

The evolution of the inter-particle porosity and the mesoporosity of the cathode, respectively, are calculated as follows,

$$\epsilon_1 = \epsilon_1^{max} - \sum_k (\epsilon_1)_k \quad (4.28)$$

$$\epsilon_2 = \left(\epsilon_2^{max} - \sum_k (\epsilon_2)_k \right) \Xi(\delta_1) \quad (4.29)$$

4.3.8. Film thickness

$Li_2S_{(solid)}$ is the primary solid precipitate and the precipitation in the inter-particle pores may occur either through a solution phase route in the bulk electrolyte or a surface-limited thin film route (Fig. 4.4). The volume fraction of the $Li_2S_{(solid)}$ thin film in the inter-particle pores is given by

$$(\omega_1)_{Li_2S} = (\epsilon_1)_{Li_2S}(1 - \chi) \quad (4.30)$$

where χ is the escape function [166], the fraction of $Li_2S_{(solid)}$ precipitated as particles in the inter-particle pores. Assuming the film to cover the external surface of the carbon particle as a hollow sphere, its thickness is given by

$$(\delta_1)_{Li_2S} = \left(\frac{3((\omega_1)_{Li_2S} - \epsilon_1^{max} + 1)}{4\pi\rho_c} \right)^{\frac{1}{3}} - R_p \quad (4.31)$$

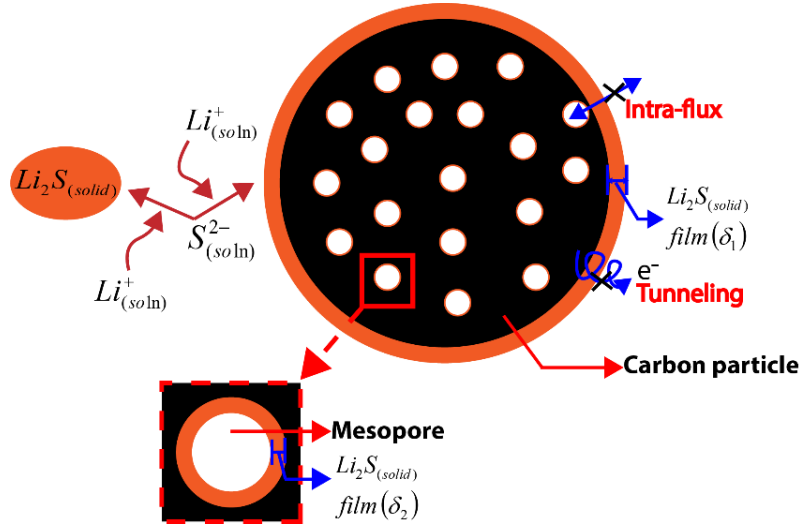


Figure 4.4. Schematic representation of the $Li_2S_{(s)}$ precipitation routes.

The total volume fraction of the $Li_2S_{(solid)}$ produced in the mesopore is simply the volume fraction of the $Li_2S_{(solid)}$ film formed over its internal carbon surface:

$$(\omega_2)_{Li_2S} = (\epsilon_1)_{Li_2S} \quad (4.32)$$

Similarly, the thickness of the $Li_2S_{(solid)}$ film formed inside the mesopore is given by

$$(\delta_2)_{Li_2S} = r_p - \left(\frac{3(\epsilon_1^{max} - (\omega_1)_{Li_2S})}{4\pi\rho_c N_p} \right)^{\frac{1}{3}} \quad (4.33)$$

4.3.9 Current balance

The sum of the Faradaic current densities of all the electrochemical reactions is set equal to the applied current density, I_G (we neglect the double layer effect)[167]

$$I_G = - \sum_j \int_B^C (a_1(i_1)_j + a_2(i_2)_j) dx \quad (4.34)$$

where the minus sign emerges as the anodic direction is positive in Eq. (4.9).

4.3.10. Cell voltage

The general form of the equilibrium potential expression for any electrochemical reaction is

$$U_j = U_j^0 - \frac{RT}{n_j F} \sum_i S_{ij} \ln(\overline{(c_1)_i}) \quad (4.35)$$

where U_j^0 is the standard potential of a electrochemical reaction j , $\overline{(c_1)_i}$ is the average concentration of a species i .

As the concentration of $Li_{(soln)}^+$ evolves significantly in Li-S batteries the anode equilibrium potential is hence determined using Nernst's equation for lithium metal oxidation

$$U_1 = \frac{RT}{F} \ln(\overline{(c_1)_{Li}}) \quad (4.36)$$

Similarly, the cathode equilibrium potential is calculated based on the $S_{2(soln)}^{2-}/S_{(soln)}^{2-}$ reduction reaction, as it is the dominant reaction in most parts of the discharge event as suggested by Kumaresan *et al.* [148],

$$U_6 = U_6^0 + \frac{RT}{F} \ln \left(\frac{\left((c_1)_{S_2^{2-}} \right)^{\frac{1}{2}}}{(c_1)_{S^{2-}}} \right) \quad (4.37)$$

The cell voltage is the difference between the cathode and anode equilibrium potentials, plus the cathode overpotential

$$U_{cell} = U_6 - U_1 + \eta \quad (4.38)$$

The cell potential drop due to electrolyte resistance during the high plateau and the intermediate stage between the discharge plateaus has been found to be more significant than the activation overpotential [126]. However, EIS studies carried out by Deng *et al.* [168], showed that the charge transfer resistance, corresponding to the activation overpotential, and the surface film resistance, are much larger than electrolyte resistance throughout the discharge event. This suggests that the cell potential can be limited by charge transfer and surface resistance even when the electrolyte conductivity is adequate.

Therefore, it is reasonable to assume that the cell potential drop is dictated by the cathode overpotential and as the latter is determined by inverting the overall current balance equation it also includes the mass transport and surface passivation effects, via our model's strong coupling of these phenomena.

4.4. Computational implementation

The model was implemented in MATLAB. The coupled partial/ordinary differential equations were solved using the finite volume method (cf. Appendix A.4).

All simulations were carried out on a PC equipped with four 3.30 GHz processors Intel® core™ i5-4590 with a typical simulation time of 1.5 to 2 days for a full polarization curve.

The discharge simulations are stopped when either one of these conditions is satisfied:

- (i) all the dissolved sulfur species get completely reduced to $S_{(soln)}^{2-}$ in which case the discharge capacity equals the theoretical capacity;

Chapter 4. Microstructurally resolved continuum discharge model

- (ii) a clogging of pores due to $Li_2S_{(solid)}$ precipitation prevents the transport of active species through the cathode and cause the loss of active surface area;
- (iii) a complete passivation by the $Li_2S_{(solid)}$ thin film, defined as a thickness beyond the electron tunneling threshold.

4.4.1. Physical model

A cathode with 70% porosity is assumed as a reference case where the areal loading of sulfur is 2.48 mg.cm^{-2} and the inter-particle porosity constitutes 25% of the volume, whereas the mesoporosity accounts for 45%. The C/S volume ratio is 1:1. 70% of the total volume of the impregnated $S_{8(solid)}$ exists inside the mesopores.

Table 4.3. General parameters of the simulated Li-S cell.

| Parameter name | Parameter symbol | Value | Unit |
|-----------------------------------|---------------------|------------------------|-----------------|
| Cathode thickness | L_{cat} | 40 ^a | μm |
| Separator thickness | L_{sep} | 20 ^a | μm |
| Separator porosity | ε_{sep} | 50 ^a | % |
| Particle radius | R_p | 100 ^b | nm |
| Pore radius | r_p | 3 ^b | nm |
| Particle number density | ρ_c | 1.79×10^{20c} | m^{-3} |
| Number pores per particle | N_p | 22222 ^c | - |
| Number of cathode bins | P | 10 ^a | - |
| Number of separator bins | Q | 5 ^a | - |
| Escape function | χ | 0.5 ^a | - |
| Choking thickness | δ_{chok} | 3 ^a | nm |
| Choking extension | L_{chok} | 4 ^a | nm |
| Tunneling threshold | δ_{tun} | 5 ^a | nm |
| Scaling factor tunneling function | L_{tun} | 2.5 ^a | nm |

^a Assumed parameters. ^b Taken from the TEM image in Ref. [158]. ^c Calculated based on the assumed inter-particle porosity and mesoporosity.

4.5. Results and discussion

A systematic study of the effects of the battery operation and C/S microstructural properties on the discharge is presented in this section. Only those parameters whose effects are being investigated are changed for the simulations reported in each subsection. This way it is possible to track the unique roles of several experimentally modifiable parameters single-handedly, paving the way for a rational design of more performant Li-S cells in general and C/S cathodes in particular.

4.5.1. Rate capability

The rate capability of the reference cathode microstructure is investigated by simulating discharge using three different current densities: 0.5, 1.0 and 1.5 mA.cm⁻² (Fig. 4.5).

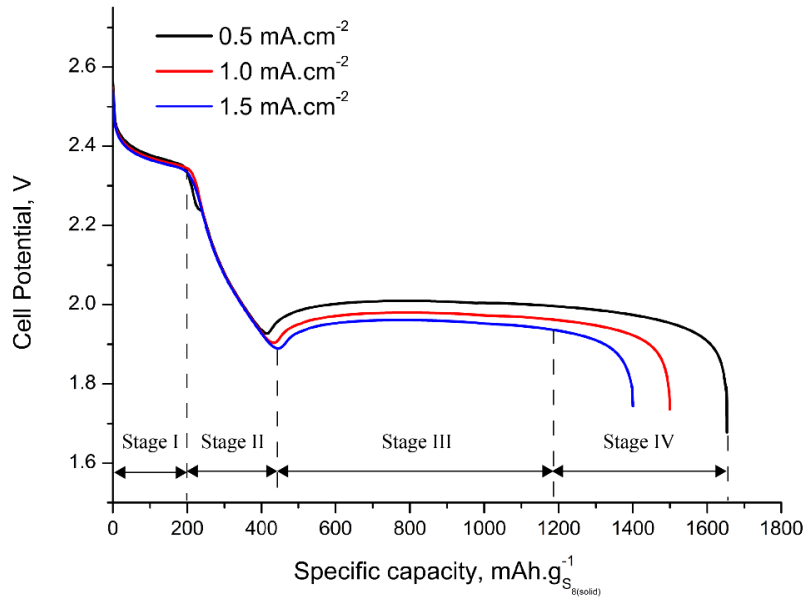


Figure 4.5. Calculated discharge profiles at current densities 0.5, 1.0 and 1.5 mA.cm⁻².

The latter part of the discharge potential decrease as the current density increases, due to the increase in the activation polarization, and also the final discharge capacities decrease, all consistent with experimental observations [158–160].

The predicted total discharge capacities are larger than those reported experimentally – mainly due to the neglect of phenomena such as improper electron wiring of the porous carbon matrix, chemical reactions of polysulfides with the lithium metal anode, and active surface area and porosity losses due to presence of a binder. Neglecting such phenomena, however, allows us to focus on the understanding of carbon microstructure design parameters’ impact on the cell performance – and resolving these for the different parts of the discharge event. In more detail, each discharge profile consists of four stages:

- Stage I corresponds to the first plateau of the discharge, when the concentrations of $S_{8(soln)}$ and $S_y^{2-(soln)}$ remain relatively constant (Figs 4.6a and b), due to a steady dissolution of $S_{8(solid)}$ and a subsequent reduction of $S_{8(soln)}$ to shorter chain polysulfides;

Chapter 4. Microstructurally resolved continuum discharge model

- Stage II begins after the complete dissolution of $S_{8(solid)}$ where the electrochemical reactions <2> to <4> (Table 4.1) become dominant, leading to the consumption of long chain polysulfides and an increase in the short chain polysulfide concentrations (Figs. 4.7c and d). The Stage II discharge potential decreases continuously until it reaches a local minimum when $Li^+_{(soln)}$ and $S^{2-}_{(soln)}$ become super-saturated. At this point the nucleation of $Li_2S_{(solid)}$ will start;
- In Stage III the electrochemical reactions <5> and <6> are dominant, but the concentrations of $S^{2-}_{(soln)}$ and $S^{2-}_{(soln)}$ remain relatively constant due to the precipitation of $Li_2S_{(solid)}$;
- The stage IV corresponds to loss of active surface area and porosity in the cathode;
- Finally, the discharge simulation stops when the inter-particle porosity falls to zero (Fig. 4.7).

These calculated concentration profiles are almost consistent to those observed in the Ref. [148]. The predicted solid species evolution during discharge is also consistent with the crystalline *in situ* XRD study [169], which suggest that reaction mechanisms in our model are reasonable.

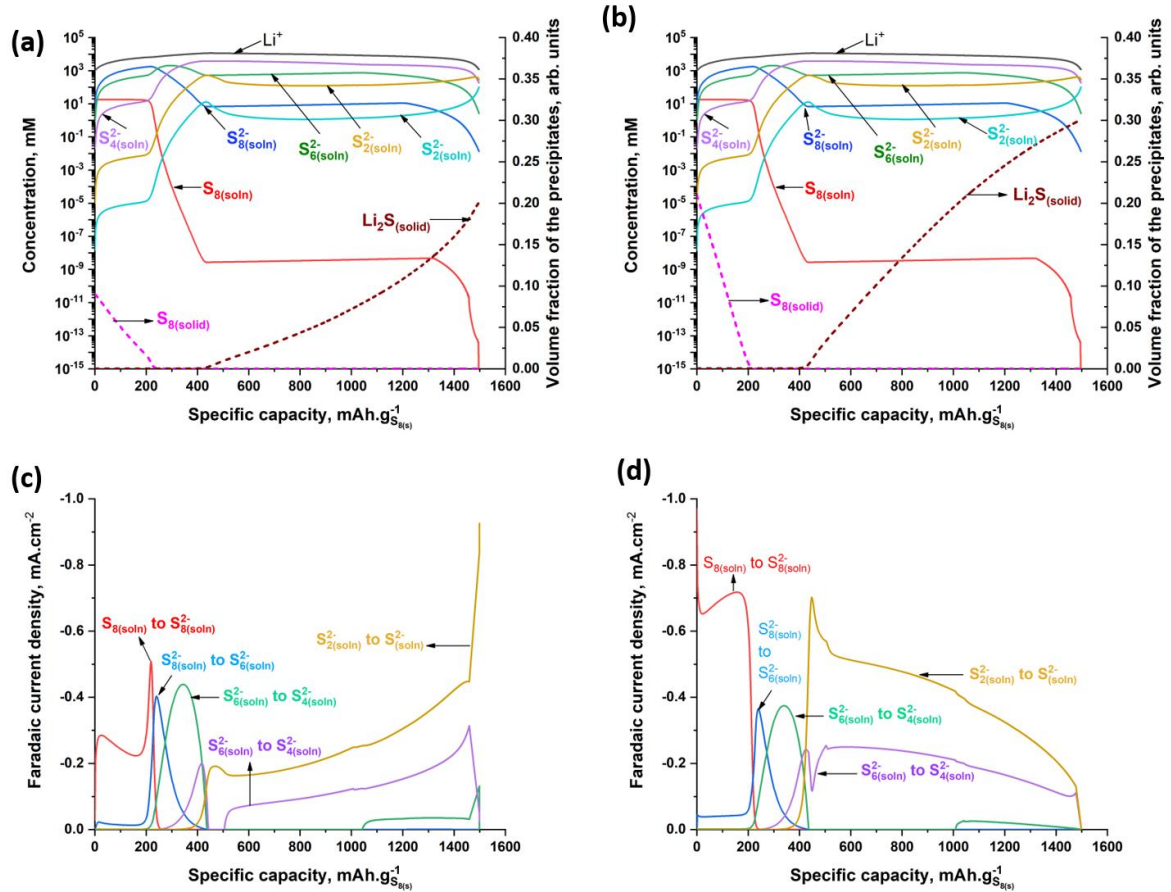


Figure 4.6. Evolution of concentration of species (solid lines) and volume fractions of the solid precipitates (dashed lines) for a discharge at 1.0 mA.cm⁻² in: (a) the inter-particle pores, and (b) the mesopores. Faradaic current densities for different electrochemical reactions in: (c) the inter-particle pores, and (d) the mesopores.

During discharge, the total concentration of polysulfides will reach a very high value (≈ 4.8 M), but the lithium ion concentration will be more than twice this value. Since the production and consumption rate of electrons in the anode and the cathode, respectively, are identical, the amount of positive and negative charges produced in the cell should also be identical. Even though our model does not have any constraints for electroneutrality, the charge difference between the lithium ions and polysulfide ions minus the initial lithium salt anions is found to be negligible for the complete cell.

At the end of discharge the $Li_2S_{(solid)}$ film thickness still allows for electron tunneling, but the inter-particle porosity of the cathode bin closest to the separator falls to zero due to clogging by $Li_2S_{(solid)}$ (Fig. 4.7(a)).

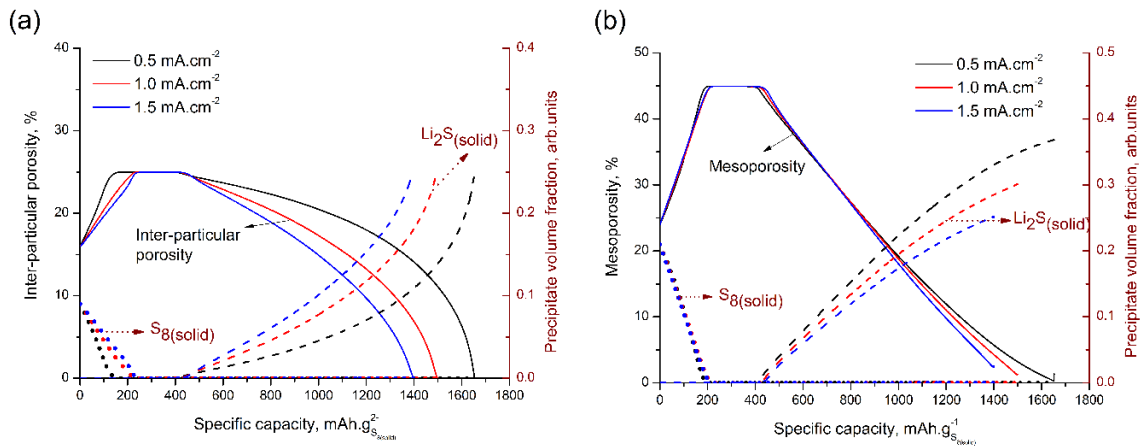


Figure 4.7. Evolution of porosities and volume fractions of the solid precipitate in: (a) the inter-particle pores, and (b) the mesopores, for the cathode bin closest to the separator.

The discharge capacities are lower than the theoretical capacity for all the three current densities due to the fact that some of the potentially electrochemically active solutes remain blocked in the separator at the end of discharge (Fig. 4.8), and as the clogging is faster during faster discharge, the discharge capacities decrease more upon increased current density. While the lack of accurately determined parameters limits the predictive power the suggested capacity limitation due to the clogging of inter-particle pores closest to the separator, has been identified experimentally [53]. Hence our model is capable of making qualitative predictions about such cathode micro-structural effects on the discharge performance. The decrease in mesoporosity is larger than the increase in $Li_2S_{(solid)}$ volume fraction (Fig. 4.7(b)), with additional losses caused due to the choking of mesopore entrances.

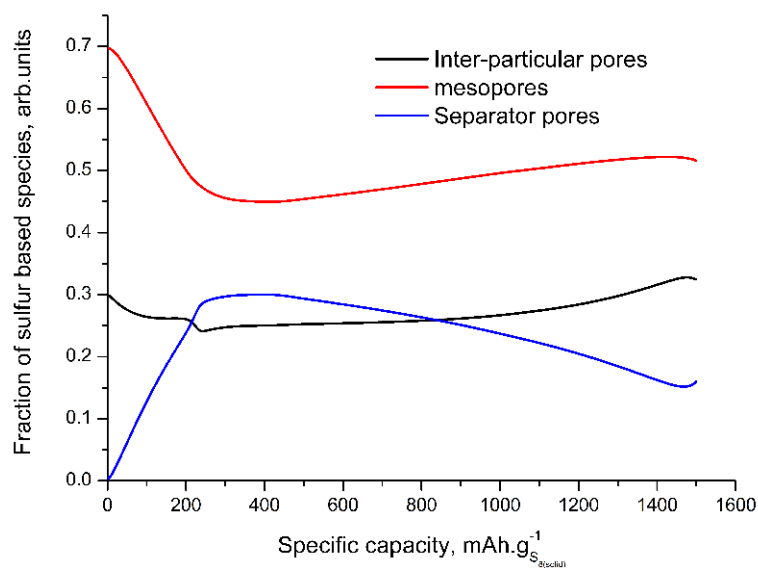


Figure 4.8. Evolution of the fractions of all the sulfur-based species, precipitates and dissolved, residing at different porous regions for a discharge at $1.0 \text{ mA}\cdot\text{cm}^{-2}$.

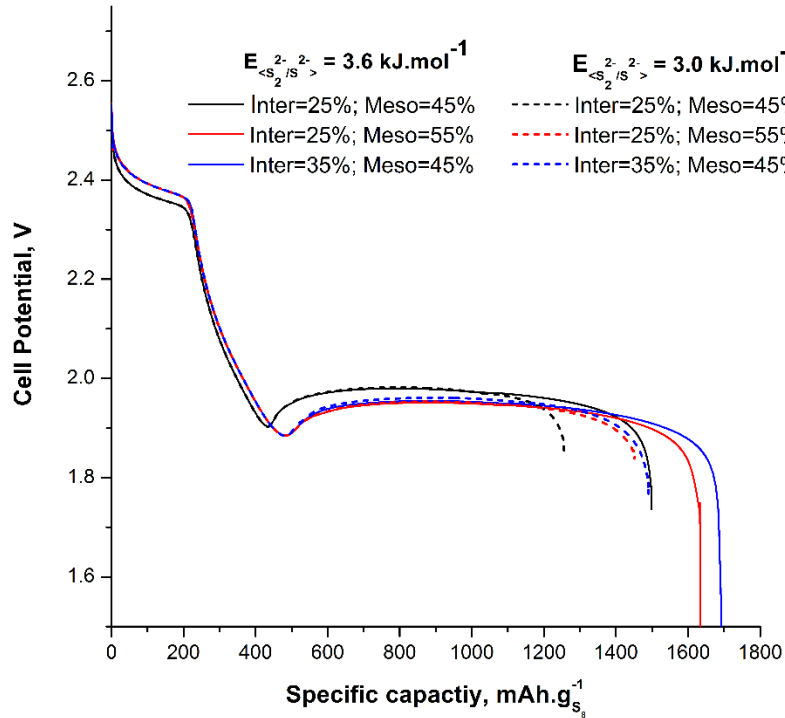
4.5.2. Impact of porosity

The discharge dependence on porosity is simulated by using different C/S cathodes. The C/S volume ratio is 1:1 for all three configurations, while the sulfur loading is reduced as the porosity is increased (Table 4.4). The mesoporosity is increased by increasing the number of mesopores per particle, while the inter-particle porosity is increased by decreasing the particle number density and in all the cathodes 70% of the total impregnated sulfur volume exists in the mesopores.

Table 4.4. Sulfur loadings for the three configurations with different carbon porosities.

| Maximum carbon porosity | Particle number density (m^{-3}) | No. of pores per particle | Areal $S_{8(\text{solid})}$ Loading ($\text{mg}\cdot\text{cm}^{-2}$) |
|---|---|---------------------------|--|
| Inter-particle=25%; Meso=45% (Reference) | 1.79×10^{20} | 22222 | 2.48 |
| Inter-particle=25%; Meso=55% | 1.79×10^{20} | 27170 | 1.65 |
| Inter-particle=35%; Meso=45% | 1.55×10^{20} | 25630 | 1.65 |

The calculated discharge capacities are shown to be limited by the clogging of inter-particle pores closest to the separator by $\text{Li}_2\text{S}_{(\text{solid})}$. Therefore to check the reproducibility of the predicted trends, discharge simulation of different cathodes are repeated for two different activation energies corresponding to $\text{S}_{2(\text{soln})}^{2-}/\text{S}_{2(\text{soln})}^{2-}$ reduction reaction ($E_{\langle \text{S}_2^{2-}/\text{S}^{2-} \rangle}$).


Figure 4.9. Simulated discharge profiles at $1.0 \text{ mA}\cdot\text{cm}^{-2}$ for the three cathode configurations with $E_{\langle \text{S}_2^{2-}/\text{S}^{2-} \rangle} = 3.6 \text{ kJ}\cdot\text{mol}^{-1}$ (solid lines) and $E_{\langle \text{S}_2^{2-}/\text{S}^{2-} \rangle} = 3.0 \text{ kJ}\cdot\text{mol}^{-1}$ (dashed lines).

The $S_{2(\text{soln})}^{2-}/S_{(\text{soln})}^{2-}$ reduction reaction is faster when the activation energy is low ($E_{\langle S_2^{2-}/S^{2-} \rangle} = 3.0 \text{ kJ.mol}^{-1}$). Therefore, the discharge capacities of all the cathodes decrease when $E_{\langle S_2^{2-}/S^{2-} \rangle}$ is decreased (Fig. 4.9), due to faster precipitation of $Li_2S_{(\text{solid})}$ and earlier clogging of inter-particle pores closest to the separator (Fig. 4.10(a)).

In general, the cathode surface area increases as the mesoporosity increases, which facilitates better active material utilization and hence, as expected, the discharge capacity increases. However, surprisingly, the increase in discharge capacity is slightly pronounced for the cathode with 35% maximum inter-particle porosity despite its surface area being the lowest among three due to its low particle number density (Table 4.4). The slight increase in the discharge capacity is achieved through its large transport path for the soluble active species, thereby facilitating better access to the carbon surface throughout the cathode. This effect is more pronounced for the discharge curve simulated using high activation energy ($E_{\langle S_2^{2-}/S^{2-} \rangle} = 3.6 \text{ kJ.mol}^{-1}$). Under such slow $S_{2(\text{soln})}^{2-}/S_{(\text{soln})}^{2-}$ reduction kinetics, the active species possess ample time to get transported across the cathode. Therefore, unlike the other two cathodes, with 25% maximum inter-particle porosity, the electrochemical and precipitation reactions take place isotropically in this cathode. This way the inter-particle porous network does not get clogged (Figs. 10a and b), facilitating the active species access to the entire carbon surface, resulting in a complete utilization.

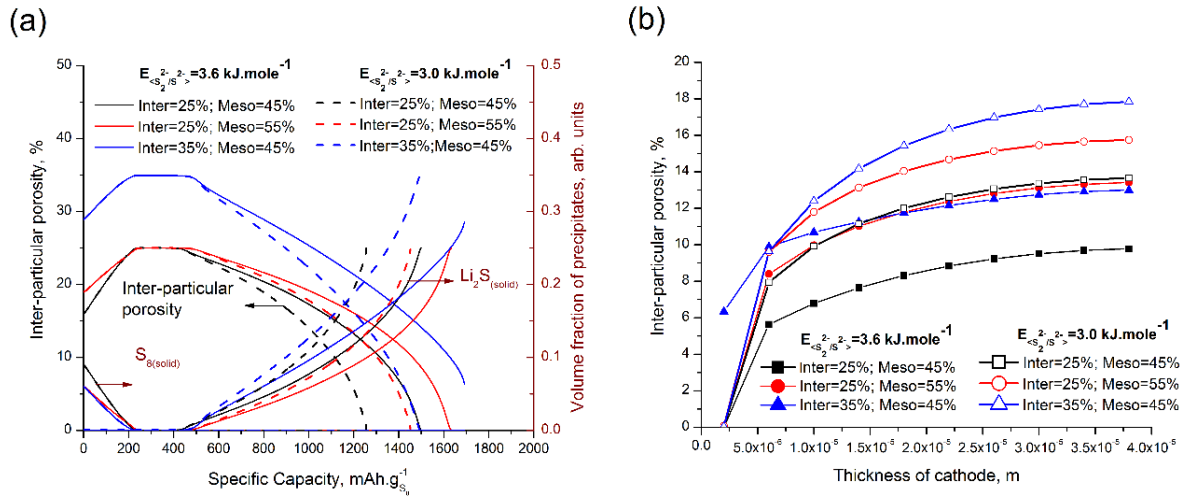


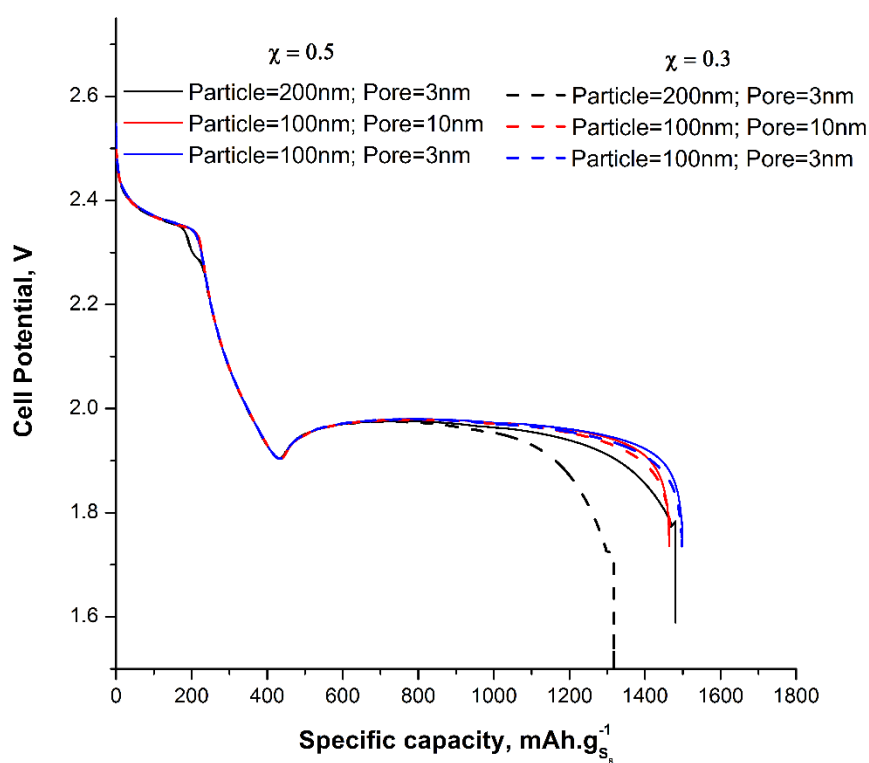
Figure 4.10. (a) The evolution of the inter-particle porosities and the volume fractions of $S_8(\text{solid})$ and $Li_2S(\text{solid})$ in the inter-particle pores, solid lines correspond to $E_{\langle S_2^{2-}/S^{2-} \rangle} = 3.6 \text{ kJ.mole}^{-1}$ and dashed lines correspond to $E_{\langle S_2^{2-}/S^{2-} \rangle} = 3.0 \text{ kJ.mole}^{-1}$ and (b) the distribution of inter-particle porosity along the cathode thickness at the end of discharge, solid points correspond to $E_{\langle S_2^{2-}/S^{2-} \rangle} = 3.6 \text{ kJ.mole}^{-1}$ and hollow points correspond to $E_{\langle S_2^{2-}/S^{2-} \rangle} = 3.0 \text{ kJ.mole}^{-1}$.

4.5.3. Impact of particle and pore sizes

The impact of carbon particle and pore sizes on the discharge performance and its sensitivity to the two different escape functions (χ) were investigated. The calculated discharge capacities are only slightly decreased by increasing the carbon particle and mesopore sizes (Fig. 4.11) for the case of $\chi = 0.5$, the value used in the rate capability analysis. Even though, their corresponding discharge capacities are almost similar, they are limited due to different physical reasons.

Table 4.5. Parameters values used for the simulated cathodes containing different particle and pore sizes.

| Carbon particle and mesopore radii | Particle number density (m^{-3}) | No. of mesopores per |
|--|---|----------------------|
| Particle=100 nm Pore=3 nm (Reference) | $1.79 \times 10^{20} \text{ m}^{-3}$ | 22222 |
| Particle=100 nm Pore= 10 nm | $1.79 \times 10^{20} \text{ m}^{-3}$ | 600 |
| Particle=200 nm Pore= 3 nm | $2.24 \times 10^{19} \text{ m}^{-3}$ | 177778 |

**Figure 4.11.** Simulated discharge profiles for cathodes with different particle and pore sizes discharged at $1.0 \text{ mA}\cdot\text{cm}^{-2}$ with $\chi = 0.5$ (solid lines) and $\chi = 0.3$ (dashed lines).

Due to the low particle number density, the inter-particle surface area is low for the cathode with larger particles (Table 4.5) and the $\text{Li}_2\text{S}_{(\text{solid})}$ film thickness grows at a faster rate (Fig. 4.12), producing an earlier choking of the mesopores with some unutilized active

species trapped inside and hence a slightly lowered discharge capacity. However, for the case $\chi = 0.3$, 70% of the $Li_2S_{(solid)}$ precipitates as a thin film, causing a rapid growth of its thickness in the cathode with larger particles, producing a much earlier choking of mesopores and a substantial decrease in the discharge capacity. The potential at the latter part of the discharge decreases for the cathode with large particles which is caused due to the larger passivation effect produce by the thick $Li_2S_{(solid)}$ film.

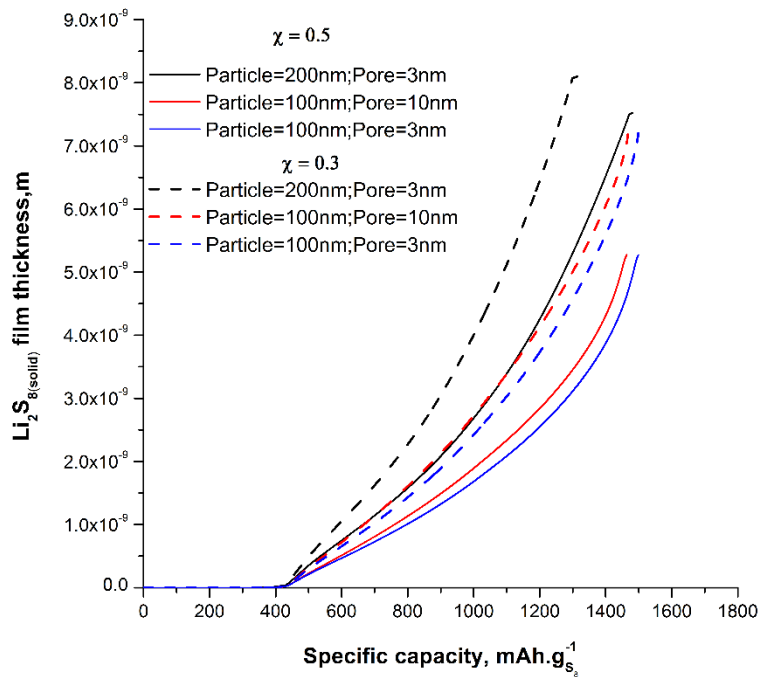


Figure 4.12. The growth of the $Li_2S_{(solid)}$ film thickness in the inter-particle pores for $\chi = 0.5$ (solid lines) and $\chi = 0.3$ (dashed lines).

The discharge capacities of the cathodes with smaller particles (100 nm), remain unchanged for two different escape functions, since their capacities are mainly affected by the clogging of inter-particle pores closest to the separator (Fig. 4.13(a)). $Li_2S_{(solid)}$ film thicknesses of the cathodes with smaller particles grow faster for the case $\chi = 0.3$. However, the thickness at the end of discharge are slightly thinner than the threshold thickness necessary to cause the complete choking of the mesopores. The mesoporous surface area decreases when the mesopore sizes are increased, thus the extent of electrochemical and subsequent precipitation reactions taking place inside are decreased along the discharge. Therefore, the $Li_2S_{(solid)}$ precipitates at a faster rate in the inter-particle pores of the cathode with large

mesopores, causing the inter-particle pores to clog earlier and slightly decreasing the discharge capacity compared to that of the cathode with small particles and mesopores (Fig. 4.11). This result suggests that the accumulation of $Li_2S_{(solid)}$ can be decreased by tailoring the microstructural parameters to produce large mesoporous surface.

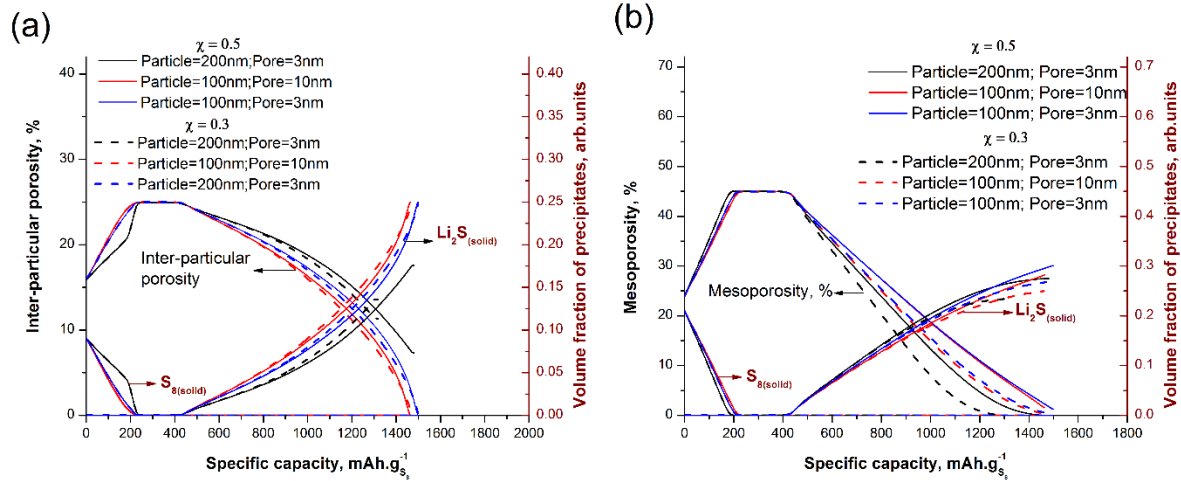


Figure 4.13. Calculated evolution of the porosities and the volume fractions of $S_{8(solid)}$ and $Li_2S_{(solid)}$ in the (a) inter-particle pores, and (b) mesopores of the carbon particles, both for the cathode bin closest to the separator. The solid lines correspond to $\chi = 0.5$ and dashed lines correspond to $\chi = 0.3$.

4.5.4. Impact of C/S ratio

Table 4.6. Areal sulfur loadings of the cathodes with different C/S composite structure

| C/S ratio | Areal $S_{8(solid)}$ loading |
|-----------------|------------------------------|
| 1:1.33 | 3.30 mg.cm ⁻² |
| 1:1 (Reference) | 2.48 mg.cm ⁻² |
| 1:0.67 | 1.66 mg.cm ⁻² |

We simulate the discharge profiles of the cathodes with different C/S volume ratios (Table 4.6) using the same current density, why the C-rate “automatically” increases as the volume fraction $S_{8(solid)}$ is decreased, causing the potential in the latter part of the discharge curve to decrease due to activation polarization (Fig. 4.14). The sensitivity of the $E_{<S_2^-/S^2->} (= 3.6$

and 3.0 kJ.mole^{-1}) is also tested for the cathodes with different $S_{8(\text{solid})}$ loadings. Although, the capacities of all the cathodes decrease when $E_{\langle S_2^{2-}/S^{2-} \rangle}$ is increased, the predicted discharge capacity trends for different $S_{8(\text{solid})}$ loadings remain unchanged.

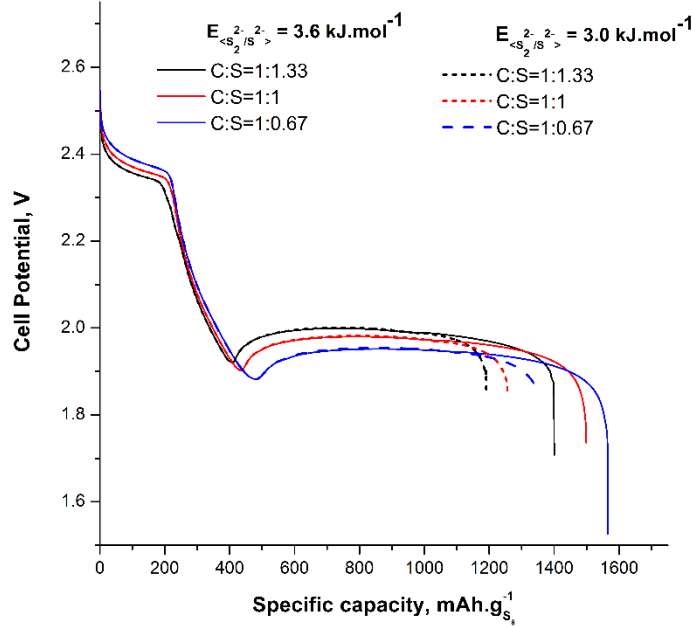


Figure 4.14. Simulated discharge profiles for cathodes with different C/S volume ratio discharged at 1.0 mA.cm^{-2} with $E_{\langle S_2^{2-}/S^{2-} \rangle}=3.6 \text{ kJ.mol}^{-1}$ (solid lines) and $E_{\langle S_2^{2-}/S^{2-} \rangle}=3.0 \text{ kJ.mol}^{-1}$ (dashed lines).

The $S_{8(\text{solid})}$ dissolution rate increases when its volume fraction is increased (Figs. 4.15(a) and (b)), producing a large amount of soluble polysulfides in the electrolyte and thereby a faster precipitation of $Li_2S_{(\text{solid})}$ in the inter-particle pores and mesopores. The calculated discharge capacities decrease for increased $S_{8(\text{solid})}$ loadings (Fig. 4.14) due to an earlier clogging of the inter-particle pores and choking of the mesopores. The calculated discharge capacity trends qualitatively resemble the experimentally observed trends [170].

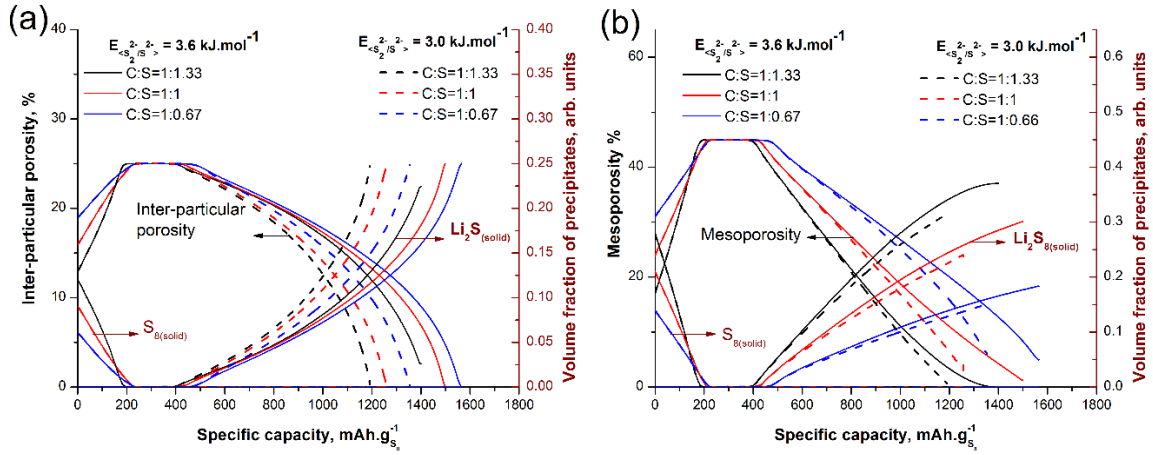


Figure 4.15. Calculated evolution of the porosities and the volume fractions of $S_{8(solid)}$ and $Li_2S_{(solid)}$ in the (a) inter-particle pores, and (b) mesopores, both for the cathode bin closest to the separator. The solid lines correspond to $E_{<S_2^{2-}/S^{2-}>} = 3.6 \text{ kJ.mol}^{-1}$ and dashed lines correspond to $E_{<S_2^{2-}/S^{2-}>} = 3.0 \text{ kJ.mol}^{-1}$.

4.6. Conclusions and perspectives

Our comprehensive multi-scale model allows to investigate the effects of the practical and experimentally modifiable operation and C/S microstructure properties on the discharge performance. The analysis of the calculated results reveals the physical reasons that limit the discharge capacities. The results qualitatively agree with the experimentally observed trends for example, the discharge capacities decrease when applied current density [158–160] and $S_{8(solid)}$ volume fraction are increased [170]. With the qualitatively validated results, our model is used to perform a prospective study of the roles of various microstructural design parameters, such as the inter-particle porosity, the mesoporosity, the particle and pore sizes, *etc.* on the final cell performance. A sensitivity analysis of the activation energy of the $S_{2(soln)}^{2-}/S_{(soln)}^{2-}$ reduction reaction shows that the discharge capacity decreases as the activation energy is increased. However, the predicted discharge capacity trends and the capacity limiting mechanisms for different cathode designs remain the same. The discharge capacity of the cathode with the larger particles decreases substantially as the escape function is decreased, since its capacity is mainly limited by the choking of mesopores by the $Li_2S_{(solid)}$ film formed over the carbon particles. In all the other cathode designs, the

discharge capacities are shown to be affected by clogging of inter-particle pores, caused by the slow transport of dissolved species.

The cathode with 35% maximum inter-particle porosity, 45% mesoporosity and 1:1 C/S ratio provided the highest capacity. This result suggests that the discharge capacity and rate capability can be improved by increasing the inter-particle porosity. This is because, the dissolved species transport through the cathode and the accommodation of the excess volume of the $Li_2S_{(solid)}$ precipitates are improved by increasing the inter-particle porosity. Furthermore, our modelling results show that the accumulation of $Li_2S_{(solid)}$ precipitates in the inter-particle pores, could be reduced by increasing the mesoporous surface area of the carbon particles. Therefore, carbon particles with high mesoporous surface area, can inhibit the early clogging inter-particle pores in the cathode, thereby resulting in the increase of its capacity. The mesoporous surface area can be increased by reducing the mesopore size and by increasing the number of mesopores.

Our discharge modelling results show that the discharge capacity, can also be improved by reducing the particle size and by increasing the number of carbon particles. Since, these aforementioned design modifications will result in the increase of the inter-particle surface area and produce thin $Li_2S_{(solid)}$ layer over the carbon surface which do not choke the mesopores.

Finally, our modelling result shows that the discharge capacity decreases when the sulfur loading of the cathode is increased. The reduction in the discharge capacities are due to the clogging of inter-particle pores and choking mesopores. Therefore, an appropriate cathode design solution such as increasing of inter-particle and decreasing particle size, could assist in improving the discharge capacity of the cathodes with high $S_{8(solid)}$ loading.

A.4. Appendix: Numerical Schemes

The discretized form of the Eq. (4.13) is derived by applying a second order finite volume method as follows

Chapter 4. Microstructurally resolved continuum discharge model

Finally, at the cathode/current collector interface ($x = L_{sep} + L_{cat}$) the fluxes of all the dissolved species is equal to zero.

Chapter 5. Cyclic voltammetry model

Contents

| | |
|---|------------|
| 5.1. Background and motivation..... | 118 |
| 5.2. Experimental Section..... | 122 |
| 5.3.1. Cell setup..... | 122 |
| 5.2.2. Preparation of polysulfides containing electrolyte solutions | 123 |
| 5.2.3. Cyclic voltammetry measurements | 123 |
| 5.3. Theoretical Methodology | 124 |
| 5.3.1. Simulated domain and governing equations | 124 |
| 5.3.2. Computational implementation | 128 |
| 5.4. CVs of dissolved S₈..... | 132 |
| 5.4.1. Determining reaction mechanism for the model | 132 |
| 5.4.2. Impact of scan rate on the characteristics of the CV of S ₈ | 139 |
| 5.5. CV of dissolved Li₂S₈..... | 141 |
| 5.6. CV of dissolved Li₂S₆..... | 144 |
| 5.7. Conclusions | 146 |
| A.5 Appendix: Numerical Schemes | 147 |
| A.5.1. Finite volume method | 147 |

Chapter 5. Cyclic voltammetry model

5.1. Background and motivation

In our discharge model presented in chapter 4, an arbitrary electrolyte was assumed to fill the pores of the cathode and the separator. Therefore, a conventionally used reaction mechanism was considered for our discharge [92,114,127,128,171]. However, hence forth we have used 1 M LiTFSI in TEGDME:DOL as the electrolyte in our experiments. Therefore, in this chapter we have investigated the validity of the conventional reaction involving solid and dissolved sulfur based species in our experimental electrolyte.

The Cyclic voltammetry is an electrochemical potential sweep technique and it has been extensively used to analyse dissolved polysulfides in nonaqueous solvents for several decades [172–178]. Cyclic voltammograms (CVs) of dissolved sulfur (S_8) in nonaqueous organic solvents, have long been known to possess two distinctive reduction peaks sometimes with a small intermediate peak termed prewave in between them which is observed in some electrolytes [172,175,176,179,180]. However, CV of S_8 in 1M LiTFSI in Diox:DME consists only one reduction peak (Fig. 5.1) [62]. While, the number of oxidation peaks vary from one to three based on the solvents used in the electrolyte solutions (Fig. 5.1 and Table 5.1) [62].

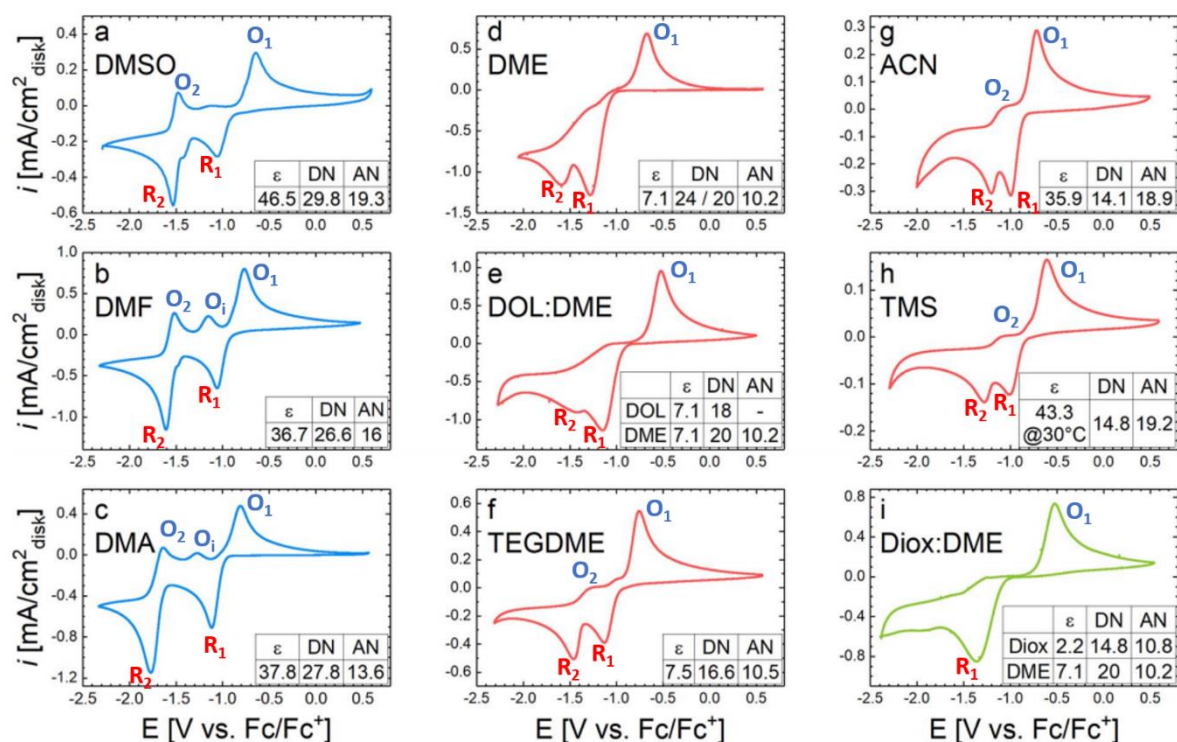


Figure 5.1. CVs recorded at 50 mV.s⁻¹ – of S₈ dissolved in 1 M LiTFSI supporting electrolytes with different solvents namely: (a) DMSO, (b) DMF, (c) DMA, (d) DME, (e) DOL:DME, (f) TEGDME, (g) ACN, (h) TMS and (i) Diox:DME [62].

Due to these significant characteristics variations, CVs of dissolved S₈ in different electrolytes were used to compare the impact of solvent properties such as donor number [178], acceptor number and dielectric constant, on the stabilities and reaction mechanisms of polysulfides [62]. The changes in the characteristics of CVs in different electrolyte can also be correlated to the changes in the galvanostatic curves such as the separation of discharge plateaus, charge/discharge polarization, etc. [62,178]. Furthermore, characteristics variations of CVs with the operation conditions in some individual electrolytes were also used to deduce the reaction mechanisms of S₈ and polysulfides.

Table 5.1. Properties of the solvents in different 1 M LiTFSI supporting electrolyte and visible cyclic voltammetry peaks measure at 50°C [62].

| Solvents | Dielectric constant (ϵ) | Donor No. (DN) | Accept or No. (AN) | Reduction peaks [V] | | Oxidation peaks [V] | | |
|----------|------------------------------------|----------------|--------------------|---------------------|----------------|---------------------|----------------|-------------------------------|
| | | | | R ₁ | R ₂ | O ₂ | O ₁ | O _i (intermediate) |
| DMSO | 46.5 | 29.8 | 19.3 | -1.05 | -1.55 | -1.50 | -0.65 | — |
| DMF | 39.7 | 26.6 | 16 | -1.10 | -1.60 | -1.55 | -0.80 | -1.20 |
| DMA | 37.8 | 27.8 | 13.6 | -1.10 | -1.80 | -1.70 | -0.85 | -1.30 |
| DME | 7.1 | 24/20 | 10.2 | -1.30 | -1.60 | — | -0.70 | — |
| DOL:DME | 7.1 (DOL) | 18 | — | -1.15 | -1.40 | — | -0.60 | — |
| TEGDME | 7.5 | 16.6 | 10.5 | -1.10 | -1.50 | -1.30 | -0.75 | — |
| ACN | 35.9 | 14.1 | 18.9 | -1.00 | -1.20 | -1.10 | -0.70 | — |
| TMS | 43.3 | 14.8 | 19.2 | -1.00 | -1.30 | -1.10 | -0.60 | — |
| Diox:DME | 2.2 (Diox) | 14.8 | 10.8 | -1.40 | — | — | -0.50 | — |
| | 7.1 (DME) | 20 | 10.2 | | | | | |

Yamin *et al.* studied the cyclic voltammetry of different polysulfides dissolved in 1M LiClO₄ in THF, where they compared impact of chain lengths, concentration and scan rate on the peak currents in order to deduce the kinetics and plausible reaction mechanisms [181]. Cyclic voltammetry was also used to quantify the crossover of polysulfides through ion-selective membranes, in order to assess their effectiveness in limiting polysulfide shuttle [109,182].

Few of the previous cyclic voltammetry studies of dissolved S₈ and lithium polysulfides have utilized mathematical models to simulate the experimental CVs and to interpret the underlying reaction mechanisms behind them. Levillain *et al.* and Jung *et al.* have proposed mathematical models to simulate the first reduction and oxidation peaks of S₈ dissolved in Dimethylformamide (DMF), which are based on partially similar reaction mechanisms involving two one-electron electrochemical reactions namely S₈/S₈^{*-} and S₈/S₈²⁻ [179,183]. Gaillard *et al.*, investigated the CV of Li₂S₆ in DMF to identify the reaction mechanism behind

the second reduction peak using Spectro electrochemical measurements and proposed a cyclic voltammetry model which considers S_4^{*-} and S_3^{*-} as the only reducible polysulfides that produce S_4^{2-} and S_3^{2-} respectively, which could then be deoxidized [184]. Gaillard *et al.*, also studied the CV of Li_2S_6 in NH_3 , in which two reductions peaks were observed, one of which increases with the temperature and decreases with the scan rate while the other exhibited the opposite trend [185]. The CV simulations using their proposed reaction mechanism have shown that the former peak corresponds the S_3^{*-}/S_3^{2-} redox reaction, where S_3^{*-} is produced by the dissociation S_6^{2-} at high temperatures, while the latter peak was assigned to the S_6^{2-}/S_6^{3-} redox reaction [185].

It is clear from the above examples, that there are several reported studies devoted to the investigation of the impacts of different electrolytes on the characteristics of CVs of dissolved S_8 . However, the comparative cyclic voltammetry studies of different types of lithium polysulfides and S_8 dissolved in a single electrolyte are very limited. Therefore, this chapter presents a comparative cyclic voltammetry study of different polysulfides solutions such as S_8 , Li_2S_8 and Li_2S_6 dissolved in 1 M LiTFSI in TEGDME:DOL, which is one of the widely used Li-S battery electrolyte. Although DME:DOL is the most widely used electrolyte, TEGDME:DOL is particularly attractive for commercial use due to its safety. DME has a very low flash point [186], therefore the electrolyte becomes highly flammable when it is used [187]. On the contrary, TEGDME has a very high flash point [188], therefore it is much safer to use. A mathematical model is used to simulate and interpret the experimental CVs, using a same set of reaction steps and parameters. The objective of this chapter is to assess the reaction steps between the dissolved polysulfides that correspond to certain characteristics of CVs and their variation with operating conditions such as the dissolved polysulfides speciation and scan rates. Through this procedure, we have attempted to determine reaction mechanism of the dissolved polysulfides in 1 M LiTFSI in TEGDME:DOL.

The contents of this chapter will soon be submitted as a research paper to a peer-reviewed journal. The co-authors for the research paper in preparation are V. Thangavel, A. Mastouri, C. Guéry, M. Morcrette and A. A. Franco.

5.2. Experimental Section

5.3.1. Cell setup

A relatively simple three electrode cell setup was used to carry out cyclic voltammetry measurements of sulfur and polysulfides in 1 M LiTFSI in TEGDME:DOL (1:1) contained in a glass beaker (Fig. 5.2). A glassy carbon electrode with diameter 1.6 mm was used as the working electrode and a Pt grid was used as the counter electrode.[161] It should be known that most of the previously reported cyclic voltammetry studies of dissolved S_8 and polysulfides were carried out using planar working electrode like glassy carbon [62,176,179,189–191], since it is considered to be a well behaved electrode [192]. Furthermore, the porous carbon working electrode was not used in this study – since it introduces complexities such as anisotropic distribution of species concentrations, additional physics and parameters for modelling, etc. which impede the proper understanding of the polysulfides reaction mechanism in the electrolyte. Ag/AgNO₃ electrode was used as the reference electrode, which consists of an Ag wire immersed in a solution containing 10 mM of AgNO₃ and 0.1 M of TBAP in acetonitrile contained in a glass tube fitted with a frit at its extremity. Since the reference and working electrolytes are different in our experiment, a liquid junction potential difference (LJP) could exist between them. However, this LJP and the overall potential of our Ag/AgNO₃ reference electrode could be assumed to remain stable, since the frit restricts the diffusion of species across it and prevents leakage of reference electrolyte into the experimental one.

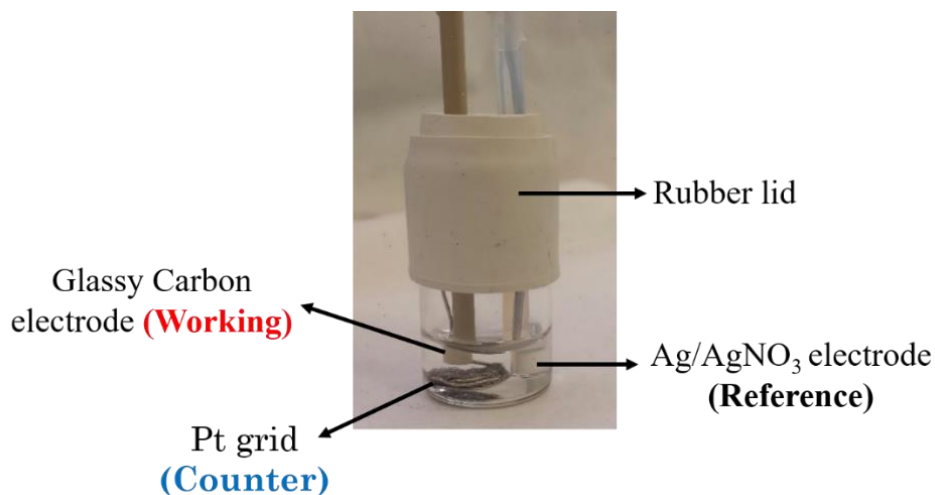


Figure 5.2. Three electrode cell setup used in this comparative cyclic voltammetry study.

5.2.2. Preparation of polysulfides containing electrolyte solutions

S₈ was dissolved in the electrolyte to a concentration of 6 mM, which is measured to be its solubility. In practical Li-S batteries, polysulfides can reach high concentrations, however the solubility of different polysulfides in 1 M LiTFSI in TEGDME:DOL are not known experimentally. Since the objective of this chapter is to understand the reaction mechanism of dissolved polysulfides in the electrolyte, the use of high polysulfides concentrations was avoided – to prevent precipitation reactions. Therefore, the polysulfides containing solutions were prepared by stirring stoichiometric quantities of Li₂S and S₈ amounting to a standard concentration of 50 mM of Li₂S_x in 5 ml of 1 M LiTFSI in TEGDME:DIOX (1:1) [161]. The preparation was carried out inside the glove box under Ar atmosphere for 5 days with temperature maintained between 25-27 °C. Followed by 3 days of decantation process, 1.5 mL of the resulting solutions were extracted and used for the cyclic voltammetry measurements.

5.2.3. Cyclic voltammetry measurements

The entire cell setup was assembled inside a glove box under Ar atmosphere and sealed using a rubber lid. Cyclic voltammetry measurements were done outside the glove box using Biologic VMP3 with the temperature maintained at 25°C. The potential between the working and reference electrodes was swiped, starting from and ending at an open circuit potential

(OCV) after reaching a minimum value during the scan towards negative direction and a maximum value for the scan towards positive direction, thereby constituting a cycle.

5.3. Theoretical Methodology

5.3.1. Simulated domain and governing equations

Since, the redox reactions in the experiment occur at the working electrode/electrolyte interface, the simulation domain consists only the diffusion layer (DL) at the vicinity of the working electrode (Fig. 5.3) whose thickness is given by [193],

$$\delta_{DL} = 6\sqrt{D_{max}t_{max}} \quad (5.1)$$

where D_{max} is the diffusion coefficient of the species which has the fastest diffusivity (Table 5.1) and t_{max} is the total duration of the experimental cyclic voltammetry measurement.

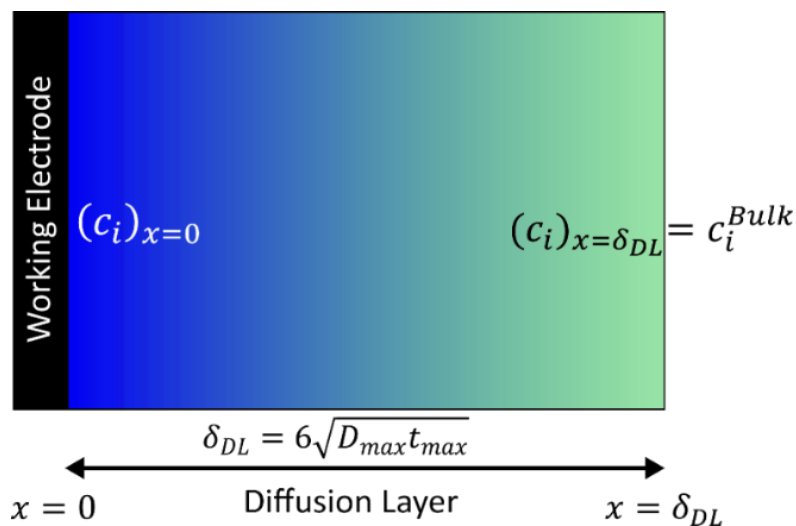


Figure 5.3. Schematic representation of the simulated domain.

Since the working glassy carbon electrode is flat and planar, the diffusion fields of different species in the DL will have points that are equivalent at a given distance (x) from the electrode surface [193]. Therefore, the net flux of species will occur perpendicular to the electrode surface along the thickness of the DL and the distribution of a species (i) concentration can be suitably described by a one-dimensional mass conservation equation, as follows

$$\frac{\partial c_i}{\partial t} = \frac{\partial}{\partial x} \left(D_i \frac{\partial c_i}{\partial x} \right) - s_i - G_i \quad (5.2)$$

Where c_i and D_i are the concentration and diffusion coefficient of species i , while s_i and G_i respectively are its sink/source terms, brought about by some homogeneous chemical and heterogeneous dissolution/precipitation reactions.

$$s_i = \sum_j \vartheta_{ij} k_j^f \left(\prod_i ((c_i)^{\vartheta_{ij}})_{\vartheta_{ij}>0} - K_j^{eq} \prod_i ((c_i)^{-\vartheta_{ij}})_{\vartheta_{ij}<0} \right) \quad (5.3)$$

In the equation above, ϑ_{ij} is the stoichiometric coefficient for the species i involved in the homogenous chemical reaction j (Eq. 5.23 or 5.25). k_j^f and k_j^r are forward and reverse kinetic constants. K_j^{eq} is the equilibrium constant of the chemical reaction j , which is given by

$$K_j^{eq} = \frac{k_j^r}{k_j^f} \quad (5.4)$$

The bulk concentrations of all the species (c_i^*) are assumed to remain constant and the concentrations of species at the boundary $x = \delta_{DL}$ are equal to those of the bulk (Eq. 5.5).

$$(c_i)_{x=\delta_{DL}} = c_i^* \quad (5.5)$$

while the flux of a species (N_i) at the electrode surface ($x = 0$) is given by the Faraday's law

$$(N_i)_{x=0} = \left(D_i \frac{\partial c_i}{\partial x} \right)_{x=0} = \frac{A}{A^0} \sum_j \frac{S_{ij} i_j}{n_j F} \quad (5.6)$$

In the equation above, A and A^0 are in electro-active and geometrical surface area, respectively of the working electrode. S_{ij} , n_j and i_j are respectively the stoichiometric coefficient of the species i (See Appendix - Eq. A-5.15), number of electrons and current density of an electrochemical reaction j of form,

$$\sum_i S_{ij} M_i^{z_i} = n_j e^- \quad (5.7)$$

Where $M_i^{z_i}$ and e^- respectively are the symbols that represent a species i and an electron. z_i is the charge of the species i .

The current density of an individual electrochemical reaction is given by the Butler Volmer equation,

$$i_j = i_j^0 \left(\prod_i \left((c_i)_{x=0}^{S_{ij}} \right)_{S_{ij}>0} e^{\left(\frac{(1-\alpha_j)n_j F(E-U_j^0)}{RT} \right)} - \prod_i \left((c_i)_{x=0}^{-S_{ij}} \right)_{S_{ij}<0} e^{\left(\frac{-\alpha_j n_j F(E-U_j^0)}{RT} \right)} \right) \quad (5.8)$$

where, U_j^0 and i_j^0 respectively are the standard potential and exchange current density of an electrochemical reaction j and E is the working electrode potential.

The total electrode current (I_t) is calculated as follows,

$$I_t = A \sum_j i_j \quad (5.9)$$

where A is the active surface area of the working electrode, which is the product of the volume of the finite volume bin closest to the electrode ($V_{x=0}^{bin}$) and the active specific surface area (a),

$$A = aV_{x=0}^{bin} \quad (5.10)$$

Finally, G_i is the source/sink term related to the heterogeneous dissolution/precipitation of sulfur based solid species over the electrode [92].

$$G_i = \sum_k \gamma_{ik} k_k^{prec} \epsilon_k ((c_i)^{\gamma_{ik}} - K_k^{sp}) \quad (5.11)$$

It should be noted that the G_i is zero in the finite volume bins which are not closest to the electrode surface. In the equation above, γ_{ik} is the stoichiometric coefficient of the species i involved in the dissolution/precipitation of the sulfur based solid species k (See Appendix - Eq. A-5.17). K_k^{sp} and ϵ_k respectively are solubility product and the volume fraction of the sulfur based solid species. k_k^{prec} rate constant of precipitation/dissolution reaction k .

$$\frac{d\epsilon_k}{dt} = V_k \epsilon_k k_k^{prec} ((c_i)^{\gamma_{ij}} - K_k^{sp}) \quad (5.12)$$

V_k is the molar volume of the sulfur based solid species. Since sulfur based solid species such as $S_{8(s)}$ and $Li_2S_{(s)}$ are insulating, their precipitation over the surface of the working electrode reduces the active surface (a) due to surface passivation.

$$a = a^0 \Theta(\delta) \quad (5.13)$$

where a^0 and $\Theta(\delta)$ are the initial specific surface area of the electrode and the electron tunnelling probability function [119],

$$\Theta(\delta) = \frac{1 - \operatorname{erf}\left(\frac{\delta - \delta_{tun}}{L_{tun}}\right)}{2} \quad (5.14)$$

In Eq. 5.14, δ_{tun} and L_{tun} respectively are threshold thickness at halved electron tunnelling and scaling factor. δ is the total thickness of sulfur based solid deposits on the working electrode,

$$\delta = \frac{\sum_k \epsilon_k}{a^{max}} \quad (5.15)$$

5.3.2. Computational implementation

The model was implemented in the MATLAB software and the coupled partial differential equations were solved spatially using the Finite Volume Method and temporally using the Crank-Nicholson method (see Appendix – A3). As mentioned in the introduction, only a single set of parameter values were used for all the simulations (Table 5.1). The CV characteristics are very sensitive to kinetic and diffusion parameters, however well-defined experimental values are not available for parameters such as exchange current densities, charge transfer coefficients of different polysulfides reactions in 1 M LiTFSI in TEGDME:DOL, etc. Therefore,

the initial values of these parameters were determined using an automatized MATLAB program which matches the simulated first reduction curves of different polysulfides with their corresponding experimental results using a Nonlinear least-squares solver called lsqnonlin. Only two or three parameters whose initial values were determined after each run of this automatized MATLAB program. These initial values of parameters were further adjusted until we were able to match all the simulated results as close as possible with the experimental ones. The parameters chosen for the cyclic voltammetry model are given in Table 5.1.

Table 5.1. Parameters of different reactions (Eq. 5.16-5.27) and diffusion coefficients of dissolved species considered in the cyclic voltammetry model.

| i. Electrochemical reaction parameters | | | | | | iv. Dissolved species parameters | |
|--|---|---------|--|---|--------------------|----------------------------------|-------------------------------|
| React. No. (<i>j</i>) | Reaction | Eq. No. | i^0 (A) | U^0 (V) | α | Species $M_i^{z_i}$ | D_i (m.s ⁻¹) |
| 1 | S_8/S_8^{2-} | (5.17) | 0.150 ^a | -0.8281 ^a | 0.460 ^c | | |
| 2 | S_8^{2-}/S_6^{2-} | (5.18) | 3×10 ^{-3a} | -0.8681 ^a | 0.500 ^b | S_8 | 1.6335×10 ^{-10a} |
| 3 | S_6^{2-}/S_4^{2-} | (5.19) | 3×10 ^{-4a} | -0.9400 ^a | 0.420 ^a | | |
| 4 | S_4^{*-}/S_4^{2-} | (5.24) | 2×10 ^{-4a} | -0.9400 ^a | 0.500 ^d | S_6^{2-} | 8.0000×10 ^{-11b} |
| 5 | S_4^{2-}/S_2^{2-} | (5.20) | 2.96×10 ^{-6a} | -1.0544 ^a | 0.200 ^a | | |
| 6 | S_3^{*-}/S_3^{2-} | (5.26) | 7.4×10 ^{-2a} | -1.1644 ^a | 0.420 ^a | S_4^{2-} | 3.5000×10 ^{-11f} |
| 7 | S_3^{2-}/S_2^{2-} | (5.27) | 1.48×10 ^{-7a} | -1.2044 ^a | 0.350 ^a | | |
| 8 | S_2^{2-}/S^{2-} | (5.21) | 3×10 ^{-9a} | -1.4000 ^a | 0.658 ^a | S_3^{*-} | 3.5000×10 ^{-11f} |
| Reaction No. (<i>j</i>) | Reaction | Eq. No. | k_j^f (s ⁻¹) | k_j^{eq} (mol ⁻¹) | S_3^{2-} | | 3.5000×10 ^{-11f} |
| 1 | $S_8^{2-} \rightleftharpoons 2S_4^{*-}$ | (5.23) | 8.4 ^a | 4.2088 ^a | S_2^{2-} | | 3.5000×10 ^{-11f} |
| 2 | $S_6^{2-} \rightleftharpoons 2S_3^{*-}$ | (5.25) | 9.5 ^a | 12.6263 ^a | S^{2-} | | 3.5000×10 ^{-11f} |
| iii. Heterogeneous precipitation/dissolution reaction parameters | | | | | | | |
| Reaction No. (<i>k</i>) | Reaction | Eq. No. | k_k^{prec} (mol ² .m ⁻⁶ .s ⁻¹) | K_k^{sp} (mol ³ .m ⁻⁹) | Solid species | V_k (m ⁻³ .mol) | |
| 1 | $S_8^{2-} \rightleftharpoons S_{8(s)}$ | (5.16) | 5 (s ⁻¹) ^e | 6 (mol.m ⁻³) ^m | $S_{8(s)}$ | 1.239×10 ^{-4b} | |
| 2 | $2Li^+ + S^{2-} \rightleftharpoons Li_2S_{(s)}$ | (5.22) | 5 ×10 ^{-7b} | 10 ^b | $Li_2S_{(s)}$ | 2.768×10 ^{-4b} | |

^aFitted parameters.^{b, c, d and e}Assumed parameters taken from Refs. [119], [179], [184] and [114] respectively.^fExperimental parameters taken from Ref. [194].^mMeasured parameter.

The concentration of the species in the diffusion layer are determined explicitly by solving a set of non-linear equations using Newton-Raphson method. If the initial concentrations of the dissolved species are zero, the solution of the non-linear equations will be infinity. Therefore, in our model we assume trace values for the concentrations of polysulfides which should not be present in the experimental electrolyte solution (Table A-5.1).

Table A-5.1. Initial concentrations of dissolved polysulfides and volume fractions of solid species.

| i. Initial concentrations of dissolved species (mM) | | | | |
|--|---------------------|-------------------------|-----------------------------|-----------------------------|
| Species No. (<i>i</i>) | Species $M_i^{z_i}$ | In 6 mM S_8 solution | In 50 mM Li_2S_8 solution | In 50 mM Li_2S_6 solution |
| 1 | Li^+ | 1000 ^c | 1100 ^c | 1100 ^c |
| 2 | S_8 | 6 ^e | 1×10^{-3a} | 6×10^{-5a} |
| 3 | S_8^{2-} | 1.78×10^{-7a} | 50 ^e | 1.78×10^{-6a} |
| 4 | S_6^{2-} | 5.0×10^{-7a} | 5.0×10^{-5a} | 50 ^e |
| 5 | S_4^{*-} | 2.015×10^{-8a} | 2.015×10^{-8a} | 2.015×10^{-8a} |
| 6 | S_4^{2-} | 2.015×10^{-8a} | 2.015×10^{-8a} | 2.015×10^{-8a} |
| 7 | S_3^{*-} | 1.990×10^{-8a} | 1.990×10^{-8a} | 1.990×10^{-6a} |
| 8 | S_3^{2-} | 1×10^{-7a} | 1×10^{-6a} | 1×10^{-7a} |
| 9 | S_2^{2-} | 5.2×10^{-7a} | 5.2×10^{-7a} | 5.2×10^{-7a} |
| 10 | S^{2-} | 8.2×10^{-7a} | 8.2×10^{-10a} | 8.2×10^{-7a} |
| ii. Initial solid species volume fractions (no units) | | | | |
| Species No. (<i>k</i>) | Solid species | In 6 mM S_8 solution | In 50 mM Li_2S_8 solution | In 50 mM Li_2S_6 solution |
| 1 | $S_{8(s)}$ | 1×10^{-10a} | 1×10^{-10a} | 1×10^{-10a} |
| 2 | $Li_2S_{(s)}$ | 1×10^{-7b} | 1×10^{-7b} | 1×10^{-7b} |

^aAssumed parameters.

^bAssumed Parameters taken from Ref. [114].

^cCalculated parameters based on charge conservation.

^eExperimental parameters.

5.4. CVs of dissolved S_8

5.4.1. Determining reaction mechanism for the model

The experimental CV of 6 mM S_8 in 1 M LiTFSI in TEGDME:DOL recorded at $5 \text{ mV}\cdot\text{s}^{-1}$, consists of two reduction (R_1 and R_2) and two oxidation (O_1 and O_2) peaks (Fig. 5.3). Initially, the simulation of the CV of dissolved S_8 at $5 \text{ mV}\cdot\text{s}^{-1}$ (Fig. 5.3), was done using the following set of reaction steps (Eq. 5.16-5.22) which is conventionally used in continuum Li-S batteries models [92,114,127,128,171],



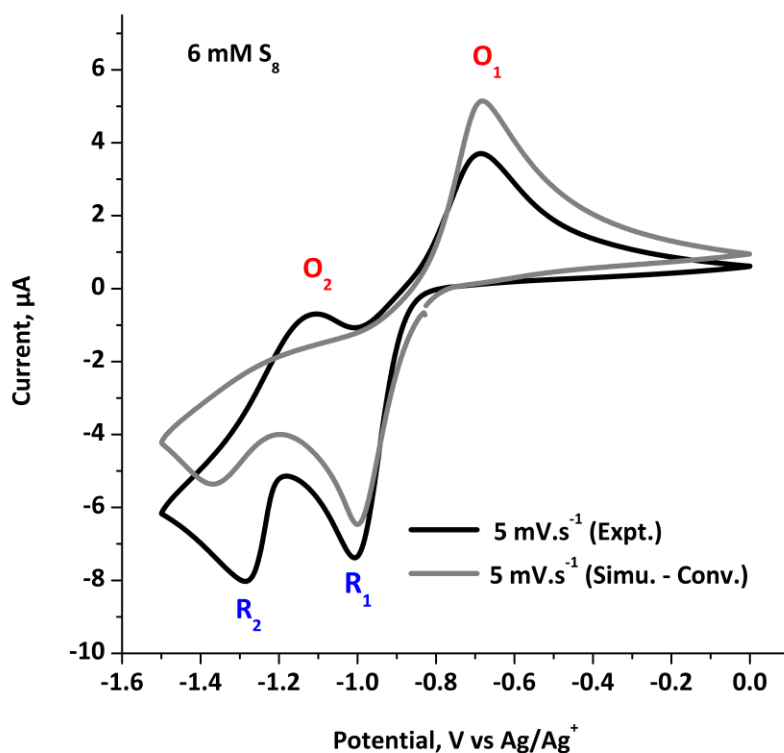


Figure 5.4. Experimental CV (Expt.) of 6 mM of S_8 in 1 M LiTFSI in TEGDME:DOL measured at $5 \text{ mV}\cdot\text{s}^{-1}$ and the corresponding simulated CV (Simu.-Conv.) produced using the conventional reaction mechanism of Li-S batteries models (Eq. 5.16 to 5.22).

The initial simulated CV of S_8 (Fig. 5.4), produced using the conventional reaction mechanism consists of two reduction peaks R_1 and R_2 and one oxidation peak O_1 . However, the oxidation peak O_2 is absent in it (Fig. 5.4). Furthermore, the experimental peak intensity of O_2 does not increase with the scan rate as much as the intensities of other peaks namely R_1 , R_2 and O_1 (Fig. 5.5). This suggests that the underlying reaction mechanism behind O_2 should implicate some electrochemical reactions which are coupled to other chemical reactions. Therefore, these aforementioned characteristics trends of O_2 cannot be reproduced by the cyclic voltammetry model using only the reaction steps (Eq. 5.16 to 5.22) considered in the conventional reaction mechanism. This conclusion was also arrived after an extensive parameter analysis.

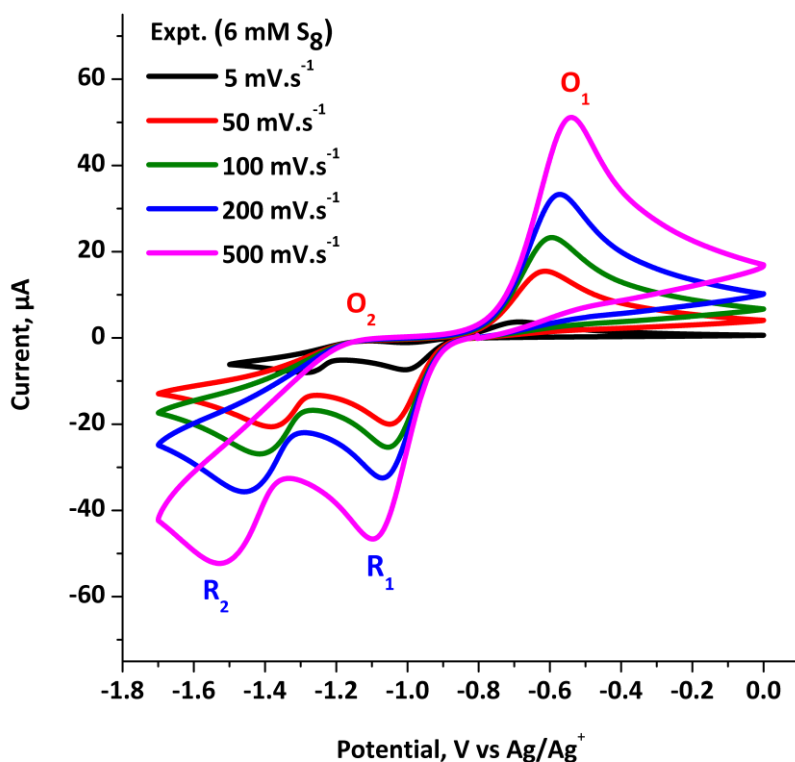


Figure 5.5. Experimental CVs (Expt.) of 6 mM of S_8 in 1 M LiTFSI in TEGDME:DOL recorded with different scan rates.

Various studies in the literature involving the spectroscopic analysis of dissolved polysulfides in the electrolyte, have shown that the stability of the polysulfide ions and radicals primarily depend on the properties of the solvents such as the donor numbers and dielectric constants [61,195]. More specifically, in-situ and operando Raman spectroscopy studies have proven that the polysulfide radicals such as S_4^{*-} and S_3^{*-} are stable in LiTFSI in TEGDME:DOL [106,196]. Therefore, the assumed reaction mechanism of the cyclic voltammetry model was replaced with a comprehensive set of reaction steps (Eq. 5.16 to 5.27) which include the following chemical and electrochemical reactions of $S_{4(l)}^{*-}$ and $S_{3(l)}^{*-}$,





Eqs. 5.23 to 5.26 have been proposed in a previously reported cyclic voltammetry model which was used to simulate the CVs of dissolved Li_2S_6 in DMF [184]. Whereas $S_{3(l)}^{2-}/S_{2(l)}^{2-}$ redox reaction was proposed by Barschasz *et al.* [60].

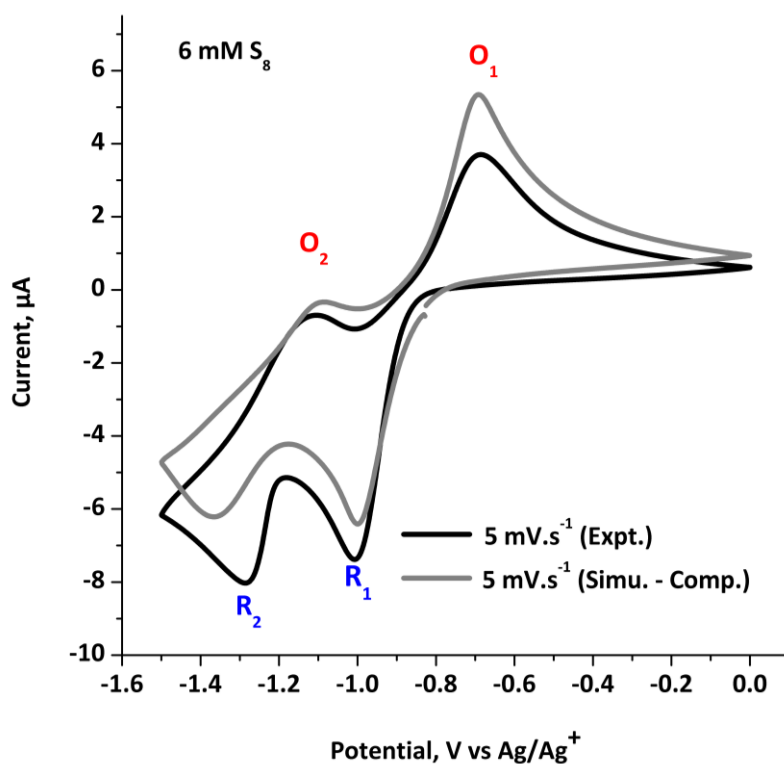


Figure 5.6. Experimental CV (Expt.) of 6 mM of S_8 in 1 M LiTFSI in TEGDME:DOL measured at $5 \text{ mV}\cdot\text{s}^{-1}$ and the corresponding simulated CV (Simu.-Comp.) – producing using the comprehensive mechanism (Eq. 5.16 to 5.27).

The simulated CV of S_8 with $5 \text{ mV}\cdot\text{s}^{-1}$ produced using the comprehensive reaction mechanism (Eq. 5.16 to 5.27) – closely resembles the experimental one, where the O_2 peak has been reproduced (Fig. 5.6).

The underlying reaction steps behind the cyclic voltammetry peaks could be assessed from the evolutions of simulated individual redox reaction currents and polysulfides concentrations at the electrode surface.

Since the individual current peaks of S_8/S_8^{2-} and S_8^{2-}/S_6^{2-} electrochemical reactions, are around -1.0 V and -1.1 V respectively, they are the underlying dominant reactions behind the reduction peak R_1 (Fig. 5.7a). This can also be understood from the concentration evolutions of both S_8 and S_8^{2-} (Fig. 5.7b), since they decrease significantly beyond -1.0 V . Similarly, the S_6^{2-}/S_4^{2-} , S_4^{*-}/S_4^{2-} and S_3^{*-}/S_3^{2-} redox reactions constitute the dominant basis for the reduction peak R_2 (Fig. 5.7a). Where S_3^{*-} and S_4^{*-} respectively are produced through the dissociations of S_6^{2-} and S_8^{2-} ions. This is evident from the increase of S_3^{*-} and S_4^{*-} concentrations with those of S_6^{2-} and S_8^{2-} respectively between -0.82 to -1.0 V (Fig. 5.7b). The S_2^{2-} concentration increases throughout the reduction scan (Fig. 5.7b) due the S_4^{2-}/S_2^{2-} and S_3^{2-}/S_2^{2-} redox reactions. However, the S_2^{2-}/S^{2-} redox reaction remain dormant during the CV, since the S^{2-} concentration does not change in any significant way (Figs. 5.7b, 5.8a and b).

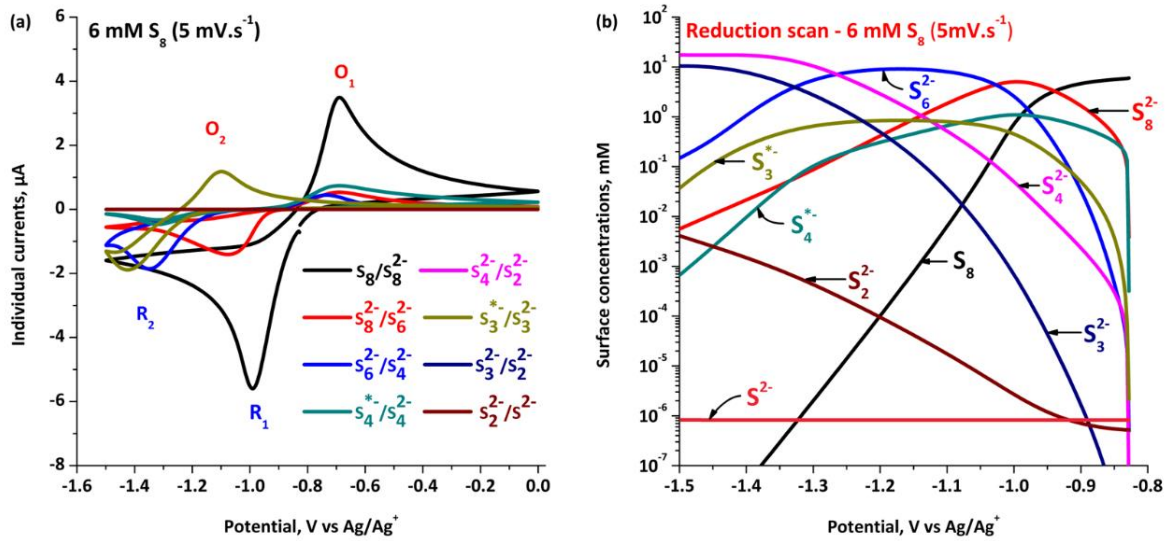


Figure 5.7. Simulated (a) individual currents of redox reactions and (b) species concentrations at the electrode surface ($(c_i)_{x=0}$) during reduction potential scans at a rate of $5 \text{ mV}\cdot\text{s}^{-1}$, for the $6 \text{ mM } S_8$ solution.

After reversing the potential scanning direction and during the period leading up to the oxidation peak O_2 (-1.5 to -1.15 V) – the concentrations of S_2^{2-} and S_4^{2-} decrease (Fig. 5.8a) due to their oxidation which produce S_3^{2-} and S_6^{2-} respectively. These reactions are the reasons behind the observed increase in S_6^{2-} concentration. Whereas, the increase of S_3^{*-} concentration is due to the oxidation of S_3^{2-} – which is evident from the S_3^{*-}/S_3^{2-} current peak at -1.15 V (Fig. 5.7a). At this potential (-1.15 V) – S_3^{*-} concentration start to decrease significantly (Fig. 5.8a). During the potential window between -1.5 to -0.9 V , the concentrations of S_8^{2-} and S_4^{*-} increase (Fig. 5.8a) due to the oxidation of S_6^{2-} and simultaneous dissociation S_8^{2-} .

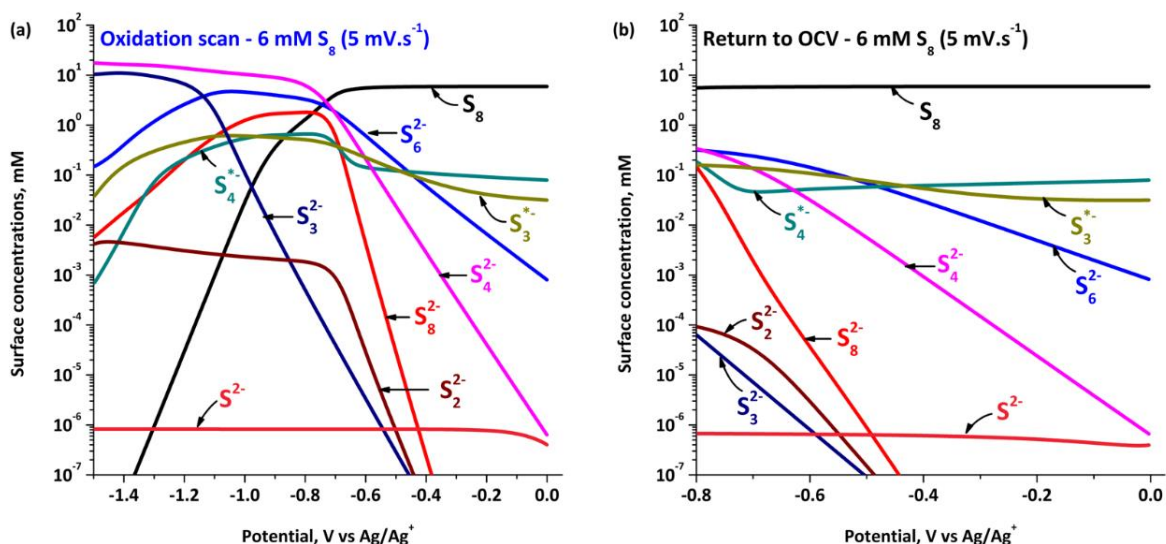


Figure 5.8. Species concentrations at the electrode surface ($(c_i)_{x=0}$) during (a) oxidation and (b) return to OCV potential scans at a rate of $5 \text{ mV}\cdot\text{s}^{-1}$, for the 6 mM S_8 solution.

Beyond -0.9 V , concentrations of all the polysulfides ions and radicals decrease, while the S_8 concentration increases (Fig. 5.8a). This indicates that all the polysulfides simultaneously undergo oxidation – to produce S_8 . This is also evident from the individual current peaks of $\text{S}_4^{*-}/\text{S}_4^{2-}$, $\text{S}_6^{2-}/\text{S}_4^{2-}$, $\text{S}_8^{2-}/\text{S}_6^{2-}$ and $\text{S}_8/\text{S}_8^{2-}$ redox reactions around -0.6 V (Fig. 5.7a), which form the basis for the oxidation peak O_1 (Fig. 5.6).

In summary, oxidations of S_2^{2-} , S_3^{2-} and S_4^{2-} ions occur during O_2 , whereas S_4^{*-} , S_6^{2-} and S_8^{2-} in addition to all the aforementioned polysulfides undergo oxidation during O_1 . After switching the potential scanning direction once again, reduction of S_8 takes place which is evident from the decrease in their concentration and increase in the concentrations of all the other polysulfides (Fig. 5.8b).

Throughout the reduction and oxidation scans of the cyclic voltammetry simulation, the Li^+ concentration and volume fractions of $\text{S}_{8(s)}$ and $\text{Li}_2\text{S}_{(s)}$ at the electrode surface do not change in any significant way (Fig. 5.9). This suggests that the depositions of $\text{S}_{8(s)}$ and $\text{Li}_2\text{S}_{(s)}$ over the working electrode surface are negligible.

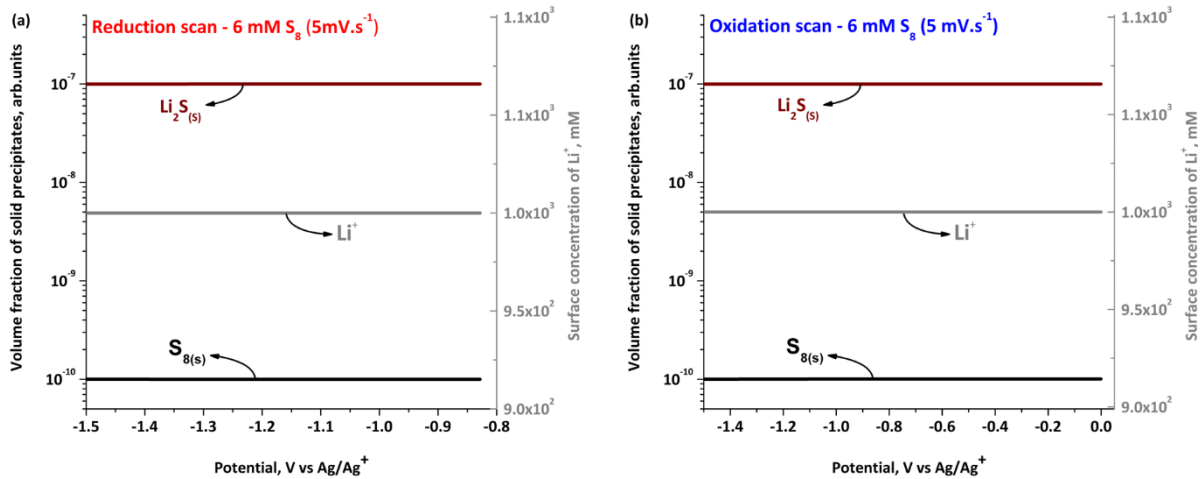


Figure 5.9. Simulated evolutions of Li^+ concentration and volume fractions of $\text{S}_{8(s)}$ and $\text{Li}_2\text{S}_{(s)}$ at the electrode surface ($x = 0$) during (a) reduction and (b) oxidations potential scans at a rate of $5 \text{ mV}\cdot\text{s}^{-1}$, for the 6 mM S_8 solution.

5.4.2. Impact of scan rate on the characteristics of the CV of S_8

Similar to those of the experimental CVs of S_8 (Fig. 5.5), the intensities of R_1 , R_2 and O_1 of the simulated CVs – increase with the scan rate (Fig. 5.10). However, the intensities of O_2 of the simulated CVs do not increase with the scan rate (Fig. 5.10), which is also a trend observed in the experiment results (Fig. 5.5).

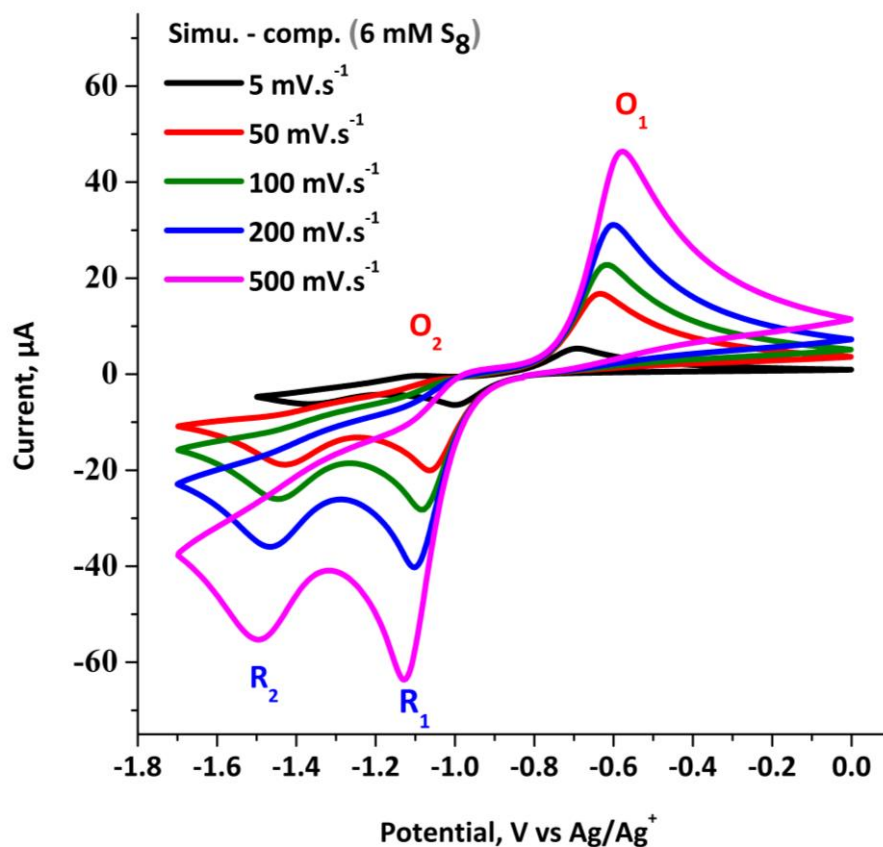


Figure 5.10. Simulated CVs (Simu.-Comp.) of 6 mM of S_8 in 1 M LiTFSI in TEGDME:DOL with different scan rates – produced using the comprehensive reaction mechanism (Eq. 5.16 to 5.27).

It is important to note that the visibility of O_2 around -1.15 V in the simulated CV of S_8 produced at 5 mV.s^{-1} (Fig. 5.6), is primarily due to the intense peak of S_3^*/S_3^{2-} reaction current at that potential (Fig. 5.7a). Since the intensity of S_3^*/S_3^{2-} current peak is kinetically controlled by the dissociation of S_6^{2-} , it does not increase when the potential scan rate is increased (Fig. 5.11), therefore the peak O_2 becomes visibly indistinctive during fast scan rates (Fig. 5.10).

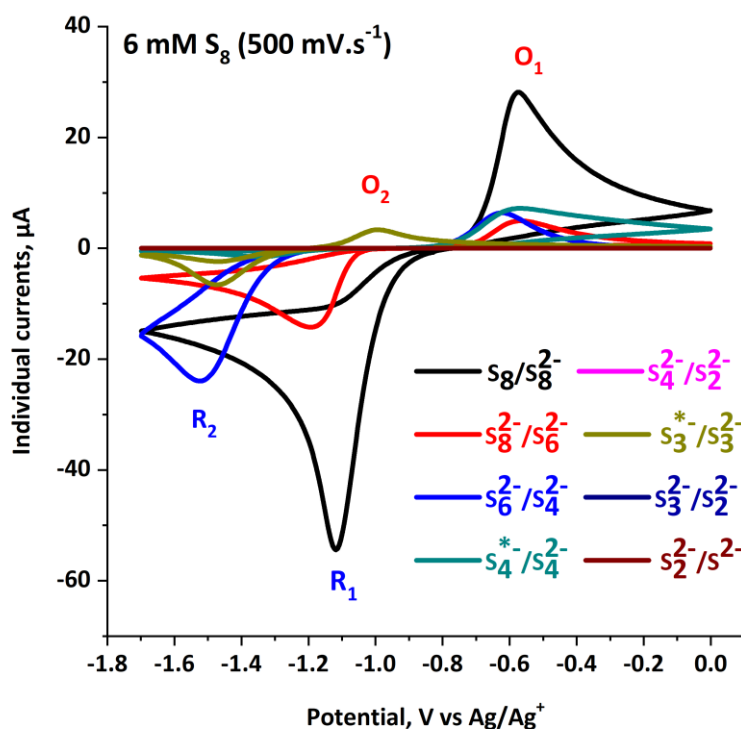


Figure 5.11. Simulated individual currents of redox reactions corresponding CV of 6 mM S_8 solution (potential scan rate of $500 \text{ mV}\cdot\text{s}^{-1}$).

5.5. CV of dissolved Li_2S_8

In order to simulate the CVs of Li_2S_8 – the initial concentration of S_8^{2-} was set to 50 mM (Table 5.2). Furthermore, the characteristics of the simulated CVs (Fig. 5.12b) – qualitatively resemble the experimental ones (Fig. 5.12a). This suggests that the characteristics of the CV primarily depend on the type of the polysulfide species present in the solution.

In general, the intensities of all the distinctive peaks (R_1 , R_2 and O_1) in the CVs of Li_2S_8 are higher (Fig. 5.12a) than those of S_8 (Fig. 5.5 and 5.10). This is due to the increase of polysulfides concentrations in the Li_2S_8 solution. Furthermore, the characteristics of the first CV of Li_2S_8 – are also different from those of S_8 , since the intensity of its reduction peak R_1 is significantly lower than that of the R_2 (Fig. 5.12a and b). The O_2 peak is not visible in the CV of dissolved Li_2S_8 , due to the fast scan rate of $100 \text{ mV}\cdot\text{s}^{-1}$.

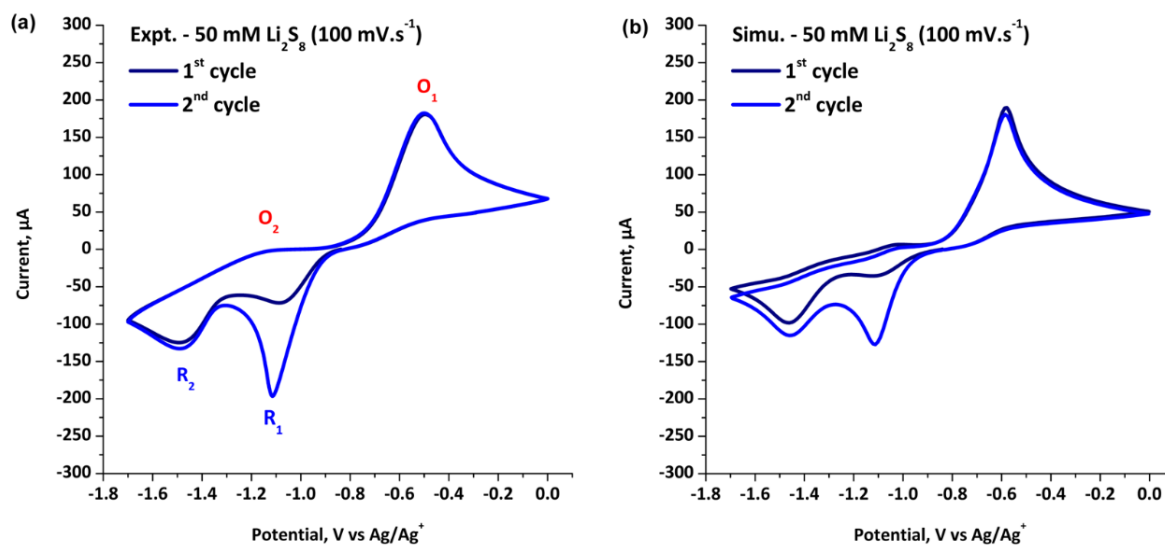


Figure 5.12. (a) Experimental and (b) simulated CV of 50 mM Li₂S₈ solution for a potential scan rate of 100 mV.s⁻¹.

Due to the absence of S₈ in 50 mM Li₂S₈ solution, the S₈/S₈²⁻ reaction current does not produce an intense peak during the first reduction scan (Fig. 5.14a). Whereas, the S₈²⁻/S₆²⁻ reaction current peaks around -1.10 V (Fig. 5.14a). The absence of intense peak of the S₈/S₈²⁻ reaction current around -1.10 V (Fig. 5.14a) – is the reason why the intensity of R₁ is relatively lower during the first reduction scan (Figs. 5.12a and b). Furthermore, S₆²⁻/S₄²⁻, S₃^{*-}/S₃²⁻ and S₄^{*-}/S₄²⁻ redox reaction currents form peaks around -1.5 V (Fig. 5.14) and they form the underlying basis for R₂ (Figs. 5.12a and b). These reactions result in the increase of S₄²⁻ and S₃²⁻ concentrations (Fig. 5.13a). Moreover, the S₂²⁻ concentration also increases due to the simultaneous reduction of S₄²⁻ (Fig. 5.13a). Similar to the dissolved S₈, the O₂ peak is less intense for the scan rate of 100 mV.s⁻¹ (Figs. 5.12), which due to the kinetic limitation of the S₆²⁻ dissociation to S₃^{*-} during fast scanning.

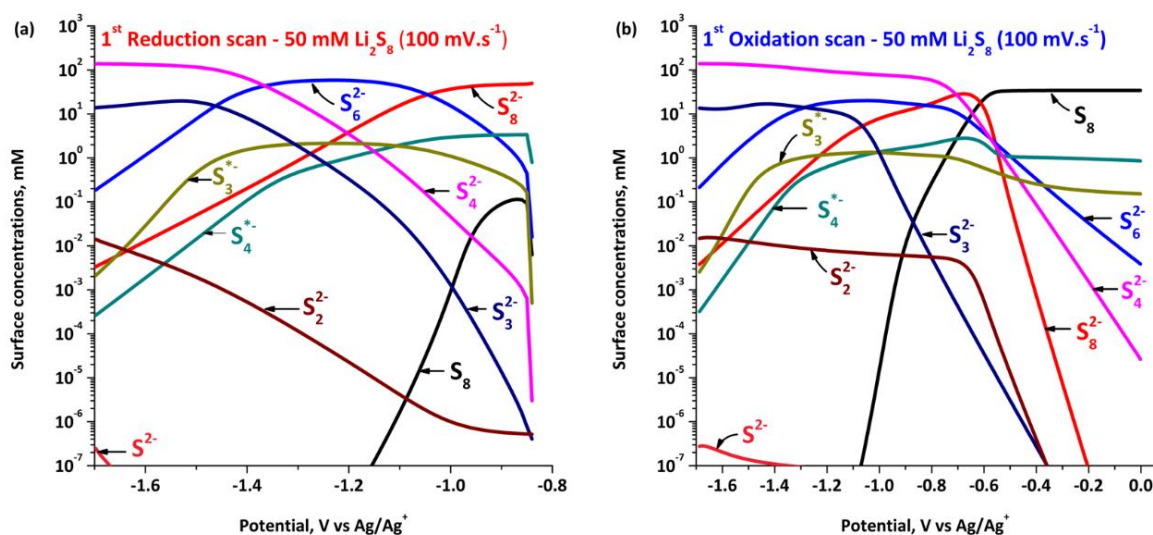


Figure 5.13. Simulated concentration evolutions of species at the electrode surface during, the first (a) reduction and (b) oxidation scans of 50 mM Li₂S₈ solution, with a scan rate of 100 mV.s⁻¹.

During the first oxidation scan after the reduction concentrations of S₂²⁻ and S₃²⁻ decrease due to their oxidations between -1.70 to -1.10 V (Fig. 5.13b). Furthermore, the S₃⁺/S₃²⁻ reaction current form an intense peak around -1.10 V (Fig. 5.14a), which is when the concentration of S₃²⁻ starts to decrease significantly due its oxidation (Fig. 5.13b). Whereas, S₄²⁻, S₆²⁻, S₈²⁻, etc. simultaneously undergo oxidations around -0.6 V – to produce S₈. Due to these reactions the concentrations of these polysulfides decrease significantly around -0.6 V, while that of the S₈ increases (Fig. 5.13b). This can also be understood from the positive peaks of S₄⁺/S₄²⁻, S₆²⁻/S₄²⁻, S₈²⁻/S₆²⁻ and S₈/S₈²⁻ reaction currents around -0.6 V (Fig. 5.14a), which form the underlying basis for O₁ (Figs. 5.12a and b). Due to the aforementioned reactions, S₈ becomes the most concentrated species near the electrode surface instead of S₈²⁻ at the end of the first oxidation scan (Fig. 5.13b).

Therefore, during the second reduction scan – both S₈/S₈²⁻ and S₈²⁻/S₆²⁻ reaction currents form peaks around -1.10 V (Fig. 5.14b). This is why the intensity of R₁ increases during the second reduction scan (Figs. 5.12a and b). However, the rest of the CV characteristics of the second cycle are similar to those of the first cycle.

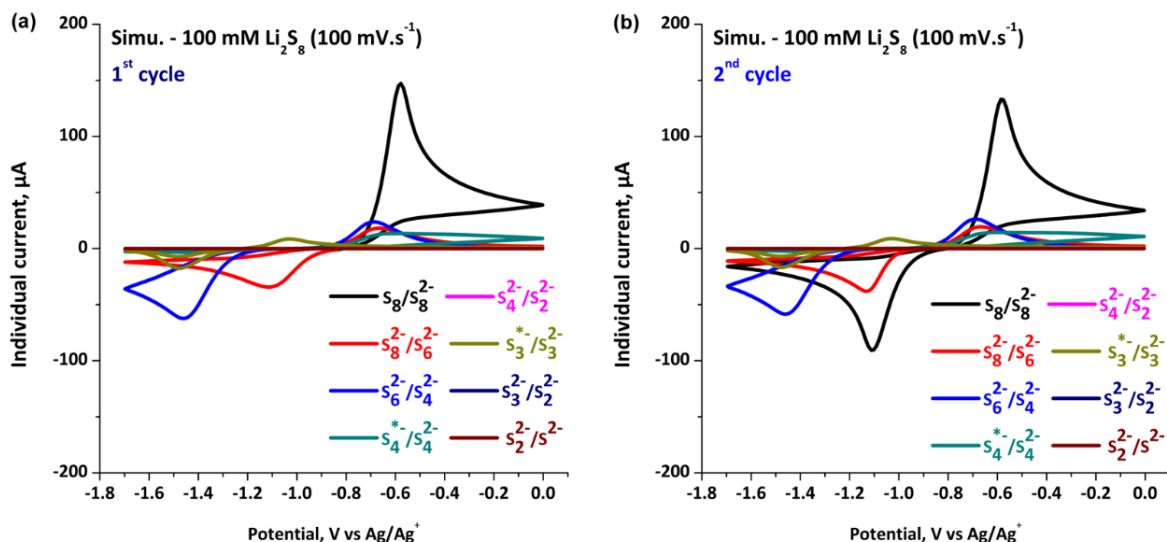


Figure 5.14. Simulated individual currents for electrochemical reactions during the (a) first and (b) second CV cycles 50 mM Li_2S_8 solution, with a scan rate of $100 \text{ mV}\cdot\text{s}^{-1}$.

5.6. CV of dissolved Li_2S_6

Similar to the case of the Li_2S_8 solution, the initial S_6^{2-} concentration in our model was set to 50 mM in order to simulate the CV of Li_2S_6 solution. The simulated CV once again closely resemble the experimental ones (Figs. 5.15a and b). However, the characteristics of the first CV of Li_2S_6 solution are different from those of the S_8 (Figs. 5.5 and 5.10) and Li_2S_8 (Figs. 5.12a and b), since only the R_2 peak is visible during the reduction scan. This again shows that the characteristics of the CV primarily depend on the type of polysulfide species in the solution.

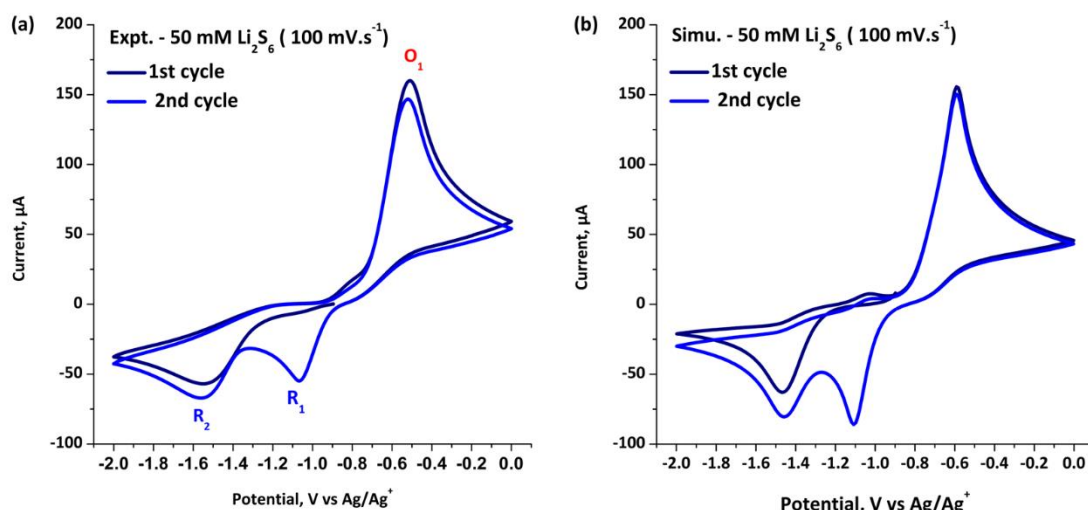


Figure 5.15. (a) Experimental and (b) simulated CVs of 50 mM Li_2S_6 solution produced using potential scan rate $100 \text{ mV}\cdot\text{s}^{-1}$.

Since the initial concentrations of both S_8 and S_8^{2-} are very low in the Li_2S_6 solution, the individual currents of $\text{S}_8/\text{S}_8^{2-}$ and $\text{S}_8^{2-}/\text{S}_6^{2-}$ reactions do not form intense peaks during the first reduction scan (Fig. 5.16a). Therefore, the peak R_1 does not appear during this scan, however the peak R_2 appears due to the $\text{S}_6^{2-}/\text{S}_4^{2-}$ and $\text{S}_3^{*}/\text{S}_3^{2-}$ reactions, whose individual currents form intense peaks around -1.50 V (Fig. 5.16a). During the first oxidation scan of Li_2S_6 , all the reduced polysulfides present near the working electrode surface undergo simultaneous oxidation around -0.6 V to produce S_8 . This is clear from the intense positive peaks of $\text{S}_4^{*}/\text{S}_4^{2-}$, $\text{S}_6^{2-}/\text{S}_4^{2-}$, $\text{S}_8^{2-}/\text{S}_6^{2-}$ and $\text{S}_8/\text{S}_8^{2-}$ redox reactions (Fig. 5.16a) that constitute the oxidation peak O_1 . Since S_8 is the most concentrated species near the working electrode surface at the beginning of the second reduction scan, $\text{S}_8/\text{S}_8^{2-}$ and $\text{S}_8^{2-}/\text{S}_6^{2-}$ reaction currents form intense peak around -1.10 V (Fig. 5.16b) – due to the simultaneous reduction reactions of both S_8 and S_8^{2-} . This is the reason behind the appearance of R_1 during the second reduction scan (Figs. 5.15a and b), other than that rest of the characteristics of the second CV of the Li_2S_6 solution are similar to those of the first curve.

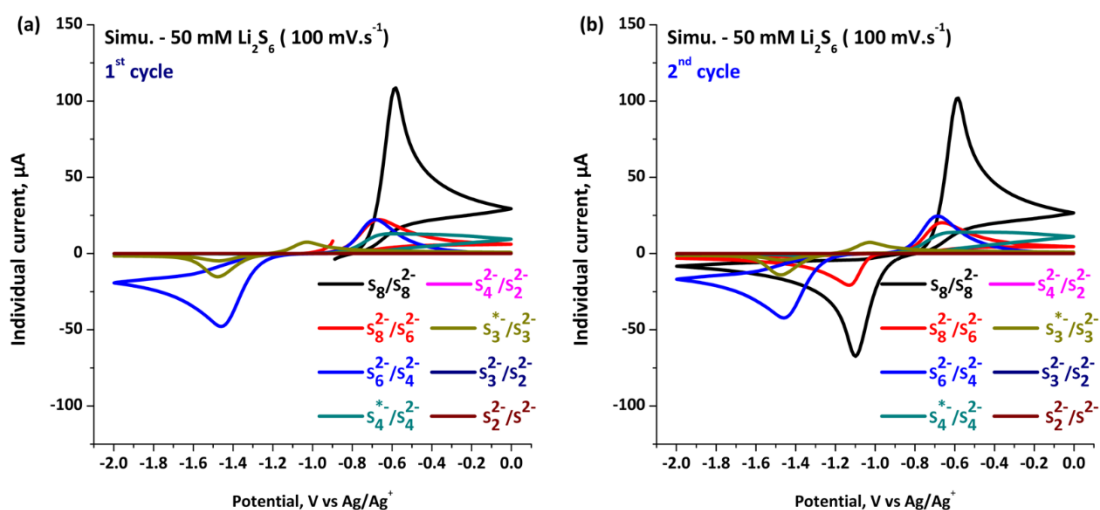


Figure 5.16. Simulated individual currents for electrochemical reactions during the (a) first and (b) second CV cycles 50 mM Li_2S_6 solution, with a scan rate of $100 \text{ mV}\cdot\text{s}^{-1}$.

5.7. Conclusions

CV investigations of different polysulfides solutions, using our relatively simple cell setup have shown that the complex characteristics of the cyclic voltammogram depend primarily on the type and concentration of the dissolved polysulfide in the electrolyte. The initial polysulfides speciation in the electrolyte, will influence the characteristics of CV, even if the Pt counter electrode is replaced with Li, which has been previously observed experimentally by Zheng *et al.* [197]. The characteristics also depend on the scan rate and cycle number. The combined experimental and modelling investigations, have also assisted in determining the reactions steps that are required to explain the reasons behind the changes in the characteristics of the CV under wide range of experimental conditions (*e.g.* initial solvate polysulfide speciation and scan rate). There are various analytical spectroscopy tools such as the UV-vis, Raman, etc. which assist in the measurement of the evolutions of different of polysulfides in the electrolyte during the operation of Li-S batteries [60,178,198,199]. However, the studies using these tools hypothesize reaction mechanism with large number of reaction steps. Therefore, modelling the CVs of dissolved sulfur and polysulfides can assist in verifying the possibility of these reaction steps.

The cyclic voltammetry simulation results have revealed that the visibility of the oxidation peak O_2 depends on the intensity of the S_3^{*-}/S_3^{2-} reaction current peak, thus it shows the presence of S_3^{*-} radical in 1 M LiTFSI in TEGDME:DIOX. This indicates that the modelling of the CV curves not only helps in identifying the initial speciation of dissolved polysulfide in the electrolyte, but it also assists in identifying the presence of some polysulfide intermediates as well. Simulation results have also shown, that the increase in intensity and appearance of CV peaks during the second cycle as in the case Li_2S_8 and Li_2S_6 solution respectively, are due to occurrence of additional electrochemical reactions and change in the polysulfide speciation at the end of the first cycle. This effect should be considered during the characterization of dissolved polysulfide using continuous cycling as in the study of effectiveness of polysulfide crossover blocking by an ion-selective membrane [109,200].

A.5 Appendix: Numerical Schemes

A.5.1. Finite volume method

The temporal unit mesh or time step is giving by

$$\Delta t = \frac{t^{n+1} - t^n}{t_{max}} \quad [A-5.1]$$

where t^{n+1} and t^n are the time at $(n + 1)^{th}$ and n^{th} iteration respectively. t_{max} is the total simulation time.

The spatial unit mesh is given by

$$\Delta x = x_{k+1} - x_k \quad [A-5.2]$$

where k refers to the nodal points (Fig. A-I) and N_{bin} is the total number of discretized bins given by

$$N_{bin} = \frac{\delta_{DL}}{\Delta x} \quad [\text{A-5.3}]$$

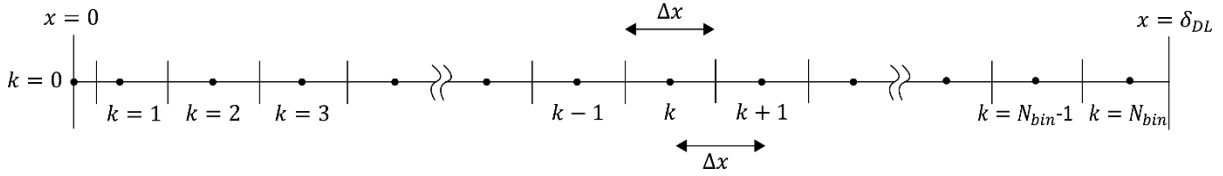


Figure A-5.1. Schematic representation of the adopted 1D meshing for the simulation domain

The discretized form of the mass conservation equations at different nodal points along the simulation domain are as follows.

At the electrode surface ($k = 0$),

$$\frac{(c_i)_0^{n+1} - (c_i)_0^n}{\Delta t} = \frac{8D_i((c_i)_1 - (c_i)_0)}{(\Delta x)^2} + (S_i)_0 \quad [\text{A-5.4}]$$

$$(S_i)_0 = -\frac{4(N_i)_{x=0}}{\Delta x} - (s_i)_0 - (G_i)_0 \quad [\text{A-5.5}]$$

At the nodal point $k = 1$,

$$\frac{(c_i)_1^{n+1} - (c_i)_1^n}{\Delta t} = \frac{D_i}{(\Delta x)^2} \left(\frac{4}{3}(c_i)_2 - 4(c_i)_1 + \frac{8}{3}(c_i)_0 \right) + (S_i)_1 \quad [\text{A-5.6}]$$

$$(S_i)_1 = (s_i)_1 \quad [\text{A-5.7}]$$

For nodal points from $k = 2$ to $N_{bin} - 1$

$$\frac{(c_i)_k^{n+1} - (c_i)_k^n}{\Delta t} = \frac{D_i((c_i)_{k+1} - 2(c_i)_k + (c_i)_{k-1})}{(\Delta x)^2} + (S_i)_k \quad [\text{A-5.8}]$$

$$(S_i)_k = (s_i)_k \quad [\text{A-5.9}]$$

At the nodal point $k = N_{bin}$

$$\frac{(c_i)_{N_{bin}}^{n+1} - (c_i)_{N_{bin}}^n}{\Delta t} = \frac{D_i((c_i)_{N_{bin}-1} - 2(c_i)_{N_{bin}})}{(\Delta x)^2} + (S_i)_{N_{bin}} \quad [\text{A-5.10}]$$

$$(S_i)_{N_{bin}} = \frac{D_i c_i^*}{(\Delta x)^2} + (s_i)_{N_{bin}} \quad [\text{A-5.11}]$$

The Crank-Nicholson method is used calculate the concentration of the species at $(n + 1)^{th}$ time step which is half implicit and is given by

$$\left(Id_{k \times k} - \frac{D_i \Delta t}{2(\Delta x)^2} M_{k \times k} \right) (c_i)_{k \times 1}^{n+1} = \left(Id_{k \times k} + \frac{D_i \Delta t}{2(\Delta x)^2} M_{k \times k} \right) (c_i)_{k \times 1}^n + \Delta t (S_i)_{k \times 1}^{n+1} \quad [\text{A-5.12}]$$

Where,

$$M_{k \times k} = \begin{pmatrix} -8 & 8 & 0 & \dots & \dots & \dots & \dots & 0 \\ 8/3 & -4 & 4/3 & 0 & \vdots & \vdots & \vdots & \vdots \\ 0 & 1 & -2 & 1 & 0 & \vdots & \vdots & \vdots \\ \vdots & 0 & 1 & -2 & 1 & \ddots & \vdots & \vdots \\ \vdots & \vdots & 0 & \ddots & \ddots & \ddots & 0 & \vdots \\ \vdots & \vdots & \vdots & \ddots & 1 & -2 & 1 & 0 \\ \vdots & \vdots & \vdots & \vdots & 0 & 1 & -2 & 1 \\ 0 & \dots & \dots & \dots & \dots & 0 & 1 & -2 \end{pmatrix} \quad [\text{A-5.13}]$$

$$Id_{k \times k} = \begin{pmatrix} 1 & 0 & \dots & \dots & \dots & \dots & \dots & 0 \\ 0 & 1 & 0 & \vdots & \vdots & \vdots & \vdots & \vdots \\ \vdots & 0 & 1 & 0 & \vdots & \vdots & \vdots & \vdots \\ \vdots & \vdots & 0 & 1 & 0 & \vdots & \vdots & \vdots \\ \vdots & \vdots & \vdots & 0 & 1 & \ddots & \vdots & \vdots \\ \vdots & \vdots & \vdots & \vdots & \ddots & \ddots & 0 & \vdots \\ \vdots & \vdots & \vdots & \vdots & \vdots & 0 & 1 & 0 \\ 0 & \dots & \dots & \dots & \dots & \dots & 0 & 1 \end{pmatrix} \quad [\text{A-5.14}]$$

The electrochemical reaction coefficients of final reaction steps are given by

$$S_{ij} = \begin{pmatrix} 0 & 0 & 0 & 0 & 0 & 0 & 0 & 0 \\ -1/2 & 0 & 0 & 0 & 0 & 0 & 0 & 0 \\ 1/2 & -1/2 & 0 & 0 & 0 & 0 & 0 & 0 \\ 0 & 2 & -1 & 0 & 0 & 0 & 0 & 0 \\ 0 & 0 & 0 & -1 & 0 & 0 & 0 & 0 \\ 0 & 0 & 3/2 & 1 & -1/2 & 0 & 0 & 0 \\ 0 & 0 & 0 & 0 & 0 & -1 & 0 & 0 \\ 0 & 0 & 0 & 0 & 0 & 1 & -1 & 0 \\ 0 & 0 & 0 & 0 & 1 & 0 & 3/2 & 1/2 \\ 0 & 0 & 0 & 0 & 0 & 0 & 0 & 1 \end{pmatrix} \quad [\text{A-5.15}]$$

The homogeneous chemical reaction coefficients of final reaction steps (Eqs. 5.23 and 5.25) are given by

$$\vartheta_{ij} = \begin{pmatrix} 0 & 0 \\ 0 & 0 \\ 1 & 0 \\ 0 & 1 \\ -2 & 0 \\ 0 & 0 \\ 0 & -2 \\ 0 & 0 \\ 0 & 0 \\ 0 & 0 \end{pmatrix} \quad [\text{A-5.16}]$$

The homogeneous chemical reaction coefficients of final reaction steps (Eqs. 5.16 and 5.22) are given by,

$$\gamma_{ik} = \begin{pmatrix} 0 & 2 \\ 1 & 0 \\ 0 & 0 \\ 0 & 0 \\ 0 & 0 \\ 0 & 0 \\ 0 & 0 \\ 0 & 0 \\ 0 & 0 \\ 0 & 1 \end{pmatrix} \quad [\text{A-5.17}]$$

Chapter 6. Nucleation and growth of Li_2S

Contents

| | |
|--|------------|
| 6.1 Introduction | 153 |
| 6.2. Experimental Setup | 155 |
| 6.3. Theoretical methodology..... | 156 |
| 6.3.1. Thermodynamics and kinetics of Li_2S nucleation | 156 |
| 6.3.2. Other reaction steps and their kinetic equations | 161 |
| 6.3.3. Population balance of Li_2S particles..... | 163 |
| 6.4. The electrochemical measurement..... | 169 |
| 6.5. Results and discussion | 170 |
| 6.5.1 The experimental vs the simulated electrochemical signals | 170 |
| 6.5.2. The simulated dissolved species concentrations and the individual reaction currents ... | 170 |
| 6.5.3 Simulated evolutions of the Li_2S deposits..... | 173 |
| 6.6. Conclusion and perspectives..... | 175 |
| A.6 Appendix: Numerical Schemes | 175 |
| A.6.1. Discretization of the population balance equation | 175 |

Chapter 6. Nucleation and growth of Li₂S

6.1 Introduction

Experimental and modelling results have shown that the precipitation of Li₂S occurs during the low potential plateau stage of the conventional Li-S battery discharge [92,142,201]. The Li₂S deposits which form over the conductive carbon surface of the cathode have very low electronic conductivity [103,202]. Therefore, they will impact the electrochemical performance due to the passivation of the electroactive surface of the cathode. However, the kinetics and the reaction mechanism behind the precipitation of Li₂S in Li-S batteries are still under debate. A better understanding of the Li₂S precipitation phenomenon will assist in improving the discharge performance of the Li-S battery.

The seminal investigation of the Li₂S precipitation phenomenon in Li-S batteries was carried out by Fan *et al.* [203]. In this work, the authors performed potentiostatic discharge experiments using Li-S cells containing porous cathodes made up of carbon fibers and electrolyte solutions based on dissolved Li₂S₈. Typically, at a stage during the potentiostatic discharge, the current density of the cell increases to a peak before it decreases (Fig. 6.1a). The SEM images show that the nucleation and growth of the Li₂S deposits over the carbon surface occur during this stage (Fig. 6.1b to 6.1d). Fan *et al.* also observed that the Li₂S nuclei and the current density peak do not appear if the constant discharge potential was above certain critical value (> 2.05 V) [203]. Furthermore, they showed that the combined nucleation and growth rate constant depend on the constant discharge potential and the solvent type used in the electrolyte.

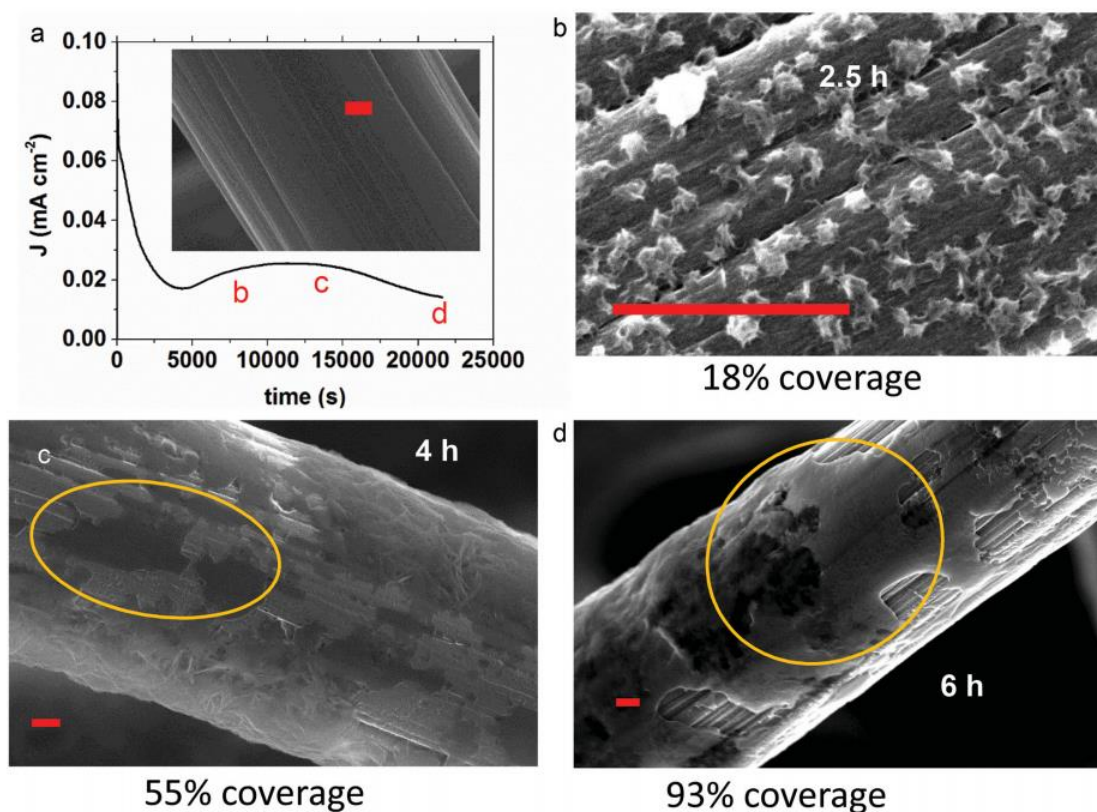


Figure 6.1. (a) Current density vs. time curve during potentiostatic discharge at 2.02 V. SEM micrographs showing Li_2S deposits over a carbon fiber at (a) 2.5, (b) 4 and (c) 6 hours [203].

Li *et al.* carried out potentiostatic experiments to investigate the impact of the electrolyte solvents on the morphologies of Li_2S deposits and the type of nucleation mechanism [143]. The dimensionless current vs. time curves of the potentiostatic experiments were compared with the simulated results of the 2D instantaneous (2DI) and progressive (2DP) Bewick, Fleishman and Thirsk (BFT) models [144] and 3D instantaneous (3DI) and progressive (3DP) Scharifker-Hills (SH) models [145,204]. The experimental curves of the ether-based solvents matched well with the simulated results of the 2DI BFT model, while those of DMF and DMA matched well with the results of the 3DP SH model [143].

It is important to note that the BFT and SH models can only simulate the current corresponding to the electrochemical growths of the existing nuclei [144,145,204]. These models also assume that the electrochemical growths of the existing nuclei have fast charge transfer steps and are controlled by the mass transport of ions to the electrode surface. Furthermore, BFT and SH models can be applied only to the potentiostatic discharge stage

where the cell current density form a peak [144,145,204]. These models have limited capability to investigate the precipitation of Li₂S in Li-S batteries, since they cannot predict the reaction mechanism behind the nucleation and growth processes, particle sizes of the deposits, their coverage over carbon surface, etc.

Ren *et al.* developed a comprehensive 1D continuum model which incorporates electrochemical nucleation and growth of Li₂S deposits [141]. This model predicts the impact of the galvanostatic discharge rates on the particle size distributions of the Li₂S deposits. The Li₂S nucleation kinetics of this model was described using the atomistic theory of nucleation which cannot predict the critical sizes of the nuclei and the initial nucleation densities were determined through fitting. Andrei *et al.* [118] and Danner *et al.* [205] developed similar 1D models which incorporated the chemical nucleation and growth of S₈ and Li₂S deposits. The model by Andrei *et al.* predicts the coverages of S₈ and Li₂S deposits over carbon surface. The model by Danner *et al.* predicts the particle size distributions of S₈ and Li₂S deposits during charge and discharge. However, both these aforementioned models assume that the nucleation of Li₂S is driven by supersaturation of S²⁻ instead of overpotential. Therefore, they completely contradict the experimental observations of Fan *et al.* [203] and Li *et al.* [143]. Furthermore, none of the aforementioned nucleation and growth models have been applied to simulate the potentiostatic discharge experiments.

Therefore, in this chapter we propose a different 1D model to simulate the potentiostatic discharge of a simple Li-S cell. Our model considers the electrochemical nucleation and growth of Li₂S deposits over the carbon surface. The Li₂S nucleation of our model was described using the classical electrochemical nucleation theory [206], which is driven by the overpotential and is capable of predicting the critical sizes of the nuclei.

6.2. Experimental Setup

The experimental work presented in this chapter was carried by Dr. Sara Drvarič Talian at National Institute of Chemistry (NIC) in Ljubljana, Slovenia. A two-electrode coffee bag cell was used for the electrochemical measurement (Fig. 6.2). A planar glassy carbon electrode with surface area 2 cm² was used as the cathode and a lithium metal foil was used as the

anode. These two electrodes were separated using two glass fiber separators and an Ohara membrane, which was placed in middle (Fig. 6.2). The glass fiber separator on the anode side was wetted with 60 μL of the pure 1 M LiTFSI in TEGDME:DOL electrolyte. The glass fiber separator in the cathode side was wetted with 60 μL of the 100 mM electrolyte solution of Li_2S_6 in 1 M LiTFSI in TEGDME:DOL. The Ohara membrane is an ion selective one which permits Li^+ to pass through it while blocking the crossover of polysulfides from the cathode to anode compartment. Therefore, this setup prevents the reactions of polysulfides with the lithium metal anode.

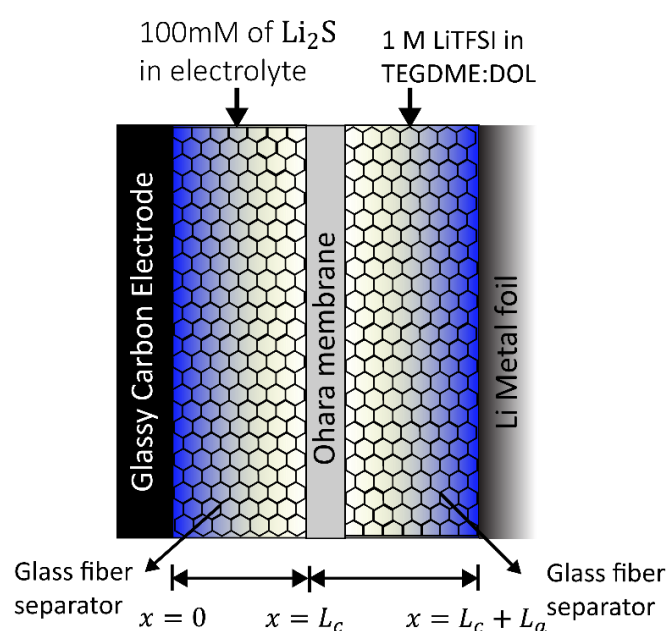


Figure 6.2. Schematic representation of the two-electrode coffee bag cell.

6.3. Theoretical methodology

6.3.1. Thermodynamics and kinetics of Li_2S nucleation

As proposed by the experimental works of Fan *et al.* [203] and Li *et al.* [143] and modelling work of Ren *et al.* [141], the following Li_2S nucleation reaction was assumed in our model,



According to the classical electrochemical nucleation theory, the overall homogenous free energy for the formation of Li₂S nuclei (ΔG^{hom}) has two components [206],

$$\Delta G^{hom} = \Delta G_{bulk} + \Delta G_{surface} \quad (6.2)$$

where, ΔG_{bulk} and $\Delta G_{surface}$ are the bulk and surface free energies, respectively. Assuming that the Li₂S nuclei are cubic, the bulk and surface energies are given by the Eqs. 6.3 and 6.4

$$\Delta G_{bulk} = r^3 \frac{n_j F \eta_j \rho_k}{M_k} \quad (6.3)$$

where, r is the side length of the Li₂S nucleus. ρ_k and M_k are the density and molar mass of the Li₂S, respectively. n_j and η_j are the number of electrons and overpotential of the Li₂S nucleation reaction (Eq. 6.1), respectively. Finally, F is the Faraday's constant.

$$\Delta G_{surface} = 6r^2 \gamma \quad (6.4)$$

Where, γ is the surface energy of the Li₂S nucleus.

According to the Eqs. 6.2 to 6.3, ΔG^{hom} depends on the particle size of the nuclei (Fig. 6.3).

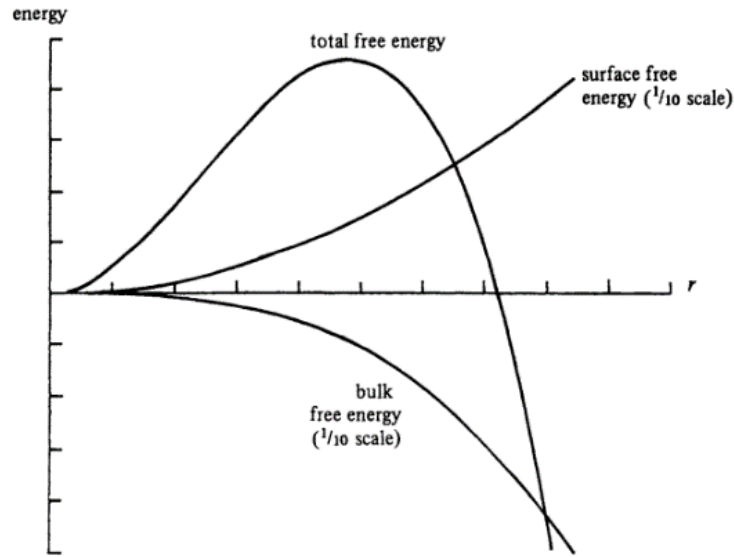


Figure 6.3. The total homogenous free energy vs. the particle size of the nuclei [206].

Furthermore, nucleation of Li₂S occurs when the particle size reaches a critical value, where the total homogenous free energy for the formation of nuclei is maximum (Eq. 6.5):

$$\frac{\partial(\Delta G^{homo})}{\partial r} = 0 \quad (6.5)$$

Therefore, the critical particle size (r_{crit}) and the critical homogenous free energy for the formation of the nuclei (ΔG_{crit}^{homo}) can be derived by differentiating Eq. 6.2 with respect to r and applying Eq. 6.5 to the differential equation.

$$r_{crit} = -\frac{4M_k}{n_j F \eta_j} \quad (6.6)$$

$$\Delta G_{crit}^{homo} = \frac{32M_k^2 \gamma^3}{n_j^2 F^2 \eta_j^2 \rho_k} \quad (6.7)$$

Since the nucleation of Li₂S occurs over the carbon electrode surface, its energy barrier is calculated using the heterogenous free energy (ΔG_{crit}^{hetero}) which is given as follows [207],

$$\Delta G_{crit}^{hetero} = \Delta G_{crit}^{homo} \left(1 + \frac{E_{bind}}{2\gamma r_{crit}^2} \right) \quad (6.8)$$

where, E_{bind} is the binding energy of the Li₂S nuclei to the carbon surface.

Assuming first order kinetics, the kinetic rate of the Li₂S nucleation reaction (k_{nuc}) is determined as follows,

$$k_{nuc} = k_{nuc}^0 \exp \left(-\frac{\Delta G_{crit}^{hetero}}{k_B T} \right) \quad (6.9)$$

where, k_{nuc}^0 is the rate constant of the Li₂S nucleation reaction. k_B and T are the Boltzmann constant and the temperature, respectively.

Furthermore, the current of the Li₂S nucleation reaction is calculated as follows,

$$i_{nuc} = \begin{cases} -n_j F k_{nuc}, & r_{crit} \geq r_{min} \\ 0, & r_{crit} < r_{min} \end{cases} \quad (6.10)$$

According to Eq. 6.10, the nucleation current is zero if the critical particle size is below a certain minimum positive value (r_{min}). In the classical electrochemical nucleation theory, the nucleation is driven by the overpotential (Eqs. 6.6 to 6.9). Furthermore, the overpotential should reach a certain critical value to produce stable nuclei due to the high energy barrier of the Li₂S nucleation reaction. Since, the particle size depends on the overpotential (Eq. 6.6),

r_{min} is considered to be the minimum size at which the Li₂S nuclei are stable. The overpotential of the Li₂S nucleation reaction (Eq. 6.1) is calculated as follows,

$$\eta_j = E_c - U_{nuc}^0 - \frac{RT}{n_j F} \ln \left(\frac{c_{Li^+}}{1000} \right)^8 - \frac{RT}{n_j F} \ln \left(\frac{c_{S_4^{2-}}}{1000} \right) \quad (6.11)$$

where, E_c and U_{nuc}^0 are cathode potential and standard potential of Li₂S nucleation reaction, respectively.

Finally, the rate of number density of Li₂S nuclei formed (\dot{N}) during the nucleation is calculated as follows,

$$\dot{N} = -\frac{4}{n_j} \left(\frac{M_k}{\rho_k} \right) \frac{i_{nuc} a^{free}}{F r_{crit}^3} \quad (6.12)$$

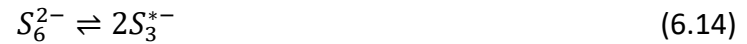
where, the number 4 is the stoichiometric coefficient of Li₂S in the nucleation reaction (Eq. 6.1). a^{free} is the specific surface area of the free electrode surface available for the nucleation of Li₂S. The parameters used in the classical nucleation theory of Li₂S are given in Table 6.1.

Table 6.1. Parameters of our Li₂S electrochemical nucleation model.

| S. No | Parameters | Values | Units | References |
|-------|-------------|---------------------------|----------------------|--------------------|
| 1 | ρ_k | 1.63 | g.cm ⁻³ | [208] |
| 2 | M_k | 45.95 | g.mol ⁻¹ | Constant |
| 3 | γ | 0.3364 | J.m ⁻² | [209] |
| 4 | E_{bind} | -0.8811×10 ⁻¹⁹ | J | [111] |
| 5 | k_{nuc}^0 | 2.6118×10 ¹²⁴ | mol. s ⁻¹ | Fitted |
| 6 | U_{nuc}^0 | 2.086 | V | Fitted |
| 7 | T | 298 | K | Measured |
| 8 | k_B | 1.38×10 ⁻²³ | J.K ⁻¹ | Universal constant |

6.3.2. Other reaction steps and their kinetic equations

The dissolved Li₂S₆ is the initial polysulfide species present in the electrolyte of the cathode compartment. Therefore, the following reaction steps (Eqs. 6.13 to 6.19) were considered to take place at the cathode surface.





These aforementioned reaction steps (Eqs. 6.13 to 6.19) were determined using the cyclic voltammetry model (Chapter 3). Furthermore, we also consider the electrochemical growth of the existing Li₂S nuclei in our model (Eq. 6.20).



Since, a two-electrode cell was used to in experiment, we also consider the reaction at the lithium metal anode (6.21).



An electrochemical reaction (Eqs. 6.13, 6.15-6.18 and 6.21), can be written in a generic form as follows,

$$\sum_i S_{ij} M_i^{z_i} = n_j e^- \quad (6.22)$$

Where $M_i^{z_i}$ and e^- respectively are the symbols that represent a species i and an electron. z_i is the charge of the species i . Furthermore, the current density of an electrochemical reaction is determined using the Butler-Volmer equation,

$$i_j = i_j^0 \left(\prod_i ((c_i)_{x=0})^{S_{ij}}_{S_{ij}>0} e^{\left(\frac{(1-\alpha_j)n_j F(E-U_j^0)}{RT}\right)} - \prod_i ((c_i)_{x=0})^{-S_{ij}}_{S_{ij}<0} e^{\left(\frac{-\alpha_j n_j F(E-U_j^0)}{RT}\right)} \right) \quad (6.23)$$

where, U_j^0 and i_j^0 respectively are the standard potential and exchange current density of an electrochemical reaction j and E is the electrode potential. c_i is the concentration of dissolved species in the electrolyte.

Eq. 6.13 is a homogenous chemical dissociation reaction of S_6^{2-} , whose kinetic equation is as follows,

$$k_j^{chem} = k_j^f \left(\prod_i ((c_i)^{\vartheta_{ij}})_{\vartheta_{ij}} - K_j^{eq} \prod_i ((c_i)^{-\vartheta_{ij}})_{\vartheta_{ij}<0} \right) \quad (6.24)$$

where, ϑ_{ij} is the stoichiometric coefficient for the species i involved in the homogenous chemical reaction j (Eq. 6.14). k_j^f and k_j^r are forward and reverse kinetic constants. K_j^{eq} is the equilibrium constant of the chemical reaction j , which is given by,

$$K_j^{eq} = \frac{k_j^r}{k_j^f} \quad (6.25)$$

6.3.3. Population balance of Li₂S particles

Since, the nucleation and growth of the Li₂S deposits are described by separate reaction steps, the particle size distribution of the deposits can be determined by the following population balance equation [207],

$$\frac{\partial f(v_r)}{\partial t} = \frac{\dot{N}}{\partial v_r} - \frac{\partial}{\partial v_r} \left(f(v_r) \frac{d\epsilon_r}{dt} \right) \quad (6.26)$$

where, v_r is the volume of a nucleus with size r . $f(v_r)$ is the number density per unit volume of the nuclei with size r . The numerical solution of the population balance equation is given in the Appendix subsection A.6.1.

Since, we consider both chemical (Eq. 6.19) and electrochemical growth (Eq. 6.20) of the existing nuclei in our model, the rate of change of volume fraction of the nuclei with size r has two components (Eq. 6.27).

$$\frac{d\epsilon_r}{dt} = \left(\frac{d\epsilon_r}{dt} \right)^{chem} + \left(\frac{d\epsilon_r}{dt} \right)^{electro} \quad (6.27)$$

The rate change of volume fraction of the nuclei with size r due to chemical reaction (6.19) is given by,

$$\left(\frac{d\epsilon_r}{dt} \right)^{chem} = \left(\frac{M_k}{\rho_k} \right) k^{prec} \epsilon_r \left(\prod_i (c_i)^{\nu_{ij}} - K^{sp} \right) \quad (6.28)$$

where k^{prec} and K^{sp} are the rate constant and solubility product of chemical precipitation of Li₂S (6.19).

The rate of change of volume fraction of the nuclei with size r due to electrochemical reaction (6.20) is given by

$$\left(\frac{d\epsilon_r}{dt} \right)^{electro} = -N_r \frac{4}{n_j} \left(\frac{M_k}{\rho_k} \right) \frac{i_j}{F} a_r^{grow} \quad (6.29)$$

where, N_r is the number density of Li₂S deposits with size r and a_r^{grow} is electroactive specific surface area around an individual deposit where the electrochemical growth reaction occurs.

6.3.4. Active surface areas and porosity

In our model the electroactive specific surface area available for an electrochemical reaction will vary based on the reaction type. As mentioned before, the nucleation of Li₂S is assumed to occur only in the free electrode surface which is uncovered by the existing Li₂S deposits. Therefore, the free active specific surface area of the Li₂S nucleation reaction is determined as follows,

$$a^{free} = a^0 - \sum N_r r^2 \quad (6.30)$$

where a^0 is the initial specific surface area of the deposit free electrode and r^2 is the basal surface area of an individual Li₂S deposit with size r .

The redox reaction in the solution phase can occur on the free electrode surface and on the surface of the Li₂S deposits which permit tunnelling of electron through them. Therefore, the electroactive surface area of the solution phase redox reactions is calculated as follows,

$$a_j = a^0 - \sum N_r r^2 + \sum N_r r^2 \Theta(r) \quad (6.31)$$

where, $\Theta(r)$ is the electron tunnelling probability function,

$$\Theta(r) = \frac{1 - \operatorname{erf}\left(\frac{r - \delta_{tun}}{L_{tun}}\right)}{2} \quad (6.32)$$

In Eq. 6.32, δ_{tun} and L_{tun} are the threshold thickness at halved electron tunnelling and scaling factor, respectively.

As proposed by Fan *et al.* [203], our model considers that the electrochemical Li₂S growth reaction occurs at the triple phase boundary between the electrolyte, the deposit and the electrode surface. Furthermore, due to the finite nature of the electrode surface, some of the phase boundaries surrounding the existing deposits could be covered by the neighbouring deposits. Therefore, the electroactive specific surface area for the electrochemical Li₂S growth reaction is determined using the following equation,

$$a^{grow} = \left(\sum N_r \Delta r^2 \right) (1 - \theta) \quad (6.33)$$

where, Δr^2 is the change in the basal surface area of an individual Li₂S deposit due to its growth. θ is the fraction of electrode surface which is covered by the existing Li₂S deposits, which is calculated using Eq. 6.33:

$$\theta = \frac{\sum N_r r^2}{a^0} \quad (6.34)$$

Due to the precipitation of Li₂S over the cathode surface, the porosity of the glass fiber separator close to the cathode surface decreases. Therefore, this porosity (is given by,

$$\varepsilon_{x=0} = \varepsilon_{x=0}^0 - \sum \epsilon_r \quad (6.35)$$

where $\varepsilon_{x=0}^0$ and ϵ_r are the initial porosity of the glass fiber separator and volume fraction of the Li₂S deposits with size r .

6.3.5. Mass balance and boundary conditions

The mass balance of a dissolved species in the cathode compartment is determined using the following equation,

$$\frac{\partial(c_i \varepsilon)}{\partial t} = \frac{\partial}{\partial x} \left(D_i \varepsilon^\beta \frac{\partial c_i}{\partial x} \right) - s_i - G_i \quad (6.36)$$

Since Li^+ can pass through the Ohara membrane, its mass balance equation (Eq. 6.35) applies to the entire cell. In the Eq. 6.35, D_i is the diffusion coefficient of a species i and β is the Bruggeman coefficient. The s_i and R_i are the homogeneous chemical reactions and heterogeneous dissolution/precipitation reactions which are determined using the following equations,

$$s_i = \sum_j \vartheta_{ij} k_j^{chem} \quad (6.37)$$

$$G_i = \sum_j \gamma_{ij} \left(k^{prec} \sum_r (\varepsilon_r) \left(\prod_i (c_i)^{\nu_{ij}} - K^{sp} \right) \right) \quad (6.38)$$

The flux at the glassy carbon surface is given by the Faraday's law,

$$(N_i)_{x=0} = \left(D_i \varepsilon^\beta \frac{\partial c_i}{\partial x} \right)_{x=0} = \frac{1}{A^0} \sum_j \frac{S_{ij} i_j}{n_j F} A_j \quad (6.39)$$

where A_j is a general symbol for the electroactive surface area for an electrochemical reaction j , which is determined by the product of the volume of the discretized bin closest to the electrode and the specific surface area of the reaction j (Eqs. 6.30, 6.31 and 6.33).

Except for Li^+ , the flux of all the dissolved species at the separator/Ohara membrane interface ($x = L_c$) at the cathode compartment is zero (Eq. 6.40).

$$(N_i)_{x=L_c} = \left(D_i \varepsilon^\beta \frac{\partial c_i}{\partial x} \right)_{x=L_c} = 0 \quad (6.40)$$

The flux of the Li⁺ at the lithium anode surface ($x = L_c + L_a$) is given by,

$$(N_i)_{x=L_c+L_a} = \left(D_i \varepsilon^\beta \frac{\partial c_i}{\partial x} \right)_{x=L_c+L_a} = \frac{i_{Li^+/Li}}{F} \quad (6.41)$$

where $i_{Li^+/Li}$ the current of the lithium oxidation reaction (Eq. 6.21). This current is equal to the total cathode current but has an opposite sign.

Finally, the total cathode current is calculated using the following equation,

$$I = \sum_j i_j A_j \quad (6.41)$$

Table 6.2. Kinetic parameters of the different reactions and the diffusion coefficient of the dissolved species taken into account in our model.

| ii. Electrochemical reaction parameters | | | | | | v. Dissolved species parameters | |
|---|---|---------|---|---|----------------------------------|---------------------------------|----------------------------|
| Reaction No. (<i>j</i>) | Reaction | Eq. No. | i^0 (A) | U^0 (V) | α | | |
| 1 | S_6^{2-}/S_4^{2-} | (6.13) | 1.90×10^{-2b} | 2.20 ^a | 0.500 ^b | Species $M_i^{z_i}$ | D_i (m.s ⁻¹) |
| 2 | S_4^{2-}/S_2^{2-} | (6.15) | 1.97×10^{-5a} | 2.17 ^a | 0.500 ^b | | |
| 3 | S_3^{*-}/S_3^{2-} | (6.16) | 9.73×10^{-4a} | 2.17 ^a | 0.420 ^a | Li ⁺ | 1.6335×10^{-10a} |
| 4 | S_3^{2-}/S_2^{2-} | (6.17) | 1.97×10^{-8a} | 2.13 ^a | 0.350 ^a | S_6^{2-} | 5.6000×10^{-10a} |
| 5 | S_2^{2-}/S^{2-} | (6.18) | 3.94×10^{-10a} | 2.11 ^a | 0.658 ^a | S_4^{2-} | 6.0000×10^{-10a} |
| 6 | S_4^{2-}/Li_2S | (6.20) | 7.2×10^{-5a} | 2.086 ^a | 0.500 ^c | S_3^{*-} | 3.5000×10^{-10e} |
| ii. Homogeneous chemical reaction parameters | | | | | | S_3^{2-} | 3.5000×10^{-10e} |
| Reaction No. (<i>j</i>) | Reaction | Eq. No. | k_j^f (s ⁻¹) | k_j^{eq} (mol ⁻¹) | | S_2^{2-} | 3.5000×10^{-10e} |
| 2 | $S_6^{2-} \rightleftharpoons 2S_3^{*-}$ | (6.12) | 9.5 ^a | 12.6263 ^a | | S^{2-} | 3.5000×10^{-10e} |
| iii. Heterogeneous precipitation/dissolution reaction parameters | | | | | | | |
| Reaction No. (<i>k</i>) | Reaction | Eq. No. | k_k (mol ² .m ⁻⁶ .s ⁻¹) | K_k^{sp} (mol ³ .m ⁻⁹) | Solid species | V_k (m ⁻³ .mol) | |
| 2 | $2Li^+ + S^{2-} \rightleftharpoons Li_2S_{(s)}$ | (619) | 5×10^{-7d} | 10 ^d | Li ₂ S _(s) | 2.768×10^{-4d} | |

^aFitted parameters.^{b, c and d}Assumed parameters taken from Refs. [92], [141] and [119], respectively.^eExperimental parameter taken from Ref. [194].

6.4. The electrochemical measurement

Due to the presence of the dissolved Li₂S₆ in the catholyte, the open circuit potential (OCV) of the coffee bag cell was around 2.30 V. Therefore, the cell was discharged galvanostatically to 2.0 V at C/20, in order to trigger the nucleation of Li₂S. Immediately after this galvanostatic step, the cell was discharged potentiostatically at a constant potential of 2.0 V.

6.5. Results and discussion

6.5.1 The experimental vs the simulated electrochemical signals

The simulated current and potential vs. time curves produced using our nucleation and growth model have excellent semi-quantitative agreement with the experimental results (Fig. 6.4).

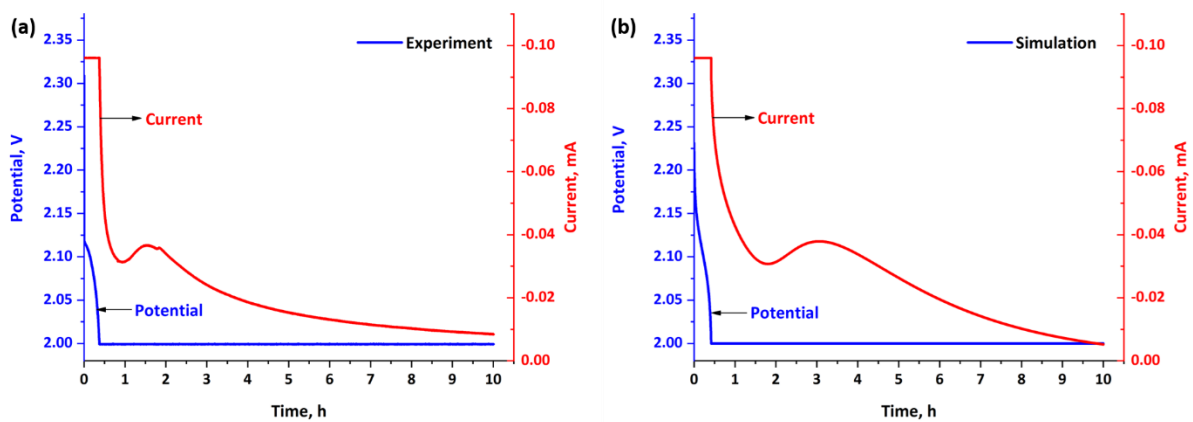


Figure 6.4. (a) Experimental and (b) simulated potential and current vs. time curves.

During the galvanostatic stage the cell potential decreases to 2.0 V (Fig. 6.4). Subsequently the overall reduction current decreases monotonically during the initial stage of the potentiostatic discharge. After this stage, the overall reduction increases to a peak before it starts to decrease once again. Finally, the overall reduction current levels off during the later stage of the potentiostatic discharge.

6.5.2. The simulated dissolved species concentrations and the individual reaction currents

During the Galvanostatic stage, the S_6^{2-} and S_3^{*-} concentrations decrease (Fig. 6.5), while, the concentrations of all the other polysulfides increase. These effects indicate that the S_6^{2-} reduction and dissociation reactions occur during this stage along with the subsequent

reduction reactions of the resulting lower order polysulfides. Furthermore, $\text{S}_6^{2-}/\text{S}_4^{2-}$ is the most dominant reaction during the galvanostatic stage, since its current is almost equal to the constant discharge current (Fig. 6.6a). Additionally, the $\text{S}_4^{2-}/\text{S}_2^{2-}$ (Fig. 6.6a) and $\text{S}_3^{*-}/\text{S}_3^{2-}$ (Fig. 6.6b) reactions also occur during the same time due to the increase in their currents.

Towards the end of the galvanostatic stage, the nucleation current starts to increase when the cell potential is slightly below 2.02 V (Fig. 6.6a). As mentioned before the nucleation process in our model is driven by its overpotential due to the high energy barrier required for the formation of stable nuclei. Therefore below 2.02 V, the overpotential of the nucleation reaction facilitates the formation of the stable Li_2S nuclei. Following this stage, the cell potential quickly drops to 2.0 V and the potentiostatic discharge starts.

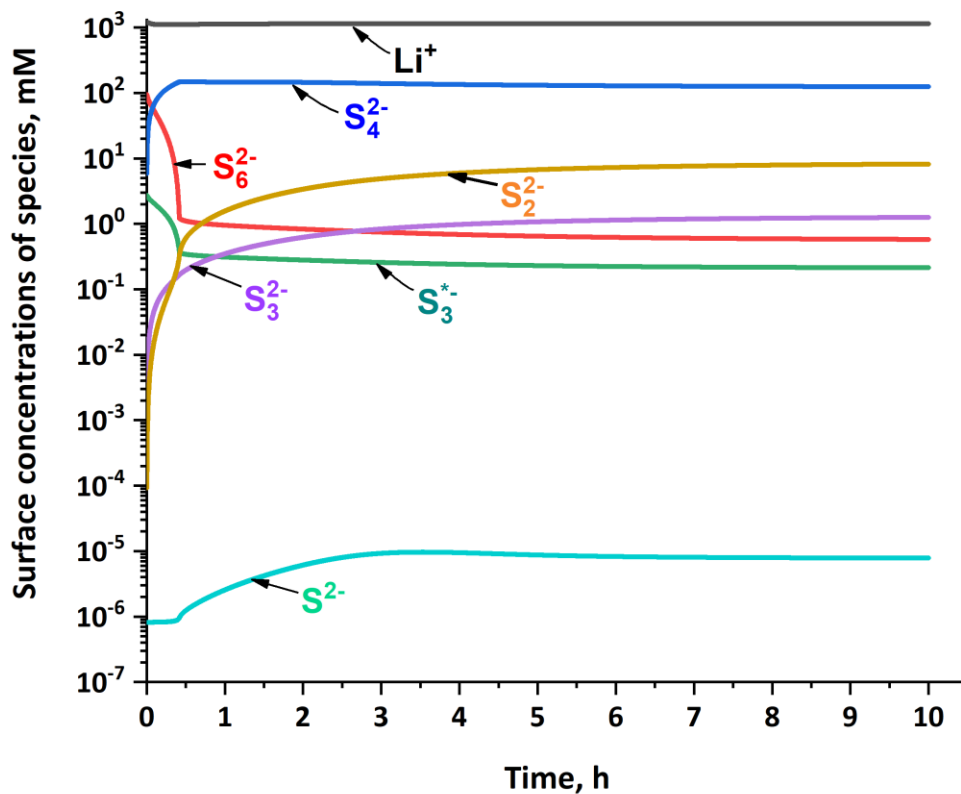


Figure 6.5. Simulated evolutions of dissolved species concentrations at the surface of the cathode during both galvanostatic and potentiostatic stages of the cell discharge.

The initial monotonic decrease of the overall reduction current during the initial stage of the potentiostatic discharge, is due the decrease in the $\text{S}_6^{2-}/\text{S}_4^{2-}$, $\text{S}_4^{2-}/\text{S}_2^{2-}$ and $\text{S}_3^{*-}/\text{S}_3^{2-}$ reaction currents (Fig. 6.6). Therefore, the reduction reactions of S_6^{2-} , S_4^{2-} and S_2^{2-} are still dominant during this stage. Furthermore, the simultaneous increase of the Li_2S nucleation and $\text{S}_3^{2-}/\text{S}_2^{2-}$ reaction currents also occur during this initial potentiostatic stage (Figs. 6.6a and b).

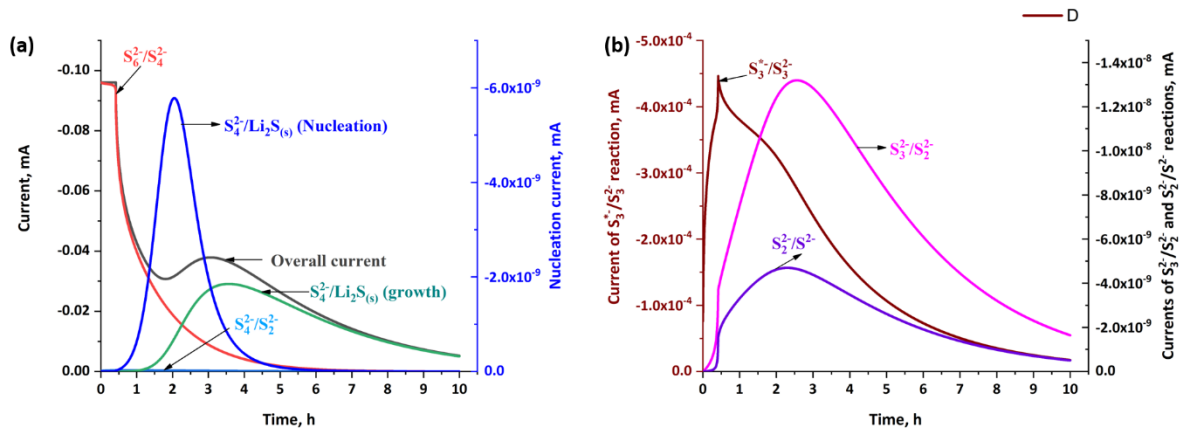


Figure 6.6. Simulated individual reaction currents during the galvanostatic and the potentiostatic stages of the cell discharge.

Following the continuous nucleation of the Li_2S deposits, the current of their electrochemical growth starts to increase (Fig. 6.6a). The increase of electrochemical Li_2S growth current is due to the increase of its electroactive specific surface area (Fig. 6.8), which correspond to the newly formed triple phase boundary surrounding the existing Li_2S deposits. The overall reduction current also increases during the same time. Therefore, the S_4^{2-} concentration decreases throughout the potentiostatic stage due to the nucleation and growth of the Li_2S (Fig. 6.5).

The nucleation current decreases after some time due to the significant decrease of the free carbon surface (Fig. 6.6a). In the other side, the current of the electrochemical growth of the Li_2S continues to increase and reaches a peak around the same time when the overall reduction current forms a peak (Fig. 6.4). Following this stage, the S^{2-} concentration starts to decrease (Fig. 6.5), which indicates that the chemical growth of the existing Li_2S nuclei also

occurs simultaneously. During the same time, the overall and the individual reduction reaction currents start to decrease and they level off during the later stage of the potentiostatic discharge (Fig. 6.6).

6.5.3 Simulated evolutions of the Li_2S deposits

During the potentiostatic stage, the total volume fraction of the Li_2S deposits starts to increase significantly at the same time when the overall reduction current starts to increase (Figs. 6.5 and 6.7a). However, the initial increase of the $\text{Li}_2\text{S}_{(s)}$ volume fraction is relatively slow. It is because this stage primarily involves the formation of the Li_2S nuclei, which is evident from the increase in the peak intensities of the Li_2S particle size distribution (Fig. 6.7b).

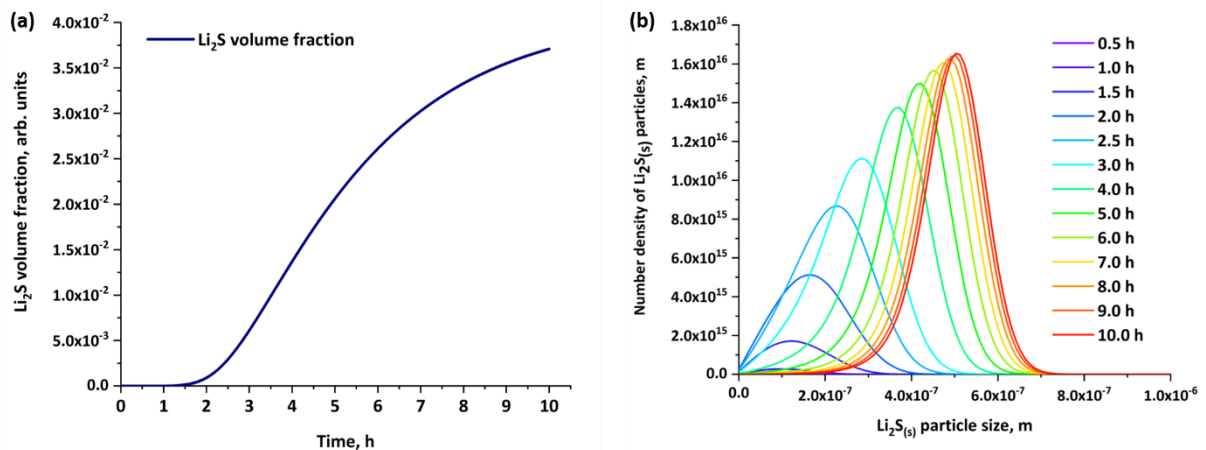


Figure 6.7. (a) Simulated evolution of the Li_2S volume fraction on the cathode during the galvanostatic and the potentiostatic stages, and (b) simulated particle size distributions of Li_2S deposits at different times.

Following the decrease of the nucleation current (Fig. 6.6a), the Li_2S volume fraction increases at a relatively faster rate (Fig. 6.7a). This is due to the chemical and electrochemical growth of the existing nuclei which occur simultaneously along with the formation of the new nuclei. Therefore, the peak intensities and their positions of the Li_2S particle size distribution

also increase significantly during this stage (Fig 6.7b). The growth of the existing Li_2S deposits is much faster when the current of the electrochemical growth reaction increases (Figs. 6.6a and 6.7a). This is due to the increase in the electroactive specific surface area surrounding the newly formed Li_2S deposits, over which the electrochemical growth reaction of the existing deposits occurs (Fig. 6.8). Furthermore, the peak positions of the Li_2S particle size distributions increase significantly during this stage.

However, the current and the electroactive specific surface area of the electrochemical growth reaction start to decrease (Figs. 6.6a and 6.8), when the Li_2S coverage over the carbon surface increases over 40 % (Fig. 6.8). Finally, the increase of the Li_2S volume fraction and the peak positions of the particle size distributions slow down significantly (Fig. 6.7), when the Li_2S coverage over the carbon surface increases over 80%. Beyond this point, the overall and the individual reaction currents level off (Fig. 6.6) due to the very low availability of electroactive surface area for the electrochemical reactions.

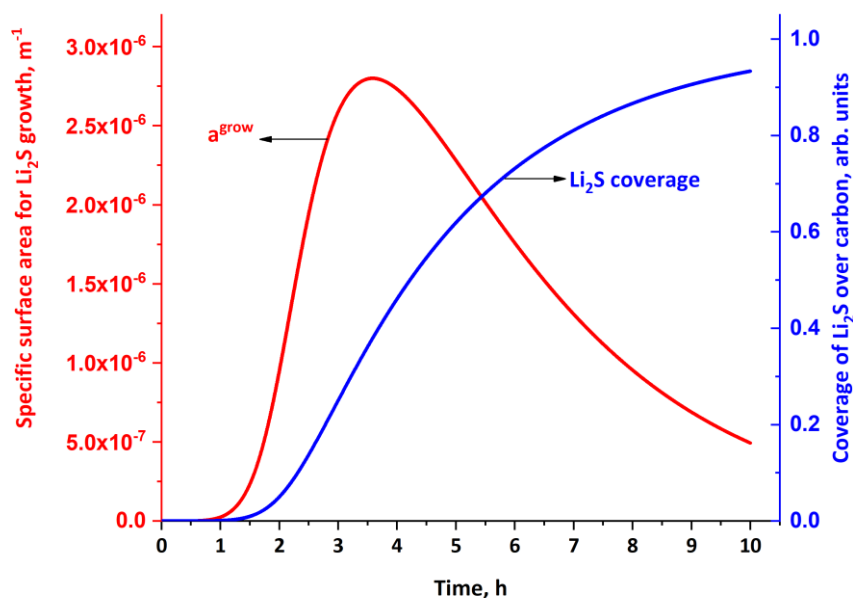


Figure 6.8. The simulated evolutions of the electroactive specific surface area for the Li_2S growth and the coverage of the Li_2S deposits over the cathode during the galvanostatic and the potentiostatic discharge stages.

6.6. Conclusion and perspectives

In this chapter, we have proposed a comprehensive nucleation and growth model to simulate and investigate the Li_2S electrodeposition during the potentiostatic discharge of a Li-S cell. The simulated results of our model have good qualitative agreements with the experimental results. Furthermore, the results of our model show that the Li_2S nucleation occurs below 2.02 V, during which its overpotential facilitates the formation of the stable nuclei. The overall current peak of the potentiostatic discharge stage is primarily dominated by the current of the electrochemical growth of the existing Li_2S deposits. This is consistent with the assumptions of the BFT and SH models [144,145,204]. However, our model shows that the electrochemical growth of the Li_2S deposits is primarily limited by the electroactive cathode surface area rather than the transport of the dissolved species. This conclusion is consistent with the experimental observations of Fan *et al.* [203]. Note that this surface limitation to the Li_2S growth may not be true in the case of conventional Li-S cells with porous electrodes which have very large surface area. The growth of the Li_2S deposits are considered to be progressive, since our modelling results show that the nucleation and growth reactions occur simultaneously.

In the future, our nucleation and growth model could be incorporated into our discharge model to investigate the electrodeposition of the Li_2S in the practical Li-S batteries. Furthermore, since the heterogenous free energy for the formation of Li_2S in our model depends on the binding and surface energies, it could be utilized to investigate the electrodeposition of the Li_2S from different electrolytes and over the surfaces of different cathode host materials.

A.6 Appendix: Numerical Schemes

A.6.1. Discretization of the population balance equation

The population balance of the Li_2S deposits was solved using a discretization method adopted from the work previously carried out in our lab by Yin *et al.* [207]. In this method, the possible particle size range of the Li_2S deposits were discretized into L equal sized bins (Fig. A-6.1).

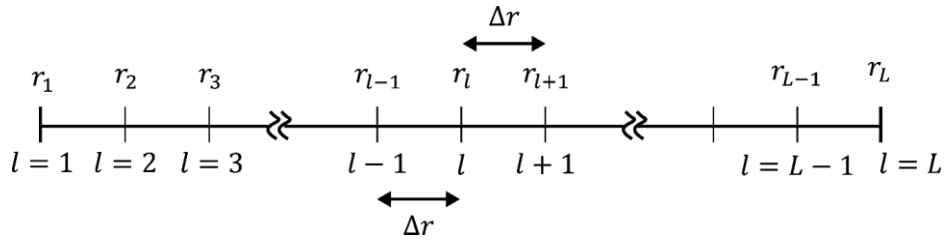


Figure A-6.1. The schematic representation of the discretization of the particle sizes of Li₂S deposits within the range $r_1 \leq r_l \leq r_L$.

The bin size is determined as follows (Fig. A-6.1),

$$\Delta r = r_{l+1} - r_l = \frac{r_L - r_1}{L} \quad (\text{A-6.1})$$

where, r_{l+1} and r_l are the particle sizes of the deposits in $(l + 1)^{th}$ and l^{th} bin. Furthermore, r_1 and r_L are the smallest and the largest particle sizes, respectively in the possible assumed particles size range.

Furthermore, the time step is calculated as follows,

$$\Delta t = t^{n+1} - t^n \quad (\text{A-6.2})$$

where, t^{n+1} and t^n are simulation time at $(n + 1)^{th}$ and n^{th} time step.

In this method, the population balance equation is discretized in terms of number density (N_r) instead of number density per unit volume ($f(v_r)$) of the Li₂S deposits of size r . Since N_r could be used directly in our model. Therefore, the discretized form of the population balance of the deposits in l^{th} particle size bin is given as follows,

$$\frac{N_l^{n+1} - N_l^n}{\Delta t} = \dot{N}_l + \frac{\Delta N_l^{total}}{\Delta t} \quad (\text{A-6.3})$$

where, N_l^{n+1} and N_l^n are the number densities of the deposits in the l^{th} bin at the $(n + 1)^{th}$ and n^{th} time step. \dot{N}_l is the nucleation source term for the particle number density of the deposits in l^{th} bin. Furthermore, ΔN_l^{total} is the total change in the particle number density of the deposits in l^{th} bin brought about by the Li₂S growth and shrinkage reactions.

The change in the particle number density in the l^{th} bin due to the growth of some of its deposits, whose size change from r_l to r_{l+1} , is computed as follows,

$$\Delta N_l^+ = \begin{cases} -\frac{\Delta \epsilon_l}{r_l^3 - r_{l+1}^3}, & \Delta \epsilon_l > 0 \\ 0, & \Delta \epsilon_l \leq 0 \end{cases} \quad (\text{A-6.4})$$

where $\Delta \epsilon_l$ is the change in the volume fraction of the deposits in the l^{th} bin.

The change in the particle number density in the l^{th} bin due to the shrinkage of some its deposits, whose size change from r_l to r_{l-1} , is determined using the Eq. A-6.5.

$$\Delta N_l^- = \begin{cases} \frac{\Delta \epsilon_l}{r_{l-1}^3 - r_l^3}, & \Delta \epsilon_l < 0 \\ 0, & \Delta \epsilon_l \geq 0 \end{cases} \quad (\text{A-6.5})$$

Note that the particle number density in the l^{th} bin will also change due to the growth and shrinkage of the deposits in the $(l - 1)^{th}$ and $(l + 1)^{th}$ bins, respectively. Therefore, the total change in the particle number density of the deposits in l^{th} bin is computed as follows,

$$\Delta N_l^{total} = -\Delta N_l^+ - \Delta N_l^- + \Delta N_{l-1}^+ + \Delta N_{l+1}^- \quad (\text{A-6.6})$$

Finally, the particle number density in the l^{th} bin at the $(n + 1)^{th}$ time step is given by the Eq. A-6.7.

$$N_l^{n+1} = N_l^n + \Delta t \dot{N}_l - \Delta N_l^+ - \Delta N_l^- + \Delta N_{l-1}^+ + \Delta N_{l+1}^- \quad (\text{A-6.7})$$

The matricized form of the Eq. A-6.7, is used to calculate the particle number density of the deposits in all the bins at the $(n + 1)^{th}$ time step as follows,

$$N^{n+1} = N^n + \Delta t \dot{N} - M^l (\Delta N^+ + \Delta N^-) + M^{l-1} \Delta N^+ + M^{l+1} \Delta N^- \quad (\text{A-6.8})$$

where, N^{n+1} and N^n are the $L \times 1$ vectors which contain the lists of particle number densities of the deposits in all the bins at the $(n + 1)^{th}$ and n^{th} time steps, respectively. \dot{N} is the $L \times 1$ vector which contains a list of nucleation source terms of all the bins.

In the equation Eq. A-6.8, ΔN^+ and ΔN^- respectively are the $L \times 1$ vectors which contain the changes in the particle number densities due to growth and shrinkage some deposits in all the bins. The ΔN^+ and ΔN^- vectors are shown in Eq. A-6.9 and A-6.10, respectively.

$$\Delta N^+ = \begin{pmatrix} \Delta N_1^+ \\ \Delta N_2^+ \\ \Delta N_3^+ \\ \vdots \\ \Delta N_{L-1}^+ \\ 0 \end{pmatrix} \quad (\text{A-6.9})$$

$$\Delta N^- = \begin{pmatrix} \Delta N_1^- \\ \Delta N_2^- \\ \Delta N_3^- \\ \vdots \\ \Delta N_{L-1}^- \\ 0 \end{pmatrix} \quad (\text{A-6.10})$$

In the equation Eq. A-6.8, the M^l , M^{l-1} and M^{l+1} are $L \times L$ matrices which are shown in Eq. A-6.11, A-6.12 and A-6.13, respectively.

$$M^l = \begin{pmatrix} 1 & 0 & 0 & \cdots & 0 & 0 \\ 0 & 1 & 0 & \vdots & \vdots & 0 \\ 0 & 0 & 1 & \ddots & \vdots & 0 \\ \vdots & \vdots & \ddots & \ddots & 0 & 0 \\ \vdots & \vdots & \vdots & 0 & 1 & 0 \\ 0 & 0 & 0 & \cdots & 0 & 0 \end{pmatrix} \quad (\text{A-6.11})$$

$$M^{l-1} = \begin{pmatrix} 0 & 0 & 0 & \cdots & 0 & 0 \\ 1 & 0 & \vdots & \vdots & \vdots & 0 \\ 0 & 1 & 0 & \ddots & \vdots & 0 \\ \vdots & 0 & \ddots & \ddots & \vdots & \vdots \\ \vdots & \vdots & 0 & 1 & 0 & 0 \\ 0 & 0 & 0 & \cdots & 1 & 0 \end{pmatrix} \quad (\text{A-6.12})$$

$$M^{l+1} = \begin{pmatrix} 0 & 1 & 0 & \cdots & 0 & 0 \\ 0 & 0 & 1 & \vdots & \vdots & \vdots \\ 0 & 0 & 0 & \ddots & \vdots & \vdots \\ \vdots & \vdots & \ddots & \ddots & 1 & 0 \\ \vdots & \vdots & \vdots & 0 & 0 & 1 \\ 0 & 0 & 0 & \cdots & 0 & 0 \end{pmatrix} \quad (\text{A-6.13})$$

Chapter 7. Experimental work and discharge model validation

Contents

| | |
|---|------------|
| 7.1. Introduction | 181 |
| 7.2. Materials used..... | 181 |
| 7.3. Surface area and porosimetry analyses of carbon nano powder | 181 |
| 7.4. Sulfur impregnation..... | 184 |
| 7.5. C/S electrode film fabrication | 188 |
| 7.5.1. Slurry preparation | 188 |
| 7.5.2. Coating of electrode film | 189 |
| 7.6. Coin cell assembly | 190 |
| 7.7. Galvanostatic measurement..... | 190 |
| 7.8. Theoretical methodology..... | 191 |
| 7.9. Results and discussion | 195 |
| 7.9.1 Galvanostatic cycling..... | 195 |
| 7.9.2. The experimental vs the simulated discharge curves..... | 196 |
| 7.9.3. The simulated evolutions of cathode porosities, solid and dissolved species..... | 197 |
| 7.10. Conclusions | 200 |

Chapter 7. Experimental work and discharge model validation

7.1. Introduction

In this chapter the experimental works such as the surface area and the porosimetry analyses of carbon particles, sulfur impregnation, carbon/sulfur (C/S) composite electrode fabrication and galvanostatic cycling of Li-S coin cells are presented. These experiments were carried out to validate our discharge model. Therefore, the experimental discharge curves are presented in comparison to the simulated ones.

7.2. Materials used

A graphitized mesoporous carbon nano powder from Sigma Aldrich (699624) was used as the carbon host material in the cathodes of our Li-S cells. A 99.5% pure sulfur powder from Alfa Aesar was used for impregnating the carbon host material of the cathode. In the carbon/sulfur cathode films, the carbon super P from Timcal and the polyvinylidene fluoride (PVDF) respectively were the conductive additive and the binder. Finally, 1 M LiTFSI in TEGDME:DOL (1:1 v/v) was the electrolyte used and it was acquired from Solvionic.

7.3. Surface area and porosimetry analyses of carbon nano powder

In order to compare the experimental and modelling results, the details about the average mesostructural properties of the cathode are needed. Therefore, the pristine and the sulfur impregnated mesoporous carbon nano powders were analysed using the Micrometrics ASAP 2020 surface area and porosity analyser. Initially, about 1 g of the pristine carbon nano powder was degassed under vacuum at 300 °C for 12 hours. The N₂ adsorption and desorption isotherms of the degassed carbon nano powder were measured at 77 K (Fig. 7.1). The hysteresis between the adsorption and desorption isotherms indicates that the carbon nano powder was porous (Fig. 7.1). Therefore, the pore size distribution was estimated using the Barret-Joyner-Halenda (BJH) model. The pore size distribution shows that the mesoporous carbon nano powder actually had micropores with diameter around 2.5 nm (Fig. 7.2). The

microporosity and total porosity of the pristine carbon nano powder was estimated using the following equation,

$$\varepsilon = \frac{V_{pore}}{V_{pore} + \frac{1}{\rho_c}} \quad 7.1$$

where V_{pore} is either micropore volume or total pore volume (Table 7.1) and ρ_c is the density of the carbon powder ($= 1.88 \text{ g. cm}^{-3}$) estimated using the pycnometer.

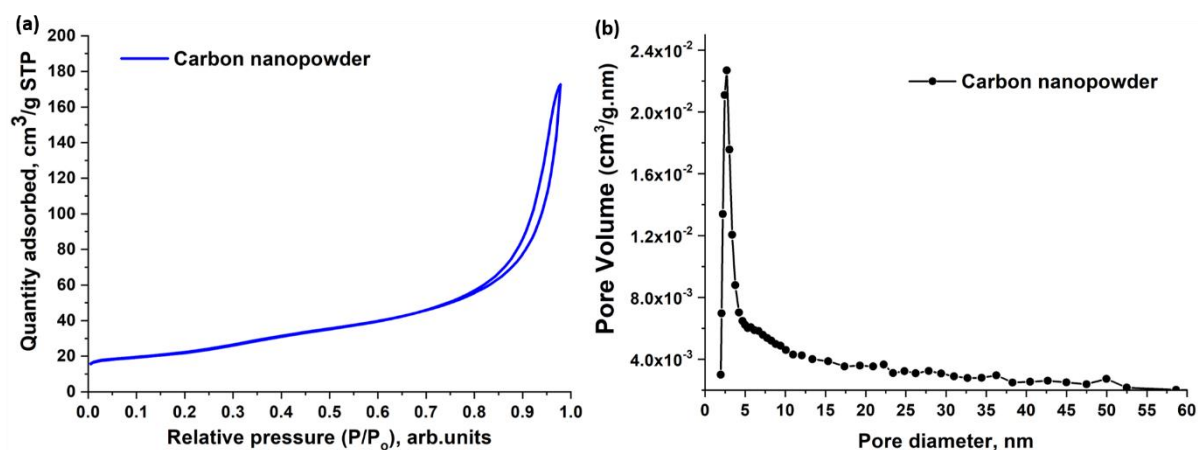


Figure 7.1. (a) The N₂ adsorption/desorption isotherm and (b) pore size distribution of pristine mesoporous carbon nano powder 699624.

Table 7.1. Mesosstructural properties of pristine carbon powder

| i. Porosimetry parameters | | |
|---|---|----------|
| Type of pore volumes | Values | Porosity |
| a. BJH adsorption cumulative pore volume ($1.7\text{nm} < d_{pore} < 300\text{nm}$) | $0.27 \text{ cm}^3 \cdot \text{g}^{-1}$ | 0.33 |
| b. t-plot micropore volume | $0.0066 \text{ cm}^3 \cdot \text{g}^{-1}$ | 0.012 |
| ii. Surface area parameters | | |
| Types of surface area | Values | |
| a. BET surface area | $80.54 \text{ m}^2 \cdot \text{g}^{-1}$ | |
| b. t-plot external surface area | $64 \text{ m}^2 \cdot \text{g}^{-1}$ | |
| c. t-plot micropore area | $16.5 \text{ m}^2 \cdot \text{g}^{-1}$ | |
| d. Calculated surface area | $65.5 \text{ m}^2 \cdot \text{g}^{-1}$ | |

The scanning electron microscopy (SEM) micrographs show that the pristine carbon nano powder is an agglomerate of carbon nanoparticles with average diameter around 50nm (Fig. 7.3). Assuming spherical carbon particles, the external specific surface area (A_c) could be calculated (Eq. 7.2) using particle radius (r_c).

$$A_c = \frac{3}{r_c \rho_c} \times 1000 \quad 7.2$$

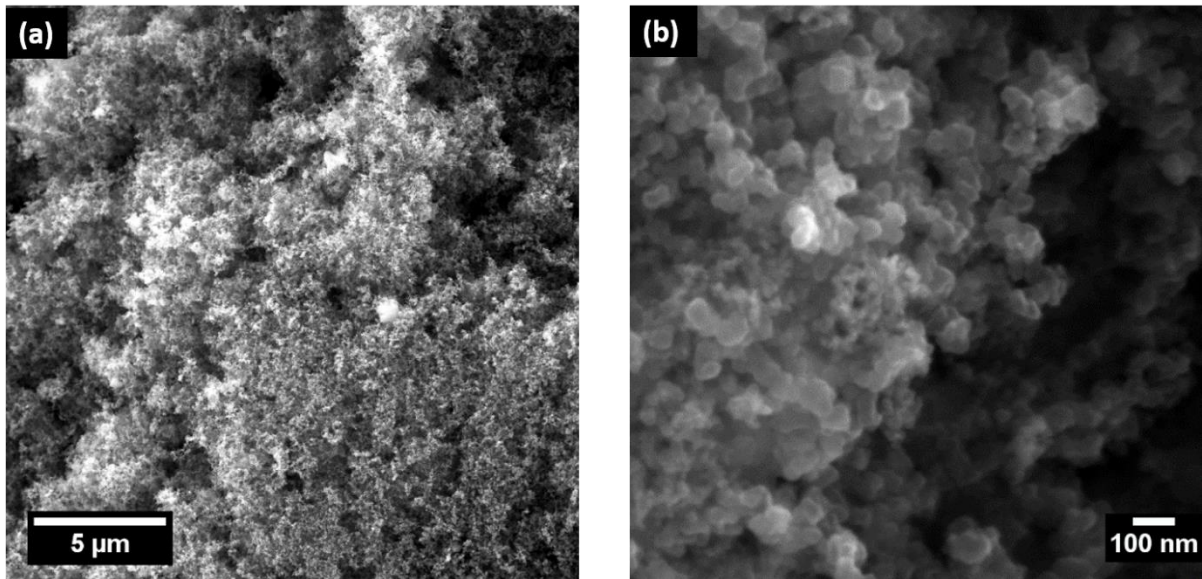


Figure 7.2. (a) Secondary electron and (b) back scattered electron SEM micrographs of pristine carbon nano powder 699624.

The calculated specific surface area is $65.5\text{m}^2.\text{g}^{-1}$, which is very close to the external surface area of the carbon nano powder ($64\text{m}^2.\text{g}^{-1}$) determined using the t-plot method (Table 7.1). However, the BET surface area of the carbon nano powder is $80.5\text{m}^2.\text{g}^{-1}$, where the additional surface corresponds to the those inside the micropores. This is because the difference between the BET and the calculated surface areas ($= 15\text{m}^2.\text{g}^{-1}$) is very close to the t-plot micropore area (Table 7.1). This analysis reveals that there are no mesopores ($d_{\text{pore}} > 4\text{nm}$) within the carbon particles themselves, since the external and micropore surface areas completely account for its total surface area. Therefore, most of the cumulative pore volume of the carbon nano powder correspond to inter-particle void volume, since the micropore volume is very low (Table 7.1).

7.4. Sulfur impregnation

Prior to sulfur impregnation, the mesoporous carbon nano powder was heated overnight at 300°C under secondary vacuum of about 10^{-4} mbar to remove the adsorbed moisture from its surface. The precipitated sulfur powder was dried overnight at 60°C under vacuum using Buchi oven. The dried carbon and sulfur powders were then taken inside the glove box and

mixed thoroughly using a mortar and a pestle. The well mixed carbon/sulfur mixture was then sealed inside an autoclave bomb parr under argon atmosphere. The autoclave bomb parr was placed inside an oven and heated at rate of $5\text{ }^{\circ}\text{C}\cdot\text{min}^{-1}$ up to $155\text{ }^{\circ}\text{C}$ which was maintained for 6 hours. Subsequently, the autoclave was allowed to cool down to room temperature. Finally, the autoclave was opened under argon atmosphere inside a glove box and the sulfur impregnated carbon nano powder was stored in a bottle for future use.

The $S_{8(s)}$ impregnated carbon nano (C/S) powder was degassed at $60\text{ }^{\circ}\text{C}$ for 6 hours and analysed using the Micrometrics ASAP 2020 surface area and porosity analyser. The hysteresis in the N_2 adsorption/desorption isotherms of the C/S powder was smaller than that of the pristine carbon nano powder. This is because the cumulative pore volume of the inter-particle mesopores has reduced to (Table 7.2), due to the presence of solid sulfur in them (Fig. 7.4).

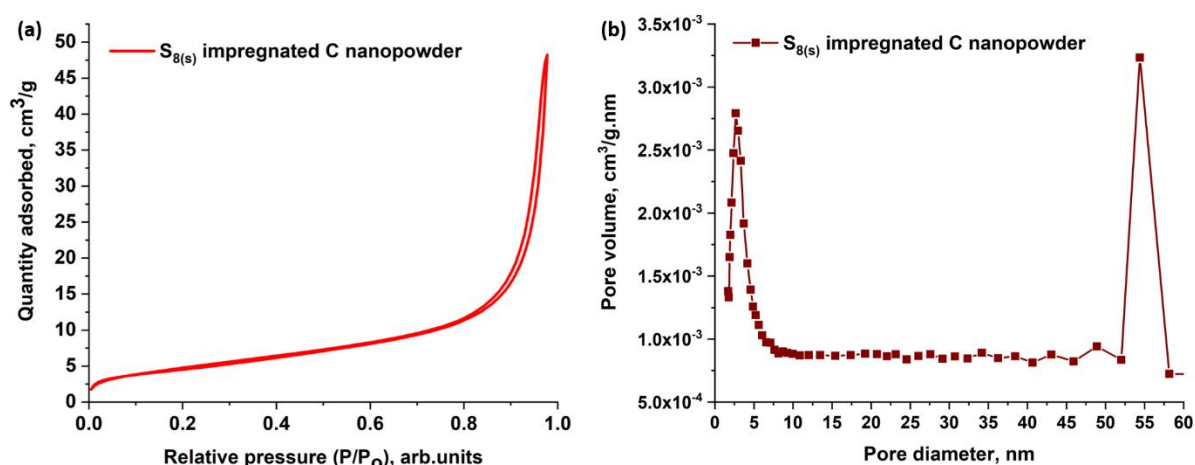


Figure 7.3. (a) The N_2 adsorption/desorption isotherm and (b) pore size distribution of $S_{8(s)}$ impregnated carbon nano powder.

The BET surface area of the C/S powder was also lower than that of the pristine carbon powder (Tables 7.1 and 7.2). This was due to the presence of large solid sulfur precipitates in the inter-particle pores of the C/S powder (Fig. 7.4).

Table 7.2. Mesostructural properties of sulfur impregnated carbon nano powder.

| iii. Porosimetry parameters | |
|--|--|
| Type of pore volumes | Values |
| a. BJH adsorption cumulative pore volume ($1.7\text{nm} < d_{\text{pore}} < 300\text{nm}$) | $0.0746 \text{ cm}^3 \cdot \text{g}^{-1}$ |
| b. t-plot micropore volume | $-0.000232 \text{ cm}^3 \cdot \text{g}^{-1}$ |
| iv. Surface area parameters | |
| Types of surface area | Values |
| e. BET surface area | $16.5 \text{ m}^2 \cdot \text{g}^{-1}$ |
| f. t-plot external surface area | $16.6 \text{ m}^2 \cdot \text{g}^{-1}$ |
| g. t-plot micropore area | Not available |

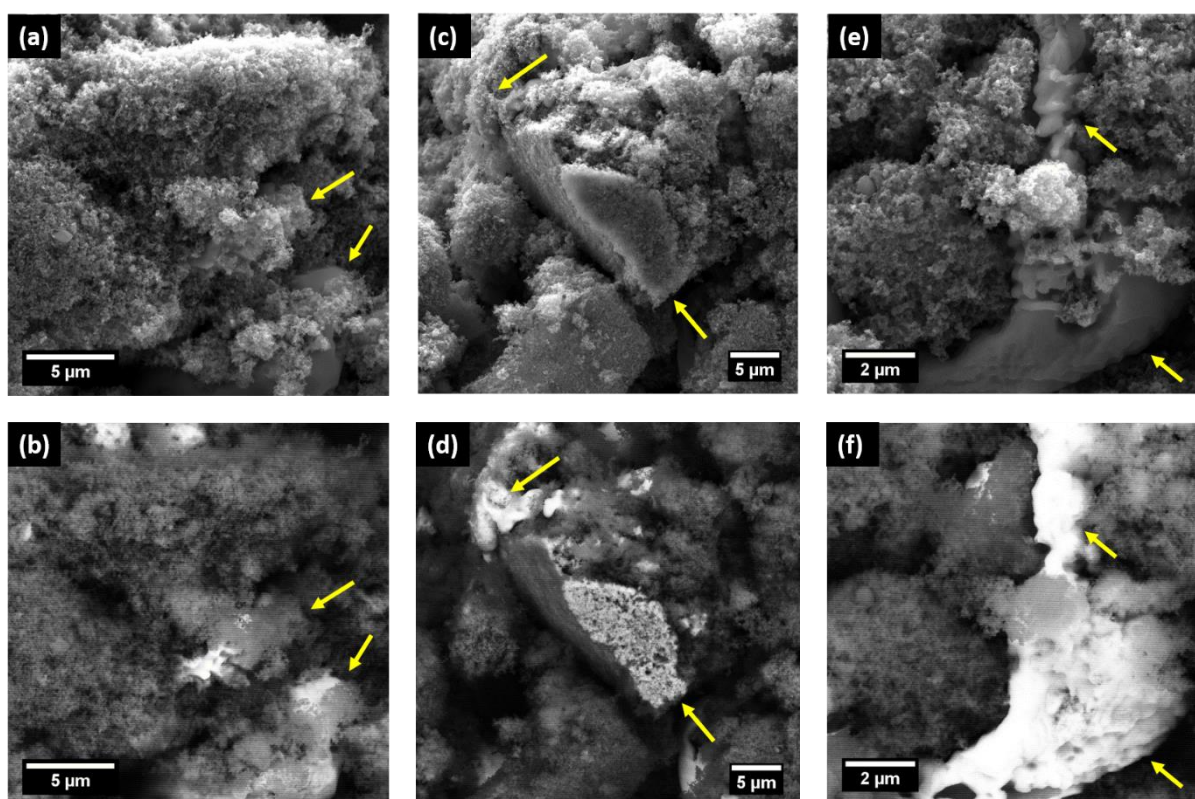


Figure 7.4. SEM micrographs of sulfur impregnated carbon (C/S) nano powder where (a), (c) and (e) are secondary electron images and (b), (d) and (f) are their respective back scattered electron images. The yellow arrows in the images show the locations of solid sulfur.

Note that the BET and the t-plot external surface areas of the C/S powder are similar (Table 7.2). This indicates that the micropores in the carbon nano powder are blocked by the solid sulfur precipitates. Furthermore, the SEM image of the C/S powder with higher magnification, shows deposits of sulfur over the surface of some of the carbon particles (Fig. 7.5). These sulfur deposits will directly block the micropores of the carbon nanoparticles. Furthermore, the relatively very low t-plot micropore volume of the C/S powder proves that the micropores of the carbon nanoparticles are blocked by the solid sulfur precipitates.

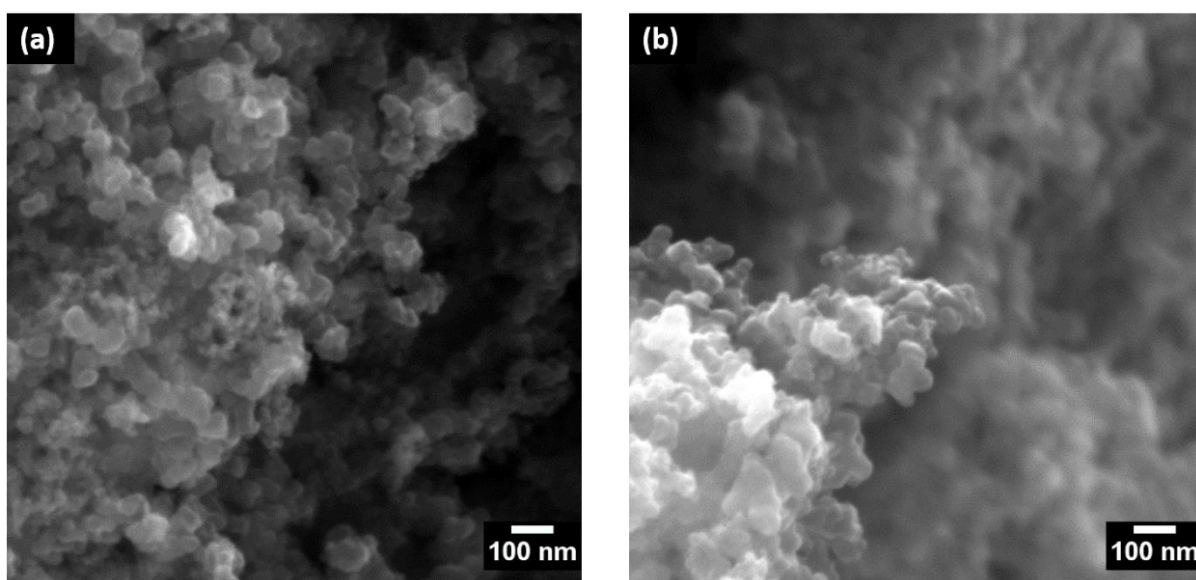


Figure 7.5. SEM back scattered electrons micrographs of: (a) pristine and (b) sulfur impregnated carbon nano powders.

The negative sign of the t-plot micropore volume of the C/S powder could be due to the sublimation of some of the solid sulfur precipitates during the porosimetry analysis. After the analysis, we found some yellow deposits on the wall of the glass sample holder of the ASAP porosimetry analyser. Therefore, we carried out Thermal Gravimetric Analyses (TGA) of the C/S powder before and after porosimetry analysis to find out the amount of solid sulfur lost from the C/S powder due to sublimation.

During TGA, the C/S powders were heated from 25 to 500 °C at a rate of 10 K.min⁻¹, under argon atmosphere. As expected, the weight loss of the C/S powder before the porosimetry or BET analysis was 49.99%, which corresponds to the weight percentage of the solid sulfur (Fig. 7.6). Whereas, the solid sulfur weight percentage of the C/S powder after the porosimetry analysis was found to be 48.36%. Therefore, during the porosimetry analysis around 1.6% of the solid sulfur precipitates sublimized during the porosimetry analysis.

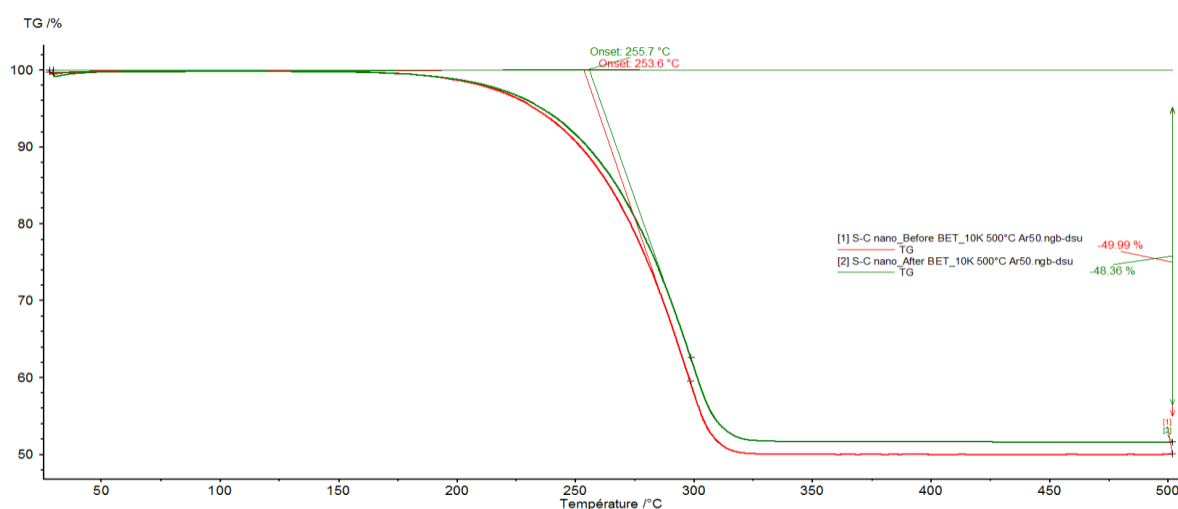


Figure 7.6. TGA results of the C/S powder before and after porosimetry analysis.

7.5. C/S electrode film fabrication

7.5.1. Slurry preparation

All the solid powder ingredients of the slurry (Table 7.3) were dried and taken inside the glove box. The solid powder ingredients were then mixed properly using a mortar and a pestle inside the glove box. The well mixed solid powder was sealed inside a bottle. NMP solvent was added to the bottle containing the well mixed solid ingredients and the whole mixture was stirred well using a magnetic stirrer for 12 hours. The masses of the solid powder mixture and the liquid NMP solvent are listed in Table 7.4.

Table 7.3. The breakdown of solid ingredients used in the slurry.

| S.No | Materials | Mass | Weight % |
|------|--|----------|----------|
| 1 | C/S (mass ratio=1:1) | 0.4425 g | 75% |
| 2 | PVdF (Binder) | 0.0885 g | 15% |
| 3 | Carbon super P (Csp) (Conductive additive) | 0.059 g | 10% |
| 4 | Total solid mixture (C/S + PvDF + Csp) | 0.590 g | 100% |

Table 7.4. The masses and the weight fractions of the solid powder mixture and the liquid NMP solvent used in the slurry.

| S.No | Materials | Mass | Weight % |
|------|--|---------|----------|
| 1 | Total solid mixture (C/S + PVdF + Csp) | 0.590 g | 16.4% |
| 2 | NMP solvent | 3.000 g | 83.6% |
| 3 | Total slurry weight (C/S + PVdF + Csp + NMP) | 3.590 g | 100% |

7.5.2. Coating of electrode film

The C/S electrode slurry was coated over an aluminium (Al) current collector using a doctor blade and an electrode coating machine. The thickness of the doctor blade was adjusted to 40 μm . The C/S electrode slurry was very viscous; therefore, it was taken out of the bottle using a spatula or a syringe while applying it to the doctor blade. The freshly coated electrode film was dried overnight at 40°C. After drying, the electrodes for making coin cells were punched using a 11 mm puncher. Finally, the punched-out electrodes were dried at 50°C for 6 hours using the Bushi oven under vacuum to remove the moisture.

7.6. Coin cell assembly

The galvanostatic measurements were carried using coin cells (Fig. 7.7), which were assembled inside the glove box under Ar atmosphere. As mentioned before, a C/S electrode film with diameter 11 mm was used as the cathode and a similar sized Li metal foil was used as the anode. Prior to the cell assembly, the surfaces of the Li metal foil were gently scratched using a spatula to remove the oxide layers. A celgard separator (SK innovation) was used to separate the anode and the cathode. The celgard separator was wetted with pure 1 M LiTFSI TEGDME:DOL (1:1 v/v) electrolyte. The electrolyte to solid sulfur (E/S) ratio was $20 \mu\text{L} \cdot \text{mg}_{\text{S}_{8(\text{s})}}^{-1}$. Due to its high viscosity, the electrolyte does not wet the separator properly. Therefore, the electrolyte was spread out evenly over the separator using the tip of the micropipette. After assembling the coin cell, it was tightly sealed inside the glove box using a pneumatic press.

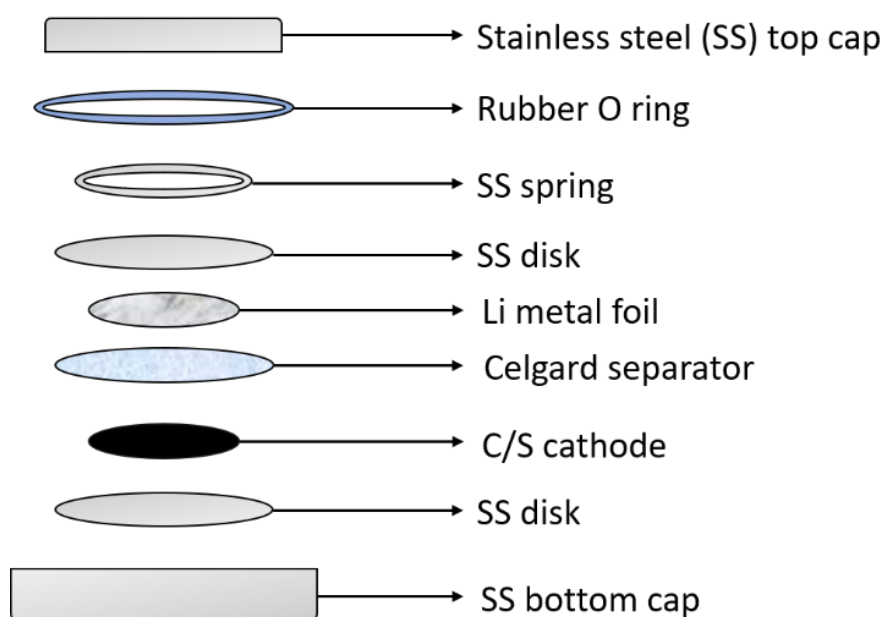


Figure 7.7. Coin cell set-up.

7.7. Galvanostatic measurement

In order to prevent the voltage loss due to self-discharge, the galvanostatic cycling of the coin cells were started immediately after their assembly. The galvanostatic measurements of the

coin cells were carried out using the VMP Biologic rectifier, outside the glove box at room temperature. Measurements at three different C-rates namely C/20, C/10 and C/5 were carried. The information of the coin cells used for different C-rates are listed in the Table 7.5.

Table 7.5. Details of the coin cells used for galvanostatic cycling at different C-rates.

| C-rate | Sulfur mass loading <i>mg. cm⁻²</i> | Electrolyte volume <i>μL</i> | Current density <i>mA. cm⁻²</i> |
|---------------|--|--|--|
| C/20 | 1.46 | 27.7 | 6.12 |
| C/10 | 1.85 | 35.0 | 15.53 |
| C/5 | 1.70 | 32.3 | 25.2 |

7.8. Theoretical methodology

We slightly modified our discharge model (Chapter 4), to well represent the experiments. The microporosity of our carbon nano powder was only 1.2% (Table 7.1) and their micropores got blocked after sulfur impregnation. Furthermore, the microporosity of our cathodes were very low even after the dissolution, since the volume fraction carbon used in our cathodes were very low (≈ 0.25). Therefore, we neglected the microporosity of the carbon particles in our model. In our modified discharge model, the intra-flux term in the mass conservation equation of the species within the inter-particle pores (Eq. 4.13) was not considered. Additionally, we also neglected the mass conservation equation of the species within the micropores of the carbon particles (Eq. 4.13). The cathode potential was calculated directly from the current balance equation,

$$I_G = - \sum_j \int_B^c (a_1(i_1)_j) dx \quad (7.3)$$

where, I_G and a_1 are the applied current density and specific surface area of the cathode. $(i_1)_j$ is the current density of the electrochemical reaction j , which is determined using the Butler-Volmer equation.

Since 1 M LiTFSI in TEGDME:DOL was used in our Li-S coin cells, we have considered a comprehensive set of cathode reaction steps (Eqs. 7.4 to 7.12) in our modified discharge model.



These aforementioned reaction steps were determined using our cyclic voltammetry model (Chapter 5). The parameters of our modified discharge model are listed in the Table 7.6. Most

of the parameter values used in our discharge model are same as those used in the cyclic voltammetry model. However, in our Li-S coin cells we have used Li metal foil as the anode. Furthermore, there are uncertainties in the conversion factors for converting the standard potentials from vs Ag/Ag⁺ to vs Li/Li⁺, due to the LJP in Ag/AgNO₃ electrode. Therefore, the standard potentials reported in the Table 7.6 were fitted by qualitatively matching the simulated results with the experiments. Additionally, we have used different form Butler-Volmer equations to calculate the current densities of different electrochemical reaction,

$$i_j = i_j^0 \left(\prod_i \left(\left(\frac{(c_1)_i}{(c_{ref})_i} \right)^{S_{ij}} \right)_{S_{ij}>0} e^{\left(\frac{(1-\alpha_j)n_j F \eta_j}{RT} \right)} \right. \\ \left. - \prod_i \left(\left(\frac{(c_1)_i}{(c_{ref})_i} \right)^{S_{ij}} \right)_{S_{ij}<0} e^{\left(\frac{-\alpha_j n_j F \eta_j}{RT} \right)} \right) \quad (7.16)$$

Where, c_{ref} and η_j are reference concentration and overpotential. The aforementioned equation is the simplified version of the Butler-Volmer equations (Eqs. 4.9-4.11) reported in chapter 4. The exchange current densities (i_j^0) were also fitted by qualitatively matching the simulated results with the experiments.

Table 7.6. Parameters of different reactions and diffusion coefficients of dissolved species considered in our modified discharge model.

| iii. Electrochemical reaction parameters | | | | | | vi. Dissolved species parameters | |
|--|---|---------|--|--|--------------------|----------------------------------|-------------------------------|
| Reaction No. (<i>j</i>) | Reaction | Eq. No. | i^0 (A) | U^0 (V) | α | Species $M_i^{z_i}$ | D_i (m.s ⁻¹) |
| 1 | S_8/S_8^{2-} | (7.5) | 3.94×10^{-4a} | 2.51 ^a | 0.460 ^c | | |
| 2 | S_8^{2-}/S_6^{2-} | (7.7) | 3.94×10^{-7a} | 2.47 ^a | 0.500 ^b | S_8 | 1.6335×10^{-10a} |
| 3 | S_6^{2-}/S_4^{2-} | (7.9) | 3.94×10^{-8a} | 2.25 ^a | 0.420 ^a | S_8^{2-} | 8.0000×10^{-11a} |
| 4 | S_4^{*-}/S_4^{2-} | (7.10) | 2.63×10^{-8a} | 2.25 ^a | 0.500 ^d | S_6^{2-} | 8.0000×10^{-11b} |
| 5 | S_4^{2-}/S_2^{2-} | (7.11) | 3.98×10^{-8a} | 2.20 ^a | 0.200 ^a | S_4^{*-} | 3.5000×10^{-11f} |
| 6 | S_3^{*-}/S_3^{2-} | (7.12) | 9.73×10^{-4a} | 2.17 ^a | 0.420 ^a | S_2^{2-} | 3.5000×10^{-11f} |
| 7 | S_3^{2-}/S_2^{2-} | (7.13) | 1.97×10^{-8a} | 2.13 ^a | 0.350 ^a | S_4^{2-} | 3.5000×10^{-11f} |
| 8 | S_2^{2-}/S^{2-} | (7.14) | 3.94×10^{-10a} | 2.11 ^a | 0.658 ^a | S_3^{*-} | 3.5000×10^{-11f} |
| iv. Homogeneous chemical reaction parameters | | | | | | S_3^{2-} | 3.5000×10^{-11f} |
| Reaction No. (<i>j</i>) | Reaction | Eq. No. | k_j^f (s ⁻¹) | k_j^{eq} (mol ⁻¹) | S_2^{2-} | 3.5000×10^{-11f} | |
| 1 | $S_8^{2-} \rightleftharpoons 2S_4^{*-}$ | (7.6) | 8.4 ^a | 4.2088 ^a | S^{2-} | 3.5000×10^{-11f} | |
| 2 | $S_6^{2-} \rightleftharpoons 2S_3^{*-}$ | (7.8) | 9.5 ^a | 12.6263 ^a | | | |
| v. Heterogeneous precipitation/dissolution reaction parameters | | | | | | | |
| Reaction No. (<i>k</i>) | Reaction | Eq. No. | k_k (mol ² .m ⁻⁶ .s ⁻¹) | K_k^{sp} (mol ³ .m ⁻⁹) | Solid species | V_k (m ⁻³ .mol) | |
| 1 | $S_8^{2-} \rightleftharpoons S_{8(s)}$ | (7.4) | 0.6 (s ⁻¹) ^a | 6 (mol.m ⁻³) ^m | $S_{8(s)}$ | 1.239×10^{-4b} | |
| 2 | $2Li^+ + S^{2-} \rightleftharpoons Li_2S_{(s)}$ | (7.15) | 3×10^{-4a} | 10 ^{2a} | $Li_2S_{(s)}$ | 2.768×10^{-4b} | |

^aFitted parameters.^{b, c, d and e}Assumed parameters taken from Refs. [119], [179], [184] and [114] respectively.^fExperimental parameters taken from Ref. [194].^mMeasured parameter.

Since, the sulfur mass loadings in our Li-S coin cells are different, the initial cathode design parameters were calculated and listed in the table 7.7.

Table 7.7. The initial cathode design parameters of our Li-S coin cells cycled which were at different C-rates.

| Parameters | Symbols | Units | C/20 | C/10 | C/5 |
|-------------------------------|-----------------------|----------|-----------------------|-----------------------|-----------------------|
| Number density of particles | ρ | m^{-3} | 3.79×10^{21} | 4.81×10^{21} | 4.42×10^{21} |
| Volume fraction of $S_{8(s)}$ | $\epsilon_{S_{8(s)}}$ | — | 0.1763 | 0.2234 | 0.2052 |
| Volume fraction of PVDF | ϵ_{PVDF} | — | 0.08156 | 0.1034 | 0.0950 |
| Maximum cathode porosity | ϵ^{max} | — | 0.6702 | 0.5821 | 0.6157 |
| Initial cathode porosity | ϵ^{init} | — | 0.4932 | 0.3581 | 0.4099 |

7.9. Results and discussion

7.9.1 Galvanostatic cycling

The main objective of this chapter is to compare the simulated results of our discharge model with the experimental ones. Therefore, the galvanostatic cycling of our Li-S coins cells were continued only for few cycles (Fig. 7.8). The highest initial discharge capacity was delivered by the cell with the lowest C-rate (C/20). Whereas, the lowest initial discharge capacity was delivered by the one with the highest C-rate (C/5). However, the overcharging of our Li-S coin cells increased when the C-rate was decreased. The overcharging is due to the polysulfides shuttle between the electrodes of our coin cells. This is because we have used $20 \mu L. mg_{S_{8(s)}}^{-1}$ of pure 1 M LiTFSI in TEGDME:DOL in our cells without any additive or ion selective membrane between the electrodes. The overcharging due the polysulfides shuttle could be potentially

reduced by decreasing the E/S ratio. However, lowering E/S ratio increases the concentration of the polysulfides in the electrolyte and its viscosity. Therefore, the decrease of E/S ratio could lead to the reduction of discharge capacities, due to the increase of the electrolyte and the ionic transport resistances in highly viscous electrolyte. These aforementioned resistance effects are not considered in our discharge model.

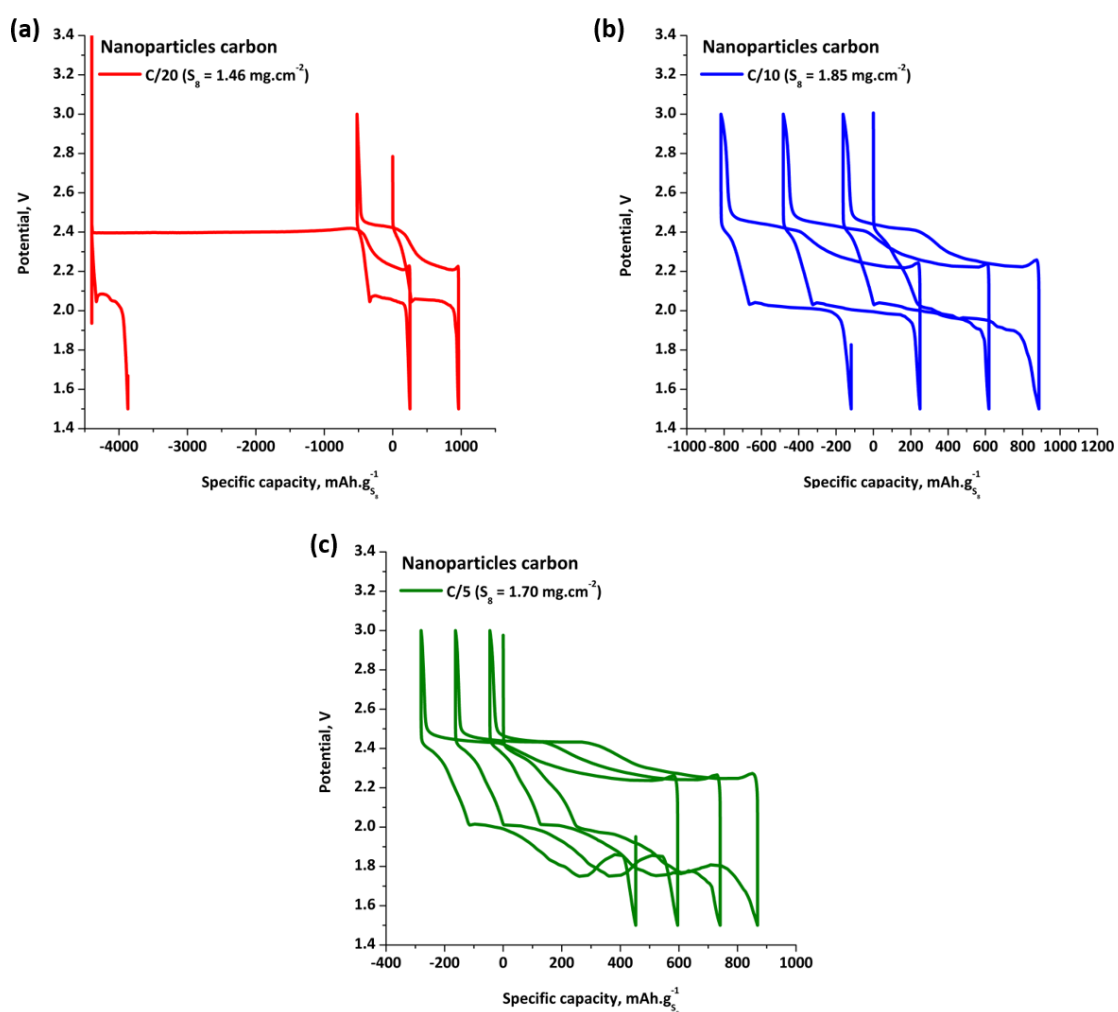


Figure 7.8. The experimental charge and discharge curves of our Li-S coin cells recorded at (a) C/20, (b) C/10 and (c) C/5.

7.9.2. The experimental vs the simulated discharge curves

The simulated discharge curves have certain qualitative resemblance with the experimental results (Fig. 7.9). The perfect matching of the simulated results with the experimental ones is difficult due to the multiple parameters corresponding to the reaction steps and the species considered in our modified discharge model. However, the trends such as the decrease of discharge capacity and the increase of polarization with the increase of C-rate are consistent with experiments. The increase of polarization with the discharge rate is due to increase of the activation overpotentials of electrochemical reactions. However, the separation between high plateau potentials is relatively large in the simulated results. This discrepancy could be due to the Bruggeman relation for calculating active surface (Eq. 7.17), which only gives an approximate estimation of the surface passivation by solid sulfur precipitates. Therefore, the Bruggeman relation could have led to the over estimation of polarization during high plateau stage of the discharge.

$$a_1 = a_1^{max} \left(1 - \frac{(\epsilon_1)_{S_8} + \chi(\epsilon_1)_{Li_2S}}{\epsilon_1^{max}} \right)^\beta \Theta(\delta_1) \quad (7.17)$$

In the Eq. 7.17, $(\epsilon_1)_{S_8}$ and $(\epsilon_1)_{Li_2S}$ are $S_{8(s)}$ and $Li_2S_{(s)}$ volume fractions, respectively. χ is the escape function, which is the fraction $Li_2S_{(s)}$ which do not form a thin layer over carbon surface. β is Bruggeman coefficient.

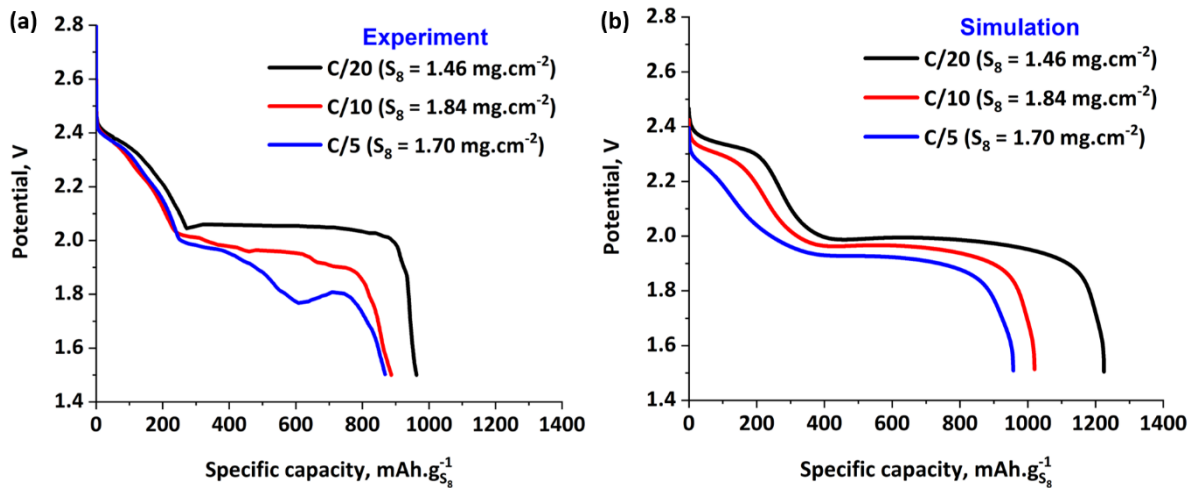


Figure 7.9. (a) Experimental and (b) simulated initial discharge curves produced at different c-rates.

7.9.3. The simulated evolutions of cathode porosities, solid and dissolved species

The initial cathode porosities and solid sulfur loadings are different in each of our Li-S coin cells. Therefore, we normalized the volume fractions of $S_{8(s)}$ and $Li_2S_{(s)}$ with the initial $S_{8(s)}$ and maximum possible $Li_2S_{(s)}$ volume fractions, respectively (Fig. 7.10a). Whereas, the cathode porosities were normalized with their corresponding maximum porosities (Fig. 7.11a and b). The $S_{8(s)}$ dissolves during the high plateau and slopy stages of the discharge (Figs 7.9b and 7.10a). However, the rate of $S_{8(s)}$ dissolution decreased when the discharge rate was increased (Fig. 7.10a). This particular trend is consistent with our kMC discharge simulation results (Chapter 3). Furthermore, the precipitation of $Li_2S_{(s)}$ starts at the beginning of the low plateau stage of the discharge. The rate of $Li_2S_{(s)}$ precipitation is similar for all the C-rates. However, the precipitation of $Li_2S_{(s)}$ starts before the complete dissolution of $S_{8(s)}$ during the C/10 and C/5 discharge simulations. This could be the physical reason behind the invisibility of the potential dips in the experimental discharge curves recorded at C/10 and C/5 (Fig. 7.9a). Finally, the cathode porosities increase during high and slopy stage of the discharge due to the dissolution of $S_{8(s)}$. Whereas, they decrease during the flat low plateau stage due to the precipitation of $Li_2S_{(s)}$. This trend is also consistent with our kMC discharge simulation results.

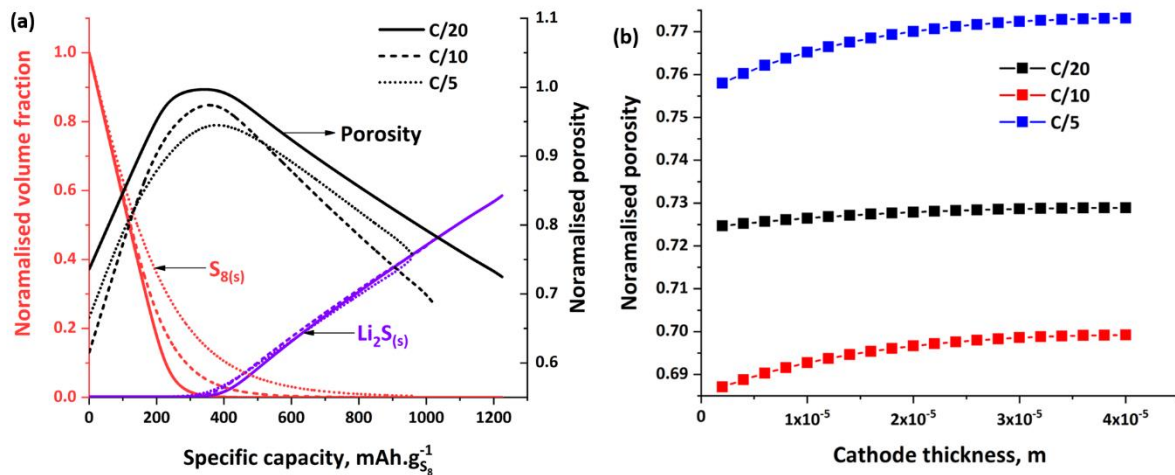


Figure 7.10. (a) The simulated evolutions of the normalized $S_{8(s)}$ and $Li_2S_{(s)}$ volume fractions and cathode porosities, and (b) the calculated normalised porosities at the end of discharge along the cathode thickness.

During the high plateau stage of the discharge, S_8 concentration decreased, while the concentrations of all the other polysulfides increased (Fig. 7.11). The concentrations of all the other polysulfides increase during this stage. Subsequently, during the slopy discharge stage the concentrations of $S_{8(l)}$, $S_{8(l)}^{2-}$ and $S_{4(l)}^{*-}$ decreased significantly, while those of the $S_{6(l)}^{2-}$ and $S_{3(l)}^{*-}$ decreased gently (Fig. 7.11). The $S_{4(l)}^{*-}$ and $S_{3(l)}^{*-}$ radicals were produced due to the dissociations of $S_{8(l)}^{2-}$ and $S_{6(l)}^{2-}$, respectively. Therefore, these aforementioned species had similar evolutions throughout the discharge. Moreover, the concentrations of $S_{4(l)}^{2-}$, $S_{3(l)}^{2-}$, $S_{2(l)}^{2-}$ and $S_{2(l)}^{*-}$ increased significantly during the slopy stage of the discharge (Fig. 7.11). Subsequently, the concentrations of all the polysulfides except those of the $S_{2(l)}^{2-}$ and $S_{2(l)}^{*-}$ decreased during the low plateau stage. However, the concentrations of all the polysulfides remained relatively flat during this stage due to the precipitation of $Li_2S_{(s)}$. Finally, towards the end of discharge the concentrations of all the polysulfides except those of the $S_{3(l)}^{2-}$, $S_{2(l)}^{2-}$ and $S_{2(l)}^{*-}$ decreased significantly. Furthermore, the certain amounts of $S_{3(l)}^{2-}$ and $S_{2(l)}^{2-}$ remained unreduced in the electrolytes in the cathode and the separator after the cell potential had reached the cut-off 1.5 V (Fig. 7.11). This is why, the discharge capacities are lower than theoretical value (Fig. 7.9). Furthermore, the discharge potential reached the cut-off 1.5 V faster during the fast discharge and more amounts of $S_{3(l)}^{2-}$ and $S_{2(l)}^{2-}$ were unreduced at the end. Therefore, the discharge capacity decreased when the C-rate was increased.

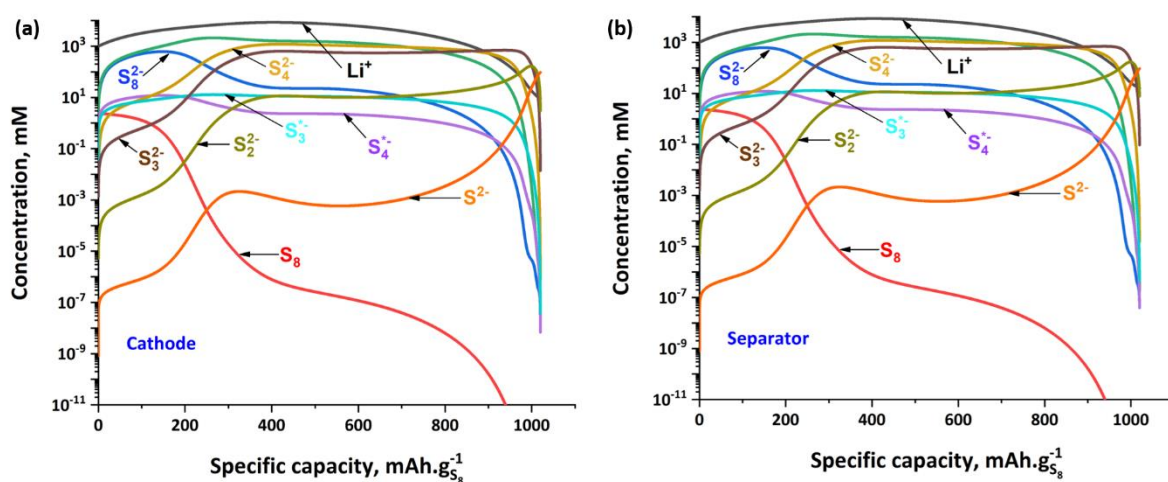


Figure 7.11. Simulated average concentrations of the dissolved species within the pores of the (a) cathode and (b) separator of the Li-S coin cell discharged at C/10.

The cathodes used in our Li-S cells were highly porous, therefore their discharge capacities were not limited by the transport of dissolved species in the electrolyte. Furthermore, our simulation results show that around 68 to 77% of the porous volume of the cathodes remain unoccupied by the $Li_2S_{(s)}$ precipitates at the end of discharge (Fig. 7.10b). However, due to their high porosities, our cathodes had very low specific surface areas. Since, the specific surface area depends on the amount of carbon per unit volume of the electrode, which is very low in our cathodes. Therefore, the low surface area could have led to the early cell potential drop could be due to increase in the overpotential of the sluggish lower order polysulfides reduction reactions.

7.10. Conclusions

In this chapter, we have presented some of the experimental results produced during this thesis work. Furthermore, we also compared the simulated results of our discharge model with the experimental results of our Li-S coin cells. The surface area and porosimetry analysis of the carbon nano powder used in the cathodes of our Li-S coin cells, showed that they are agglomerates of 50 nm carbon particles which have micropores of diameter 2.5 nm. However, the microporosity of the carbon nano powder was very low and their micropores get blocked after sulfur impregnation. Our Li-S coin cells overcharged during galvanostatic cycling due to the polysulfides shuttle between their electrodes. This could be eliminated either by adding additives such as $LiNO_3$ to our electrolyte or by placing an ion-selective membrane between the electrodes.

We modified our discharge model by considering a comprehensive set of reaction steps determined using our cyclic voltammetry model, which is presented in Chapter 5. The simulated results of our modified discharge model have qualitative agreement with the experiments. However, the exact matching of the simulated results with the experiments was not achieved. This is mainly due to the complications arising from the multiple parameters of the reaction steps and species considered in our model. However, simulation results of our model have assisted in assessing the phenomena behind the characteristics of the

experimental discharge curves. The simulated results revealed that the $S_{8(s)}$ dissolution rate decreases with the discharge rate which is consistent with our kMC simulation results. Furthermore, the simulated results also show the $Li_2S_{(s)}$ precipitation start before the complete of dissolution $S_{8(s)}$ during discharge at C/10 and C/5. This could be the reason behind the invisibility of the potential dips in their corresponding experimental discharge curves. Overall, the reduction of higher order polysulfides dominate during the high and slopy stages of discharge. Whereas, the reductions of medium and low order polysulfides dominate the low plateau stage. These results are consistent with the numerous previously reported experimental results [58,59]. Furthermore, our simulations results show that radicals such as S_3^{*-} are produced during the high plateau stage of the discharge, which get consumed during the subsequent slopy and low plateau stages. This is also consistent with the previously reported experimental results [106].

Finally, the simulation results reveal that the discharge capacities are not reduced due to the transport limitations of species in this electrolyte. This is because the cathodes used in our Li-S cells had very high porosity. However, the surface areas of our cathodes were very low. Our simulations show that there were some lower order polysulfides which remain unreduced in the electrolytes of the cathode and the separator. This suggests that the discharge capacities are kinetically limited by the sluggish reduction reactions of these lower order polysulfides. Therefore, the discharge capacity could be increased by using cathodes with higher surface areas.

Chapter 8. General conclusions and perspectives

Chapter 8. General conclusions and perspectives

Li-S batteries are the most attractive among the next generation of batteries, primarily due to its viability. Since, Li-S batteries are being used in some commercial applications. Numerous developments have been done in the past decade in terms of carbon/sulfur composite architectures, protective coating over Li metal anode, etc. which have improved the discharge capacities and cyclability of Li-S batteries. However, due the complex nature of its operating principle, the assessment of the phenomena that occur during the operation of Li-S batteries is not trivial. Moreover, the phenomena behind certain performance limitations and electrochemical characteristics are still under debate in Li-S batteries. A better understanding of these phenomena could assist in the further improvement of the Li-S batteries performance. Therefore, we have developed multiple models that could be applied to investigate certain phenomena that occur at different spatial scales of the Li-S batteries. Furthermore, the main focus of this thesis work was given to the assessment of the underlying phenomena and limitations behind the electrochemical performance of Li-S batteries. It was achieved through the thorough analysis of the simulated results produced using our comprehensive models which consider multiple species, reaction steps and spatial scales. Less focus was given to the exact matching of the simulation results with the experiments.

Numerous atomistic/molecular and continuum level models have been reported in the literature of Li-S batteries. However, very few mesoscopic models have been reported in the literature, which are either too small or less comprehensive. Therefore, to bridge the gap between the atomistic and continuum levels, we have developed a novel 3D kinetic Monte-Carlo (kMC) model, which explicitly simulates the discharge of *in silico* created carbon/sulfur (C/S) mesostructures at the mesoscopic level. This is also the first kMC model applied to Li-S batteries, which considers multiple reaction and diffusion events, that occur from the start to the end of discharge. However, the number of considered events were simplified to reduce the computational cost. The correlation of the simulated effective evolutions with the calculated approximate discharge curves, shows that the $S_{8(s)}$ dissolution and the reduction of higher order polysulfides occur during the high plateau and slopy stages of the discharge. Whereas, the reduction of higher order polysulfides and the electrodeposition of the $Li_2S_{(s)}$ occur during the low plateau stage of the discharge. Due to the S_8 dissolution and the

$Li_2S_{(s)}$ electrodeposition, the cathode porosity initially increases and then decreases during discharge. These effective evolutions during the discharge are consistent with the numerous previous reported modelling [119,141] and experimental results [58,59].

Furthermore, the impacts of the discharge rate and the solid sulfur loading on the mesoscale evolutions of the $Li_2S_{(s)}$ deposits over the carbon surface, were also investigated. It was done by analysing the kMC simulation results using the radial distribution function and the cluster recognition algorithm. The results of these analysis, show that the $Li_2S_{(s)}$ coverage over the carbon surface increases faster during fast discharge. Furthermore, relatively more big clusters of $Li_2S_{(s)}$ deposits are produced during fast discharge. Moreover, during slow discharge some of the $Li_2S_{(s)}$ deposits are formed slightly away from the surface. These variations in the mesoscale evolutions of the $Li_2S_{(s)}$ deposits for two different discharge rates are mainly due to the competition between the diffusion and reaction events of S_2^{2-} . Additionally, these results suggest that the passivation of the carbon surface by the $Li_2S_{(s)}$ deposits, increases faster during fast discharge. Furthermore, the analysis of our kMC results, show that relatively thick $Li_2S_{(s)}$ deposits are produced in the C/S mesostructure which has high sulfur loading (high- S loaded mesostructure). This is mainly due to the low availability of free carbon surface which remains uncovered during the majority of the discharge due to the slow dissolution of $S_{8(s)}$. Furthermore, the thick $Li_2S_{(s)}$ deposits also impede the transport of the dissolved species to the electrode surface. Our kMC results also show that the electrodeposition of $Li_2S_{(s)}$ in the high- S loaded mesostructure, starts before the complete dissolution of $S_{8(s)}$ and its corresponding effective mesostructure porosity remains low throughout the discharge. These aforementioned effects suggest that the passivation of the carbon surface and the blocking of mesopores by the $S_{8(s)}$ and $Li_2S_{(s)}$ precipitates, could increase with the sulfur mass loading. Finally, the effects of the discharge rate and the sulfur mass loading on the $Li_2S_{(s)}$ electrodeposition, could partly explain why the discharge capacities reduce, when these aforementioned parameters are increased.

Our kMC model is very generic, and it is not limited to the geometrical and effective structural properties of the *in silico* created C/S mesostructures reported in this thesis work. It can also be applied to investigate the discharge of mesostructures, which are produced from the experimental tomographic images.

As mentioned before, our kMC model simulates the discharge of the C/S cathode composites at the mesoscopic level. Therefore, it does not simulate the macroscopic phenomena that limit the discharge capacities of Li-S batteries. Consequently, we have developed a continuum model to investigate the limitations to the discharge of Li-S batteries, caused by its design and discharge parameters. However, unlike most of the continuum models applied to Li-S batteries, our model considers a multi-scale description of the cathode. In our model, we consider that the cathode is made up of mesoporous carbon particles which have inter-particle pores between them. The chemical and electrochemical reactions are considered to take place in both mesopores and inter-particle pores. Furthermore, we also consider the mass exchange between these pores with different scales. Our simulation results, show that the discharge capacity is mainly limited by the transport of dissolved species in the cathode, which is made up of highly mesoporous carbon particles (45%), which have very low inter-particle porosity between them (25%). Furthermore, the discharge capacity was improved by increasing the inter-particle porosity (35%). These results indicate that the inter-particle porosity of the cathode is a crucial parameter, since the inter-particle pores permit the transport of dissolved species in the cathode and accommodate the volume expansion of the Li_2S precipitates. Therefore, these results show that the rate capability of Li-S batteries could be improved by increasing the inter-particle porosity. Furthermore, the discharge capacity could also be improved by increasing the mesoporosity (55%). Since, the surface area of the carbon particles increases when the mesoporosity is increased, which facilitates more reactions within the mesopores. Additionally, the increase of mesoporosity will also increase the accommodation of $Li_2S_{(s)}$ within the mesopores of the carbon particle. Therefore, comparatively less amount $Li_2S_{(s)}$ gets accumulated in the inter-particle pores of the cathode containing carbon particles with very high mesoporosity (55%). Less $Li_2S_{(s)}$ accumulation in the inter-particle pores will prevent their early clogging during discharge, thereby assisting in the increase of its capacity.

The inter-particle surface area increases when the size of the carbon particles is decreased. It also increases when the number or amount of carbon particles in the cathode is increased. Therefore, the inter-particle surface area is low for the cathode with large carbon particles. Our simulations, results show that the thickness of the $Li_2S_{(s)}$ layer formed over the external surface of the mesoporous carbon increases faster during discharge in the cathode with large

carbon particles. This is because, the aforementioned cathode does not have enough surface to distribute and form a thin layer of $Li_2S_{(s)}$ over the external surface of the carbon particles. Consequently, the mesopores get clogged by the aforementioned thick $Li_2S_{(s)}$ layer. Furthermore, some of the unutilized polysulfides get trapped inside them. This will reduce the discharge capacity of the cathode. In conclusion, our discharge model results suggest that the discharge capacity of the cathode can be improved through,

- The increase of the inter-particle porosity of the cathode;
- The increase of mesoporosity of the carbon particles;
- The increase of the inter-particle surface area of the cathode, by decreasing the size of the carbon particles and by increasing the amount of carbon particles;
- The increase of the mesoporous surface area of the carbon particles, by decreasing the mesopore size and by increasing the number of mesopores.

The discharge model presented in the chapter 4, considers the existence of an arbitrary electrolyte in the pores of the cathode and the separator. Therefore, we have assumed a reaction mechanism which is conventionally used in many continuum models applied to Li-S batteries. However, in the subsequent chapters, we have used 1 M LiTFSI in TEGDME:DOL in our experiments. Therefore, in order to determine reaction mechanism of the polysulfides in 1 M LiTFSI in TEGDME:DOL, we carried out cyclic voltammetry experiments using the electrolyte solutions containing dissolved S_8 , Li_2S_8 and Li_2S_6 . We also developed a mathematical model to simulate and interpret the reaction steps behind the characteristics of the experimental cyclic voltammograms (CVs). The CV of the dissolved S_8 measured at $5 \text{ mV}\cdot\text{s}^{-1}$, consists of two reduction peaks (R_1 and R_2) and two oxidation peaks (O_1 and O_2). However, the simulated CV produced using the conventional reaction mechanism did not reproduce the O_2 peak. Furthermore, the experimental intensity of the O_2 peak does not increase when the scan rate is increased, which suggests that its underlying reaction mechanism must contain some electrochemical steps that are coupled to chemical reaction steps. Therefore, these results prove that the conventional reaction mechanism used in many Li-S batteries models are not sufficient to simulate the complete characteristics of the experimental CV of the dissolved S_8 in TEGDME:DOL.

In situ and operando Raman spectroscopic studies have shown that S_3^{*-} and S_4^{*-} radicals are produced in Li-S batteries containing 1 M LiTFSI in TEGDME:DOL [106,196]. Therefore, we updated the reaction mechanism of our cyclic voltammetry model by adding dissociation reactions of S_8^{2-} and S_6^{2-} which produce S_4^{*-} and S_3^{*-} radicals. Furthermore, we also considered the reduction and oxidation reactions of S_4^{*-} and S_3^{*-} radicals. The simulated CV of dissolved S_8 produced using the newly updated comprehensive reaction mechanism matched well with the experimental result, by reproducing the O_2 peak. Our simulation results show that the O_2 peak corresponds to the oxidation of S_3^{*-} to S_3^{-2} . Furthermore, similar to the experimental CVs the intensity of the simulated O_2 peak, did not increase with the scan rate. This is because the production of S_3^{*-} and its subsequent reduction to S_3^{2-} , are kinetical controlled by the chemical dissociation of S_6^{2-} . Additionally, the characteristics of the simulated CVs of dissolved Li_2S_8 and Li_2S_6 and their evolution during the second cycle also match well with the experiment results. These results further confirm that the updated comprehensive reaction mechanism well represent the actual polysulfides reactions in 1 M LiTFSI in TEGDME:DOL. Finally, in the models reported in chapters 6 and 7, we have considered comprehensive set of reaction steps which were determined using the cyclic voltammetry model.

The phenomena behind the $Li_2S_{(s)}$ precipitation in Li-S batteries are still being debated. Therefore, we have developed a comprehensive 1D continuum model based on the classical electrochemical nucleation theory to investigate the electrodeposition of the $Li_2S_{(s)}$ over a glassy carbon cathode which was placed inside a coffee bag cells. The electrodeposition of the $Li_2S_{(s)}$ occurred from a solution of 100 mM Li_2S_6 in 1 M LiTFSI in TEGDME:DOL, which was the catholyte used in the coffee bag cell. The cell was galvanostatically discharged to reduce its potential to 2V and to trigger nucleation of $Li_2S_{(s)}$, which was then followed by a potentiostatic discharge step. During the potentiostatic discharge stage, the overall reduction current initially increases until it reaches a peak, and then it decreases. The simulated results of our nucleation and growth model, have good semi-quantitative agreement with the experimental results. Our simulations results show that nucleation of $Li_2S_{(s)}$ starts, when the cell potential fell slightly below 2.02 V, during which the overpotential of the nucleation reaction was favourable for producing stable nuclei. Our simulation results, also show that current of the electrochemical growth of existing $Li_2S_{(s)}$ deposits, dominate the overall

current peak formed during the potentiostatic discharge stage. The current of the electrochemical $Li_2S_{(s)}$ growth reaction initially increases due to increase of the electroactive surface area corresponding to the triple phase boundaries which surrounds the newly formed $Li_2S_{(s)}$ deposits. However, this electroactive surface decreases after some time due to the growth and increase of the $Li_2S_{(s)}$ coverage over the carbon surface, which also led to the decrease of the electrochemical $Li_2S_{(s)}$ growth current. Furthermore, the overall current and electrochemical $Li_2S_{(s)}$ growth current, level off when the $Li_2S_{(s)}$ coverage increases over 80%. Our simulations results show that the nucleation of $Li_2S_{(s)}$ are driven by its overpotential and the electrochemical $Li_2S_{(s)}$ growth reaction is limited by the electroactive surface area. These conclusions are consistent with the experimental observations of Fan *et al.* [203]. In the future, the $Li_2S_{(s)}$ nucleation and growth reaction could be incorporated in our discharge model to investigate the impact of galvanostatic discharge on the $Li_2S_{(s)}$ in the practical Li-S batteries. Furthermore, the free energy for the formation heterogeneous nuclei, in our model depend on the binding and surface energies. Therefore, our nucleation and growth model could be used to investigate the electrodeposition of $Li_2S_{(s)}$ over different electrode surfaces and using different electrolytes.

In chapter 7, we have presented the results of our experimental works, which were carried to validate our discharge model. The galvanostatic cycling of the Li-S coins were carried out for this purpose. Each of these Li-S coin cells, consists of a C/S cathode, a Li metal anode and a celgard separator which is wetted with the pure 1 M LiTFSI in TEGDME:DOL electrolyte. The porosimetry and surface area analysis of the carbon powder used in our C/S cathodes, are agglomerates of 50 nm carbon nanoparticles which have micropores of size 2.5 nm. However, the microporosity of the carbon powder was very low and its micropores got blocked after sulfur impregnation. Therefore, we modified our discharge model by neglecting the microporosity within carbon particles. Furthermore, we also considered the comprehensive reaction mechanism, which was determined using the cyclic voltammetry model. The simulated results of our modified discharge model semi-quantitative match with the experiments. The exact matching of the simulation results with the experiment was not achieved due to the complications arising from the numerous parameters of the reaction steps and species considered in our model. The simulation results of our model show the discharge capacities are kinetically limited by the sluggish reactions of the lower order

polysulfides rather than transport of the dissolved species in the electrolyte within the cathode. This is mainly because, our C/S cathodes have very high porosities, which assists with the better transportation of the species within the cathode. Due to their high porosities, the volume percentages of the carbon particles in our cathodes are low. Furthermore, the electroactive specific surface areas of our cathodes are also low, since they have less amount carbon particles per unit volume of the electrode. Therefore, due to the low electroactive surface area in our cathode, the activation overpotential of the sluggish lower polysulfides reduction reactions, could have led to the potential towards the end of discharge. This conclusion suggests that the discharge capacity can be improved by increasing the electroactive surface area. This could be achieved either by increasing the volume percentage of the carbon particles or by using highly mesoporous carbon particles in the cathode.

In conclusion, we have developed multiple models to address some of the assessment and optimization issues related to Li-S batteries. Our models also assist in analysing the results of different electrochemical experiments such as the galvanostatic discharge, potentiostatic discharge and cyclic voltammetry. The most important perspective of this PhD work, would be the determination of parameter values using specially dedicated experiments or through first principles calculations. Finally, we did not study the charge process of the Li-S batteries, using our models. Therefore, in the future our discharge model could be adapted to simulate the charge process of Li-S batteries, by including phenomena such as nucleation and growth $S_{8(s)}$, polysulfides shuttle, etc.

Résumé développé de la thèse en Français (Summary in French)

L'énergie est cruciale pour notre vie dans ce monde technologique moderne. En outre, le progrès technologique de notre époque a contribué à l'amélioration des conditions socioéconomiques dans le monde entier. Il est donc indispensable de produire l'énergie nécessaire afin de répondre à la demande créée par ces développements technologiques et par l'amélioration des conditions de vie du monde entier. Cependant, la majorité de l'énergie actuellement consommée est produite à partir des ressources limitées tels que les combustibles fossiles. Lorsqu'ils brûlent, les combustibles fossiles émettent des gaz à effet de serre qui sont les principales causes de l'augmentation de la température mondiale et du changement climatique. C'est le problème le plus existentiel de notre époque, car l'augmentation de la température de plus de 1,5°C peut provoquer des événements catastrophiques dans le monde entier, tels que la fonte des calottes glaciaires, la montée du niveau de la mer, des conditions météorologiques extrêmes, etc. Par conséquent, pour limiter l'augmentation de la température mondiale en dessous de 1,5 °C, nous devons passer d'une économie énergétique basée sur les combustibles fossiles à une économie énergétique renouvelable. L'éolien et le solaire sont parmi les technologies d'énergie renouvelable les moins chères et celles qui ont le moins d'impact sur l'environnement. Cependant, les sources d'énergie de ces technologies sont intermittentes. En effet, le soleil ne brille pas toute la journée et le vent ne souffle pas tout le temps à la même vitesse. De plus, la demande d'énergie dans un endroit donné varie en fonction de l'heure de la journée et des conditions météorologiques. Par conséquent, l'énergie produite à partir des sources intermittentes doit être stockée lorsque la demande est faible. Les batteries sont considérées comme des candidats prometteurs pour stocker l'énergie produite par les sources intermittentes. Ceci est principalement dû à l'avènement des réseaux intelligents, qui nécessitent des systèmes de stockage d'énergie distribués. En outre, la plupart des gaz à effet de serre sont émis par le transport routier dans les pays développés. Par conséquent, la seule façon d'atténuer ces émissions est de passer des véhicules à moteur à combustion interne (ICE) classiques aux véhicules électriques (VE).

Les batteries lithium-ion (LIB) sont actuellement utilisées dans les VE. Les cathodes des LIBs sont principalement des oxydes de transition métalliques, qui ont une masse molaire élevée. Par conséquent, les cathodes limitent les capacités spécifiques et les densités énergétiques des LIBs [210]. Ainsi, afin d'augmenter l'énergie pouvant être stockée dans les batteries, la prochaine génération de batteries, telles que le lithium soufre (Li-S), le lithium oxygène (Li-O₂), etc. est en développement. Les batteries Li-S sont les plus prometteuses parmi la prochaine génération de batteries en raison de leur matière active cathodique : le soufre solide. La réaction cathodique globale des batteries Li-S est la suivante,



La masse molaire de soufre est faible (32 g.mol⁻¹) et c'est l'un des matériaux les plus abondants sur terre. Comme chaque mole de soufre accepte deux moles de Li⁺, les batteries Li-S ont une densité énergétique supérieure à 2567 Wh.kg⁻¹ [210]. Le soufre solide est isolant, donc les cathodes des batteries Li-S sont des composites carbone/soufre (C/S) poreux. Le carbone dans la cathode aide à la conductivité électronique et agit également comme matériau hôte pour retenir les précipités solides tels que les précipités S_{8(s)} et Li₂S_(s). Des feuillards de Li métallique sont utilisés comme anode dans les batteries Li-S, qui sont séparées de la cathode par un séparateur polymère poreux. Des électrolytes organiques non aqueux à base d'éther remplissent les pores du séparateur et de la cathode. Les courbes galvanostatiques typiques des batteries Li-S ont deux plateaux, et les mécanismes de réaction derrière eux sont assez complexes. En effet, différentes réactions chimiques, électrochimiques et de précipitation/dissolution se produisent pendant le fonctionnement des batteries Li-S. Ces réactions impliquent de multiples espèces telles que le soufre solvaté, des polysulfures et des espèces solides à base de soufre.

De nombreux développements ont été réalisés pour améliorer la capacité de décharge, l'efficacité coulombique et la cyclabilité des batteries Li-S. Cependant, en raison de la complexité de son principe de fonctionnement, l'évaluation de certains phénomènes et l'identification des limites des batteries Li-S est difficile. Une meilleure compréhension de ces

phénomènes pourrait aider à améliorer les performances de ces batteries. Pour cette raison, au cours de mon doctorat, nous avons développé de multiples modèles mathématiques qui pourraient être appliqués à l'étude des phénomènes qui se produisent à différentes échelles spatiales des batteries Li-S.

Dans la littérature, très peu de modèles mésoscopiques ont été rapportés. Ces modèles pourraient être utilisés pour étudier les phénomènes des batteries Li-S qui se produisent à l'échelle mésoscopique. Pour cette raison nous avons développé un nouveau modèle de type Monte-Carlo cinétique 3D (kMC), qui simule explicitement la réaction et la diffusion de différentes espèces à base de soufre dans les mésostructures carbone/soufre (C/S) créées *in silico* [211]. Notre modèle kMC est utilisé pour étudier la décharge des cathodes C/S à l'échelle mésoscopique. Les différentes étapes de réaction et de diffusion considérées dans notre modèle kMC, sont celles qui se produisent du début à la fin de la décharge. Cependant, le nombre d'étapes considérées a été simplifié afin de réduire les coûts informatiques de nos simulations. Les évolutions effectives au sein de la mésostructure C/S, lors de la simulation de décharge kMC, peuvent être quantifiées et visualisées à l'aide de tout logiciel de visualisation. De plus, des courbes de décharge approximatives peuvent être calculées à partir des concentrations de S_4^{2-} et S_2^{2-} .

La corrélation entre les évolutions effectives simulées et les courbes de décharge approximatives calculées montre que la réaction de dissolution de $S_{8(s)}$ et la réduction des polysulfures avec des longues chaînes se produisent pendant le plateau à haut potentiel et au cours de l'étape intermédiaire (pente entre les deux plateaux) de la décharge. Alors que la réduction des polysulfures avec de chaînes courtes et l'électrodéposition du ou des $Li_2S_{(s)}$ se produisent pendant l'étape du plateau à bas potentiel. De plus, nos résultats sur les kMCs montrent que la porosité mésostructurelle diminue au cours des stades de plateau à haut potentiel et de l'étape intermédiaire de la décharge en raison de la dissolution des $S_{8(s)}$. Tandis qu'il diminue en raison de la précipitation de $Li_2S_{(s)}$ pendant la phase du plateau à bas potentiel de la décharge. Ces évolutions effectives au cours de la décharge sont cohérentes avec les résultats expérimentaux précédemment rapportés [58,59].

Les impacts du taux de C et de la charge massique $S_{8(s)}$ - sur les propriétés mésoéchelle des $Li_2S_{(s)}$ déposés sur la surface du carbone - ont été étudiés en analysant les emplacements $Li_2S_{(s)}$ à l'aide de la fonction de distribution radiale (RDF) et de l'algorithme de reconnaissance des

clusters. Les RDF aident à déterminer la couverture du carbone par $\text{Li}_2\text{S}_{(s)}$ et le nombre de dépôts formés à différentes distances de la surface du carbone. Les résultats du RDF montrent que la couverture du carbone par $\text{Li}_2\text{S}_{(s)}$ augmente plus rapidement lors d'une décharge rapide. De plus, les résultats montrent également que les dépôts de $\text{Li}_2\text{S}_{(s)}$ se forment légèrement à l'écart de la surface du carbone lors d'une décharge lente. Ces propriétés méso-échelle des dépôts de $\text{Li}_2\text{S}_{(s)}$ indiquent que la réaction de nucléation est plus rapide lors d'une décharge rapide, alors que la croissance des dépôts existants est plus rapide lors d'une décharge lente. Ces variations dans la dynamique de nucléation et de croissance avec le taux C, sont dus à la concurrence entre les phénomènes de diffusion et de réaction du S_2^{2-} .

L'analyse utilisant l'algorithme de reconnaissance des clusters montre qu'un nombre relativement plus important de grands clusters $\text{Li}_2\text{S}_{(s)}$ sont produits pendant la décharge rapide. Par contre, un nombre relativement plus restreint de grands clusters de $\text{Li}_2\text{S}_{(s)}$ sont produits pendant la décharge lente. En vue que les particules S_2^{2-} sont plus mobiles pendant la décharge lente, elles sont donc séparées les unes des autres avant d'être réduites pour produire du $\text{Li}_2\text{S}_{(s)}$. En raison de l'augmentation rapide de la couverture $\text{Li}_2\text{S}_{(s)}$ et de la formation de grands amas, la passivation de la surface du carbone augmente plus rapidement pendant la décharge rapide. Cela pourrait être en partie la raison de la réduction de la capacité de décharge lorsque le taux C est augmenté.

La dissolution de $\text{S}_{8(s)}$ est relativement lente dans la mésostructure C/S qui a une charge massique élevée en soufre (mésostructure fortement chargée en S). En raison de cette lente dissolution, la surface de carbone disponible est faible pendant la majeure partie de la décharge. Par conséquent, la croissance du $\text{Li}_2\text{S}_{(s)}$ sur les dépôts existants est beaucoup plus rapide que la formation de cristaux de $\text{Li}_2\text{S}_{(s)}$ dans la mésostructure contenant une quantité importante de S. En raison de cette croissance rapide, les dépôts de $\text{Li}_2\text{S}_{(s)}$ sur le carbone dans la mésostructure avec une quantité élevée de S sont très épais. De plus, les dépôts épais de $\text{Li}_2\text{S}_{(s)}$ empêchent également le transport des espèces solvatées vers la surface de l'électrode. Par conséquent, en raison de l'effet combiné de la dissolution lente de $\text{S}_{8(s)}$ et des dépôts épais de $\text{Li}_2\text{S}_{(s)}$, la passivation de la surface aura lieu toujours dans la mésostructure ayant une quantité élevée de S.

Nos résultats kMC montrent également que la précipitation de $\text{Li}_2\text{S}_{(s)}$ commence avant la dissolution complète de $\text{S}_{8(s)}$ dans la mésostructure contenant une quantité importante de S,

donc la porosité de la mésostructure est faible pendant toute la simulation de décharge. Ce résultat suggère que les pores entre les particules peuvent être obstrués lorsque la quantité de soufre augmente. Enfin, l'augmentation de la passivation et la possibilité d'obstruction des pores pourraient expliquer en partie pourquoi les capacités de décharge diminuent lorsque la quantité de soufre augmente. Notre modèle kMC ne se limite pas aux propriétés structurales géométriques et effectives supposées de nos mésostructures C/S créées in silico. Il peut également être utilisé pour étudier la décharge des mésostructures, qui sont produites à partir des images tomographiques expérimentales.

Bien que notre modèle kMC soit capable d'étudier les phénomènes méso-échelle qui se produisent dans les composites cathodiques C/S, il ne peut décrire les phénomènes macroscopiques qui limitent les capacités de décharge des batteries Li-S. Par conséquent, nous avons développé un modèle de continuum pour étudier les impacts des architectures des composites C/S sur la décharge. Puisque la plupart des améliorations apportées à la performance des batteries Li-S ont été réalisées grâce à l'adaptation de l'architecture du composite C/S, notre modèle de décharge du continuum a considéré une description multi-échelle de la cathode [157].

Dans notre modèle, nous avons considéré que la cathode est constituée de particules de carbone mésoporeuses qui ont des pores inter-particulaires entre elles. Les réactions chimiques et électrochimiques sont considérées comme ayant lieu à la fois dans les mésopores et les pores inter-particulaires. De plus, les diffusions d'espèces solvatées à travers les pores inter-particulaires (entre les particules de carbone) ont été considérées. Nous considérons également un phénomène appelé intra-flux, qui décrit l'échange de masse entre ces pores à différentes échelles. La capacité de décharge de la cathode contenant des particules de carbone très mésoporeuses (45%) est principalement limitée par l'inhibition du transport des espèces solvatées due à l'obstruction des pores inter-particulaires. De plus, la capacité de décharge a été améliorée en augmentant la porosité inter-particulaire (35%). Ceci montre que la porosité inter-particulaire de la cathode est un paramètre crucial, car elle permet le transport d'espèces solvatées dans la cathode et permet l'expansion en volume des précipités Li_2S . Par conséquent, ces résultats montrent que la capacité de décharge des batteries Li-S pourrait être améliorée en augmentant la porosité inter-particulaire.

De plus, l'augmentation de la mésoporosité des particules de carbone améliorera également la capacité de décharge, puisqu'elle augmentera la surface spécifique des mésopores ce qui facilitera l'utilisation correcte des polysulfures électroactifs. De plus, il augmentera les dépôts de $\text{Li}_2\text{S}_{(s)}$ dans les mésopores. Par conséquent, l'augmentation de la mésoporosité diminuera la quantité de précipités $\text{Li}_2\text{S}_{(s)}$ qui sont pris en compte dans les pores inter-particulaires. Comme moins de précipités de $\text{Li}_2\text{S}_{(s)}$ sont logés dans les pores interparticulaires, leur colmatage précipité pendant la décharge est inhibé dans la cathode avec des particules de carbone ayant une mésoporosité très élevée (55%).

Les résultats de notre modèle de décharge montrent que l'épaisseur de la couverture de $\text{Li}_2\text{S}_{(s)}$ formée sur la surface externe des particules de carbone, dépendra de l'aire de la surface inter-particulaire. Dans la cathode à faible surface interparticulaire, une couverture épaisse de $\text{Li}_2\text{S}_{(s)}$ est produite sur les particules de carbone. En effet, la cathode à faible surface inter-particulaire n'a pas assez de surface pour distribuer et former une couverture fine de $\text{Li}_2\text{S}_{(s)}$ sur les particules de carbone. Les mésopores sont bloqués, quand la couverture de $\text{Li}_2\text{S}_{(s)}$ devient trop épaisse. De plus, ces mésopores obstrués peuvent piéger certains des polysulfures inutilisés qui s'y trouvent. Elles entraînent donc une réduction de la capacité de décharge de la cathode. Par conséquent, la capacité de décharge diminue lorsque la surface inter-particulaire est réduite. L'aire de surface interparticulaire peut être augmentée en augmentant le nombre de particules de carbone et en diminuant la taille des particules de carbone. En conclusion, la capacité de décharge d'une cathode peut être augmentée soit en augmentant la porosité et la mésoporosité inter-particulaires, soit en diminuant la taille des particules de carbone ou en augmentant le nombre de particules de carbone. Dans notre modèle de décharge multi-échelle présenté dans le chapitre 4, nous avons supposé que le volume vide des pores de la cathode et du séparateur est rempli par un électrolyte arbitraire. Par conséquent, nous avons supposé un mécanisme de réaction conventionnellement utilisé dont les étapes de réaction sont données ci-dessous,

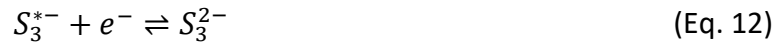
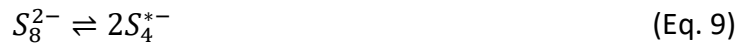




Cependant, on sait que la stabilité et le mécanisme de réaction des polysulfures changent en fonction de l'électrolyte. De plus, 1 M LiTFSI dans TEGDME:DOL a été utilisé dans les expériences rapportées dans les chapitres 5 à 7. C'est pourquoi, au chapitre 5, nous avons étudié la validité du mécanisme de réaction conventionnel utilisé en effectuant des mesures de voltampérométrie cyclique à l'aide de solutions électrolytiques contenant S_8 , Li_2S_8 et Li_2S_6 solvatées.

L'analyse et l'interprétation des réactions à l'origine des caractéristiques des voltammogrammes cycliques expérimentaux (CV) ont été effectuées à l'aide d'un modèle mathématique. Le CV expérimental de la S_8 solvatée mesuré à $5 \text{ mV}\cdot\text{s}^{-1}$, se compose de deux pics de réduction (R_1 et R_2) et de deux pics d'oxydation (O_1 et O_2). De plus, les CV expérimentaux de S_8 mesurés à différentes vitesses de balayage montrent que l'intensité du pic d' O_2 n'augmente pas lorsque la vitesse de balayage augmente. Cela suggère que les réactions électrochimiques qui sont couplées à des réactions chimiques, forment la base du pic d' O_2 . Cependant, le mécanisme de réaction conventionnel comprend de telles étapes de réaction. Par conséquent, le CV simulé produit à l'aide du mécanisme de réaction conventionnel n'a pas reproduit le pic d' O_2 . Ces résultats prouvent que le mécanisme de réaction conventionnel utilisé dans de nombreux modèles de batteries Li-S n'est pas suffisant pour simuler les caractéristiques complètes du CV expérimental du S_8 solvaté dans 1 M LiTFSI dans TEGDME:DOL.

Des études spectroscopiques Raman in situ et opérationnelles ont montré que les radicaux S_3^{*-} et S_4^{*-} sont produits dans des batteries Li-S contenant 1 M LiTFSI en TEGDME:DOL [106,196]. Par conséquent, nous avons mis à jour le mécanisme de réaction de notre modèle de voltampérométrie cyclique en incluant quelques étapes supplémentaires dans la réaction qui impliquent des radicaux S_3^{*-} et S_4^{*-} .

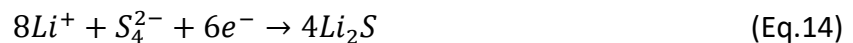


Les équations 9 à 12 ont déjà été rapportées par Gaillard *et al.* et elles ont été déterminées en utilisant les CV du Li_2S_6 solvaté dans le DMF [184]. Alors que la réaction d'oxydoréduction S_3^{*-}/S_3^{2-} a été proposée par Barschasz *et al.* [60].

Le CV simulé de S_8 solvaté, produit à l'aide du mécanisme de réaction mis à jour, non seulement reproduisait l' O_2 , mais ses intensités simulées n'augmentaient pas avec la vitesse de balayage. Les évolutions simulées des courants de réaction individuels montrent que le pic O_2 correspond à l'oxydation de S_3^{2-} à S_3^{*-} . La production de S_3^{*-} et sa réduction ultérieure en S_3^{2-} , sont cinétiquement contrôlées par la dissociation chimique de S_6^{2-} . Puisque la vitesse de la réaction de dissociation S_6^{2-} ne dépend pas de la vitesse de balayage, les productions de S_3^{*-} et S_3^{2-} n'augmentent pas avec la vitesse de balayage. Par conséquent, l'intensité du pic d' O_2 n'augmente pas avec la vitesse de balayage.

L'intensité expérimentale du pic R_1 était faible dans le premier CV du Li_2S_8 solvaté. Alors que le pic R_1 était totalement invisible dans celui du Li_2S_6 solvaté. Les évolutions du courant de réaction individuel montrent que le pic R_1 correspond aux réactions de réduction S_8/S_8^{2-} et S_8^{2-}/S_6^{2-} . Initialement, la solution solvatée de Li_2S_8 et Li_2S_6 ne contient pas de S_8 . Par conséquent, le pic R_1 était moins intense dans le premier CV du Li_2S_8 et il est complètement invisible dans celui du Li_2S_6 . Ces deux effets sont dus à l'absence de réaction S_8/S_8^{2-} . Ces résultats confirment en outre que le mécanisme de réaction complet mis à jour représente bien les réactions réelles des polysulfures dans 1 M LiTFSI en TEGDME:DOL. Par conséquent, nous avons examiné un ensemble complet d'étapes de réaction dans le modèle présenté dans les chapitres 6 et 7.

Le mécanisme de réaction et la limitation des précipitations de $\text{Li}_2\text{S}_{(s)}$ dans les batteries Li-S sont encore en discussion. C'est pourquoi, au chapitre 6, nous avons développé un modèle complet de continuum 1D basé sur la théorie classique de la nucléation électrochimique pour étudier la précipitation du $\text{Li}_2\text{S}_{(s)}$ dans une pouch cell simplifiée. Notre modèle, considère que la nucléation et la croissance de $\text{Li}_2\text{S}_{(s)}$ se produisent en raison d'un type de réaction similaire qui est mentionné ci-dessous,



De plus, notre modèle est capable de prédire la distribution granulométrique et la couverture $\text{Li}_2\text{S}_{(s)}$, ce qui est obtenu par l'incorporation de l'équation bilan de la population des particules.

Une électrode plane en carbone vitreux a été utilisée comme cathode pour la « pouch cell » et une feuille de Li métallique a été utilisée comme anode. Les électrodes étaient séparées par deux séparateurs en fibre de verre et une membrane Ohara sélective d'ions. Le catholyte était 100 mM Li_2S_6 dans 1 M LiTFSI dans TEGDME:DOL et 1 M LiTFSI pur dans TEGDME:DOL était utilisé comme anolyte. La pouch cell a été déchargée galvanostatiquement pour réduire son potentiel à 2V et déclencher la nucléation de $\text{Li}_2\text{S}_{(s)}$, qui a été suivie par une étape de décharge potentiostatique. Pendant la phase de décharge potentiostatique, on observe l'apparition d'un pic.

Les résultats simulés de notre modèle de nucléation et de croissance ont un bon accord semi-quantitatif avec les résultats expérimentaux. Les résultats de la simulation montrent que la réduction de S_6^{2-} à S_4^{2-} domine l'étape de décharge galvanostatique. De plus, les résultats montrent également que la nucléation de $\text{Li}_2\text{S}_{(s)}$ commence lorsque le potentiel cellulaire tombe légèrement en dessous de 2,02 V. En dessous de 2,02 V, le sur-potentiel de la réaction de nucléation est favorable à la production de noyaux stables. Nos résultats de simulation montrent également que le courant de la croissance électrochimique des dépôts existants de $\text{Li}_2\text{S}_{(s)}$ domine le pic de courant global formé pendant l'étape de décharge potentiostatique.

Dans notre modèle, nous avons supposé que la réaction de croissance électrochimique de $\text{Li}_2\text{S}_{(s)}$ se produit à la limite de la triple phase qui entoure les dépôts de $\text{Li}_2\text{S}_{(s)}$ existants.

Initialement, en raison de la nucléation de $\text{Li}_2\text{S}_{(s)}$, l'aire de surface de la limite triphasée augmente, donc le courant de la réaction de croissance électrochimique de $\text{Li}_2\text{S}_{(s)}$ augmente également pendant le même temps. Cependant, la surface de la limite triphasée diminue lorsque la couverture de $\text{Li}_2\text{S}_{(s)}$ dépasse 40 %. Par conséquent, le courant de la réaction de croissance électrochimique de $\text{Li}_2\text{S}_{(s)}$ et le courant total diminuent en raison de l'augmentation de la couverture de $\text{Li}_2\text{S}_{(s)}$ sur la surface de l'électrode. De plus, le courant total et les courants de toutes les réactions électrochimiques se stabilisent lorsque la couverture de $\text{Li}_2\text{S}_{(s)}$ augmente de plus de 80%. Les résultats de nos simulations montrent que la nucléation de $\text{Li}_2\text{S}_{(s)}$ est pilotée par son sur potentiel et que la réaction de croissance électrochimique de $\text{Li}_2\text{S}_{(s)}$ est limitée par la surface électroactive. Ces conclusions concordent avec les observations expérimentales de Fan *et al.* [212]. Cependant, la limitation de la surface de la croissance électrochimique de $\text{Li}_2\text{S}_{(s)}$ peut ne pas se produire dans les cathodes poreuses qui ont une très grande surface spécifique. À l'avenir, la réaction de nucléation et de croissance du $\text{Li}_2\text{S}_{(s)}$ pourrait être incorporée dans notre modèle de décharge pour étudier l'impact de la décharge galvanostatique sur le $\text{Li}_2\text{S}_{(s)}$ dans les batteries Li-S pratiques. De plus, l'énergie libre pour la formation de noyaux hétérogènes dans notre modèle, dépend des énergies de liaison et de surface. Par conséquent, notre modèle de nucléation et de croissance pourrait être utilisé pour étudier l'électrodéposition de $\text{Li}_2\text{S}_{(s)}$ sur différentes surfaces d'électrodes et en utilisant différents électrolytes.

Au chapitre 7, nous avons présenté les résultats de nos travaux expérimentaux qui ont été réalisés pour valider notre modèle de rejets. Le cycle galvanostatique de nos cathodes (composites C/S) a été réalisé à l'aide de piles bouton Li-S. Chacune de ces piles, se compose d'une cathode C/S, d'une anode en Li métallique et d'un séparateur celgard qui est mouillé avec 1 M LiTFSI pur dans un électrolyte TEGDME:DOL. La porosimétrie et l'analyse de surface de la poudre de carbone utilisée dans nos cathodes C/S, montrent que le précurseur carboné est formé par des agglomérats de nanoparticules de carbone de 50 nm qui ont des micropores de 2,5 nm. Cependant, la microporosité de la poudre de carbone était très faible et ses micropores ont été bloqués après imprégnation au soufre. Nous avons donc modifié notre modèle de décharge en négligeant la microporosité des particules de carbone. Cela a été fait en négligeant le terme intra-flux dans l'équation de conservation de masse de l'espèce dans les pores inter-particulaires. De plus, nous avons également ignoré la conservation de masse

de l'espèce dans les mésopores. En outre, nous avons également examiné le mécanisme de réaction global, qui a été déterminé à l'aide du modèle de voltampérométrie cyclique.

Les résultats simulés de notre modèle de décharge modifié correspondent de façon semi-quantitative aux expériences. La correspondance exacte des résultats de la simulation avec l'expérience n'a pas été obtenue en raison des complications découlant des nombreux paramètres des étapes de réaction et des espèces considérées dans notre modèle. Les résultats de simulation de notre modèle montrent que les capacités de décharge sont cinétiquement limitées par la lenteur des réactions des polysulfures d'ordre inférieur plutôt que par le transport des espèces solvatées dans l'électrolyte de la cathode. Ceci est principalement dû au fait que nos cathodes C/S ont des porosités très élevées, ce qui permet un meilleur transport de l'espèce à l'intérieur de la cathode. En raison de leur porosité élevée, les pourcentages en volume des particules de carbone dans nos cathodes sont faibles. De plus, les surfaces spécifiques électroactives de nos cathodes sont également faibles, car elles contiennent moins de particules de carbone par unité de volume de la cathode. Par conséquent, en raison de la faible surface électroactive de notre cathode, le surpotentiel d'activation des réactions lentes de réduction des polysulfures inférieurs pourrait avoir entraîné une baisse potentielle vers la fin de la décharge. Cette conclusion suggère que la capacité de décharge peut être améliorée en augmentant la surface électroactive. On pourrait y parvenir soit en augmentant le pourcentage en volume des particules de carbone, soit en utilisant des particules de carbone très mésoporeuses dans la cathode.

En conclusion, nous avons développé de multiples modèles pour évaluer et optimiser les phénomènes de décharge des batteries Li-S. Nos modèles aident également à analyser les résultats de différentes expériences électrochimiques telles que la décharge galvanostatique, la décharge potentiostatique et la voltampérométrie cyclique. Les perspectives de ce travail de doctorat comprennent la détermination des paramètres du modèle à l'aide des expériences dédiées et l'incorporation de mécanismes à notre modèle de décharge pour le transformer en un modèle pour le cycle complet.

Bibliography

- [1] BP Statistical Review of World Energy, BP, London, 2018.
<https://www.bp.com/content/dam/bp/business-sites/en/global/corporate/pdfs/energy-economics/statistical-review/bp-stats-review-2018-full-report.pdf> (accessed February 15, 2019).
- [2] M. Roser, Life Expectancy, Our World Data. (2013). <https://ourworldindata.org/life-expectancy> (accessed February 10, 2019).
- [3] M. Roser, Child Mortality, Our World Data. (2013). <https://ourworldindata.org/child-mortality> (accessed February 10, 2019).
- [4] M. Kremer, Population Growth and Technological Change: One Million B.C. to 1990, *Q. J. Econ.* 108 (1993) 681–716. <https://doi.org/10.2307/2118405>.
- [5] D. Larcher, J.-M. Tarascon, Towards greener and more sustainable batteries for electrical energy storage, *Nat. Chem.* 7 (2015) 19–29. <https://doi.org/10.1038/nchem.2085>.
- [6] M. Höök, X. Tang, Depletion of fossil fuels and anthropogenic climate change—A review, *Energy Policy*. 52 (2013) 797–809. <https://doi.org/10.1016/j.enpol.2012.10.046>.
- [7] C.L. Quéré, R.M. Andrew, P. Friedlingstein, S. Sitch, J. Hauck, J. Pongratz, P.A. Pickers, J.I. Korsbakken, G.P. Peters, J.G. Canadell, A. Arneeth, V.K. Arora, L. Barbero, A. Bastos, L. Bopp, F. Chevallier, L.P. Chini, P. Ciais, S.C. Doney, T. Gkritzalis, D.S. Goll, I. Harris, V. Haverd, F.M. Hoffman, M. Hoppema, R.A. Houghton, G. Hurtt, T. Ilyina, A.K. Jain, T. Johannessen, C.D. Jones, E. Kato, R.F. Keeling, K.K. Goldewijk, P. Landschützer, N. Lefèvre, S. Lienert, Z. Liu, D. Lombardozzi, N. Metz, D.R. Munro, J.E.M.S. Nabel, S. Nakaoka, C. Neill, A. Olsen, T. Ono, P. Patra, A. Peregon, W. Peters, P. Peylin, B. Pfeil, D. Pierrot, B. Poulter, G. Rehder, L. Resplandy, E. Robertson, M. Rocher, C. Rödenbeck, U. Schuster, J. Schwinger, R. Séférian, I. Skjelvan, T. Steinhoff, A. Sutton, P.P. Tans, H. Tian, B. Tilbrook, F.N. Tubiello, I.T. van der Laan-Luijkx, G.R. van der Werf, N. Viovy, A.P. Walker, A.J. Wiltshire, R. Wright, S. Zaehle, B. Zheng, Global Carbon Budget 2018, *Earth Syst. Sci. Data*. 10 (2018) 2141–2194. <https://doi.org/10.5194/essd-10-2141-2018>.
- [8] Intergovernmental Panel on Climate Change, Global warming of 1.5°C, 2018.
<http://www.ipcc.ch/report/sr15/> (accessed February 10, 2019).
- [9] M. Jaforullah, A. King, Does the use of renewable energy sources mitigate CO₂ emissions? A reassessment of the US evidence, *Energy Econ.* 49 (2015) 711–717.
<https://doi.org/10.1016/j.eneco.2015.04.006>.
- [10] Renewable capacity highlights, IRENA, Abu Dhabi, 2018. https://irena.org/-/media/Files/IRENA/Agency/Publication/2018/Mar/RE_capacity_highlights_2018.pdf (accessed October 2, 2019).
- [11] Renewable power generation costs in 2017: Key findings and executive summary, IRENA, Abu Dhabi, 2018. https://www.irena.org/-/media/Files/IRENA/Agency/Publication/2018/Jan/IRENA_2017_Power_Costs_2018.pdf.
- [12] C. Zarfl, A.E. Lumsdon, J. Berlekamp, L. Tydecks, K. Tockner, A global boom in hydropower dam construction, *Aquat. Sci.* 77 (2015) 161–170. <https://doi.org/10.1007/s00027-014-0377-0>.
- [13] Wind Energy Basics, (n.d.). <http://windeis.anl.gov/guide/basics/> (accessed March 19, 2019).
- [14] Advantages and Challenges of Wind Energy, Energy.Gov. (n.d.).
<https://www.energy.gov/eere/wind/advantages-and-challenges-wind-energy> (accessed March 19, 2019).
- [15] O. Edenhofer, Intergovernmental Panel on Climate Change, Working Group 3, Renewable energy sources and climate change mitigation: summary for policymakers and technical summary : special report of the intergovernmental panel on climate change., Cambridge University Press, New York, 2011.

- [16] G. Berndes, N. Bird, A. Cowie, *Bioenergy, Land Use Change and Climate Change Mitigation*, IEA Bioenergy:ExCo:2011:04, Rotorua, New Zealand, 2011.
- [17] A. Sowa-Watrak, I. Klosok-Bazan, M. Gono, R. Gono, The criteria for suitable location of geothermal power plant, in: 2017 18th Int. Sci. Conf. Electr. Power Eng. EPE, IEEE, Kouty nad Desnou, Czech Republic, 2017: pp. 1–5. <https://doi.org/10.1109/EPE.2017.7967356>.
- [18] W.A. Duffield, J.H. Sass, *Geothermal Energy—Clean Power From the Earth’s Heat*, U.S. Geological Survey, Reston, Virginia, 2003. <https://pubs.usgs.gov/circ/2004/c1249/>.
- [19] H. Ibrahim, A. Ilinca, J. Perron, Energy storage systems—Characteristics and comparisons, *Renew. Sustain. Energy Rev.* 12 (2008) 1221–1250. <https://doi.org/10.1016/j.rser.2007.01.023>.
- [20] Electric Energy Storage, *Cent. Clim. Energy Solut.* (2018). <https://www.c2es.org/content/electric-energy-storage/> (accessed March 27, 2019).
- [21] eco2mix consommation en, RTE Fr. (2014). <https://www.rte-france.com/en/eco2mix/eco2mix-consommation-en> (accessed March 27, 2019).
- [22] eco2mix mix énergétique en, RTE Fr. (2014). <https://www.rte-france.com/en/eco2mix/eco2mix-mix-energetique-en> (accessed March 25, 2019).
- [23] L. Gagnon, *Mémoire concernant la contribution possible de la production éolienne en réponse à l’accroissement de la demande québécoise d’électricité d’ici 2010*, Régie de l’énergie, Québec, Canada, 2010.
- [24] K.K. Zame, C.A. Brehm, A.T. Nitica, C.L. Richard, G.D. Schweitzer III, Smart grid and energy storage: Policy recommendations, *Renew. Sustain. Energy Rev.* 82 (2018) 1646–1654. <https://doi.org/10.1016/j.rser.2017.07.011>.
- [25] B. Römer, P. Reichhart, J. Kranz, A. Picot, The role of smart metering and decentralized electricity storage for smart grids: The importance of positive externalities, *Energy Policy.* 50 (2012) 486–495. <https://doi.org/10.1016/j.enpol.2012.07.047>.
- [26] Energy storage, (n.d.). <https://www.iea.org/tcep/energyintegration/energystorage/> (accessed April 1, 2019).
- [27] T. Ioannis, *Li-ion batteries for mobility and stationary storage applications*, European Union, Luxembourg, 2018.
- [28] Greenhouse gas emissions from transport, *Eur. Environ. Agency.* (n.d.). <https://www.eea.europa.eu/data-and-maps/indicators/transport-emissions-of-greenhouse-gases/transport-emissions-of-greenhouse-gases-11> (accessed March 31, 2019).
- [29] D. Linden, T.B. Reddy, eds., *Handbook of batteries*, 3. ed, McGraw-Hill, New York, NY, 2002.
- [30] G.J. May, A. Davidson, B. Monahov, Lead batteries for utility energy storage: A review, *J. Energy Storage.* 15 (2018) 145–157. <https://doi.org/10.1016/j.est.2017.11.008>.
- [31] A.-I. Stan, M. Swierczynski, D.-I. Stroe, R. Teodorescu, S.J. Andreasen, K. Moth, A comparative study of lithium ion to lead acid batteries for use in UPS applications, in: 2014 IEEE 36th Int. Telecommun. Energy Conf. INTELEC, IEEE, Vancouver, BC, 2014: pp. 1–8. <https://doi.org/10.1109/INTLEC.2014.6972152>.
- [32] J.-M. Tarascon, M. Armand, Issues and challenges facing rechargeable lithium batteries, *Nature.* 414 (2001) 359–367. <https://doi.org/10.1038/35104644>.
- [33] M. Winter, B. Barnett, K. Xu, Before Li Ion Batteries, *Chem. Rev.* 118 (2018) 11433–11456. <https://doi.org/10.1021/acs.chemrev.8b00422>.
- [34] G.N. Lewis, F.G. Keyes, The potential of the lithium electrode, *J. Am. Chem. Soc.* 35 (1913) 340–344. <https://doi.org/10.1021/ja02193a004>.
- [35] M.S. Whittingham, History, Evolution, and Future Status of Energy Storage, *Proc. IEEE.* 100 (2012) 1518–1534. <https://doi.org/10.1109/JPROC.2012.2190170>.
- [36] D.W. Murphy, F.J. Di Salvo, J.N. Carides, J.V. Waszczak, Topochemical reactions of rutile related structures with lithium, *Mater. Res. Bull.* 13 (1978) 1395–1402. [https://doi.org/10.1016/0025-5408\(78\)90131-9](https://doi.org/10.1016/0025-5408(78)90131-9).
- [37] M. Lazzari, A Cyclable Lithium Organic Electrolyte Cell Based on Two Intercalation Electrodes, *J. Electrochem. Soc.* 127 (1980) 773. <https://doi.org/10.1149/1.2129753>.

- [38] T. Nagaura, Lithium ion rechargeable battery, *Prog. Batter. Sol. Cells.* 9 (1990) 209.
- [39] Y. Nishi, The development of lithium ion secondary batteries, *Chem. Rec.* 1 (2001) 406–413. <https://doi.org/10.1002/tcr.1024>.
- [40] A. Rosenman, E. Markevich, G. Salitra, D. Aurbach, A. Garsuch, F.F. Chesneau, Review on Li-Sulfur Battery Systems: an Integral Perspective, *Adv. Energy Mater.* 5 (2015) 1500212. <https://doi.org/10.1002/aenm.201500212>.
- [41] P.G. Bruce, S.A. Freunberger, L.J. Hardwick, J.-M. Tarascon, Li–O₂ and Li–S batteries with high energy storage, *Nat. Mater.* 11 (2012) 19–29. <https://doi.org/10.1038/nmat3191>.
- [42] A.C. Luntz, B.D. McCloskey, Nonaqueous Li–Air Batteries: A Status Report, *Chem. Rev.* 114 (2014) 11721–11750. <https://doi.org/10.1021/cr500054y>.
- [43] L.D. Griffith, A.E.S. Sleightholme, J.F. Mansfield, D.J. Siegel, C.W. Monroe, Correlating Li/O₂ Cell Capacity and Product Morphology with Discharge Current, *ACS Appl. Mater. Interfaces.* 7 (2015) 7670–7678. <https://doi.org/10.1021/acsami.5b00574>.
- [44] A. Torayev, A. Rucci, P.C.M.M. Magusin, A. Demortière, V. De Andrade, C.P. Grey, C. Merlet, A.A. Franco, Stochasticity of Pores Interconnectivity in Li–O₂ Batteries and its Impact on the Variations in Electrochemical Performance, *J. Phys. Chem. Lett.* 9 (2018) 791–797. <https://doi.org/10.1021/acs.jpcllett.7b03315>.
- [45] Li-S, UAV, Bus, Truck, EV and Marine Batteries, Oxis Energy. (n.d.). <https://oxisenergy.com/products/> (accessed April 3, 2019).
- [46] T. Cleaver, P. Kovacic, M. Marinescu, T. Zhang, G. Offer, Perspective—Commercializing Lithium Sulfur Batteries: Are We Doing the Right Research?, *J. Electrochem. Soc.* 165 (2018) A6029–A6033. <https://doi.org/10.1149/2.0071801jes>.
- [47] A. Fotouhi, D. Auger, L. O’Neill, T. Cleaver, S. Walus, Lithium-Sulfur Battery Technology Readiness and Applications—A Review, *Energies.* 10 (2017) 1937. <https://doi.org/10.3390/en10121937>.
- [48] Iori E. Apodaca, 2015 Mineral year book. SULFUR [ADVANCE RELEASE], U.S. Geological Survey, 2017. <https://minerals.usgs.gov/minerals/pubs/commodity/sulfur/myb1-2015-sulfu.pdf> (accessed April 3, 2019).
- [49] F.Y. Fan, W.C. Carter, Y.-M. Chiang, Mechanism and Kinetics of Li₂S Precipitation in Lithium-Sulfur Batteries, *Adv. Mater.* 27 (2015) 5203–5209. <https://doi.org/10.1002/adma.201501559>.
- [50] R. Demir-Cakan, Chapter 1: Introduction to Rechargeable Lithium–Sulfur Batteries, in: R. Demir-Cakan (Ed.), *Li- Batter. Chall. Chem. Mater. Future Perspect.*, WORLD SCIENTIFIC (EUROPE), London, 2017: pp. 335–350. https://doi.org/10.1142/9781786342508_0001.
- [51] S. Walus, Lithium/Sulfur batteries : development and understanding of the working mechanisms, (n.d.) 284.
- [52] H. Danuta, U. Juliusz, Electric dry cells and storage batteries, US3043896A, 1962. <https://patents.google.com/patent/US3043896A/en#patentCitations> (accessed September 5, 2019).
- [53] S.-E. Cheon, K.-S. Ko, J.-H. Cho, S.-W. Kim, E.-Y. Chin, H.-T. Kim, Rechargeable Lithium Sulfur Battery, *J. Electrochem. Soc.* 150 (2003) A800. <https://doi.org/10.1149/1.1571533>.
- [54] E. Peled, A. Gorenshtein, M. Segal, Y. Sternberg, Rechargeable lithium–sulfur battery (extended abstract), *J. Power Sources.* 26 (1989) 269–271. [https://doi.org/10.1016/0378-7753\(89\)80133-8](https://doi.org/10.1016/0378-7753(89)80133-8).
- [55] X. Ji, K.T. Lee, L.F. Nazar, A highly ordered nanostructured carbon–sulphur cathode for lithium–sulphur batteries, *Nat. Mater.* 8 (2009) 500–506. <https://doi.org/10.1038/nmat2460>.
- [56] A. Manthiram, Y. Fu, Y.-S. Su, Challenges and Prospects of Lithium–Sulfur Batteries, *Acc. Chem. Res.* 46 (2013) 1125–1134. <https://doi.org/10.1021/ar300179v>.
- [57] L.F. Nazar, M. Cuisinier, Q. Pang, Lithium-sulfur batteries, *MRS Bull.* 39 (2014) 436–442. <https://doi.org/10.1557/mrs.2014.86>.
- [58] A. Kawase, S. Shirai, Y. Yamoto, R. Arakawa, T. Takata, Electrochemical reactions of lithium–sulfur batteries: an analytical study using the organic conversion technique, *Phys Chem Chem Phys.* 16 (2014) 9344–9350. <https://doi.org/10.1039/C4CP00958D>.

- [59] M. Cuisinier, P.-E. Cabelguen, S. Evers, G. He, M. Kolbeck, A. Garsuch, T. Bolin, M. Balasubramanian, L.F. Nazar, Sulfur Speciation in Li–S Batteries Determined by Operando X-ray Absorption Spectroscopy, *J. Phys. Chem. Lett.* 4 (2013) 3227–3232. <https://doi.org/10.1021/jz401763d>.
- [60] C. Barchasz, F. Molton, C. Duboc, J.-C. Leprêtre, S. Patoux, F. Alloin, Lithium/Sulfur Cell Discharge Mechanism: An Original Approach for Intermediate Species Identification, *Anal. Chem.* 84 (2012) 3973–3980. <https://doi.org/10.1021/ac2032244>.
- [61] K.H. Wujcik, D.R. Wang, A. Raghunathan, M. Drake, T.A. Pascal, D. Prendergast, N.P. Balsara, Lithium Polysulfide Radical Anions in Ether-Based Solvents, *J. Phys. Chem. C.* 120 (2016) 18403–18410. <https://doi.org/10.1021/acs.jpcc.6b04264>.
- [62] Q. He, Y. Gorlin, M.U.M. Patel, H.A. Gasteiger, Y.-C. Lu, Unraveling the Correlation between Solvent Properties and Sulfur Redox Behavior in Lithium-Sulfur Batteries, *J. Electrochem. Soc.* 165 (2018) A4027–A4033. <https://doi.org/10.1149/2.0991816jes>.
- [63] J.W. Dibden, J.W. Smith, N. Zhou, N. Garcia-Araez, J.R. Owen, Predicting the composition and formation of solid products in lithium–sulfur batteries by using an experimental phase diagram, *Chem. Commun.* 52 (2016) 12885–12888. <https://doi.org/10.1039/C6CC05881G>.
- [64] S.M. Al-Mahmoud, J.W. Dibden, J.R. Owen, G. Denuault, N. Garcia-Araez, A simple, experiment-based model of the initial self-discharge of lithium-sulphur batteries, *J. Power Sources.* 306 (2016) 323–328. <https://doi.org/10.1016/j.jpowsour.2015.12.031>.
- [65] M.R. Busche, P. Adelhelm, H. Sommer, H. Schneider, K. Leitner, J. Janek, Systematical electrochemical study on the parasitic shuttle-effect in lithium-sulfur-cells at different temperatures and different rates, *J. Power Sources.* 259 (2014) 289–299. <https://doi.org/10.1016/j.jpowsour.2014.02.075>.
- [66] D. Moy, A. Manivannan, S.R. Narayanan, Direct measurement of polysulfide shuttle current: A window into understanding the performance of lithium-sulfur cells, *J. Electrochem. Soc.* 162 (2015) A1–A7.
- [67] Y.V. Mikhaylik, J.R. Akridge, Polysulfide Shuttle Study in the Li/S Battery System, *J. Electrochem. Soc.* 151 (2004) A1969–A1976. <https://doi.org/10.1149/1.1806394>.
- [68] F.Y. Fan, Y.-M. Chiang, Electrodeposition Kinetics in Li-S Batteries: Effects of Low Electrolyte/Sulfur Ratios and Deposition Surface Composition, *J. Electrochem. Soc.* 164 (2017) A917–A922.
- [69] R. Demir-Cakan, Targeting the role of lithium sulphide formation for the rapid capacity fading in lithium-sulphur batteries, *J. Power Sources.* 282 (2015) 437–443. <https://doi.org/10.1016/j.jpowsour.2015.02.066>.
- [70] X.-B. Cheng, J.-Q. Huang, Q. Zhang, Review—Li Metal Anode in Working Lithium-Sulfur Batteries, *J. Electrochem. Soc.* 165 (2018) A6058–A6072. <https://doi.org/10.1149/2.0111801jes>.
- [71] B. Zhang, X. Qin, G.R. Li, X.P. Gao, Enhancement of long stability of sulfur cathode by encapsulating sulfur into micropores of carbon spheres, *Energy Env. Sci.* 3 (2010) 1531–1537. <https://doi.org/10.1039/C002639E>.
- [72] J. Schuster, G. He, B. Mandlmeier, T. Yim, K.T. Lee, T. Bein, L.F. Nazar, Spherical Ordered Mesoporous Carbon Nanoparticles with High Porosity for Lithium-Sulfur Batteries, *Angew. Chem. Int. Ed.* 51 (2012) 3591–3595. <https://doi.org/10.1002/anie.201107817>.
- [73] N. Jayaprakash, J. Shen, S.S. Moganty, A. Corona, L.A. Archer, Porous Hollow Carbon@Sulfur Composites for High-Power Lithium-Sulfur Batteries, *Angew. Chem.* 123 (2011) 6026–6030. <https://doi.org/10.1002/ange.201100637>.
- [74] N. Li, M. Zheng, H. Lu, Z. Hu, C. Shen, X. Chang, G. Ji, J. Cao, Y. Shi, High-rate lithium–sulfur batteries promoted by reduced graphene oxide coating, *Chem Commun.* 48 (2012) 4106–4108. <https://doi.org/10.1039/C2CC17912A>.
- [75] L. Ji, M. Rao, H. Zheng, L. Zhang, Y. Li, W. Duan, J. Guo, E.J. Cairns, Y. Zhang, Graphene Oxide as a Sulfur Immobilizer in High Performance Lithium/Sulfur Cells, *J. Am. Chem. Soc.* 133 (2011) 18522–18525. <https://doi.org/10.1021/ja206955k>.

- [76] L. Ji, M. Rao, S. Aloni, L. Wang, E.J. Cairns, Y. Zhang, Porous carbon nanofiber–sulfur composite electrodes for lithium/sulfur cells, *Energy Env. Sci.* 4 (2011) 5053–5059. <https://doi.org/10.1039/C1EE02256C>.
- [77] G. Zheng, Y. Yang, J.J. Cha, S.S. Hong, Y. Cui, Hollow Carbon Nanofiber-Encapsulated Sulfur Cathodes for High Specific Capacity Rechargeable Lithium Batteries, *Nano Lett.* 11 (2011) 4462–4467. <https://doi.org/10.1021/nl2027684>.
- [78] D.-W. Wang, G. Zhou, F. Li, K.-H. Wu, G.Q. (Max) Lu, H.-M. Cheng, I.R. Gentle, A microporous–mesoporous carbon with graphitic structure for a high-rate stable sulfur cathode in carbonate solvent-based Li–S batteries, *Phys. Chem. Chem. Phys.* 14 (2012) 8703. <https://doi.org/10.1039/c2cp40808b>.
- [79] R. Dominko, A. Vizintin, G. Aquilanti, L. Stievano, M.J. Helen, A.R. Munnangi, M. Fichtner, I. Arcon, Polysulfides Formation in Different Electrolytes from the Perspective of X-ray Absorption Spectroscopy, *J. Electrochem. Soc.* 165 (2018) A5014–A5019. <https://doi.org/10.1149/2.0151801jes>.
- [80] E. Markevich, G. Salitra, A. Rosenman, Y. Talyosef, F. Chesneau, D. Aurbach, The effect of a solid electrolyte interphase on the mechanism of operation of lithium–sulfur batteries, *J. Mater. Chem. A.* 3 (2015) 19873–19883. <https://doi.org/10.1039/C5TA04613K>.
- [81] E. Markevich, G. Salitra, Y. Talyosef, F. Chesneau, D. Aurbach, Review—On the Mechanism of Quasi-Solid-State Lithiation of Sulfur Encapsulated in Microporous Carbons: Is the Existence of Small Sulfur Molecules Necessary?, *J. Electrochem. Soc.* 164 (2017) A6244–A6253. <https://doi.org/10.1149/2.0391701jes>.
- [82] R. Cao, W. Xu, D. Lv, J. Xiao, J.-G. Zhang, Anodes for Rechargeable Lithium-Sulfur Batteries, *Adv. Energy Mater.* 5 (2015) 1402273. <https://doi.org/10.1002/aenm.201402273>.
- [83] Y. Yang, G. Zheng, Y. Cui, A membrane-free lithium/polysulfide semi-liquid battery for large-scale energy storage, *Energy Env. Sci.* 6 (2013) 1552–1558. <https://doi.org/10.1039/C3EE00072A>.
- [84] R. Demir-Cakan, M. Morcrette, Gangulibabu, A. Guéguen, R. Dedryvère, J.-M. Tarascon, Li–S batteries: simple approaches for superior performance, *Energy Environ. Sci.* 6 (2013) 176. <https://doi.org/10.1039/c2ee23411d>.
- [85] J.-Q. Huang, Q. Zhang, H.-J. Peng, X.-Y. Liu, W.-Z. Qian, F. Wei, Ionic shield for polysulfides towards highly-stable lithium–sulfur batteries, *Energy Env. Sci.* 7 (2014) 347–353. <https://doi.org/10.1039/C3EE42223B>.
- [86] H. Kim, J.T. Lee, D.-C. Lee, M. Oschatz, W.I. Cho, S. Kaskel, G. Yushin, Enhancing performance of Li–S cells using a Li–Al alloy anode coating, *Electrochem. Commun.* 36 (2013) 38–41. <https://doi.org/10.1016/j.elecom.2013.09.002>.
- [87] P. Johansson, R. Demir-Cakan, A. Hayashi, M. Tatsumisago, Lithium–Sulfur Battery Electrolytes, in: *Li- Batter.*, n.d.: pp. 149–194. https://doi.org/10.1142/9781786342508_0004.
- [88] L. Suo, Y.-S. Hu, H. Li, M. Armand, L. Chen, A new class of Solvent-in-Salt electrolyte for high-energy rechargeable metallic lithium batteries, *Nat. Commun.* 4 (2013) 1481. <https://doi.org/10.1038/ncomms2513>.
- [89] L. Cheng, L.A. Curtiss, K.R. Zavadil, A.A. Gewirth, Y. Shao, K.G. Gallagher, Sparingly Solvating Electrolytes for High Energy Density Lithium–Sulfur Batteries, *ACS Energy Lett.* 1 (2016) 503–509. <https://doi.org/10.1021/acsenergylett.6b00194>.
- [90] X. Li, M. Banis, A. Lushington, X. Yang, Q. Sun, Y. Zhao, C. Liu, Q. Li, B. Wang, W. Xiao, C. Wang, M. Li, J. Liang, R. Li, Y. Hu, L. Goncharova, H. Zhang, T.-K. Sham, X. Sun, A high-energy sulfur cathode in carbonate electrolyte by eliminating polysulfides via solid-phase lithium-sulfur transformation, *Nat. Commun.* 9 (2018) 4509. <https://doi.org/10.1038/s41467-018-06877-9>.
- [91] A.A. Franco, Chapter 8: Computational Modeling of Lithium–Sulfur Batteries: Myths, Facts, and Controversies, in: R. Demir-Cakan (Ed.), *Li- Batter. Chall. Chem. Mater. Future Perspect.*, WORLD SCIENTIFIC (EUROPE), London, 2017: pp. 335–350. https://doi.org/10.1142/9781786342508_0008.

- [92] K. Kumaresan, Y. Mikhaylik, R.E. White, A Mathematical Model for a Lithium–Sulfur Cell, *J. Electrochem. Soc.* 155 (2008) A576–A582. <https://doi.org/10.1149/1.2937304>.
- [93] L. Wang, T. Zhang, S. Yang, F. Cheng, J. Liang, J. Chen, A quantum-chemical study on the discharge reaction mechanism of lithium-sulfur batteries, *J. Energy Chem.* 22 (2013) 72–77. [https://doi.org/10.1016/S2095-4956\(13\)60009-1](https://doi.org/10.1016/S2095-4956(13)60009-1).
- [94] Z. Liu, H. Deng, W. Hu, F. Gao, S. Zhang, P.B. Balbuena, P.P. Mukherjee, Revealing reaction mechanisms of nanoconfined Li_2S : implications for lithium–sulfur batteries, *Phys. Chem. Chem. Phys.* 20 (2018) 11713–11721. <https://doi.org/10.1039/C8CP01462K>.
- [95] X. Liu, X. Shao, F. Li, M. Zhao, Anchoring effects of S-terminated Ti_2C MXene for lithium-sulfur batteries: A first-principles study, *Appl. Surf. Sci.* 455 (2018) 522–526. <https://doi.org/10.1016/j.apsusc.2018.05.200>.
- [96] Q. Zhang, Y. Wang, Z.W. Seh, Z. Fu, R. Zhang, Y. Cui, Understanding the Anchoring Effect of Two-Dimensional Layered Materials for Lithium–Sulfur Batteries, *Nano Lett.* 15 (2015) 3780–3786. <https://doi.org/10.1021/acs.nanolett.5b00367>.
- [97] G.S. Yi, E.S. Sim, Y.-C. Chung, Effect of lithium-trapping on nitrogen-doped graphene as an anchoring material for lithium–sulfur batteries: a density functional theory study, *Phys Chem Chem Phys.* 19 (2017) 28189–28194. <https://doi.org/10.1039/C7CP04507G>.
- [98] K.C. Wasalathilake, M. Roknuzzaman, K. (Ken) Ostrikov, G.A. Ayoko, C. Yan, Interaction between functionalized graphene and sulfur compounds in a lithium–sulfur battery – a density functional theory investigation, *RSC Adv.* 8 (2018) 2271–2279. <https://doi.org/10.1039/C7RA11628D>.
- [99] Z. Liu, P.B. Balbuena, P.P. Mukherjee, Evaluating silicene as a potential cathode host to immobilize polysulfides in lithium–sulfur batteries, *J. Coord. Chem.* 69 (2016) 2090–2105. <https://doi.org/10.1080/00958972.2016.1184265>.
- [100] T.-Z. Hou, X. Chen, H.-J. Peng, J.-Q. Huang, B.-Q. Li, Q. Zhang, B. Li, Design Principles for Heteroatom-Doped Nanocarbon to Achieve Strong Anchoring of Polysulfides for Lithium-Sulfur Batteries, *Small.* 12 (2016) 3283–3291. <https://doi.org/10.1002/smll.201600809>.
- [101] Z. Feng, C. Kim, A. Vijn, M. Armand, K.H. Bevan, K. Zaghbi, Unravelling the role of Li_2S_2 in lithium–sulfur batteries: A first principles study of its energetic and electronic properties, *J. Power Sources.* 272 (2014) 518–521. <https://doi.org/10.1016/j.jpowsour.2014.07.078>.
- [102] Z. Liu, P.B. Balbuena, P.P. Mukherjee, Revealing Charge Transport Mechanisms in Li_2S_2 for Li–Sulfur Batteries, *J. Phys. Chem. Lett.* 8 (2017) 1324–1330. <https://doi.org/10.1021/acs.jpcllett.6b03063>.
- [103] H. Park, N. Kumar, M. Melander, T. Vegge, J.M. Garcia Lastra, D.J. Siegel, Adiabatic and Nonadiabatic Charge Transport in Li–S Batteries, *Chem. Mater.* 30 (2018) 915–928. <https://doi.org/10.1021/acs.chemmater.7b04618>.
- [104] S. Jeschke, P. Johansson, Predicting the Solubility of Sulfur: A COSMO-RS-Based Approach to Investigate Electrolytes for Li-S Batteries, *Chem. - Eur. J.* 23 (2017) 9130–9136. <https://doi.org/10.1002/chem.201701011>.
- [105] X. Chen, T. Hou, K.A. Persson, Q. Zhang, Combining theory and experiment in lithium–sulfur batteries: Current progress and future perspectives, *Mater. Today.* 22 (2019) 142–158. <https://doi.org/10.1016/j.mattod.2018.04.007>.
- [106] J. Hannauer, J. Scheers, J. Fullenwarth, B. Fraisse, L. Stievano, P. Johansson, The Quest for Polysulfides in Lithium-Sulfur Battery Electrolytes: An Operando Confocal Raman Spectroscopy Study, *ChemPhysChem.* 16 (2015) 2755–2759. <https://doi.org/10.1002/cphc.201500448>.
- [107] K.H. Wujcik, T.A. Pascal, C.D. Pemmaraju, D. Devaux, W.C. Stolte, N.P. Balsara, D. Prendergast, Characterization of Polysulfide Radicals Present in an Ether-Based Electrolyte of a Lithium-Sulfur Battery During Initial Discharge Using In Situ X-Ray Absorption Spectroscopy Experiments and First-Principles Calculations, *Adv. Energy Mater.* 5 (2015) 1500285. <https://doi.org/10.1002/aenm.201500285>.

- [108] C. Park, M. Kanduč, R. Chudoba, A. Ronneburg, S. Risse, M. Ballauff, J. Dzubiella, Molecular simulations of electrolyte structure and dynamics in lithium–sulfur battery solvents, *J. Power Sources*. 373 (2018) 70–78. <https://doi.org/10.1016/j.jpowsour.2017.10.081>.
- [109] C. Li, A.L. Ward, S.E. Doris, T.A. Pascal, D. Prendergast, B.A. Helms, Polysulfide-Blocking Microporous Polymer Membrane Tailored for Hybrid Li-Sulfur Flow Batteries, *Nano Lett.* 15 (2015) 5724–5729. <https://doi.org/10.1021/acs.nanolett.5b02078>.
- [110] S. Perez Beltran, P.B. Balbuena, Formation of Multilayer Graphene Domains with Strong Sulfur-Carbon Interaction and Enhanced Sulfur Reduction Zones for Lithium-Sulfur Battery Cathodes, *ChemSusChem*. (2018). <https://doi.org/10.1002/cssc.201702446>.
- [111] Z. Liu, P.P. Mukherjee, Mesoscale Elucidation of Surface Passivation in the Li–Sulfur Battery Cathode, *ACS Appl. Mater. Interfaces*. 9 (2017) 5263–5271. <https://doi.org/10.1021/acsami.6b15066>.
- [112] T.A. Pascal, I. Villaluenga, K.H. Wujcik, D. Devaux, X. Jiang, D.R. Wang, N. Balsara, D. Prendergast, Liquid Sulfur Impregnation of Microporous Carbon Accelerated by Nanoscale Interfacial Effects, *Nano Lett.* 17 (2017) 2517–2523. <https://doi.org/10.1021/acs.nanolett.7b00249>.
- [113] A.F. Hofmann, D.N. Fronczek, W.G. Bessler, Mechanistic modeling of polysulfide shuttle and capacity loss in lithium–sulfur batteries, *J. Power Sources*. 259 (2014) 300–310. <https://doi.org/10.1016/j.jpowsour.2014.02.082>.
- [114] T. Zhang, M. Marinescu, S. Walus, G.J. Offer, Modelling transport-limited discharge capacity of lithium-sulfur cells, *Electrochimica Acta*. 219 (2016) 502–508. <https://doi.org/10.1016/j.electacta.2016.10.032>.
- [115] A. Yermukhambetova, C. Tan, S.R. Daemi, Z. Bakenov, J.A. Darr, D.J.L. Brett, P.R. Shearing, Exploring 3D microstructural evolution in Li-Sulfur battery electrodes using in-situ X-ray tomography, *Sci. Rep.* 6 (2016). <https://doi.org/10.1038/srep35291>.
- [116] F.Y. Fan, W.C. Carter, Y.-M. Chiang, Mechanism and Kinetics of Li₂S Precipitation in Lithium-Sulfur Batteries, *Adv. Mater.* 27 (2015) 5203–5209. <https://doi.org/10.1002/adma.201501559>.
- [117] F.Y. Fan, Y.-M. Chiang, Electrodeposition Kinetics in Li-S Batteries: Effects of Low Electrolyte/Sulfur Ratios and Deposition Surface Composition, *J. Electrochem. Soc.* 164 (2017) A917–A922. <https://doi.org/10.1149/2.0051706jes>.
- [118] P. Andrei, C. Shen, J.P. Zheng, Theoretical and experimental analysis of precipitation and solubility effects in lithium-sulfur batteries, *Electrochimica Acta*. 284 (2018) 469–484. <https://doi.org/10.1016/j.electacta.2018.07.045>.
- [119] V. Thangavel, K.-H. Xue, Y. Mammeri, M. Quiroga, A. Mastouri, C. Guéry, P. Johansson, M. Morcrette, A.A. Franco, A Microstructurally Resolved Model for Li-S Batteries Assessing the Impact of the Cathode Design on the Discharge Performance, *J. Electrochem. Soc.* 163 (2016) A2817–A2829. <https://doi.org/10.1149/2.0051614jes>.
- [120] Y.X. Ren, T.S. Zhao, M. Liu, P. Tan, Y.K. Zeng, Modeling of lithium-sulfur batteries incorporating the effect of Li₂S precipitation, *J. Power Sources*. 336 (2016) 115–125. <https://doi.org/10.1016/j.jpowsour.2016.10.063>.
- [121] T. Zhang, M. Marinescu, L. O’Neill, M. Wild, G. Offer, Modeling the voltage loss mechanisms in lithium–sulfur cells: the importance of electrolyte resistance and precipitation kinetics, *Phys. Chem. Chem. Phys.* 17 (2015) 22581–22586. <https://doi.org/10.1039/C5CP03566J>.
- [122] T. Zhang, M. Marinescu, S. Walus, P. Kovacic, G.J. Offer, What Limits the Rate Capability of Li-S Batteries during Discharge: Charge Transfer or Mass Transfer?, *J. Electrochem. Soc.* 165 (2018) A6001–A6004.
- [123] A. Mistry, P.P. Mukherjee, Precipitation–Microstructure Interactions in the Li-Sulfur Battery Electrode, *J. Phys. Chem. C*. 121 (2017) 26256–26264. <https://doi.org/10.1021/acs.jpcc.7b09997>.

- [124] S. Perez Beltran, P.B. Balbuena, Formation of Multilayer Graphene Domains with Strong Sulfur–Carbon Interaction and Enhanced Sulfur Reduction Zones for Lithium–Sulfur Battery Cathodes, *ChemSusChem*. 11 (2018) 1970–1980. <https://doi.org/10.1002/cssc.201702446>.
- [125] Z. Liu, P.P. Mukherjee, Mesoscale Elucidation of Surface Passivation in the Li–Sulfur Battery Cathode, *ACS Appl. Mater. Interfaces*. 9 (2017) 5263–5271. <https://doi.org/10.1021/acsami.6b15066>.
- [126] T. Zhang, M. Marinescu, L. O’Neill, M. Wild, G. Offer, Modeling the voltage loss mechanisms in lithium–sulfur cells: the importance of electrolyte resistance and precipitation kinetics, *Phys. Chem. Chem. Phys.* 17 (2015) 22581–22586. <https://doi.org/10.1039/C5CP03566J>.
- [127] M. Ghaznavi, P. Chen, Sensitivity analysis of a mathematical model of lithium–sulfur cells part I: Applied discharge current and cathode conductivity, *J. Power Sources*. 257 (2014) 394–401. <https://doi.org/10.1016/j.jpowsour.2013.10.135>.
- [128] T. Zhang, M. Marinescu, S. Walus, P. Kovacic, G.J. Offer, What Limits the Rate Capability of Li-S Batteries during Discharge: Charge Transfer or Mass Transfer?, *J. Electrochem. Soc.* 165 (2018) A6001–A6004.
- [129] V. Thangavel, O.X. Guerrero, M. Quiroga, A.M. Mikala, A. Rucci, A.A. Franco, A three dimensional kinetic Monte Carlo model for simulating the carbon/sulfur mesostructural evolutions of discharging lithium sulfur batteries, *Energy Storage Mater.* 24 (2020) 472–485. <https://doi.org/10.1016/j.ensm.2019.07.011>.
- [130] Y. Ma, H. Zhang, B. Wu, M. Wang, X. Li, H. Zhang, Lithium Sulfur Primary Battery with Super High Energy Density: Based on the Cauliflower-like Structured C/S Cathode, *Sci. Rep.* 5 (2015) 14949. <https://doi.org/10.1038/srep14949>.
- [131] J. Zheng, M. Gu, M.J. Wagner, K.A. Hays, X. Li, P. Zuo, C. Wang, J.-G. Zhang, J. Liu, J. Xiao, Revisit Carbon/Sulfur Composite for Li-S Batteries, *J. Electrochem. Soc.* 160 (2013) A1624–A1628. <https://doi.org/10.1149/2.013310jes>.
- [132] A. Stukowski, Visualization and analysis of atomistic simulation data with OVITO—the Open Visualization Tool, *Model. Simul. Mater. Sci. Eng.* 18 (2010) 015012. <https://doi.org/10.1088/0965-0393/18/1/015012>.
- [133] M.A. Quiroga, A.A. Franco, A Multi-Paradigm Computational Model of Materials Electrochemical Reactivity for Energy Conversion and Storage, *J. Electrochem. Soc.* 162 (2015) E73–E83. <https://doi.org/10.1149/2.1011506jes>.
- [134] G. Blanquer, Y. Yin, M.A. Quiroga, A.A. Franco, Modeling Investigation of the Local Electrochemistry in Lithium–O₂ Batteries: A Kinetic Monte Carlo Approach, *J. Electrochem. Soc.* 163 (2016) A329–A337. <https://doi.org/10.1149/2.0841602jes>.
- [135] Y. Yin, R. Zhao, Y. Deng, A.A. Franco, Compactness of the Lithium Peroxide Thin Film Formed in Li–O₂ Batteries and Its Link to the Charge Transport Mechanism: Insights from Stochastic Simulations, *J. Phys. Chem. Lett.* 8 (2017) 599–604. <https://doi.org/10.1021/acs.jpcclett.6b02732>.
- [136] G. Shukla, D. del Olmo Diaz, V. Thangavel, A.A. Franco, Self-Organization of Electroactive Suspensions in Discharging Slurry Batteries: A Mesoscale Modeling Investigation, *ACS Appl. Mater. Interfaces*. 9 (2017) 17882–17889. <https://doi.org/10.1021/acsami.7b02567>.
- [137] G. Shukla, A.A. Franco, Handling Complexity of Semisolid Redox Flow Battery Operation Principles through Mechanistic Simulations, *J. Phys. Chem. C*. 122 (2018) 23867–23877. <https://doi.org/10.1021/acs.jpcc.8b06642>.
- [138] M. Marinescu, T. Zhang, G.J. Offer, A zero dimensional model of lithium–sulfur batteries during charge and discharge, *Phys. Chem. Chem. Phys.* 18 (2016) 584–593. <https://doi.org/10.1039/C5CP05755H>.
- [139] T. Danner, G. Zhu, A.F. Hofmann, A. Latz, Modeling of nano-structured cathodes for improved lithium-sulfur batteries, *Electrochimica Acta*. 184 (2015) 124–133. <https://doi.org/10.1016/j.electacta.2015.09.143>.
- [140] A.D. Dysart, J.C. Burgos, A. Mistry, C.-F. Chen, Z. Liu, C.N. Hong, P.B. Balbuena, P.P. Mukherjee, V.G. Pol, Towards next generation lithium-sulfur batteries: non-conventional carbon

- compartments/sulfur electrodes and multi-scale analysis, *J. Electrochem. Soc.* 163 (2016) A730–A741. <https://doi.org/10.1149/2.0481605jes>.
- [141] Y.X. Ren, T.S. Zhao, M. Liu, P. Tan, Y.K. Zeng, Modeling of lithium-sulfur batteries incorporating the effect of Li₂S precipitation, *J. Power Sources*. 336 (2016) 115–125. <https://doi.org/10.1016/j.jpowsour.2016.10.063>.
- [142] J.P. Neidhardt, D.N. Fronczek, T. Jahnke, T. Danner, B. Horstmann, W.G. Bessler, A Flexible Framework for Modeling Multiple Solid, Liquid and Gaseous Phases in Batteries and Fuel Cells, *J. Electrochem. Soc.* 159 (2012) A1528–A1542. <https://doi.org/10.1149/2.023209jes>.
- [143] Z. Li, Y. Zhou, Y. Wang, Y.-C. Lu, Solvent-Mediated Li₂S Electrodeposition: A Critical Manipulator in Lithium-Sulfur Batteries, *Adv. Energy Mater.* 9 (2019) 1802207. <https://doi.org/10.1002/aenm.201802207>.
- [144] A. Bewick, M. Fleischmann, H.R. Thirsk, Kinetics of the electrocrystallization of thin films of calomel, *Trans. Faraday Soc.* 58 (1962) 2200. <https://doi.org/10.1039/tf9625802200>.
- [145] M. Jafarian, M.G. Mahjani, F. Gobal, I. Danaee, Effect of potential on the early stage of nucleation and growth during aluminum electrocrystallization from molten salt (AlCl₃–NaCl–KCl), *J. Electroanal. Chem.* 588 (2006) 190–196. <https://doi.org/10.1016/j.jelechem.2005.12.028>.
- [146] S. Waluś, C. Barchasz, R. Bouchet, J.-C. Leprêtre, J.-F. Colin, J.-F. Martin, E. Elkaïm, C. Baetz, F. Alloin, Lithium/Sulfur Batteries Upon Cycling: Structural Modifications and Species Quantification by In Situ and Operando X-Ray Diffraction Spectroscopy, *Adv. Energy Mater.* 5 (2015) 1500165. <https://doi.org/10.1002/aenm.201500165>.
- [147] M. Ester, H.-P. Kriegel, J. Sander, X. Xu, CiteSeerX — A density-based algorithm for discovering clusters in large spatial databases with noise, (n.d.). <https://citeseerx.ist.psu.edu/viewdoc/summary?doi=10.1.1.121.9220> (accessed February 5, 2019).
- [148] K. Kumaresan, Y. Mikhaylik, R.E. White, A Mathematical Model for a Lithium – Sulfur Cell, (2008) 576–582. <https://doi.org/10.1149/1.2937304>.
- [149] J.P. Neidhardt, D.N. Fronczek, T. Jahnke, T. Danner, B. Horstmann, W.G. Bessler, A Flexible Framework for Modeling Multiple Solid , Liquid and Gaseous Phases in Batteries and Fuel Cells, 159 (2012) 1528–1542. <https://doi.org/10.1149/2.023209jes>.
- [150] D.N. Fronczek, W.G. Bessler, Author ' s personal copy Insight into lithium e sulfur batteries : Elementary kinetic modeling and impedance simulation Author ' s personal copy, 244 (2013) 183–188.
- [151] A.F. Hofmann, D.N. Fronczek, W.G. Bessler, Mechanistic modeling of polysul fi de shuttle and capacity loss in lithium e sulfur batteries, *J. Power Sources*. 259 (2014) 300–310. <https://doi.org/10.1016/j.jpowsour.2014.02.082>.
- [152] M. Ghaznavi, P. Chen, Sensitivity analysis of a mathematical model of lithium e sulfur cells : Part II : Precipitation reaction kinetics and sulfur content, *J. Power Sources*. 257 (2014) 402–411. <https://doi.org/10.1016/j.jpowsour.2013.12.145>.
- [153] M. Ghaznavi, P. Chen, Sensitivity analysis of a mathematical model of lithium e sulfur cells part I : Applied discharge current and cathode conductivity, *J. Power Sources*. 257 (2014) 394–401. <https://doi.org/10.1016/j.jpowsour.2013.10.135>.
- [154] M. Ghaznavi, P. Chen, *Electrochimica Acta* Analysis of a Mathematical Model of Lithium-Sulfur Cells Part III : Electrochemical Reaction Kinetics , Transport Properties and Charging, *Electrochimica Acta*. 137 (2014) 575–585. <https://doi.org/10.1016/j.electacta.2014.06.033>.
- [155] T. Danner, G. Zhu, A.F. Hofmann, A. Latz, *Electrochimica Acta* Modeling of nano-structured cathodes for improved lithium-sulfur batteries, *Electrochimica Acta*. 184 (2015) 124–133. <https://doi.org/10.1016/j.electacta.2015.09.143>.
- [156] A.D. Dysart, J.C. Burgos, A. Mistry, C. Chen, Z. Liu, C.N. Hong, P.B. Balbuena, P.P. Mukherjee, V.G. Pol, Towards Next Generation Lithium-Sulfur Batteries : Non-Conventional Carbon Compartments / Sulfur Electrodes and Multi-Scale Analysis, 163 (2016) 730–741. <https://doi.org/10.1149/2.0481605jes>.

- [157] V. Thangavel, K.-H. Xue, Y. Mammeri, M. Quiroga, A. Mastouri, C. Guéry, P. Johansson, M. Morcrette, A.A. Franco, A Microstructurally Resolved Model for Li-S Batteries Assessing the Impact of the Cathode Design on the Discharge Performance, *J. Electrochem. Soc.* 163 (2016) A2817–A2829.
- [158] N. Jayaprakash, J. Shen, S.S. Moganty, a. Corona, L. a. Archer, Porous hollow carbon@sulfur composites for high-power lithium-sulfur batteries, *Angew. Chem. - Int. Ed.* 50 (2011) 5904–5908. <https://doi.org/10.1002/anie.201100637>.
- [159] J. Shim, K.A. Striebel, E.J. Cairns, The Lithium Sulfur Rechargeable Cell Effects of Electrode Composition and Solvent on Cell Performance, (2002) 1321–1325. <https://doi.org/10.1149/1.1503076>.
- [160] S.-E. Cheon, K.-S. Ko, J.-H. Cho, S.-W. Kim, E.-Y. Chin, H.-T. Kim, Rechargeable Lithium Sulfur Battery, *J. Electrochem. Soc.* 150 (2003) A796. <https://doi.org/10.1149/1.1571532>.
- [161] V. Thangavel, M. Morcrette, A. Franco, HELIS project D6.2 deliverable report - databases for results produced using interfacial models, (2017). https://www.helis-project.eu//docstation/com_content/article/181/helis_project_deliverable_d6_2_final.pdf.
- [162] D. a. G. Bruggeman, Berechnung verschiedener physikalischer Konstanten von heterogenen Substanzen. I. Dielektrizitätskonstanten und Leitfähigkeiten der Mischkörper aus isotropen Substanzen, *Ann. Phys.* 416 (1935) 969–664. <https://doi.org/10.1002/andp.19354160802>.
- [163] T.F. Fuller, M. Doyle, J. Newman, Simulation and Optimization of the Dual Lithium Ion Insertion Cell, *J. Electrochem. Soc.* 141 (1994) 1–10. <https://doi.org/10.1149/1.2054684>.
- [164] B.Y.M. Kunitz, AN E M P I R I C A L FORMULA FOR T H E RELATION B E T W E E N VISCOSITY OF SOLUTION AND VOLUME OF SOLUTE ., (1926) 715–725.
- [165] K. Xue, T. Nguyen, A.A. Franco, Impact of the Cathode Microstructure on the Discharge Performance of Lithium Air Batteries : A Multiscale Model P + Q Air inlet, 161 (2014) 3028–3035. <https://doi.org/10.1149/2.002408jes>.
- [166] K. Xue, E. Mcturk, L. Johnson, P.G. Bruce, A. a Franco, A Comprehensive Model for Non-Aqueous Lithium Air Batteries Involving Different Reaction Mechanisms, 162 (2015) 614–621. <https://doi.org/10.1149/2.0121504jes>.
- [167] M. a. Quiroga, K.-H.K.-H. Xue, T.-K.T.-K. Nguyen, M. Tułodziecki, H.H. Huang, A. a. Franco, M. Tu odziecki, A Multiscale Model of Electrochemical Double Layers in Energy Conversion and Storage Devices, *J. Electrochem. Soc.* 161 (2014) E3302–E3310. <https://doi.org/10.1149/2.029408jes>.
- [168] Z. Deng, Z. Zhang, Y. Lai, J. Liu, J. Li, Y. Liu, Electrochemical Impedance Spectroscopy Study of a Lithium/Sulfur Battery: Modeling and Analysis of Capacity Fading, *J. Electrochem. Soc.* 160 (2013) A553–A558. <https://doi.org/10.1149/2.026304jes>.
- [169] N.A. Ca??as, S. Wolf, N. Wagner, K.A. Friedrich, In-situ X-ray diffraction studies of lithium-sulfur batteries, *J. Power Sources.* 226 (2013) 313–319. <https://doi.org/10.1016/j.jpowsour.2012.10.092>.
- [170] N. Ding, S. Wei, T.S.A. Hor, Z. Liu, Y. Zong, Key parameters in design of lithium sulfur batteries, *J. Power Sources.* 269 (2014) 111–116. <https://doi.org/10.1016/j.jpowsour.2014.07.008>.
- [171] M. Ghaznavi, P. Chen, Analysis of a Mathematical Model of Lithium-Sulfur Cells Part III: Electrochemical Reaction Kinetics, Transport Properties and Charging, *Electrochimica Acta.* 137 (2014) 575–585. <https://doi.org/10.1016/j.electacta.2014.06.033>.
- [172] M.V. Merritt, D.T. Sawyer, Electrochemical reduction of elemental sulfur in aprotic solvents. Formation of a stable S8-species, *Inorg. Chem.* 9 (1970) 211–215.
- [173] N. XIE, Y. HUANG, Studies on electroreduction mechanism of sulfur in aprotic medium II: Researches of the second redox step, *Chin J Org Chem.* 47 (1989) 227–232.
- [174] N. XIE, Y. HUANG, Studies on electroreduction mechanism of sulfur in aprotic medium I: Researches of the first redox step, *Chin J Org Chem.* 46 (1988) 631–638.

- [175] B.-S. Kim, S.-M. Park, In situ spectroelectrochemical studies on the reduction of sulfur in dimethyl sulfoxide solutions, *J. Electrochem. Soc.* 140 (1993) 115–122.
- [176] D.-H. Han, B.-S. Kim, S.-J. Choi, Y. Jung, J. Kwak, S.-M. Park, Time-Resolved In Situ Spectroelectrochemical Study on Reduction of Sulfur in N,N[^{sup}']-Dimethylformamide, *J. Electrochem. Soc.* 151 (2004) E283–E290. <https://doi.org/10.1149/1.1773733>.
- [177] F. Gaillard, E. Levillain, Visible time-resolved spectroelectrochemistry: application to study of the reduction of sulfur (S₈) in dimethylformamide, *J. Electroanal. Chem.* 398 (1995) 77–87.
- [178] Q. Zou, Y.-C. Lu, Solvent-Dictated Lithium Sulfur Redox Reactions: An Operando UV–vis Spectroscopic Study, *J. Phys. Chem. Lett.* 7 (2016) 1518–1525. <https://doi.org/10.1021/acs.jpcllett.6b00228>.
- [179] Y. Jung, S. Kim, B.-S. Kim, D.-H. Han, S.-M. Park, J. Kwak, Effect of organic solvents and electrode materials on electrochemical reduction of sulfur, *Int J Electrochem Sci.* 3 (2008) 566–577.
- [180] N.S.A. Manan, L. Aldous, Y. Alias, P. Murray, L.J. Yellowlees, M.C. Lagunas, C. Hardacre, Electrochemistry of Sulfur and Polysulfides in Ionic Liquids, *J. Phys. Chem. B.* 115 (2011) 13873–13879. <https://doi.org/10.1021/jp208159v>.
- [181] H. Yamin, A. Gorenshtein, J. Penciner, Y. Sternberg, E. Peled, Oxidation/Reduction Mechanisms of Polysulfides in THF Solutions, *J. Electrochem. Soc.* (1988) 4.
- [182] S.E. Doris, A.L. Ward, P.D. Frischmann, L. Li, B.A. Helms, Understanding and controlling the chemical evolution and polysulfide-blocking ability of lithium–sulfur battery membranes cast from polymers of intrinsic microporosity, *J. Mater. Chem. A.* 4 (2016) 16946–16952. <https://doi.org/10.1039/C6TA06401A>.
- [183] E. Levillain, F. Gaillard, P. Leghie, A. Demortier, J.P. Lelieur, On the understanding of the reduction of sulfur (S₈) in dimethylformamide (DMF), *J. Electroanal. Chem.* 420 (1997) 167–177.
- [184] F. Gaillard, E. Levillain, J.P. Lelieur, Polysulfides in dimethylformamide: Only the radical anions S₃⁻ and S₄⁻ are reducible, *J. Electroanal. Chem.* 432 (1997) 129–138.
- [185] E. Levillain, A. Demortier, J.P. Lelieur, Reduction of S₋₃ and S₂₋₆ polysulfide ions in liquid ammonia, *J. Electroanal. Chem.* 394 (1995) 205–210.
- [186] S. Hess, M. Wohlfahrt-Mehrens, M. Wachtler, Flammability of Li-Ion Battery Electrolytes: Flash Point and Self-Extinguishing Time Measurements, *J. Electrochem. Soc.* 162 (2015) A3084–A3097. <https://doi.org/10.1149/2.0121502jes>.
- [187] M.R. Kaiser, S. Chou, H.-K. Liu, S.-X. Dou, C. Wang, J. Wang, Structure-Property Relationships of Organic Electrolytes and Their Effects on Li/S Battery Performance, *Adv. Mater.* 29 (2017) 1700449. <https://doi.org/10.1002/adma.201700449>.
- [188] D. Di Lecce, L. Carbone, V. Gancitano, J. Hassoun, Rechargeable lithium battery using non-flammable electrolyte based on tetraethylene glycol dimethyl ether and olivine cathodes, *J. Power Sources.* 334 (2016) 146–153. <https://doi.org/10.1016/j.jpowsour.2016.09.164>.
- [189] Y.-C. Lu, Q. He, H.A. Gasteiger, Probing the Lithium–Sulfur Redox Reactions: A Rotating-Ring Disk Electrode Study, *J. Phys. Chem. C.* 118 (2014) 5733–5741. <https://doi.org/10.1021/jp500382s>.
- [190] D. Zheng, X. Zhang, J. Wang, D. Qu, X. Yang, D. Qu, Reduction mechanism of sulfur in lithium–sulfur battery: From elemental sulfur to polysulfide, *J. Power Sources.* 301 (2016) 312–316. <https://doi.org/10.1016/j.jpowsour.2015.10.002>.
- [191] A. Evans, M.I. Montenegro, D. Pletcher, The mechanism for the cathodic reduction of sulphur in dimethylformamide: low temperature voltammetry, *Electrochem. Commun.* 3 (2001) 514–518.
- [192] J.W. Dibden, N. Meddings, J.R. Owen, N. Garcia-Araez, Quantitative Galvanostatic Intermittent Titration Technique for the Analysis of a Model System with Applications in Lithium–Sulfur Batteries, *ChemElectroChem.* (2017). <https://doi.org/10.1002/celec.201701004>.
- [193] R.G. Compton, E. Laborda, K.R. Ward, *Understanding voltammetry: simulation of electrode processes*, Imperial College Press, London, 2014.

- [194] S. Drvarič Talian, J. Moškon, R. Dominko, M. Gaberšček, Reactivity and Diffusivity of Li Polysulfides: A Fundamental Study Using Impedance Spectroscopy, *ACS Appl. Mater. Interfaces*. 9 (2017) 29760–29770. <https://doi.org/10.1021/acsami.7b08317>.
- [195] M. Cuisinier, C. Hart, M. Balasubramanian, A. Garsuch, L.F. Nazar, Radical or Not Radical: Revisiting Lithium-Sulfur Electrochemistry in Nonaqueous Electrolytes, *Adv. Energy Mater.* 5 (2015) 1401801. <https://doi.org/10.1002/aenm.201401801>.
- [196] H.-L. Wu, L.A. Huff, A.A. Gewirth, In Situ Raman Spectroscopy of Sulfur Speciation in Lithium–Sulfur Batteries, *ACS Appl. Mater. Interfaces*. 7 (2015) 1709–1719. <https://doi.org/10.1021/am5072942>.
- [197] D. Zheng, X. Zhang, J. Wang, D. Qu, X. Yang, D. Qu, Reduction mechanism of sulfur in lithium–sulfur battery: From elemental sulfur to polysulfide, *J. Power Sources*. 301 (2016) 312–316. <https://doi.org/10.1016/j.jpowsour.2015.10.002>.
- [198] Y. Gorlin, M.U.M. Patel, A. Freiberg, Q. He, M. Piana, M. Tromp, H.A. Gasteiger, Understanding the Charging Mechanism of Lithium-Sulfur Batteries Using Spatially Resolved Operando X-Ray Absorption Spectroscopy, *J. Electrochem. Soc.* 163 (2016) A930–A939. <https://doi.org/10.1149/2.0631606jes>.
- [199] J. Conder, R. Bouchet, S. Trubesinger, C. Marino, L. Gubler, C. Villevieille, Direct observation of lithium polysulfides in lithium–sulfur batteries using operando X-ray diffraction, *Nat. Energy*. 2 (2017) 17069. <https://doi.org/10.1038/nenergy.2017.69>.
- [200] S.E. Doris, A.L. Ward, P.D. Frischmann, L. Li, B.A. Helms, Understanding and controlling the chemical evolution and polysulfide-blocking ability of lithium–sulfur battery membranes cast from polymers of intrinsic microporosity, *J. Mater. Chem. A*. 4 (2016) 16946–16952. <https://doi.org/10.1039/C6TA06401A>.
- [201] S.-H. Yu, X. Huang, K. Schwarz, R. Huang, T.A. Arias, J.D. Brock, H.D. Abruña, Direct visualization of sulfur cathodes: new insights into Li–S batteries *via operando* X-ray based methods, *Energy Environ. Sci.* 11 (2018) 202–210. <https://doi.org/10.1039/C7EE02874A>.
- [202] Y. Yang, G. Zheng, S. Misra, J. Nelson, M.F. Toney, Y. Cui, High-Capacity Micrometer-Sized Li₂S Particles as Cathode Materials for Advanced Rechargeable Lithium-Ion Batteries, *J. Am. Chem. Soc.* 134 (2012) 15387–15394. <https://doi.org/10.1021/ja3052206>.
- [203] F.Y. Fan, W.C. Carter, Y.-M. Chiang, Mechanism and Kinetics of Li₂S Precipitation in Lithium-Sulfur Batteries, *Adv. Mater.* 27 (2015) 5203–5209. <https://doi.org/10.1002/adma.201501559>.
- [204] B. Scharifker, G. Hills, Theoretical and experimental studies of multiple nucleation, *Electrochimica Acta*. 28 (1983) 879–889. [https://doi.org/10.1016/0013-4686\(83\)85163-9](https://doi.org/10.1016/0013-4686(83)85163-9).
- [205] T. Danner, A. Latz, On the influence of nucleation and growth of S₈ and Li₂S in lithium-sulfur batteries, *Electrochimica Acta*. 322 (2019) 134719. <https://doi.org/10.1016/j.electacta.2019.134719>.
- [206] D. PLETCHER, R. GREFF, R. PEAT, L.M. PETER, J. ROBINSON, 9 - Electrocrystallisation, in: D. PLETCHER, R. GREFF, R. PEAT, L.M. PETER, J. ROBINSON (Eds.), *Instrum. Methods Electrochem.*, Woodhead Publishing, 2010: pp. 283–316. <https://doi.org/10.1533/9781782420545.283>.
- [207] Y. Yin, A. Torayev, C. Gaya, Y. Mammeri, A.A. Franco, Linking the Performances of Li–O₂ Batteries to Discharge Rate and Electrode and Electrolyte Properties through the Nucleation Mechanism of Li₂O₂, *J. Phys. Chem. C*. 121 (2017) 19577–19585. <https://doi.org/10.1021/acs.jpcc.7b05224>.
- [208] F. Kubel, B. Bertheville, H. Bill, Crystal structure of dilithiumsulfide, Li₂S, *Z. Für Krist. - New Cryst. Struct.* 214 (1999). <https://doi.org/10.1515/ncrs-1999-0303>.
- [209] H. Park, H.S. Koh, D.J. Siegel, First-Principles Study of Redox End Members in Lithium–Sulfur Batteries, *J. Phys. Chem. C*. 119 (2015) 4675–4683. <https://doi.org/10.1021/jp513023v>.
- [210] R. Demir-Cakan, Li-S Batteries: The Challenges, Chemistry, Materials and Future Perspectives, *WORLD SCIENTIFIC (EUROPE)*, 2017. <https://doi.org/10.1142/q0074>.
- [211] V. Thangavel, O.X. Guerrero, M. Quiroga, A.M. Mikala, A. Rucci, A.A. Franco, A three dimensional kinetic Monte Carlo model for simulating the carbon/sulfur mesostructural

- evolutions of discharging lithium sulfur batteries, *Energy Storage Mater.* (2019). <https://doi.org/10.1016/j.ensm.2019.07.011>.
- [212] F.Y. Fan, W.C. Carter, Y.-M. Chiang, Mechanism and Kinetics of Li_2S Precipitation in Lithium-Sulfur Batteries, *Adv. Mater.* 27 (2015) 5203–5209. <https://doi.org/10.1002/adma.201501559>.

Appendix I: List of acronyms and abbreviations

| | |
|----------|---|
| 1D | One-dimensional |
| 2DI | Two-dimensional Instantaneous |
| 2DP | Two-dimensional Progressive |
| 3D | Three-dimensional |
| 3DI | Three-dimensional Instantaneous |
| 3DP | Three-dimensional Progressive |
| AB | Acetylene Black |
| BET | Brunauer-Emmet-Teller |
| BFT | Bewick, Fleishman and Thirsk |
| BJH | Barret-Joyner-Halenda |
| C/S | Carbon/Sulfur |
| COSMO-RS | Conductor like Screening Model for Real Solvent |
| CVs | Cyclic voltammograms |
| DBSCAN | Denisty-Based Spatial Clustering of Applications with Noise |
| DEC | Diethyl carbonate |
| DFT | Density Functional Theory |
| DL | Diffusion Layer |
| DMA | Dimethylacetamide |
| DMC | Dimethyl carbonate |
| DME | Dimethoxy ethane |
| DMF | Dimethylformamide |
| DoDs | Depths of Discharge |
| DOL | Dioxolane |
| E/S | Electrolyte/Sulfur |
| EC | Ethylene carbonate |
| EIS | Electrochemical Impedance Spectroscopy |
| EU | European Union |
| EVs | Electric Vehicles |
| G1 | Monoglyme |

| | |
|-------------------|--|
| G2 | Diglyme |
| G3 | Triglyme |
| G4 | Tetraglyme |
| GDP | Gross Domestic Product |
| GHG | Greenhouse Gas |
| HELiS | High Energy Lithium Sulphur batteries and cells |
| HFE | Hydrofluorinated ether |
| ICEs | Internal Combustion Engines |
| IPCC | Intergovernmental Panel for Climate Change |
| IRENA | International Renewable Energy Agency |
| kMC | kinetic Monte-Carlo |
| LIBs | Lithium-ion Batteries |
| Li-O ₂ | Lithium-oxygen |
| Li | Lithium |
| Lithium-ion | Lithium-ion |
| LJP | Liquid Junction Potential |
| LRCS | Laboratoire de Réactivité et Chimie des Solides |
| lsqnonlin | Nonlinear least-squares |
| LUC | Land Use Change |
| NIC | National Institute of Chemistry |
| NMP | N-Methyl-2-Pyrrolidone |
| OCP | Open Circuit Potential |
| OECD | Organization for Economic Co-operation and Development |
| PEG | Polyethylene Glycol |
| PEGDME | Polyethylene glycol dimethyl ether |
| PSH | Pumped Storage Hydropower |
| PVDF | Polyvinylidene fluoride |
| QSSR | Quasi-Solid-State Reaction |
| RDF | Radial Distribution Function |
| SEI | Solid Electrolyte Interphase |
| SEM | Scanning Electron Microscopy |

| | |
|--------|--------------------------------------|
| SH | Scharifker-Hill |
| SLI | Starting, Lighting and Ignition |
| TBAP | Tetra butyl ammonium perchlorate |
| TEGDME | Tetra ethylene glycol dimethyl ether |
| TEM | Transmission Electron Microscopy |
| TGA | Thermal Gravimetric Analysis |
| THF | Tetrahydrofuran |
| UAV | Unmanned Ariel Vehicle |
| UPS | Uninterruptible Power Supply |
| USA | United States of America |
| VE | Véhicules Electriques |
| VSSM | Variable Step Size Method |
| XAS | X-ray Absorption Spectroscopy |
| XRD | X-ray Diffraction |

Appendix II: List of nomenclatures

| Symbol | Description |
|----------------|---|
| K_j^{ele} | Kinetic rate constant of electrochemical reaction j |
| I | Current |
| n_j | Number of electrons in electrochemical reaction j |
| q_e | Charge of an electron |
| δ_e | Electron tunnelling distance |
| K_i^{diff} | Kinetic rate constant for the diffusion species i |
| k_B | Boltzmann constant |
| T | Temperature |
| r_i | Radius of species i |
| z | Diffusion distance |
| μ | Viscosity of the electrolyte |
| U^0 | Standard potential |
| K_T | Total rate constant |
| K_n | Rate constant of the n^{th} event |
| K_k^{chem} | Rate constant of a chemical reaction k |
| ρ_1 | First random number |
| ρ_2 | Second random number |
| Δt | Time step |
| ΔQ | Specific capacity change |
| $m_{S_{B(s)}}$ | Mass of solid sulfur |
| c_i | Concentration of species i |
| n_i | Number of specie i |
| N_A | Avogadro's Number |
| ε | Porosity |
| U | Equilibrium potential |
| R | Universal gas constant |
| F | Faraday's constant |

| | |
|-----------------|---|
| ρ_c | Number density of carbon particles |
| R_p | Radius of carbon particle |
| ε_1 | Inter-particle porosity |
| ε_2 | Mesoporosity |
| a_1 | Inter-particle specific surface area |
| a_2 | Mesoporous specific surface area |
| β | Bruggeman coefficient |
| η | Overpotential |
| i | Current density |
| E_j | Activation energy of electrochemical reaction j |
| P_{ij} | Stoichiometric coefficient of oxidized species i in electrochemical reaction j |
| Q_{ij} | Stoichiometric coefficient of reduced species i in electrochemical reaction j |
| I_G | Applied current |
| R_k | Rate of the precipitation/dissolution reaction k |
| k_k^{prec} | Rate constant of the precipitation/dissolution reaction k |
| h | Planck constant |
| κ | Frequency factor |
| D | Diffusion coefficient |
| g | Source/sink term for electrochemical reaction |
| G | Source/sink term for precipitation/dissolution reaction k |
| f | Intra-flux |
| γ_{ik} | Stoichiometric coefficient of species i in precipitation/dissolution reaction k |
| K_k^{sp} | Solubility product of precipitation/dissolution reaction k |
| K_{flux} | Rate constant of Intra-flux |
| δ_1 | Thickness of $\text{Li}_2\text{S}_{(s)}$ layer over mesoporous carbon particle |
| φ | Volume fraction of the suspended particles |
| \bar{V} | Partial molar volume |
| M_k | Molar mass of solid species k |
| ρ_k | Density of solid species k |
| ϵ_k | Volume fraction of solid species k |

| | |
|------------------------|--|
| $\omega_{Li_2S_{(s)}}$ | Volume fraction of $Li_2S_{(s)}$ which form as thin layer over carbon particle |
| δ_{DL} | Diffusion layer |
| t | Time |
| s_i | Source/sink term of species i brought about homogenous chemical reactions |
| k_j^f | Forward rate constant of homogenous chemical reaction j |
| K_j^{eq} | Equilibrium constant of chemical reaction j |
| ϑ_{ij} | Stoichiometric coefficient of species i of chemical reaction j |
| A | Electroactive surface area of the electrode |
| A^0 | Initial surface area of the electrode |
| a | Specific surface area of the electrode |
| N_i | Flux of species i |
| c_i^* | Bulk concentration of species i |
| S_{ij} | Stoichiometric coefficient |
| i_j | Current density of reaction j |
| E | Electrode potential |
| α_j | Transfer coefficient of electrochemical reaction j |
| I_t | Total current |
| Δx | Bin size of the control volume |
| r | Particle size of $Li_2S_{(s)}$ deposit |
| η_j | Overpotential of electrochemical reaction j |
| γ | Surface energy of $Li_2S_{(s)}$ deposit |
| ΔG_{bulk} | Bulk free energy for the formation $Li_2S_{(s)}$ nuclei |
| $\Delta G_{surface}$ | Surface free energy for the formation $Li_2S_{(s)}$ nuclei |
| ΔG^{homo} | Homogenous free energy for formation $Li_2S_{(s)}$ nuclei |
| ΔG^{hetero} | Heterogenous free energy for formation $Li_2S_{(s)}$ nuclei |
| E_{bind} | Binding energy of $Li_2S_{(s)}$ deposit over carbon surface |
| k_{nuc} | Rate of the $Li_2S_{(s)}$ nucleation reaction |
| k_{nuc}^0 | Rate constant of the $Li_2S_{(s)}$ nucleation reaction |
| i_{nuc} | Current density of the $Li_2S_{(s)}$ nucleation reaction |

| | |
|----------------|--|
| \dot{N} | Rate of increase of number density of $Li_2S_{(s)}$ nuclei |
| a^{free} | Deposit free specific surface area of the electrode |
| N_r | Number density of the $Li_2S_{(s)}$ deposits with size r |
| ϵ_r | Volume fraction of the $Li_2S_{(s)}$ deposits with size r |
| v_r | Volume of a $Li_2S_{(s)}$ deposit with size r |
| δ_{tun} | Electron tunnelling through $Li_2S_{(s)}$ deposits |
| L_{tun} | Scaling factor of the electron tunnelling probability function |
| a^{grow} | Specific surface area of the electrochemical $Li_2S_{(s)}$ growth reaction |
| Δr | Bin size of the $Li_2S_{(s)}$ particle size range |

Abstract (Résumé)

Résumé de la thèse en français

Les batteries Li-S ont attiré beaucoup d'attention au cours de la dernière décennie en raison de leur très haute densité d'énergie théorique de 2567 Wh.kg^{-1} . Cependant, l'évaluation de certains mécanismes des batteries Li-S et de leur limitation reste difficile. Dans le cadre de mes travaux de doctorat, nous avons mis au point de multiples modèles mathématiques qui aident à l'évaluation et à l'optimisation de certains phénomènes liés aux batteries Li-S. Nous avons développé un nouveau modèle de type Monte-Carlo cinétique 3D (kMC), qui simule la décharge des composites carbone/soufre (C/S) à l'échelle mésoscopique. Notre modèle kMC fournit également un aperçu des impacts du régime de décharge et de la quantité de soufre sur la microstructure des dépôts de $\text{Li}_2\text{S}_{(s)}$ à la surface du carbone. Nous avons également développé un modèle multi-échelles type de continuum pour étudier les impacts de l'architecture a électrodes de C/S sur la décharge a batteries. Afin de déterminer le mécanisme de réaction des polysulfures solvatés dans notre électrolyte expérimental (1 M LiTFSI dans TEGDME:DOL (v/v=1:1)), nous avons effectué des mesures par voltampérométrie cyclique de différentes solutions contenant du soufre solvaté et des polysulfures. Un modèle mathématique a été utilisé pour interpréter les caractéristiques des voltammogrammes cycliques expérimentaux. De plus, nous avons également développé un modèle de nucléation et de croissance pour comprendre les phénomènes d'électrodéposition de $\text{Li}_2\text{S}_{(s)}$ dans une cellule Li-S simplifiée. Enfin, nous avons réalisé des expériences galvanostatiques pour valider notre modèle de décharge.

Mots Clés: Batteries au lithium-soufre (Li-S), modèles mathématiques, modèle de type Monte-Carlo cinétique (kMC) 3D, modèle multi-échelle de type continuum pour simuler la décharge des batteries Li-S, modèle de nucléation et de croissance $\text{Li}_2\text{S}_{(s)}$, voltampérométrie cyclique de différentes solutions contenant du soufre et des polysulfures, décharge potentiostatique et galvanostatique des batteries Li-S.

Thesis abstract in English

Li-S batteries have attracted a lot of attention in the past decade due to their very high theoretical energy density of 2567 Wh.kg^{-1} . However, the assessment of some of Li-S batteries phenomena and limitations still remain challenging. In my PhD work, we have developed multiple mathematical models, which assist with assessment and optimization of some the Li-S batteries phenomena. We developed a novel 3D kinetic Monte-Carlo (kMC) model, which simulates the discharge of carbon/sulfur (C/S) composites at the mesoscopic level. Our kMC model also provides insights into the impacts of the discharge rate and sulfur loading on the mesoscale properties of the $\text{Li}_2\text{S}_{(s)}$ deposits over the carbon surface. We also developed a multi-scale continuum model to investigate the impacts of the C/S cathode design parameters on the discharge of Li-S batteries. In order to determine the reaction mechanism of the dissolved polysulfides in our experimental electrolyte (1 M LiTFSI in TEGDME:DOL (v/v=1:1)), we carried out cyclic voltammetry measurements of different electrolyte solutions containing dissolved sulfur and polysulfides. A mathematical model was used to interpret the reactions behind the characteristics of experimental cyclic voltammograms. Furthermore, we also developed a nucleation and growth model to understand the phenomena behind the $\text{Li}_2\text{S}_{(s)}$ electrodeposition in a simplified Li-S cell. Finally, we carried out some galvanostatic experiments using Li-S coin cells to validate our discharge model.

Keywords: Lithium sulfur (Li-S) batteries, mathematical models, 3D kinetic Monte-Carlo (kMC) model, Multi-scale continuum Li-S batteries discharge model, $\text{Li}_2\text{S}_{(s)}$ nucleation and growth model, cyclic voltammetry of dissolved sulfur and polysulfides, potentiostatic and galvanostatic discharge of Li-S batteries.